Demultiplexer Based on Integrated Concave Grating

By

Zhijian Sun

A Thesis
Submitted to the Faculty of Graduate Studies
In Partial Fulfillment of the Requirements
for the Degree of

Doctor of Philosophy

Department of Physics
University of Manitoba
Winnipeg, Manitoba

THE UNIVERSITY OF MANITOBA

FACULTY OF GRADUATE STUDIES

*****

COPYRIGHT PERMISSION PAGE

DEMULTIPLEXER BASED ON INTEGRATED CONCAVE GRATING

BY

ZHIJIAN SUN

A Thesis/Practicum submitted to the Faculty of Graduate Studies of The University of Manitoba in partial fulfillment of the requirements of the degree of

DOCTOR OF PHILOSOPHY

ABSTRACT

With the use of Wavelength Division Multiplexing (WDM) technology, the information capacity of a fiber optic communication system is greatly increased. The key components in WDM systems are wavelength multiplexers and demultiplexers. Integrated concave diffraction gratings may serve as WDM demultiplexers. The typical channel spacing of a demultiplexer based on integrated concave gratings reported by other groups is around 1 nm.

In this thesis, we demonstrated an integrated concave grating demultiplexer with 60 output channels and 0.144 nm channel spacing. The fiber-to-fiber insertion loss for the demultiplexer is from 18.6 dB for the longest wavelength channel to 29.8 dB for the shortest wavelength channel. Another integrated concave grating demultiplexer reported in this thesis has 120 output channels and 0.29 nm channel spacing. The fiber-to-fiber loss for this demultiplexer is between 20 dB and 30 dB for most channels. Simulation results shows that the high insertion loss and the loss difference from channel to channel are predominantly due to waveguide absorption and increase dramatically for wavelengths below 1539 nm. Demultiplexers with 256 output channels and 0.2 nm channel spacing; 64 output channels and 0.3 nm channel spacing; 64 output channels and 0.6 nm channel spacing are also addressed in this thesis. The polarization dependent losses for all demultiplexers are around 0.45 dB. The birefringence is typically 1.2 nm for our demultiplexers. A layer structure used to control the birefringence is studied.

In the future WDM networks, an integrated multiwavelength laser is required. Such a laser can be formed by integrating a concave diffraction grating with semiconductor amplifiers. Concave gratings with multiple passbands make it difficult to control the

absolute lasing wavelength. A chirped concave gratings only has one dominant passband, therefore is a good candidate for multiwavelength laser. Concave gratings with several chirping schemes are investigated in this thesis. The extinction ratio between the dominant passband and other passbands can be as high as 20.9 dB. Demultiplexers based on chirped concave gratings are designed.

ACKNOWLEDGEMENTS

I would like to thank my advisor Dr. K. A. McGreer for his technical advice and encouragement throughout this research project and the carefully reading of my thesis. I have greatly benefited in many ways by working with him.

All the fabrication work reported in this thesis was done at the Alberta Microelectronic Center (AMC). During my work at AMC, Dr. J. N. Broughton taught me how to do photolithography; how to use Reactive Ion Etch (RIE) set up, SEM and other equipment. He also provided some samples for me during my study. I would like to thank him for his technical help.

I would also like to thank graduate students: Heather Hnatiuk, Michael Smith, and Daniel Jackson, for their help and discussions during research.

TRLabs (Telecommunications Research Labs) has provided all facilities for my studies.

Finally I would like to express my gratitude to my wife for her support in completing this thesis.

CONTENTS

LIST OF FIGURES

LIST OF TABLES

CHAPTER ONE

INTRODUCTION

1.1 BACKGROUND

As the result of the proliferation of the internet and multimedia communication for business, education, and recreation, the demand to transport large volumes of data is explosively growing. The per-user demand for bandwidth is rising by a factor of eight per year while the number of users is increasing dramatically (Green, 1996). The transmission capacity per fiber for most advanced system is now 10 Gbits/s, and will be increased to 40 Gbits/s within next few years (Emura, 1996). Systems operating at more than 160 Gbit/s will be required by the year 2005 according to Juma (1997).

Transmission capacity can nominally be increased by raising the single-channel bit rate in a time division multiplexing (TMD) process. Another approach is wavelength division multiplexing (WDM), in which data are transmitted at lower bit rate over multiple wavelengths, or channels. The high-speed networks of the future will most likely combine the two approaches, increasing both the number of channels and the data rate per channel.

The WDM concept first appeared in 1970 according to a published report (Delange, 1970). However, it was the middle of 1977 before fundamental research on WDM technology actually started. WDM systems which offer four, eight, or 16 channels have been widely implemented in long haul communications since 1996, and those with 32 or 40 channels will be put into market in 1998 (Chaffee, 1997). The maximum channel number is limited by the bandwidth of optical fiber amplifiers. Today, commercially available fiber amplifiers have bandwidth of about 30 nm, which limits the maximum channel number under 40 with 0.8 nm channel spacing. Recently, Lucent Technology has produced a two-stage fiber amplifier with bandwidth of 80 nm (Lewotsky, 1997). With the use of this kind of new fiber amplifier, more than 100 channels can be carried in the future WDM systems. The key components in WDM systems are wavelength multiplexers and demultiplexers. Currently, commercially available components are mainly based on thin film interference filters, fiber Bragg gratings, micro-optic techniques, or phased-array waveguide gratings. When systems need to operate at 64 or more channels, WDM component manufactures will face new challenges in producing multiplexers with those techniques. A possible choice is to use integrated concave gratings to make multi/demultiplexers.

A vertically etched reflection concave grating, which can perform the task of both dispersing the light and bringing it to a focus, may be integrated with both input and output waveguides. The classical concave grating design is the Rowland circle grating (Rowland, 1883). Rowland showed that if a point source is located on a circle which touches the pole of the grating, but which has the half radius of curvature of the grating blank, then to a first approximation the diffracted image will also be on that circle. Based on this classical concave grating design, Cremer et al. (1990, 1991, 1992) successfully fabricated demultiplexers in InGaAsP/InP, with a channel spacing of around 4 nm. Clemens et al. (1992, 1994) realized same type of device in SiO_2/Si and reduced channel spacing to 2 nm. This is the typical channel spacing for integrated demultiplexers based on classical Rowland circle concave gratings, although a demultiplexer with channel spacing of 0.78 nm has been reported (Tong et al., 1994). For all of those demultiplexers, grating facets were normal to the incident light. In order to increase the reflection of the concave grating, the grating facets were usually coated with gold. This complicated the fabrication process. One of the important parameters in fabricating this kind of demultiplexer is the verticality of grating sidewalls. The grating with a 3° sidewall tilt will increase the loss by about 6 dB according to Liu et al. (1993).

McGreer (1996a) has reported a recursive method to design concave gratings that allows greater flexibility than the classical Rowland circle design. With this new method, a flat-field broadband spectrograph and a tunable planar concave grating demultiplexer were designed by McGreer (1995b, 1996b). These gratings were designed for glass

waveguides in which the angle of incidence and the angle of reflection for optical rays on the facets is

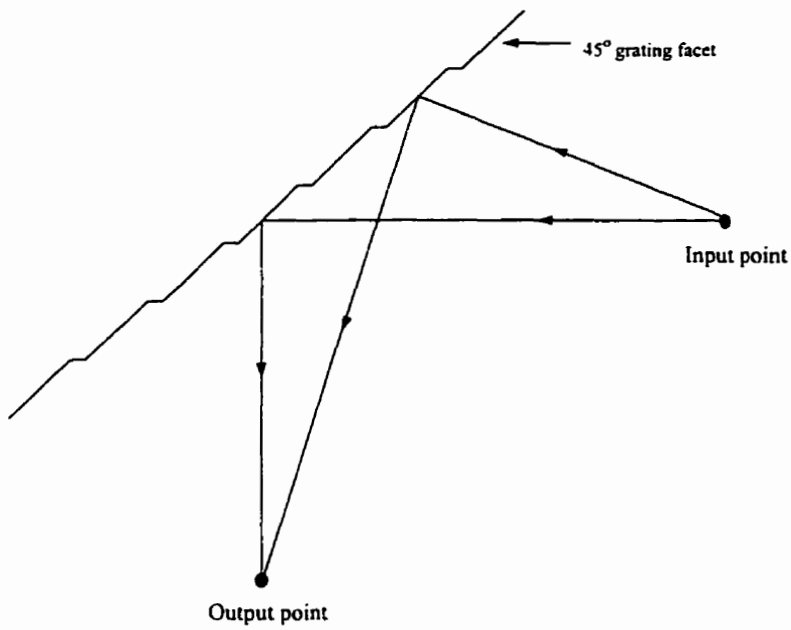

Fig. 1.1 Concave grating design using facets with an angle of incidence that is nominally 45° to take advantage of total internal reflection

nominally 45°, as shown in Fig. 1.1. Since light at 45° incidence to the glass/air interface has total internal reflection, there is no need to coat the facets with gold, thus simplifying fabrication process. Hnatiuk et al. (1996) demonstrated this kind of device. The loss in the grating was approximately 1.7 dB, and was attributed to the facet normal being out of the plane of the waveguide (the tilt of grating sidewalls) by an angle of 6°. This shows the advantage of facets with an angle of incidence of 45°; unfortunately the devices used for the demonstration have a dispersion that is too low for WDM applications. Keeping the same input and output points and increasing the dispersion would increase the loss

considerably. To overcome this difficulty, a retro-reflector facet design has been proposed by McGreer (1996c).

Fig. 1.2 illustrates how facets with total internal reflection may be used while allowing for the optimum selection of dispersion. A pair of facets is associated with (x_i, y_i) point. A light ray hits the first facet at an incidence angle of 45°, is reflected to the adjacent facet again at 45° incidence, and is reflected towards its point of origin.

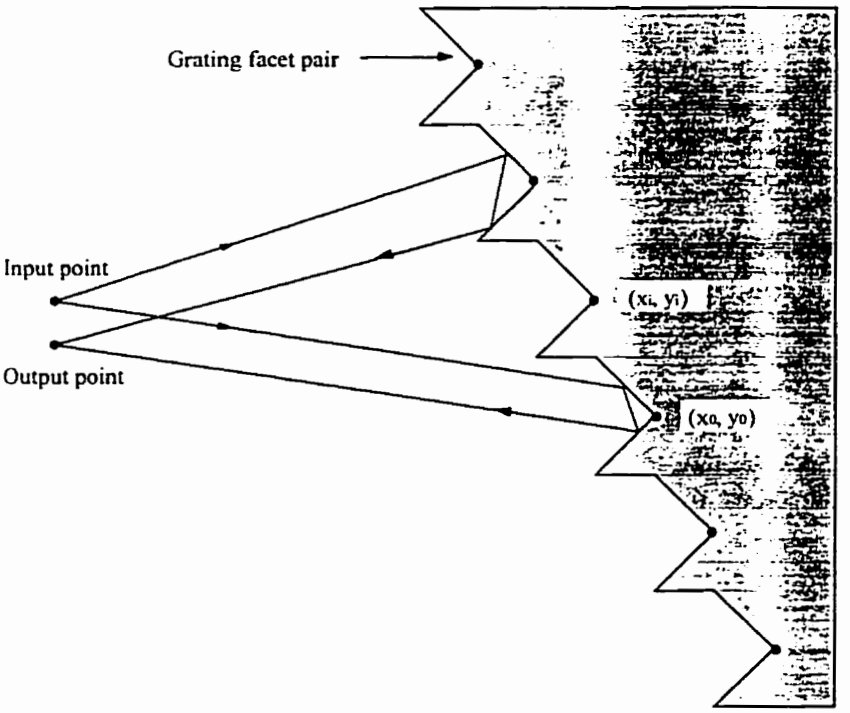

Fig. 1.2 Concave grating design using facet pairs with two total internal reflections

the retroreflection is analogous to the reflection from a corner cube. These facet pairs are equivalent to facets that have a reflection coefficient of unity and a tilt angle optimized to reflect light to the point of incidence. A disadvantage of this design is the low fabrication

tolerance on the tilt of grating sidewalls. Tremendous efforts have been made in this work to optimize fabrication process to obtain vertically etched gratings. With this novel design, we have fabricated a sixty channels demultiplexer with 0.144 nm channel spacing and (Sun et al., 1997a). The channel spacing of this demultiplexer is about one order of magnitude smaller than that of a typical demultiplexer based on Rowland circle design. We have also reported demultiplexers with 0.29 nm channel spacing and 120 channels (Sun et al., 1997b, 1998). With some improvement in design and fabrication, this kind of demultiplexer will have a very promising market in the future optic fiber communications.

The concave grating based on the Rowland circle design has been integrated with detectors (Cremer et al., 1992, and Fallahi et al., 1993) and semiconductor amplifiers (Soole et al., 1992a, 1992b) to function as multiwavelength receivers and multiwavelength lasers. These are the key components in multiwavelength networks. However, the concave gratings employed in their multiwavelength lasers had multiple passbands. In which passbands, and in how many passbands, laser oscillation occurred for each channel was determined only by the amplifiers. This makes it difficult to control the absolute lasing wavelength, and multiple passband lasing results in instability in the laser output (Doerr, 1995). In this thesis concave gratings with several chirping schemes are studied. The chirped concave grating yields only one dominant passband. The extinction ratio between the dominant passband and other passbands can be as high as 20.9 dB, while it was only 13 dB for chirped phased-array waveguide gratings designed by Doerr et al. (1997). Demultiplexers based on chirped concave gratings are designed in this thesis.

1.2 OBJECTIVES

This thesis focuses on fabrication, characterization, simulation, and design of demultiplexers based on integrated concave gratings with total internal reflection facets (retro-reflection), which are designed by a recursive approach. The objectives are:

1. To investigate the fabrication processes and optimize the performance of demultiplexers.
2. To fully characterize demultiplexers.
3. To model demultiplexers and compare simulation results with experimental results.
4. To do some primary investigations on birefringence control.
5. To study integrated concave gratings with different chirping schemes, such as linear, parabolic, and exponential chirping.
6. To design demultiplexers with the above chirped concave gratings

1.3 SIGNIFICANCE OF THE THESIS

Our work on integrated concave grating demultiplexers has the following significance:

1. The first demonstration of demultiplexers with total internal reflection (retro-reflection) facets was given.
2. The highest resolution for integrated concave gratings in the world was achieved.
3. The first design of demultiplexers based on chirped concave gratings that only had one dominant passband was given.

1.4 OUTLINE OF THE THESIS

This thesis consists of eight chapters. In Chapter Two, state-of-the-art of WDM demultiplexers based on technologies other than integrated concave gratings is reviewed. Two concave grating design theories, among which one is based on classical Rowland circle and the other is based on a recursive approach, are illustrated in Chapter Three. The design for demultiplexers by a recursive approach is explained in this chapter. By using Fraunhofer diffraction theory in two dimensions, demultiplexers are modeled at the end of Chapter Three. The fabrication process for demultiplexers based on integrated concave gratings is thoroughly investigated in Chapter Four. Chapter Five is dedicated to fully characterize the performance of demultiplexers. Birefringence control by employing layer structure is addressed in Chapter Six. Chapter Seven studies concave gratings with several chirping profiles, and demultiplexers based on chirped concave gratings are designed. The main accomplishments and recommendations for future work are summarized in Chapter Eight.

CHAPTER TWO

REVIEW: WDM TECHNOLOGY

As lightwave technology is introduced, we have ample bandwidth from fiber optics (thousands of GHz). However, the state-of-art switching speed from the silicon IC technology remains on the order of 10 GHz. When many practical factors are considered, the speed can be even lower. Therefore, as lightwave technology is introduced, the electronics part of the network becomes the speed bottleneck. Synchronous optic network (SONET), which is a recently standardized worldwide lightwave transmission system (Ballart et al., 1989), is designed to overcome this speed bottleneck. However, the fastest bit-rate for SONET system (OC-192) is 10 Gb/s. Obviously, there is a speed limit for SONET system (tens of GHz) and the cost for implementing SONET will increase dramatically as the bit-rate is increased (Liu, 1996). Parallel transmission by WDM technology is a key to high utilization of fiber bandwidths.

2.1 OUTLINE OF WDM SYSTEMS

In a point-to-point WDM system, several wavelength-specific transmitters are multiplexed to form a continuous spectrum of data channels (see Fig. 2.1). These signals are transmitted down an optical fiber and periodically amplified. At the receiving side, the spectrum is demultiplexed back into individual channels. The most common forms of WDM systems use fiber pairs, one for transmit and one for receive (Alexander 1997). Bidirectional systems implement a single fiber for both transmit and receive function.

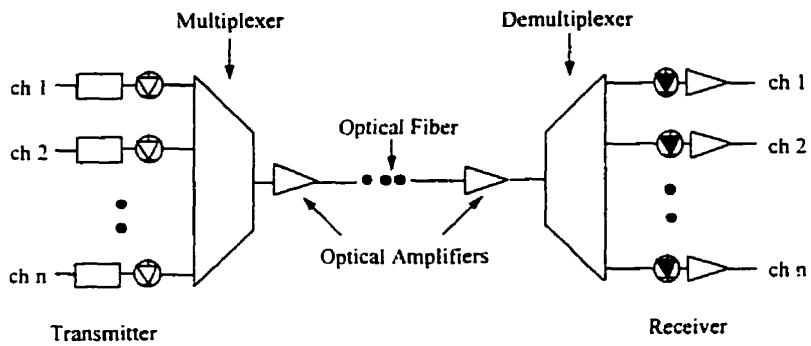

Fig. 2.1 Fundamental configuration for WDM transmission

The advantages of WDM systems are: transmission capacity increase per fiber, system cost reduction, simultaneous transmission of different modulation-scheme signals, and services channel expandability after fiber installation. WDM technology has been widely applied to point-to-point systems, and will be applied to local area networks (LAN), wide area networks (WAN) and cable TV systems in the near future (Leonberger et al., 1997). In fact, a regional prototype WDM network has already appeared in the San Francisco Bay area (Edwards, 1996).

In WDM system design, performance of optical multi/demultiplexers should be the primary consideration, together with fibers, light sources, optical amplifiers, and photodetectors. Since multi/demultiplexers are discussed in the following sections, the latter part of this section will focus on the status of other optical devices and components.

2.1.1 OPTICAL FIBERS

To take advantage of low loss transmission and the availability of Erbium Doped Fiber Amplifiers (EDFAs), currently silica fiber is generally operated in the third transmission window of 1550 nm (Juma, 1997). Once the multiple-wavelength signal is in the fiber, the real challenges begin. Conventional fiber was optimized for signals on a single wavelength; with multiple wavelengths and channels generally closely spaced, fiber nonlinearities introduce crosstalk between channels, thus limiting the number of wavelengths carried. One significant nonlinearity is four-wave mixing (FWM), in which two signals at different frequencies interact through the nonlinear refractive index of the fiber to produce additional signals at the sum and difference between the frequencies. The nonlinear effects increase as the frequencies are more closely spaced, with increasing power per channel and with decreasing dispersion of the medium.

Performance is decreased both by loss of power and, in case of evenly spaced channels, by cross talk, as the nonlinearity generated components can fall directly onto existing channels. Potentially, channels separated by 4 nm can be limited by FWM to link fiber lengths of less than 500 km (Lerner, 1997).

One simple approach to lessen these nonlinearities is to use unequal channel spacing (Taga, 1996). This design avoids crosstalk but not power loss and makes inefficient use of the available bandwidth. A more-sophisticated approach is to use semiconductor laser amplifiers at the midpoint of a link to perform phase conjugation or spectral inversion of the signal (Kikuchi 1994). This automatically recovers the original signal at the end point, but introduces complexity into the network.

A third technique is to use higher dispersion fiber, alternating these sections with sections of dispersion-compensating fiber, so that the average dispersion is low, but each fiber section has high dispersion. Using this technique, researchers have demonstrated transmission of sixteen 10-Gbits/s channels over 1000-km links (Bergano 1996).

A second nonlinearity is stimulated Raman scattering (SRS), in which light stimulates molecular vibration, generating scattered light at a slightly longer wavelength than the original signal. Again crosstalk and loss of signal energy result. This effect is exacerbated with more closely spaced and more powerful channels. While currently there is no apparent way to counteract SRS, it is less constricting than FWM—eight wavelengths spaced 4 nm apart can still travel 1000 km without significant degradation by SRS (Lerner, 1997). However, care has to be taken to limit channel power to the minimum needed for good signal-to-noise ratios.

A third nonlinearity is stimulated Brillouin scattering (SBS). SBS describes the interaction between the optical signal and the acoustic waves in the fiber that causes power from the optical signal to be scattered backwards towards the transmitter. This narrowband process affects each channel in a WDM system; is noticeable in WDM

systems when per-channel power exceed 5 to 6 dBm; and is particularly troublesome in high-power, single-channel systems (Alexander, 1997).

A fourth nonlinearity is self-phase modulation (SPM) which refers to the modulation that a light pulse has on its own phase. It acts in each WDM channel independently. When a signal is phase-modulated, its spectrum becomes broadened. This widening can lead to crosstalk or an unexpected additional dispersion penalty. SPM is controlled by a careful choice of channel power.

The last nonlinearity is cross-phase modulation that refers to the modulation of a channel's phase due to intensity fluctuations in another channel. This effect is unique to WDM systems. Its degradation effects are similar to those due to SPM. Increasing channel spacing help to decrease these effects.

2.1.2 OPTICAL AMPLIFIERS

Any long-distance optical communication network needs some sort of repeater to amplify signals to counteract the attenuation that inevitably occurs in even the most transparent fiber. Initially, such amplifiers were optoelectronic repeaters —detectors to convert optical signals to electronic ones, circuits to reshape electronic pulses, and transmitters to send a new optical signal, modulated by the electronic one. Such repeaters were limited by the electronic speeds at the time they were installed and had to be tailored to a particular transmission format and rate. Thus on terrestrial lines, they had to be reinstalled whenever capacity was to be increased. This process is generally impractical with oceanic

cable, so entirely new lines had to be laid in to increase capacity. In addition, one repeater would be needed for each wavelength transmitted, making WDM an impossibly expensive proposition.

Optical amplifiers eliminate these problems because they amplify lightwave signals without converting them to electronic pulses. Signal rates and format can thus be changed at the network nodes without replacing amplifiers or replacing cable. Such amplifiers are exceedingly simple in principle—they can be thought of as lasers without the mirrors. Optical fiber amplifiers consist of an active medium that is pumped by an energy source into a population inversion, where higher energy states are more populated than lower ones. When the signal passes through the medium, the medium is stimulated to emit photons, thus amplifying the signal. Although the signal makes only one pass through the medium, amplification is by as much as 30-40 dB.

There are three main types of optical amplifiers: optical fiber amplifiers, semiconductor optical amplifiers and Raman fiber amplifiers. Fiber amplifiers use rare-earth elements—typically erbium, but also praseodymium, thulium, neodymium, and others— as dopants in a glass optical fiber and are optically pumped (Potenza, 1996). Since erbium-doped fiber amplifiers (EDFAs) have the greatest gain around 1550 nm they are generally used in WDM systems. Commercially available EDFAs have bandwidth of about 30 nm, which limits the maximum channel number under 40 with 0.8 nm channel spacing. Recently, Lucent Technology has produced a two-stage EDFA with bandwidth of 80 nm (Lewotsky, 1997). This kind of EDFA will increase the channel number of a WDM system to 100. Semiconductor optical amplifiers are made up of

semiconductor alloys involving phosphorous, gallium, indium, and arsenic and are electrically pumped. Raman amplifiers use germanium-doped fibers and high pumping powers to exploit nonlinearities, thus achieving gain. Both semiconductor optical amplifiers and Raman amplifiers have specialized uses for telecommunications (Lerner, 1997) and are not discussed further here.

2.1.3 LASER SOURCES

The laser source in a WDM system is usually a distributed-feedback laser diode with direct amplitude modulation. The key concerns are that the wavelength of the laser falls in the center of the channel wavelength and that the output wavelength stays there. According to the International Telecommunication Union (ITU), the center of a channel wavelength is selected from a grid of frequencies referenced to 193.1 THz and spaced every 100 GHz (0.8 nm) (Alterman, 1996). Wavelength deviation is one of the most important design factors in a WDM system. Wavelength deviations result from various factors including deviation from target wavelength during production, temperature fluctuation, feedback effect due to reflected light and frequency chirp due to direct modulation (Agrawal, 1992).

2.1.4. PHOTODETECTORS

The role of an optical receiver is to convert the optical signal back into electrical form and recover the data transmitted through the optical communication system. Its main

component is a photodetector that converts light into electricity through the photoelectric effect. A photodetector should have high sensitivity, fast response, low noise, low cost and high reliability. Its size should be comparable to the fiber-core size. Two types of photodetectors, p-i-n and avalanche photodiodes are generally used in an optical communication system.

2.2 OPTICAL MULTI/DEMULTIPLEXERS

Optical multi/demultiplexers are made based on thin film interference filtering, fiber optics, bulk optics, and integrated optics. Multi/demultiplexers based on these technologies are discussed in the following subsections.

2.2.1 THIN FILM INTERFERENCE FILTERING MULTI/DEMULTIPLEXERS

Thin film interference filters are simple; easy-to-construct components for widely spaced WDM multiplexers. These filters consist of a stack of dielectric thin films of alternating high and low refractive index. The optical thickness (physical thickness multiplied by the refractive index) of each layer is typically an integral number of quarter-wavelengths; for telecommunications wavelengths, this corresponds to a physical thickness of 0.25 μm or less. The order and thickness of individual films can be tailored to produce almost any spectral profile. Designers can widen the spectral top of the filter and steepen the slopes

to improve the squareness of a filter by cascading two or more cavities on a common substrate using a quarter-wave coupling layer (Scobey et al., 1997).

The coating materials commonly used in thin film filters for multiplexers (zinc sulfide, zinc selenide, or cryolite) are hygroscopic, absorpting moisture readily and requiring environment isolation with an epoxy-cemented cover slip. The materials also suffer from excessive scatter and absorption losses. Some manufacturers choose refractory metaloxide thin films with bulk density and low optical loss, which are produced either by high-power, low-pressure reactive sputtering technique, or ion assisted deposition. To improve the thermal stability of the filters, materials with low coefficients of thermal expansion and low refractive-index variation as a function of temperature are selected.

The basic demultiplexer based on a thin film interference filter consists of a single filter with three ports: a main trunk line input, an output, and a drop port, as shown in Fig.2.2. Graded Refractive Index (GRIN) rod lens collimate the diverging light from the

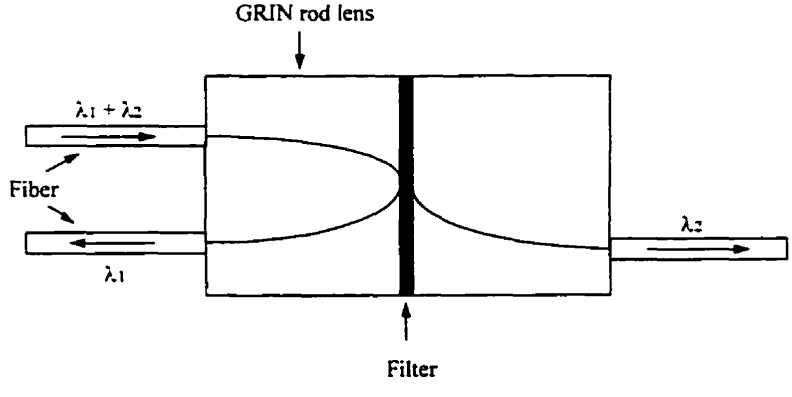

Fig.2.2 Schematic of a three-port demultiplexer

fiber and direct it to the filter, then re-image the collimated light back into the fiber. The packaged device can be cascaded to form a multichannel device by connecting or splicing the output of a three-port multiplexer to the input of a second multiplexer (Winzer et al., 1981). The number of multiplexers in the cascade indicates the number of channels. Cumulative insertion loss and loss variation with temperature effectively limit the technique of cascading three-port multiplexers to eight channels or fewer.

To produce a 16-channel demultiplexer, one can use a miniature optical bench to relay light between filters (Nosu et al. 1979). As shown in Fig. 2.3, light from input or common fiber is collimated by a lens directed at a slight angle toward a filter block, with filters mounted on parallel sides. The beam undergoes multiple reflections from the filter input faces, and at each reflection, one wavelength is removed. For multiplexing operations, the process is simply reversed-input from the individual channels enters the filter block and propagates through to the common fiber. The design can be extended to 32 channels, and 50 GHz channel spacings are realizable (Scobey et al., 1997).

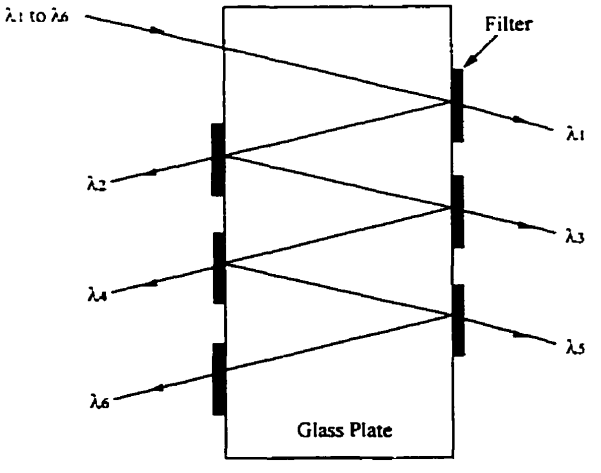

Fig. 2.3 In a 16-channel demultiplexer, as in this six-channel design, collimated light at a slight angle from the normal enters the filter block, where it undergoes multiple reflections from the filter input faces. At each reflection, one wavelength is removed.

For practical WDM systems, flat and wide band characteristics are required in order to suppress loss variation due to wavelength drift of the light source. Multiplexers based on thin film interference filters have ideal flat and wide band characteristics. They also have moderate insertion loss (3 to 5 dB), high channel isolation (30-50 dB), and very low temperature sensitivity (2 to 0.5 pm/°C). The disadvantages of this kind of demultiplexer are high cost and low yields. As the number of channels increases, sophisticated methods are needed to keep demultiplexers size and complexity manageable (Lerner 1997).

2.2.2 MULTI/DEMULTIPLEXERS BASED ON FIBER OPTICS

Multi/demultiplexers based on fiber optics are composed of all fibers, and generally have advantages of low loss and polarization insensitivity. There are two such kinds of devices; one is based on fiber Bragg grating and the other is based on fused biconical taper.

2.2.2.1 Fiber Bragg Grating Multi/demultiplexers

Based on the Bragg effect, fiber Bragg gratings essentially act like wavelength-selective mirrors. A grating will reflect light with a wavelength corresponding to twice the grating period multiplied by the effective index of refraction; this is called the Bragg condition. Light at other wavelengths will meanwhile transmit without significant attenuation. In effect, the grating operates as a narrow-band filter. The components are formed by

exposing the core of a photorefractive fiber to a periodic pattern of ultraviolet (UV) light. Fiber can be rendered photosensitive by doping the core with germanium, phosphorous, or boron during fabrication of the preform (Hill et al., 1978). Fibers can also be sensitized by loading them with hydrogen under temperature and/or pressure, that is, by putting them in a chamber pressurized with hydrogen (Juma, 1997).

Very precise gratings can be formed by using an electron-beam phase mask and either an argon fluoride (193 nm) or krypton fluoride (248 nm) excimer laser or a frequency-doubled argon-ion laser (244 nm) as the UV source. A phase mask is essentially a binary grating in which the groove profile and depth have been specially tailored to diffract most of the incident UV energy into the plus and minus first-diffraction orders while minimizing the energy in the zero and higher orders. By using apodization techniques, fiber Bragg gratings which have flat and wide-band characteristics can be produced (Singh et al, 1997). This kind of feature is important for WDM applications.

Currently two approaches are being pursued to make multiplexers based on fiber Bragg gratings. The first approach uses optical circulators and gratings. Typically a circulator is a three-port device, as shown in Fig.2.4. A signal entering port 1 exits through port 2, while a signal entering through port 2 leaves via port 3. In a WDM configuration, multiple wavelengths (say eight) enter through port 1. If a Bragg grating (with the Bragg wavelength corresponding to λ_3) is connected to port 2, then λ_3 will be reflected and exit through port 3, while the remaining wavelengths will leave through port

2. While simple to design, however, optical circulators are labor-intensive to manufacture.

The other method incorporates fiber Bragg gratings and couplers in a Mach-Zehnder interferometer configuration (Bilodeau et al., 1995). As shown in Fig. 2.5, two identical Bragg gratings are formed, one in each arm of the device. Consider a stream of

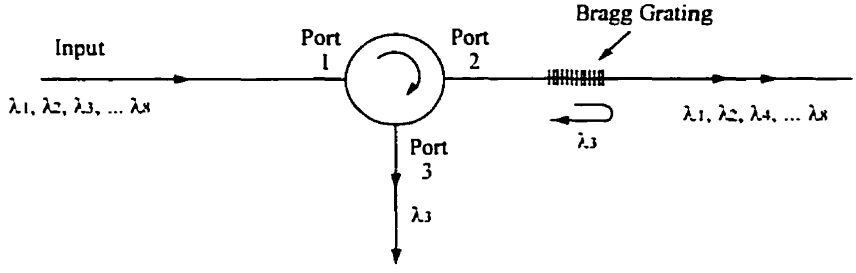

Fig. 2.4 In demultiplexing action, the Bragg grating attached to Port 2 redirects one wavelength of the multiple-wavelength signal

wavelengths, say eight (λ_1, λ_2, ...λ_8) entering input port A. Assuming the Bragg grating's reflection wavelength is λ_3, light of λ_3 together with other wavelengths will be split equally between the two arms of the coupler; however, λ_3 will be reflected by the two identical gratings. On reaching the coupling region, there will be a coherent recombination, and λ_3 will exit through port B. The remaining wavelengths will continue to propagate, recombine, and exit through port D. Because of the symmetry of the device, wavelength λ_3 can be added at port C to come out with other wavelengths at port D. It's challenge to maintain two arms identical all the time for this kind of configuration.

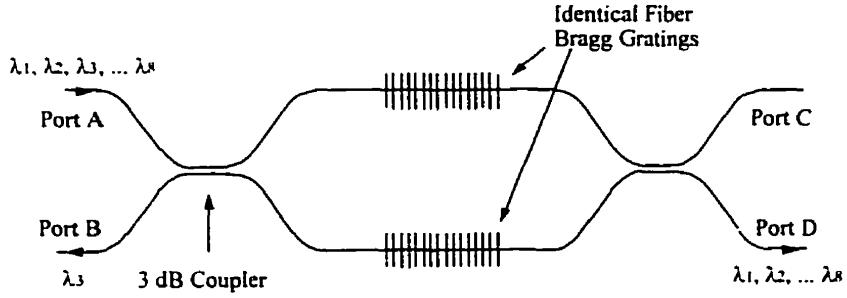

Fig. 2.5 Identical Bragg gratings in a Mach-Zehnder interferometer configuration act together to redirect one wavelength of multiple-wavelength signal

In practice, multiple stages of the above configuration (or the circulator configuration), one for each wavelength, are cascaded to form a complete WDM devices. The entire manufacturing process can be automated. The advantages of this type of multi/demultiplexer are low insertion loss and polarization insensitivity. When a multiplexer with 64 channels are needed, 64 three-port or four-port devices are cascaded. The size of the device is very large, and most importantly, its cost is very high.

2.2.2.2 Fused Biconical Taper Multi/Demultiplexers

A fused biconical taper, as shown in Fig. 2.6, is made by the fusion and tapering technique: two identical optical fibers are fused laterally together and elongated with a heat source. When the taper angle is everywhere small enough to ensure negligible loss of power from the fundamental mode as it propagates along the structure, the propagation and, by extension, the fused biconical taper itself is said adiabatic: the fiber transmission is not affected by the tapering process (Stewart et al, 1985). This kind of fused biconical taper is used to make the coupler that is the most common all-fiber component in fiber

optic communication. However when the slopes are abrupt, such as those of the structure

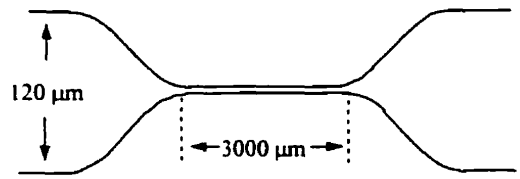

Fig. 2.6 Profile of an abruptly tapered fiber

shown in Fig 2.6, one may observe, as the fiber is elongated, large oscillations in the transmitted power. For a given elongation, similar oscillations are seen in the transmission as a function of wavelength (Fig. 2.7) or of the refractive index surrounding the tapered part of the fiber. The fused biconical taper is then said nonadiabatic. The nonadiabatic fused biconical taper can be used to make narrow band and large band filters (Gonthier et al., 1989).

Demultiplexers are obtained by concatenating several fused biconical tapers (typically two to four, depending on the FWHM of each channel) with quasi-sinusoidal wavelength responses such that of Fig. 2.7 but with different periods. If the absorbing jacket is not removed between the tapers, it traps the cladding modes. The resulting transmission is then obtained by multiplying the transmissions of all the tapers. With careful choice of the periods and the maxima, one can obtain the desired channel center wavelengths and FWHM for each channel (Lacroix et al., 1986).

Fused biconical taper multi/demultiplexers are used to combine/separate wavelengths between 0.98-μm, 1.31-μm, 1.48-μm, 1.55-μm and 1.65-μm regions.

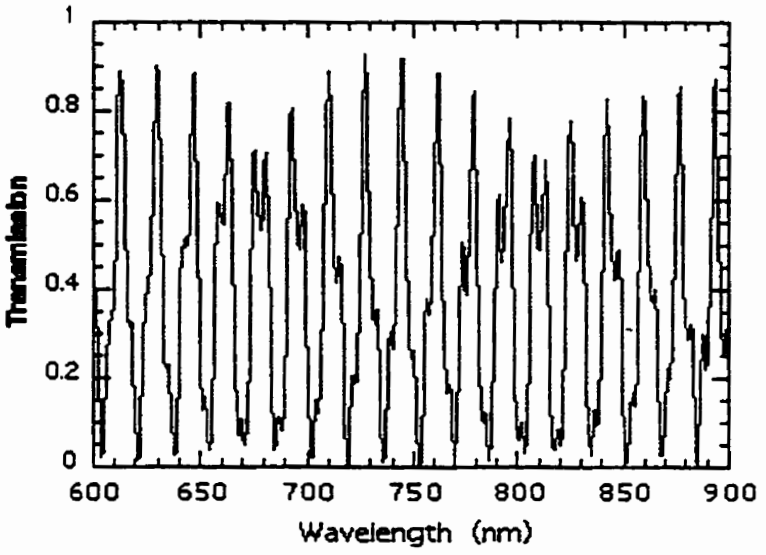

Fig. 2.7 Fundamental mode transmission of the tapered fiber (Fig. 2.6) as a function of wavelength; down load from http://opt-fibers.phys.polymtl.ca/Fibers_html

Although this kind of multi/demultiplexer has an extremely low insertion loss (typically 0.2 dB), it has low channel isolation (typically between 16-20 dB).

2.2.3 MULTI/DEMULTIPLEXERS BASED ON BULK OPTICS

2.2.3.1 Micro-optical Multi/Demultiplexers

A diffraction grating, combined with a suitable lens can be used to make a demultiplexer. As shown in Fig. 2.8, an input fiber and multiple output fibers are arranged on the focal plane of either a convex lens or graded-index (GRIN) lens. Wavelength multiplexed ligh

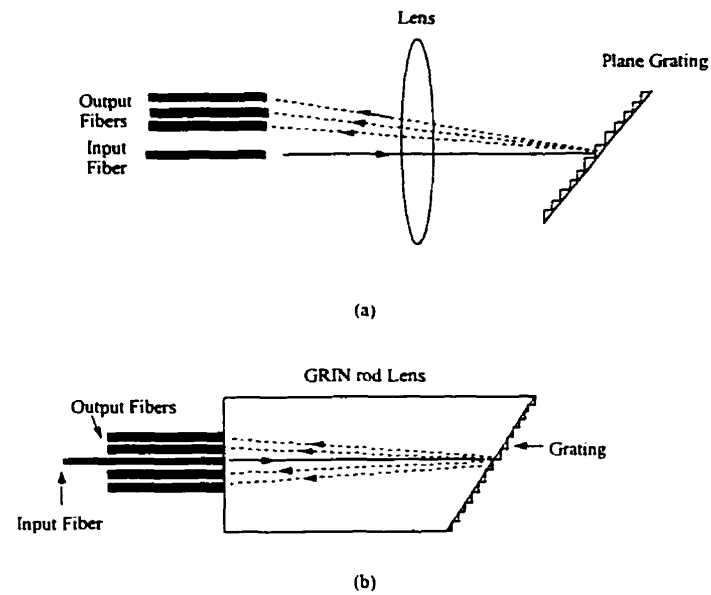

Fig.2.8 Wavelength demultiplexer based on the Littrow configuration grating: (a) a convex lens is used for focusing; (b) a GRIN lens is used for focusing

from the input fiber is collimated by the lens and reaches the diffraction grating. The light is angularly dispersed according to different wavelengths and reflected at the same time. Then, the different wavelengths pass through the lens and focused to their corresponding output fibers. A blazed grating that can efficiently diffract light into a specific diffraction order is widely used. There are two types of blazed gratings. One is fabricated by conventional mechanical ruling and the other by anisotropic etching of single-crystal silicon (Fujii et al., 1980). Since the silicon grating provides design freedom (i.e., blaze wavelength and grating constant), high efficiency, and a stable surface, it is superior to the conventional mechanically ruled grating for practical use.

Based on the above micro-optic technique, demultiplexers with 132 channels are commercially available now. However, the spectral profile of the passband is rounded, which is not suitable for WDM applications. They will not be widely used unless a flattening scheme is used. Since optical alignment is needed for each channel, they are not suitable for mass production.

2.2.3.2 Polarization Division Multi/demultiplexers

When all WDM channels have the same polarization, as depicted in Fig. 2.9, another way to demultiplex a wavelength channel is to rotate the polarization of the selected channel by 90° and then use either a polarization beam splitter (PBS) for separation or a polarizer for filtering (Liu, 1996). To rotate the polarization of the selected wavelength light signal, the basic principle is to provide a polarization mode coupling mechanism that is wavelength dependent. Polarization mode coupling is a phenomenon in which one polarization is coupled to its orthogonal polarization. When the wavelength of the incident light meets a certain wavelength-dependent coupling condition of the device, there will be a strong coupling between the two orthogonal polarization modes. When the wavelength does not meet the condition, there is no coupling and the incident light will pass through the device with its polarization unchanged.

To provide a wavelength-dependent mode coupling, a waveguide that is birefringent and has a periodic refractive index change can be used. A waveguide that is birefringent means different polarized lightwaves "see" different refractive indices. This

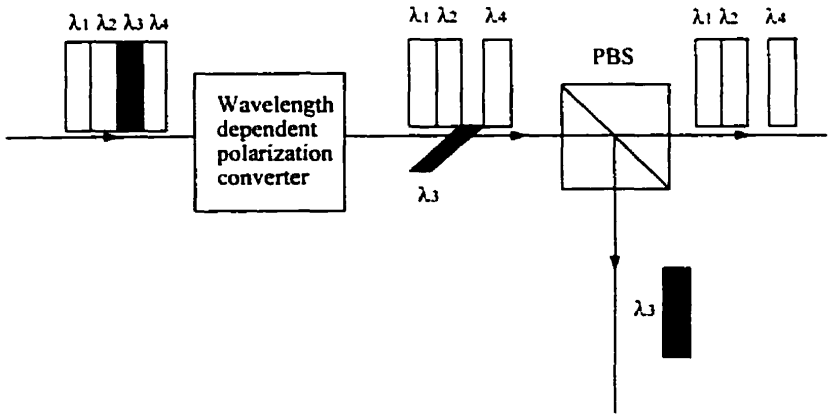

Fig. 2.9 Wavelength tuning over the polarization domain

happens when waveguide is made of an anisotropic material and its dielectric constant is represented by a dielectric tensor. When the period of the refractive index variation satisfies the condition

$$\Lambda(n_1 - n_2) = \lambda \tag{2.1}$$

a strong coupling can occur, where n_1 and n_2 are the effective indices of the two orthogonal polarizations.

Like fused biconical taper multi/demultiplexers, polarization division multi/demultiplexers are usually used to combine/separate wavelengths between 0.98-μm, 1.31-μm, 1.48-μm, 1.55-μm and 1.65-μm regions. A disadvantage of this kind of multi/demultiplexer is that before the incident light enters to the device, all WDM channels have to be in the same polarization state. This brings complexity to the system design.

2.2.4 MULTI/DEMULTIPLEXERS BASED ON INTEGRATED OPTICS

Multi/demultiplexers based on integrated optics are attractive for both mass production and the ability to support a large number of channels. There are three kinds of multi/demultiplexers based on integrated optics: phased-array multi/demultiplexers, concave grating multi/demultiplexers and Mach-Zehnder interferometer (MZI) multi/demultiplexers.

2.2.4.1 Phased-array Multi/Demultiplexers

Phased-array multiplexers were proposed by Smit (1988). The first devices operating at short wavelength were reported by Vellekoop and Smit (Vellekoop et al., 1989). Takahashi et al. (1990) reported the first devices operating in the long wavelength window. Dragone (1991) extended the phased-array concept from 1×N to N×N devices, the wavelength routers, which play an important role in multiwavelength network applications.

Fig. 2.10 shows the schematic layout of a phased-array demultiplexer. The operation is understood as follows. When the beam propagating through the transmitter waveguide enters the Free Propagation Region (FPR) it is no longer laterally confined and becomes divergent. On arriving at the input aperture the beam is coupled into the waveguide array and propagates through the individual array waveguides to the output aperture. The length of the array waveguides is chosen such that the optical path length difference between adjacent waveguides equals an integer multiple of the

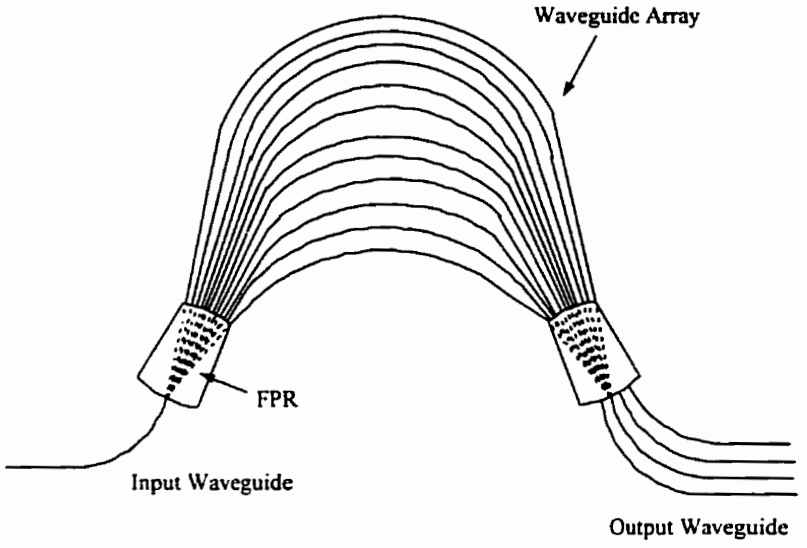

Fig. 2.10 Schematic of a phased-array demultiplexer

central wavelength of the demultiplexer. For this wavelength the fields in the individual waveguides will arrive at the output aperture with equal phase (apart from an integer multiple of 2π), and the field distribution at the input aperture will be reproduced at the output aperture. The divergent beam at the input aperture is thus transformed into a convergent one with equal amplitude and phase distribution, and an image of the input field at the object plane will be formed at the center of the image plane. The dispersion of the demultiplexer is due to the linearly increasing length of the array waveguides, which will cause the phase change induced by a change in the wavelength to vary linearly along the output aperture. As a consequence, the outgoing beam will be tilted and the focal point will shift along the image plane. By placing receiver waveguides at proper positions along the image plane, spatial separation of the different wavelength channels is obtained.

Recently, a novel type of phased-array multiplexer based on multimode interference (MMI) couplers was proposed and experimentally demonstrated on InP (Dam et al., 1995), and a design for a low-contrast waveguide structure has been proposed (Lierstuen et al., 1995). It is obtained by replacing the Free Propagation Regions of the "classical" phased-array waveguide grating by MMI-couplers.

Because the phased-array multi/demultiplexer is an integrated optic, it can be manufactured using potentially low-cost, high-throughput photolithographic techniques. However, these waveguides can typically introduce polarization-dependent losses (0.3-0.5 dB) and large insertion losses (7 to 10 dB). The channel isolation is not as good as that of multi/demultiplexer based on thin film interference filters (typically 22 dB). The spectral profile of the passband is also rounded; however, many kinds of methods, including the Y-branch (Koch, 1995), sinc-function field (Okamoto et al., 1995), multimode interference (Soole et al., 1996), two focal point method (Trouchet et al., 1997), and parabolic tapers (Okamoto et al., 1996) have been proposed to flatten the passband. The coefficients of thermal variation are 10 to 15 pm/°C, which is too high for practical operation, leading to the requirement for temperature control.

When channel number is over 64, the size of a phased-array based multiplexer will be very large, and the nonuniformity of refractive index and the variation in waveguide thickness across arrayed-waveguides will cause phase errors, resulting in high cross talk and low isolation. It is more efficient to realize multiplexers based on integrated concave gratings when a large number of channels are needed (Maschmeyer et al., 1996).

2.2.4.2 Concave Grating Multi/Demultiplexers

Multi/demultiplexers based on integrated concave gratings have been addressed in Chapter One, section 1.1. To avoid redundancy, we will not discuss them here. To the author's knowledge, multi/demultiplexers based on integrated concave gratings are not commercially available now. However, concave grating multi/demultiplexers are more compact than phased-array multi/demultiplexers and MZI multi/demultiplexers.

2.2.4.3 Mach-Zehnder Interferometer Multi/Demultiplexers

An N:1 Mach-Zehnder interferometer (MZI) multi/demultiplexer is composed of N-1 2×2 MZI s in m stages, where $N = 2^m$ (Nakato et al, 1990). To understand the principle, first consider the basic 2×2 MZI.

As shown in Fig. 2.11, each 2×2 MZI consists of three stages: a 3-dB coupler, two-branch phase shifter, and another 3-dB coupler. At each 3-dB coupler, the transfer matrix between the input and output waves can be expressed as (Liu, 1996)

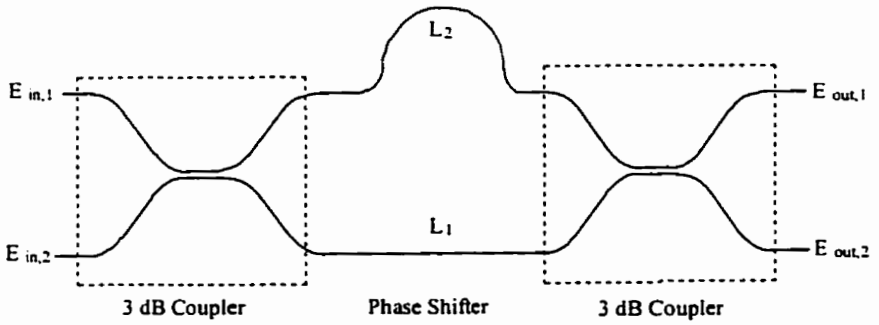

Fig.2.11 Mach-Zehnder interferometer

$$\begin{bmatrix} E_{out,1} \\ E_{out,2} \end{bmatrix} = \frac{1}{\sqrt{2}} \begin{bmatrix} 1 & j \\ j & 1 \end{bmatrix} \begin{bmatrix} E_{in,1} \\ E_{in,2} \end{bmatrix} = M_{3dB} \begin{bmatrix} E_{in,1} \\ E_{in,2} \end{bmatrix} \tag{2.2}$$

The phase shifter consists of two branches. When the two inputs come from the same light source, the light output from the two branches has a phase difference, $\Delta\phi$

$$\Delta\phi = \frac{2\pi n}{\lambda} L_1 - \frac{2\pi n}{\lambda} L_2 \tag{2.3}$$

For convenience, we define $L_{eff} = nL$ as the effective waveguide length where n is the refractive index of waveguide. As a result, $\Delta\phi = k\Delta L_{eff}$, with $k = 2\pi/\lambda$. At a given $\Delta\phi$, the output light from the two branches can be related to the input by

$$M_{shift} = \begin{bmatrix} e^{jk\Delta L_{eff}/2} & 0 \\ 0 & e^{-jk\Delta L_{eff}/2} \end{bmatrix} \tag{2.4}$$

where the average phase shift is ignored for simplicity.

From Equations (2.2) and (2.4), the MZI can be characterized by the combined matrix

$$M_{MZI} = M_{3dB} M_{shift} M_{3dB} = j \begin{bmatrix} \sin(k\Delta L_{eff}/2) & \cos(k\Delta L_{eff}/2) \\ \cos(k\Delta L_{eff}/2) & -\sin(k\Delta L_{eff}/2) \end{bmatrix} \tag{2.5}$$

If the incident light inputs, $E_{in,1}$ and $E_{in,2}$, are at wavelengths λ_1, λ_2, from Equation (2.5), the output power is:

$$P_{out,1} = \sin^2(k_1 \Delta L_{eff}/2) P_{in,1} + \cos^2(k_2 \Delta L_{eff}/2) P_{in,2} \tag{2.6}$$

$$P_{out,2} = \cos^2(k_1 \Delta L_{eff}/2) P_{in,1} + \sin^2(k_2 \Delta L_{eff}/2) P_{in,2} \tag{2.7}$$

where $k_1 = 2\pi/\lambda_1$, $k_2 = 2\pi/\lambda_2$.

From Equations (2.6) and (2.7), a proper ΔL_{eff} can be used to completely mix two inputs. Specifically, if

$$k_1 \Delta L_{eff} = 2m_1\pi \tag{2.8}$$

$$k_2 \Delta L_{eff} = (2m_2 + 1)\pi \tag{2.9}$$

with certain integers m_1 and m_2, then $P_{out,1} = 0$ and $P_{out,2} = P_{in,1} + P_{in,2}$. When $m_1 = m_2$, combining Equations (2.8) and (2.9) yields

$$(k_1 - k_2)\Delta L_{eff} = \pi \tag{2.10}$$

Because $k_1 - k_2 = 2\pi(f_1 - f_2)/c$,

$$\Delta L_{eff} = \frac{c}{2\Delta f} \tag{2.11}$$

Equation (2.11) gives the design of the MZI at a given frequency separation Δf.

Using the 2×2 MZI discussed above as the basic component, one can build a multiplexer of any size of $N = 2^n$. An eight-channel MZI multiplexer with channel spacing of 5 GHz was demonstrated by Toba et al (1987). Fig. 2.12 shows layout of an integrated four-channel MZI multiplexer by (Verbeek et al, 1988). By using seven serially connected MZI filters, Oda et al (1989) have demonstrated a MZI multiplexer with 128 channels. MZI multiplexers have been used in system demonstrations (Toba et al, 1990).

Compared with phased-array and concave grating multi/demultiplexers, MZI multi/demultiplexers have large size, especially for ones with large number of channels. MZI multi/demultiplexers with two channels are commercially available now with isolation of about 20 dB.

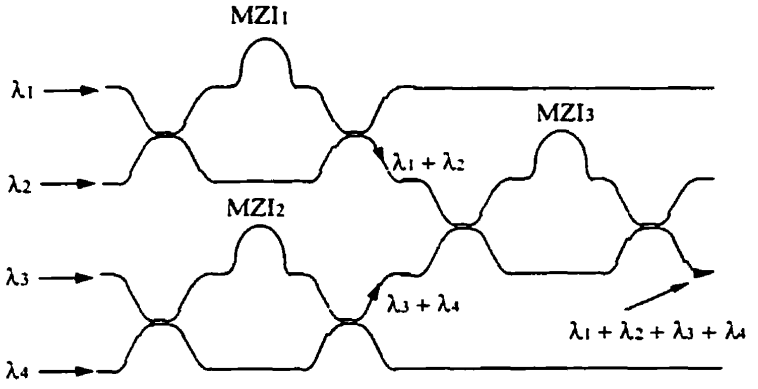

Fig. 2.12 MZI multiplexer with four channels

2.3 CONCLUSIONS

Currently, most WDM systems offer four, eight and 16 channels with channel spacing larger than 200 GHz(1.6 nm); multi/demultiplexers based on thin film interference filters are widely used by system designers because of their superior performance. But when the channel number is over 32 and channel spacing is only 100 GHz (0.8 nm), the cost for multi/demultiplexer based on thin film interference filters will increase dramatically. Therefore, multi/demultiplexer based on fiber Bragg gratings, micro-optics and phased-array waveguide gratings will be favored. Polarization division and fused biconical taper multi/demultiplexers are only used to combine/separate widely separated wavelengths. When a multi/demultiplexer with over 100 channels is needed, multi/demultiplexer based on integrated concave gratings will have advantage over multi/demultiplexers based on other techniques due to its compactness. In this thesis, demultiplexers based on concave gratings are studied.

CHAPTER THREE

DESIGN AND MODELING OF CONCAVE GRATING

Planar concave gratings play an important role in integrated optics. They act as wavelength multiplexers and demultiplexers in WDM systems, as external cavities in multiwavelength lasers, and as sensor elements in integrated optical spectrum analyzers. In the first section, two different design theories for planar concave gratings are illustrated; one is based on Rowland circle, the other is produced with a recursive procedure. With the latter theory, designs for demultiplexers with different properties are explained. In the second section, some simulations on concave gratings are performed by using Fraunhofer diffraction theory in two dimensions.

3.1 THE THEORY OF CONCAVE GRATING

3.1.1 PLANAR CONCAVE GRATING BASED ON ROWLAND CIRCLE

The theory of the spherical concave grating was developed, to a large degree, by Rowland (1883); later contributions were made by Beutler (1945), Noda (1974), and Harada (1980).

Figure 3.1 shows a concave grating of radius of curvature R, together with a second circle of radius R/2 which is known as the Rowland circle. The Rowland circle

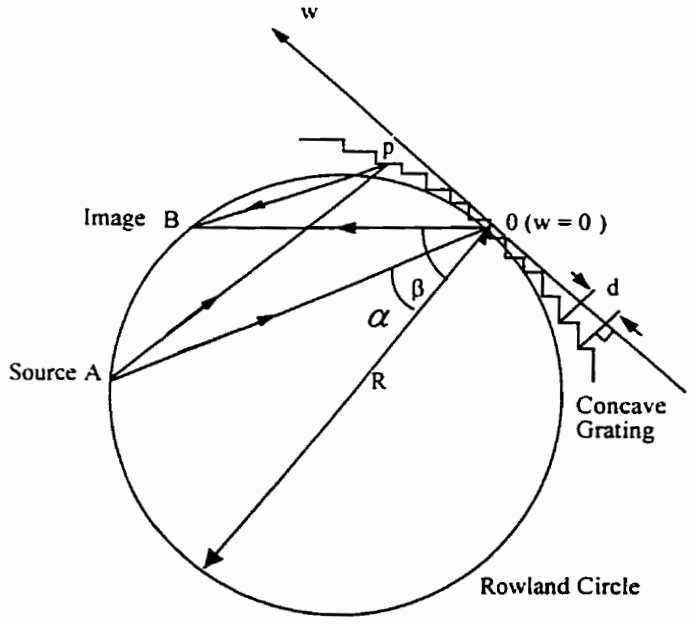

Fig. 3.1 Geometry of a concave grating based on a Rowland circle. Both of the source point A and image point B lie on the Rowland circle.

tangential to the grating surface at the point O. This point is referred as the grating pole. If the projection of the grating spacing onto the tangent that passes through O (w axis shown in Fig. 3.1) is a constant d, then light originating from a point source A on the Rowland circle will be focused to another point B lying on the same circle. The focal point is wavelength dependent according to the dispersive nature of the grating. With A and B defined by their angular position α and β relative to the grating normal at the pole, the focal point may be found for any general wavelength λ from the relation

$$d(\sin\alpha + \sin\beta) = \frac{m\lambda}{n} \tag{3.1}$$

where m is the diffraction order, λ is the free-space wavelength, and n is the refractive index of the propagation medium. In this special case (for which the locus of the focal points is restricted to the Rowland circle), the incident and diffracted angles are related by the same equation (3.1) as in the case of a planar grating.

Equation (3.1) allows us to calculate the focal position, but it tells us nothing about the image quality. Such information can be obtained by evaluating an expression for the path length (AP + BP) for a ray that is incident upon the grating at some general point P. This problem has been considered by Beutler (1945) for the case of a spherical concave grating with A and B at arbitrary positions (not confined to the Rowland circle). He showed that the path length could be expressed as a series of terms in the coordinates of P. Although Beutler's general terms are fairly cumbersome, in the case of planar concave grating, significant simplification can be made as follows. First, simplification results from the two-dimensional nature of the system. For off-axis sources, the tangential

rays and sagittal rays forms two different foci in an image system, and the aberration resulting from the displacement of these two foci is called astigmatism. The most dramatic aberration of the spherical concave grating when used in Rowland circle mounting is that of astigmatism. In planar concave grating, light rays are always on the meridional plane, which results in zero astigmatism. The reduced dimensionality makes it possible to specify the path length in terms of a simple coordinate of P —the w coordinate (the zero point being the grating pole). The path length (AP + BP) may therefore be expanded in a series of the form

$$(AP + BP) = (AO + BO) + F_1(w) + F_2(w) + F_3(w) + \ldots, \qquad (3.2)$$

where each individual term may be identified with some aspect of either the focal position or the image quality. Further simplification results from positioning A and B upon the Rowland circle. Based on the theory of the spherical concave grating, Marz (1992) and Poguntke (1993) developed the theory for the planar concave grating. The difference ΔL in path length for rays passing via P and O is defined as the light path function as

$$\Delta L = ((AP+BP)-(AO+BO))$$

$$= -w(\sin\alpha + \sin\beta) + \frac{w^4}{8R^3}\left[\frac{\sin^2\alpha}{\cos\alpha} + \frac{\sin^2\beta}{\cos\beta}\right] + \frac{w^5}{8R^4}\left[\frac{\sin^3\alpha}{\cos^2\alpha} + \frac{\sin^3\beta}{\cos^2\beta}\right], \qquad (3.3)$$

where the expansion is performed up to the fifth order in w.

It is generally possible to obtain a sufficiently high resolution from a grating that has dimensions small in comparison to the radius of curvature R. In this case, if the grating is used in the region around O (i.e., it is centered at w=0), the increasing power of

R in the denominator causes the magnitude of the terms in (3.3) to decrease with increasing order. The validity of this statement will be demonstrated later.

In order for the grating to diffract the light from A, and for the light to constructively interfere at B, the path length for rays passing via any two neighboring grating elements should differ by an integer number of wavelengths. The integer here is the diffraction order m. If one grating element has an end at O, then other grating elements should be located around the grating surface such that their corresponding ends are defined by points for which

$$\Delta L = im\frac{\lambda}{n}, \tag{3.4}$$

where i is an integer that gives the "number" of the grating element (i.e., the *i*th element counted from O), and takes both positive and negative values.

We should initially consider the region around the grating pole. Since for this region w << R, the fourth- and fifth-order terms of (3.3) are negligible in comparison to the leading term. In this case the w coordinate of the *i*th grating element may be found from the expression

$$-w_i(\sin\alpha + \sin\beta) = im\frac{\lambda}{n} \tag{3.5}$$

This shows that the region of the grating around O will focus light of wavelength λ from A to the point B provided that the grating spacing in this region has a constant projection d_0 onto w axis. The constant d_0 in this instance is given by

$$d_0 = \left|\frac{w_i}{i}\right| = \frac{m\lambda}{n(\sin\alpha + \sin\beta)} \tag{3.6}$$

Equation (3.6) is identical to (3.1), therefore it is confirmed that a circular grating used in the Rowland circle configuration should, to a first approximation, have a spacing whose projection onto w axis is a constant. This describes the "classic" circular grating from Rowland's era; such a grating is ideally suited to the ruling engine fabrication technology that was used at that time. However, this solution is based upon the assumption that certain high-order terms in the path length expansion may be neglected, and is consequently only approximate in nature. In the case of a grating formed by photolithography, we are free to set the spacing for each grating tooth individually. This makes it possible to "tailor" the grating spacing in order to modify the image quality. This technique may be used to improve the device performance.

We now turn our attention to the higher-order terms of (3.3). These terms become more significant as one moves away from the grating pole, and in the case of a grating whose spacing has a constant projection onto w axis, they describe path length errors that degrade the image quality. The fourth-order term in w is analogous to the spherical aberration of lenses. The phase of light arriving at B via different grating elements is no longer periodic, and so the interference of light at B does not occur in an ideally constructive manner. These effects can be corrected for by appropriately "tailoring" the grating spacing. An equivalent equation to (3.5), but one which is now correct up to the fifth order in w, may be written as

$$-w_i(\sin\alpha+\sin\beta)+\frac{w_i^4}{8R^3}\left[\frac{\sin^2\alpha}{\cos\alpha}+\frac{\sin^2\beta}{\cos\beta}\right]+\frac{w_i^5}{8R^4}\left[\frac{\sin^3\alpha}{\cos^2\alpha}+\frac{\sin^3\beta}{\cos^2\beta}\right]=\frac{im\lambda}{n} \qquad (3.7)$$

Solving for w_i gives a slightly modified position for the *i*th diffraction element. If the position of each element is defined according to (3.7), the resulting grating will be

aberration-free up to the fifth order. The magnitudes of the different terms of (3.7) depend upon the magnitudes of the device parameters R, α, and β. We require that the magnitude of the lowest -order (i.e., largest magnitude) uncorrected term be less than a quarter wavelength at either extreme of the grating. The correction may, of course, be performed for only one wavelength even though the grating is to be used over a finite spectral range. Residual aberration effects will exist for other wavelengths, and so the correction should, in general, be performed for the central wavelength in the desired operating range.

In consideration of the higher-order terms of (3.7), it has become necessary to give a more general definition to the parameter d. The "tailored" spacing of an aberration-corrected grating no longer has a constant projection onto w axis. It has, however, been seen that the positions of the grating elements remain unchanged in the region around the grating pole O (d_0 = d). In addition, we note that at O the actual grating spacing is identical to its projection onto the w axis. We therefore define d to be the actual grating spacing at O; in this way its value remains unaffected by the correction process.

3.1.2 PLANAR CONCAVE GRATINGS BASED ON A RECURSIVE DEFINITION OF FACET POSITIONS

In the last section, the concave grating theory uses the approach of expanding the light path function in a power series and analyzing the lower-order terms. McGreer (1996a) has proposed a recursion formula approach to design concave grating. The recursion formula approach is general and can be used to generate gratings that are similar to many

of the concave gratings calculated from the power-series approach. In many cases, the recursion formula approach is easier to implement than the power-series approach.

3.1.2.1 Generation of concave grating

A planar concave grating consists of a series of facets whose location can be determined by two constraint conditions

$$\varepsilon_{1,i}(x_i, y_i)=0, \qquad \varepsilon_{2,i}(x_i, y_i)=0 \tag{3.8}$$

where i is an index for each facet. The index of one facet differs from the index of an adjacent facet by unity. Here (x_i, y_i) is the location of the center of the *i*th facet (Fig. 3.2). $\varepsilon_{1,i}(x_i, y_i)$ and $\varepsilon_{2,i}(x_i, y_i)$ are referred to as the constraint functions. Explicit definitions of possible constraint functions will be given later. In equation (3.9), $\varepsilon_{1,i}(x_i, y_i)$ and $\varepsilon_{2,i}(x_i, y_i)$ are estimated by an arbitrary point (x, y) which is close to a point (x_i, y_i) where the constraint conditions for the *i*th facet are satisfied.

$$\varepsilon_{1,i}(x_i, y_i) \cong a_{11}(x-x_i) + a_{12}(y-y_i)$$

$$\varepsilon_{2,i}(x_i, y_i) \cong a_{21}(x-x_i) + a_{22}(y-y_i) \tag{3.9}$$

where $a_{\alpha,1} = (\partial\varepsilon_{\alpha,i}/\partial x)$ and $a_{\alpha,2} = (\partial\varepsilon_{\alpha,i}/\partial y)$, where α equals 1 or 2. The derivatives are evaluated at (x, y) and can be calculated analytically for all the cases. From equation (3.9), one can estimate (x_i, y_i) with an adjacent arbitrary point (x, y) as

$$x_i \cong x- [a_{22}\varepsilon_{1,i}(x, y) - a_{12}\varepsilon_{2,i}(x, y)]/ (a_{11}a_{22} - a_{21}a_{12})$$

$$y_i \cong y- [a_{11}\varepsilon_{2,i}(x, y) - a_{21}\varepsilon_{1,i}(x, y)]/ (a_{11}a_{22} - a_{21}a_{12}) \tag{3.10}$$

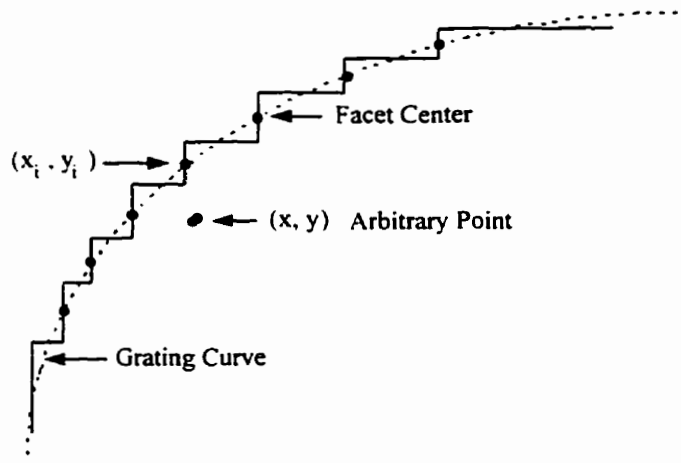

Fig. 3.2 Generation of grating facets according to constraint conditions; grating curve is a smooth curve that goes through the centers of facets; (x_i, y_i) is the center of the *i*th facet.

Several iterations can be used in this root-finding procedure to find a single (x_i,y_i) value; however, in practice, two iterations have been found to be sufficient. Let j be the index of the facet between the zeroth facet and the *i*th facet, i.e., $j = i-1$ for $i > 1$ and $j = i+1$ for $i < -1$. When (x_j, y_j) is known, it can be used as the initial value for (x,y) in the root-finding procedure to determine (x_i, y_i).

A concave grating can be generated through a recursive application of the root-finding procedure. First, a value for (x_0, y_0) is chosen as the grating pole. Then the root-finding procedure is applied for $i > 0$ to find the values of (x_i, y_i) in sequence from (x_1, y_1) to one end of the grating. Similarly, a recursive application of the root-finding procedure is used for $i < 0$ to find the values of (x_i, y_i) in sequence from (x_{-1}, y_{-1}) to the other end of the grating. This is referred to as the recursive grating generation.

3.1.2.2 Constraint function for a stigmatic point

The first constraint function mentioned in section 3.1.2.1 can be defined as

$$\varepsilon_{1,i}(x, y) = r_1 + r_2 + im\lambda_0/n - r_{1,0} - r_{2,0} \quad (3.11)$$

where r_k is the distance between (x, y) and (a_k, b_k), and $r_{i,\alpha}$ is the distance between (x_i, y_i) and (a_α, b_α) . The path lengths referred to in (3.11) are illustrated in Fig. 3.3. Here n is the effective index of the optical mode that propagates and m is an integer referred to as the grating order.

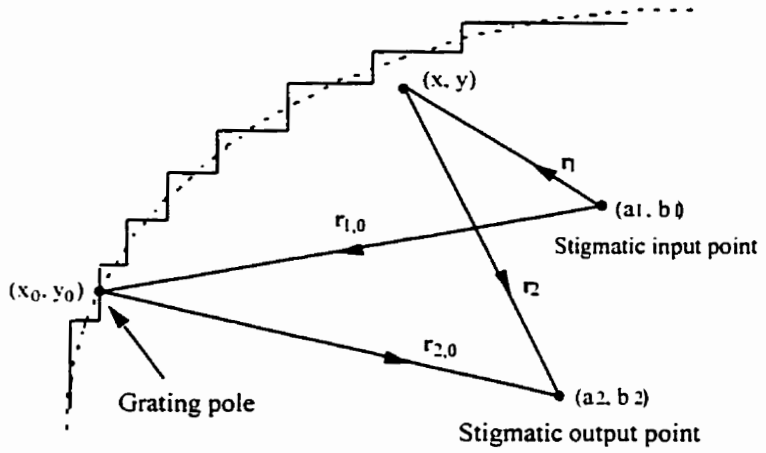

Fig. 3.3 Definition of path lengths used in the constraint function; r_1, the distance between the stigmatic input point (a_1,b_1) and an arbitrary point (x, y); r_2, the distance between the stigmatic output point (a_2,b_2) and (x,y); $r_{1,0}$, the distance between (a_1,b_1) and the grating pole (x_0,y_0); and $r_{2,0}$, the distance between (a_2,b_2) and (x_0,y_0)

The constraint condition $\varepsilon_{1,i}(x_i, y_i) = 0$ derived from the above constraint function is equivalent to requiring the path-length function to be invariant along the grating. The wavelength λ_0 which satisfies the above constraint condition is called the stigmatic wavelength. When incident at (a_1,b_1), light of the stigmatic wavelength λ_0 diffracts to (a_2,b_2) without any aberration. Here (a_1,b_1) is referred to as the stigmatic input point, and (a_2,b_2) is referred to as the stigmatic output point. A grating that is stigmatic at one wavelength is said to have one stigmatic point. It is instructive to compare the above constraint function (3. 11) to a modified path-length function as defined below:

$$F_i(\lambda) = r_{3,i} + r_{4,i} + im\lambda/n - r_{3,0} - r_{4,0} \tag{3.12}$$

where (a_3,b_3) is an arbitrary input point and (a_4,b_4) is an arbitrary output point. Here λ is an arbitrary free-space optical wavelength. If the grating is to be used in a WDM demultiplexer, (a_3,b_3) will be fixed at (a_1,b_1). If the modified path-length function is zero for every facet at a particular wavelength, there will be no aberration of any order for that wavelength.

3.1.2.3 Constraint function for a range of wavelengths

In a demultiplexer, the input point is fixed; light with a range of wavelengths is focused on the output focal curve at different points according to its wavelength. The second constraint function can be specifically designed to minimize the defocusing for a range of wavelengths. Light along two rays that reflect two adjacent facets i and j arrives at the stigmatic point in phase if $\lambda = \lambda_0$. If the wavelength shifts, the two rays arrive in phase at a point on the focal curve that is displaced from the stigmatic point. The displacement required per wavelength shift is the dispersion caused by diffraction from a section of the grating near the *i*th facet, and the reciprocal of the dispersion is denoted by $(\partial\lambda/\partial u_2)_i$ when the wavelength shift is infinitesimal. As illustrated in Fig. 3.4, u_2 refers to the component of the displacement along the output focal curve from (a_2,b_2) to (a_4,b_4). The value of this dispersion can be found by applying Fermat's principle at the *i*th facet and differentiating to give

$$\frac{m}{n}\left(\frac{\partial\lambda}{\partial u_2}\right)_i = \frac{\partial(r_{4,j} - r_{4,i})}{\partial u_2} \tag{3.13}$$

If all the rays are to arrive in phase at the same point for the shifted wavelength, the dispersion near each facet must have the same value, which is referred to as $(\partial\lambda/\partial u_2)_0$.

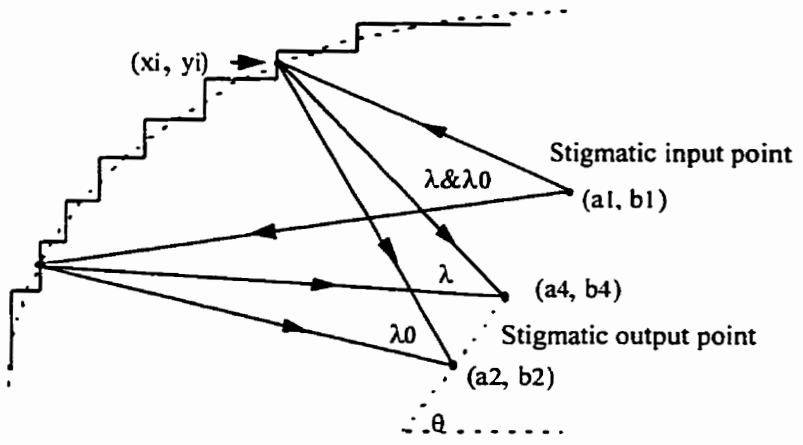

Fig. 3.4 Demultiplexer based on concave grating. Light with different wavelengths is incident on a common point (a_1,b_1). Light of the stigmatic wavelength is focused to the stigmatic output point (a_2,b_2). Light with an arbitrary wavelength λ is focused on the output focal curve at (a_4,b_4).

Therefore,

$$\frac{im}{n}\left(\frac{\partial\lambda}{\partial u_2}\right)_0 = \sum_{k=1}^{i}\frac{m}{n}\left(\frac{\partial\lambda}{\partial u_2}\right)_k = \frac{\partial(r_{4,0}-r_{4,1})}{\partial u_2}+\frac{\partial(r_{4,1}-r_{4,2})}{\partial u_2}+\frac{\partial(r_{4,2}-r_{4,3})}{\partial u_2}+\bullet\bullet\bullet\frac{\partial(r_{4,j-1}-r_{4,j})}{\partial u_2}$$

$$=\frac{\partial(r_{4,0}-r_{4,j})}{\partial u_2} \tag{3.14}$$

$$\frac{\partial(r_{4,0}-r_{4,j})}{\partial u_2}=\frac{\partial(r_{4,0}-r_{4,j})}{\partial a_4}\times\frac{\partial a_4}{\partial u_2}+\frac{\partial(r_{4,0}-r_{4,j})}{\partial b_4}\times\frac{\partial b_4}{\partial u_2} \tag{3.15}$$

Supposing θ is the angle of the displacement vector from (a_2,b_2) to (a_4,b_4), i.e., θ is the angle that the output focal curve makes with respect to the x axis at the point where the output focal curve intersects the stigmatic point, we have

$$a_4 = u_2\cos\theta,\ b_4 = u_2\sin\theta \tag{3.16}$$

$$\frac{\partial a_4}{\partial u_2} = \cos\theta, \frac{\partial b_4}{\partial u_2} = \sin\theta \tag{3.17}$$

By combining equations (3.14) to (3.17),

$$\frac{\partial(r_{4,j} - r_{4,0})}{\partial a_4}\cos(\theta) + \frac{\partial(r_{4,j} - r_{4,0})}{\partial b_4}\sin(\theta) + \frac{im}{n}\left(\frac{\partial \lambda}{\partial u_2}\right)_0 = 0, \tag{3.18}$$

So, we can choose the following function as the second constraint function to minimize the defocusing for a range of wavelengths:

$$\varepsilon_{2,j}(x, y) = \frac{\partial(r_{4,j} - r_{4,0})}{\partial a_4}\cos(\theta) + \frac{\partial(r_{4,j} - r_{4,0})}{\partial b_4}\sin(\theta) + \frac{im}{n}\left(\frac{\partial \lambda}{\partial u_2}\right)_0, \tag{3.19}$$

A constraint function that is equivalent to the one given by (3.19) is

$$\varepsilon_{2,j}(x, y) = \left(\frac{\partial F_j}{\partial u_2}\right)_{\lambda=\lambda_0} \tag{3.20}$$

The effect of setting the constraint function to zero is to minimize the rate that the path-length function increases as the wavelength moves away from the stigmatic wavelength. This will minimize the increase in destructive interference of light reflecting off different facets and thereby increase the bandwidth of the grating response. In addition to minimizing defocusing, the above constraint function has the advantage that the linear dispersion coefficient and θ are explicitly specified as parameters that control the generation of the grating rather than uncontrolled parameters to be calculated after the grating is generated. Having prior control of θ is a strong advantage for applications in which a specific orientation of the output focal curve is required, such as would be the case if the focal curve were required to be aligned to the edge of a device. This kind of concave grating can not be designed on Rowland circle.

3.1.2.4 Focal curve calculation

The focal curve and dispersion can be determined from the modified path-length function after a concave grating has been generated. The dispersion and focal curve are given by $(\partial F/\partial w)_{w=0} = 0$ and $(\partial^2 F/\partial^2 w)_{w=0} = 0$, respectively, where w is the displacement along the grating curve from (x_0, y_0) to (x,y) (Capron, 1993). The derivatives may be replaced by discrete derivatives. That is, the dispersion and focal curve are given by $F_1 - F_{-1} = 0$ and $F_1 - 2F_0 + F_{-1} = 0$, respectively. The condition defining the focal curve is equivalent to

$$r_{3,1} - 2\, r_{3,0} + r_{3,-1} + r_{4,1} - 2\, r_{4,0} + r_{4,-1} = 0 \qquad (3.21)$$

3.1.3 DEMULTIPLEXERS BASED ON CONCAVE GRATINGS

3.1.3.1 Design parameters

Using the formalisms given in section 3.1.2, five demultiplexers based on concave gratings were designed. Those demultiplexers had common parameters: $a_1 = 22.5$ mm, $b_1 = 0$ mm, $a_2 = 22.5$ mm, $b_2 = -0.765$ mm, $n = 1.484$, $\lambda_0 = 1548$ nm, $\theta = 90°$. Table 3.1 lists other parameters for five different demultiplexers.

In Table 3.1, only average facet size of a grating is given for each design. In fact, across a grating, the facet size varies linearly with respect to facet number. Fig. 3.5 shows facet size as a function of facet number for each design where the first facet begins from the bottom of a grating.

Fig. 3.6 is the mask used to fabricate the devices. There are 12 devices on the mask with the left-hand side being the image of the right-hand side.

Fig. 3.7a is the close up of a demultiplexer with 256 channels. On each device, there are 14 input waveguides whose width alternates with 7 μm and 10 μm, and separated by 40 μm; there are 64, 128, or 256 output waveguides, each of which has four straight segments separated by curved waveguides with a radius of 250 μm. The output waveguides have a nominal spacing of 10 μm and a width of 7 μm at the point where they collect light and a spacing of 500, 250, or 125 μm and a width of 4 μm at the output edge of a chip. Fig. 3.7b is the schematic diagram of a demultiplexer. Light is coupled into one of 14 input ridge waveguides, and at the end of the input waveguide, diverges freely inside a slab waveguide until it is reflected by the diffraction grating. The diffracted light is collected by output waveguides. For the convenience of test, output waveguides are numbered on the chip by binary code. The number of a waveguide increases from right to left in a chip, which means the no.1 waveguide is the shortest waveguide among all output waveguides, as we can see from Fig. 3.7.

Table 3.1 Parameters for Five Demultiplexers

design type	diffraction order	channel spacing (nm)	$(d\lambda/du_2)_0$ nm/mm	output number	facet size μm	min λ nm	Max λ Nm	range in λ nm
A	75	0.144	0.015	64	17.1	1550	1560	10
B	40	0.3	0.03	64	18.2	1540	1560	20
C	20	0.3	0.03	128	9.1	1529	1567	38
D	15	0.2	0.02	256	4.6	1519	1570	51
E	20	0.6	0.06	64	18.2	1529	1567	38

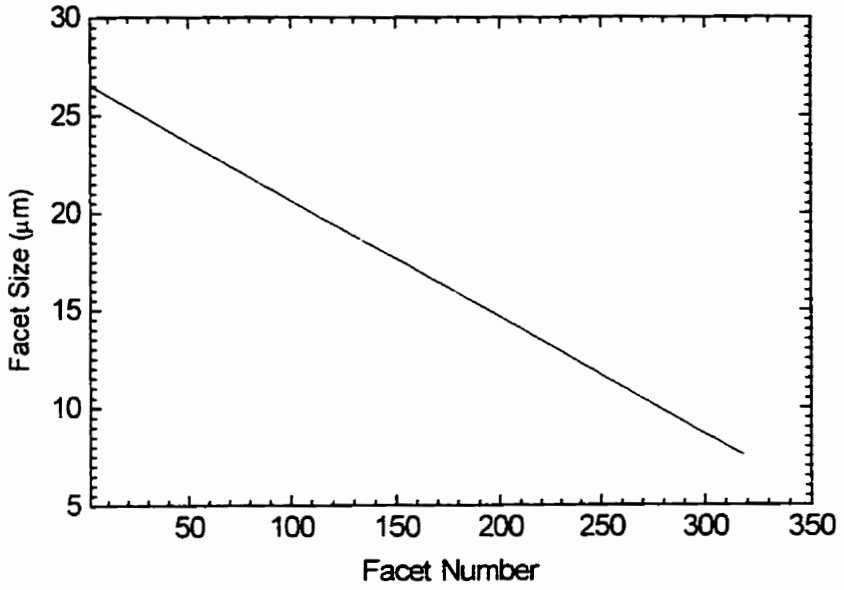

Fig. 3.5a Design A

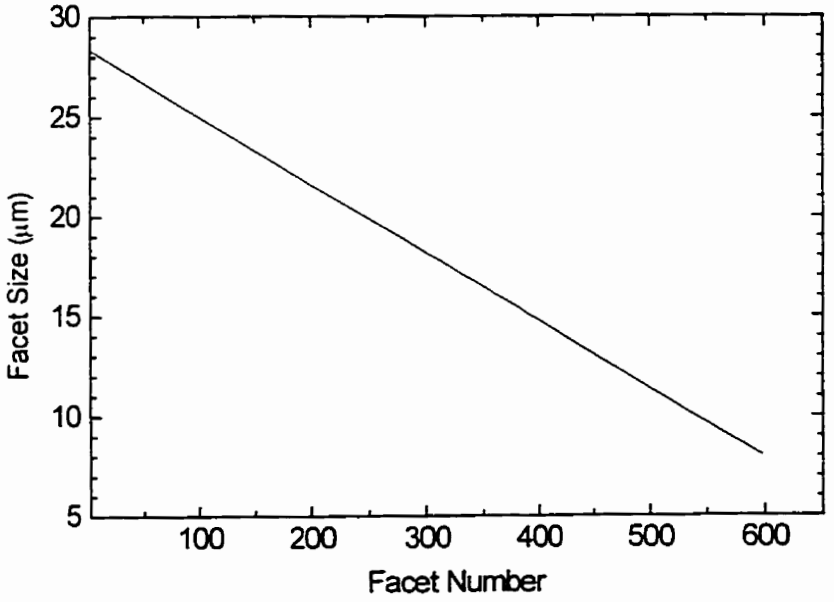

Fig. 3.5b Design B

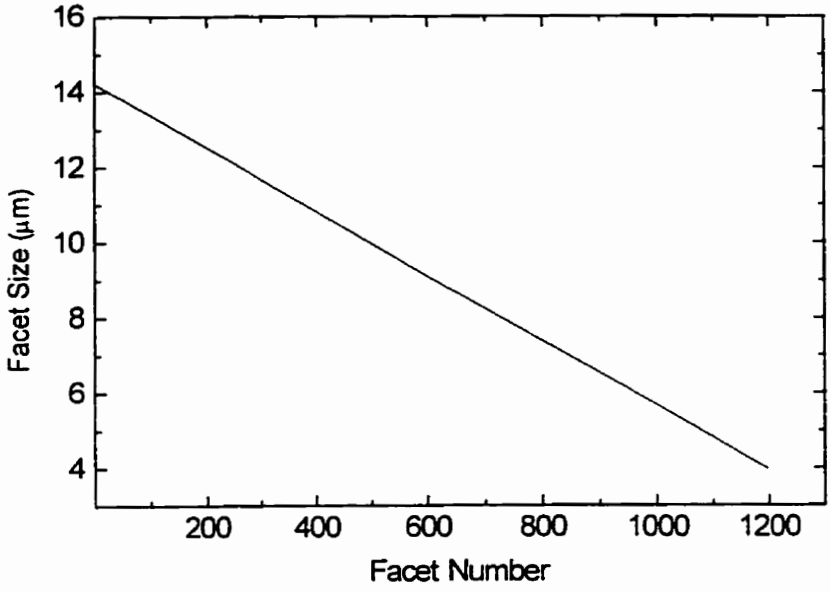

Fig. 3.5c Design C

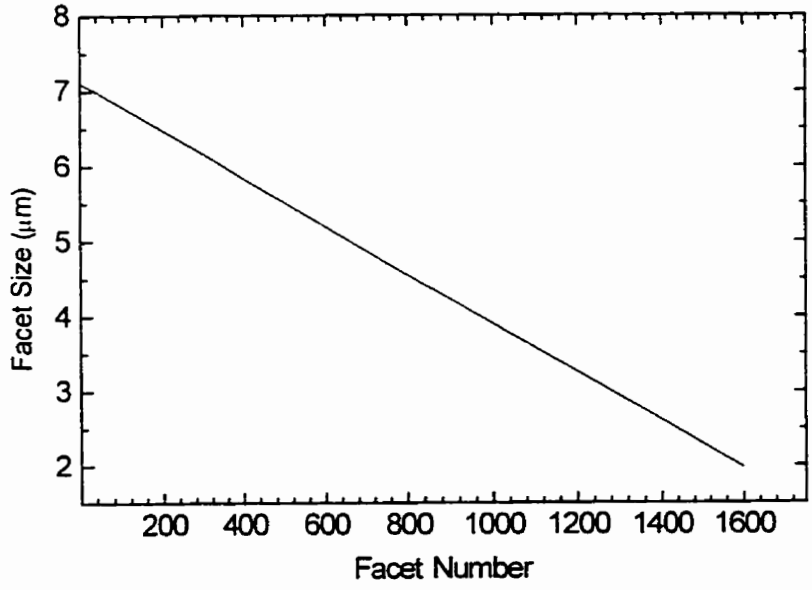

Fig. 3.5d Design D

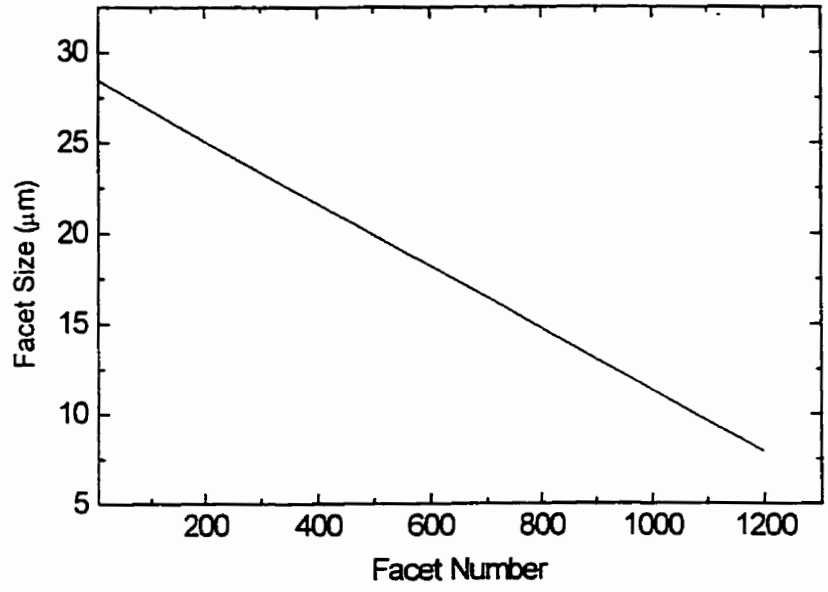

Fig. 3.5e Design E

Fig. 3.5 Facet size as a function of facet number for each design

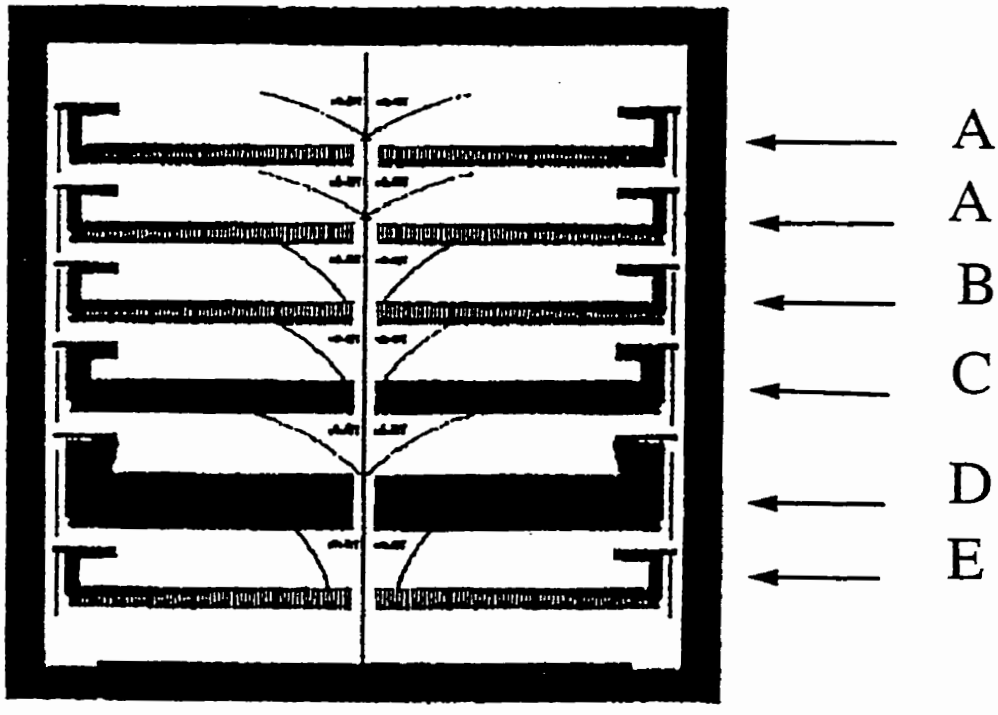

Fig. 3.6 The mask used to fabricate demultiplexers

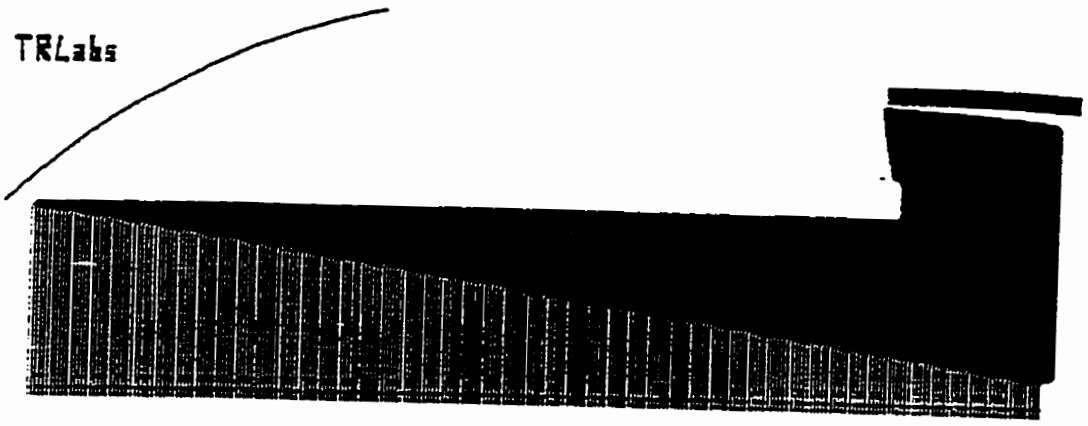

Fig. 3.7a The lay-out of a demultiplexer with 256 channels

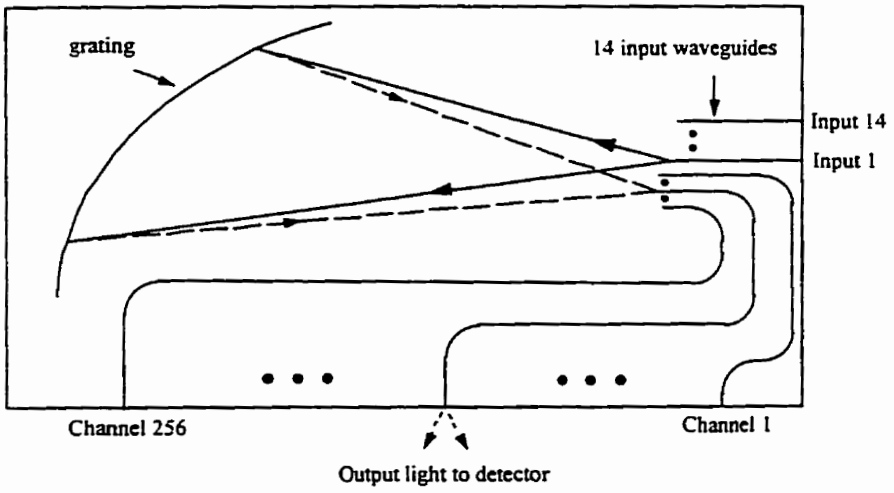

Fig. 3.7b The schematic view of a demultiplexer

3.1.3.2 Facet design

In the above demultiplexer design, the Eagle configuration, in which light is approximately retroreflected, is used. Therefore the light is approximately incident on the

facets near normal incidence. The simplest fabrication process for integrated grating is to form the facets by Reactive Ion Etch (RIE) alone. With this process, the reflective surface is the interface between the waveguide and air. The reflection coefficient from this interface can be roughly estimated by assuming that the incident light is in the form of a plane wave, in which case, the reflection coefficient is given by the Fresnel equation

$$R = \left[\frac{n-1}{n+1}\right]^2 \tag{3.22}$$

For semiconductor waveguides this reflection coefficient is approximately 0.32 (giving a loss contribution of -4.9 dB) and for glass waveguides this reflection coefficient is approximately 0.034 (giving a loss contribution of -15 dB). Reflection coefficients for the guided modes are somewhat different from this and are different for the TE modes and TM modes (Vassallo, 1990). Facet reflectivity can be enhanced by depositing gold on the facets.

An alternative approach to enhancing the facet reflectivity is to use a grating configuration that does not have light arriving at normal incidence to the facets. We have designed gratings in glass waveguides in which the angle of incidence and the angle of reflection for optical rays on the facets is nominally 45°. For the glass/air interface, the critical angle is around 42°. With 45° incidence, plane wave light will undergo total internal reflection at the glass/air interface. In our grating design, a facet pair equivalent to a retroreflecion prism is used, as shown in Fig. 3.8. A light ray is incident on the first facet at an angle of 45°, reflected to the adjacent facet again at 45° incidence, and reflected towards its point of origin.

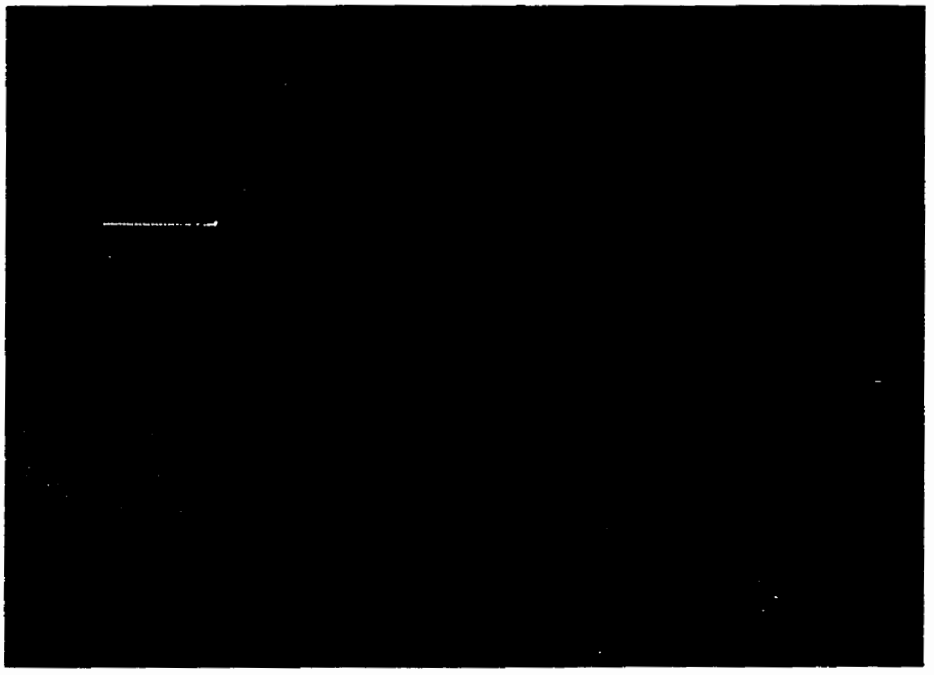

Fig. 3.8a Photograph of grating facets

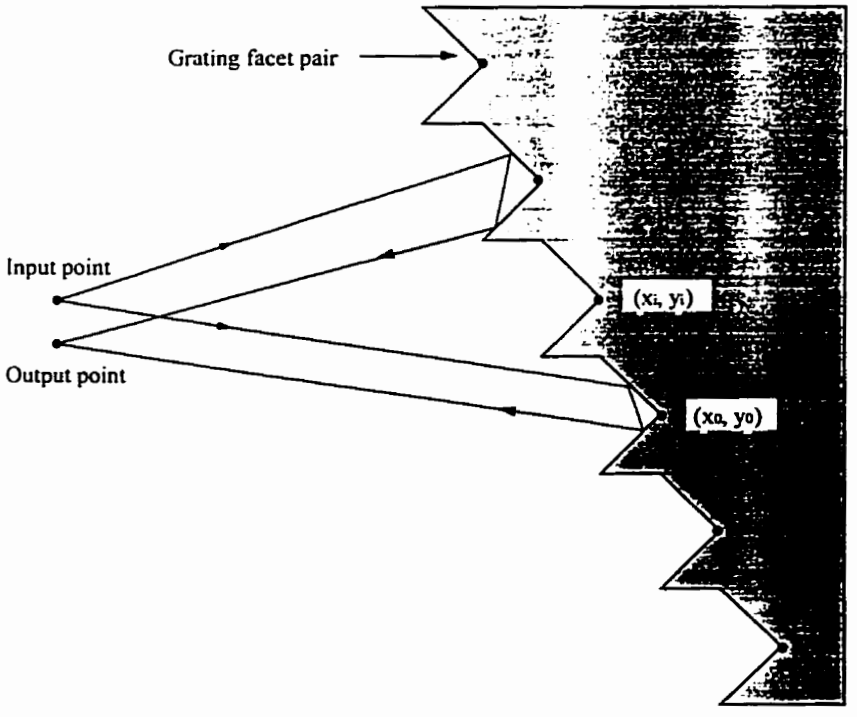

Fig. 3.8b Schematic view of grating facets

3.2 SIMULATIONS ON CONCAVE GRATING

3.2.1 DIFFRACTION FROM CONCAVE GRATING IN PLANAR WAVEGUIDES

Concave grating performance can be modeled with the scalar wave approximation (McGreer, 1995). A schematic view of the grating, along with the coordinate system to be used is shown in Fig. 3.9. The electric field at the input point (a_1, b_1) is modeled as a Gaussian field with a mode width of w_0,

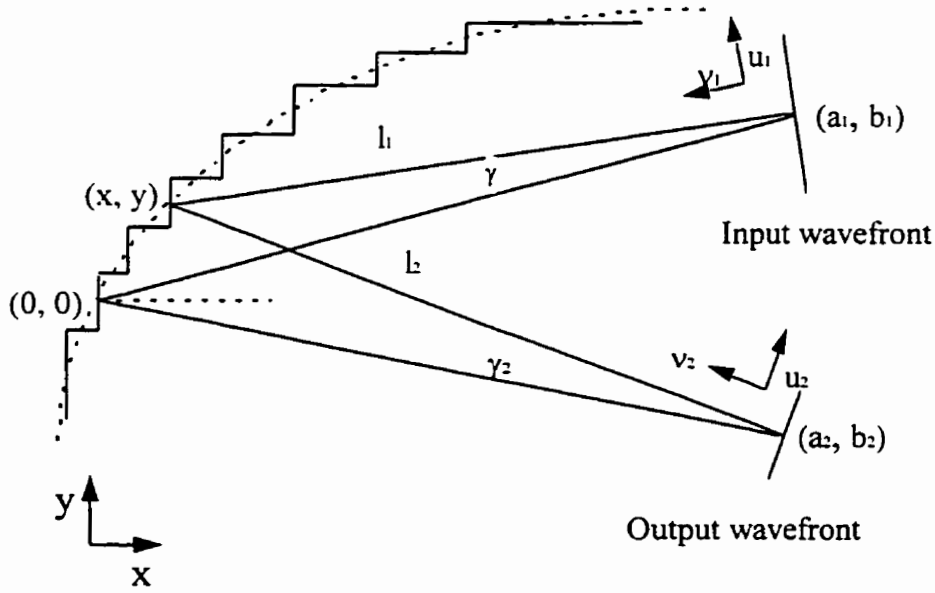

Fig.3.9 Schematic view of a concave grating and coordinate systems used in calculations

$$E(u_1) = E_0 \exp\left(-\frac{u_1^2}{w_0^2}\right) \tag{3.23}$$

The field at distance l_1 from the input and at angle γ from normal incidence is given by Fraunhofer diffraction theory in two dimensions (Papoulis, 1968)

$$E(l_1, \gamma) = \frac{1+\cos\gamma}{2\sqrt{\lambda l_1}} \exp(ikl_1 - i\frac{\pi}{4}) \times \int_{-\infty}^{\infty} E(u_1) \exp(-ik\gamma u_1) du_1 \tag{3.24}$$

where k is the wavenumber within the slab waveguide, i.e., $k = 2\pi/\lambda$, and λ is the wavelength of light in the waveguide. Evaluating the integral and dropping the constant phase factor gives E_i, the electric field at the *i*th grating facet

$$E_i = E_0 \frac{1+\cos(\gamma)}{2} \frac{w_0\sqrt{\pi}}{\sqrt{\lambda l_1}} \exp(ikl_1) \exp(-\frac{\gamma^2}{\sigma^2}) \tag{3.25}$$

where $\sigma = \lambda/\pi w_0$.

The output point (a_2, b_2) is a distance u_2 along the focal curve. The field at that point is found with the Kirchhoff formula by integrating over each facet then summing the results from all facets

$$E(u_2) = \sum_i Q \int_{D/2}^{D/2} E_i \frac{1}{\sqrt{\lambda l_2}} \exp(i(kl_2 - \pi/4)) dy \tag{3.26}$$

where Q is the inclination factor given by $Q = [\cos(\beta_1)+\cos(\beta_2)]/2$. Here β_1 is angle between the facet normal and the light incident on the facet and β_2 is angle between the facet normal and the light reflection from the facet. D is the effective facet width, which in general varies across the grating. Inserting (3.25) into (3.26) and dropping the constant phase factor gives

$$E(u_2) = E_0 \sum_i Q \frac{w_0\sqrt{\pi}}{\lambda\sqrt{l_1 l_2}} \exp(-\frac{\gamma^2}{\sigma^2}) \times \int_{D/2}^{D/2} \exp(ik(+l_2)) dy' \tag{3.27}$$

Within one facet, γ, l_1, and l_2 have been assumed to be constant except when they contribute to the phase. The optical path length is given by $l = l_1 + l_2$, which can be written as $l = l_1 + l_2 + \alpha y'$ where l_1 and l_2 henceforth refer to the distances to the center of a grating facet at (x, y), y' is the distance along the y-axis from the center of the facet, and $\alpha = dl/dy$. For facets along the y-axis $\alpha = (y-b_1)/l_1 + (y-b_2)/l_2$. Since the integral of $\exp(ik\alpha y')$ is $D\mathrm{sinc}(kD\alpha/2)$, the field at the output is

$$E(u_2) = E_0 \sum_i Q \frac{Dw_0\sqrt{\pi}}{\lambda\sqrt{l_1 l_2}} \exp(-\frac{\gamma^2}{\sigma^2}) \times \exp(ik(l_1 + l_2)) \sin c(kD\alpha / 2) \qquad (3.28)$$

This equation is the basis for numerical modeling of grating performance. The output intensity is proportional to the square of the magnitude of the field and output power is proportional to the integral of the intensity.

3.2.2 SPECTRAL RESPONSES OF DEMULTIPLEXERS BASED ON CONCAVE GRATINGS

To get spectral response of a demultiplexer based on concave gratings, the point where an input ridge waveguide meets the slab waveguide is chosen as an input point, and the point where an output ridge waveguides meets the slab waveguide is chosen as an output point. By changing wavelength in a certain range and integrating the intensity across the output waveguide, the spectral responses of a demultiplexer are obtained. Fig. 3.10 shows simulated transmission losses versus wavelengths for a channel of the demultiplexer of design A, design B, design C, design D and design E respectively. In doing simulations, only diffraction loss is considered here. In Chapter five, we will take account of

waveguide losses and coupling losses in simulation. From Fig. 10 it can be seen that the Full Width of Half Maximum (FWHM) of design A, design B, design C, design D and design E is 0.1 nm, 0.2 nm, 0.19 nm, 0.15 nm and 0.4 nm respectively. Since our gratings are optimized to the input point, the channel 1 which is the closest to the input point has the lowest diffraction loss, while the last channel which is the furthest from the input point has the highest diffraction loss. In Fig. 3.10d, channel 192 is used, and the diffraction loss for this channel is 4.2 dB. Channel one is used in Fig. 3.10a, Fig. 3.10b and Fig. 3.10e and the diffraction loss for these three designs is 1.3 dB, 0.7 dB and 0.4 dB respectively. So, the higher the resolution of a demultiplexer, the higher the diffraction loss is.

The diffraction pattern is the Fourier transform of the light distribution across the grating (Lizuka, 1985). For the light source with Gaussian profile, the light distribution

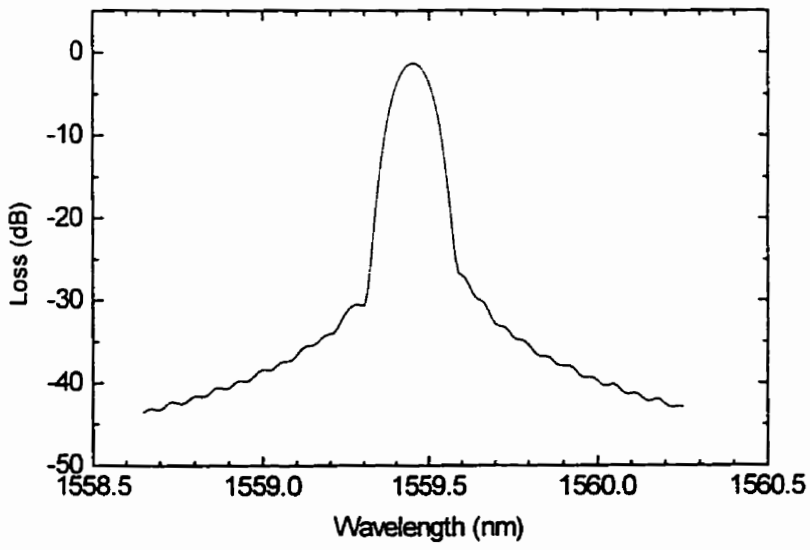

Fig. 3.10a Design A with FWHM of 0.1 nm and diffraction loss of 1.3 dB for channel 1

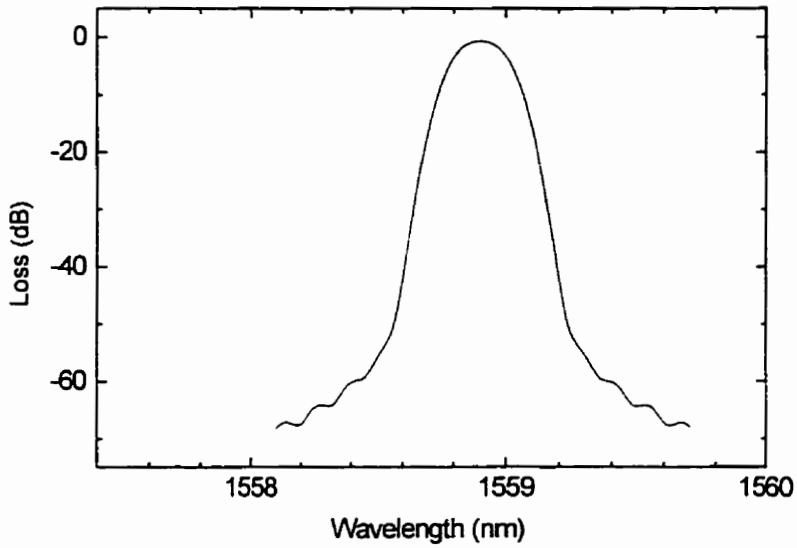

Fig. 3.10b Design B with FWHM of 0.2 nm and diffraction loss of 0.7 dB for channel 1

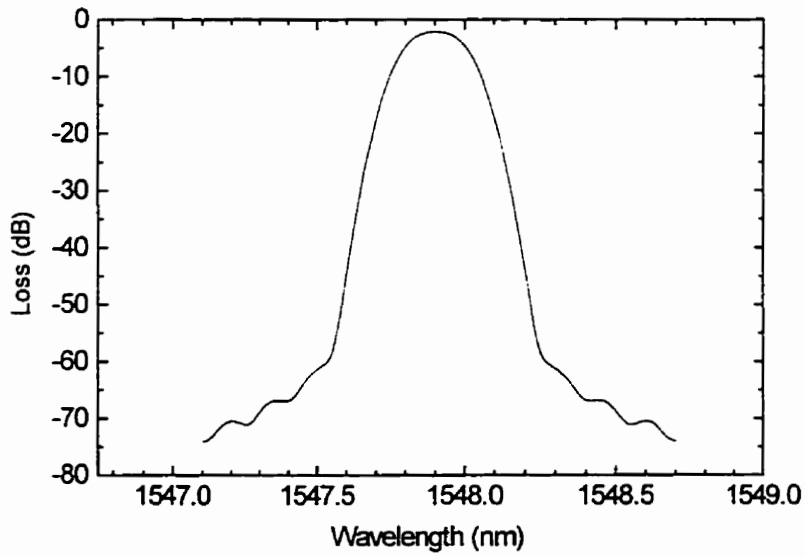

Fig. 3.10c Design C with FWHM of 0.19 nm and diffraction loss of 2.1 dB for channel 64

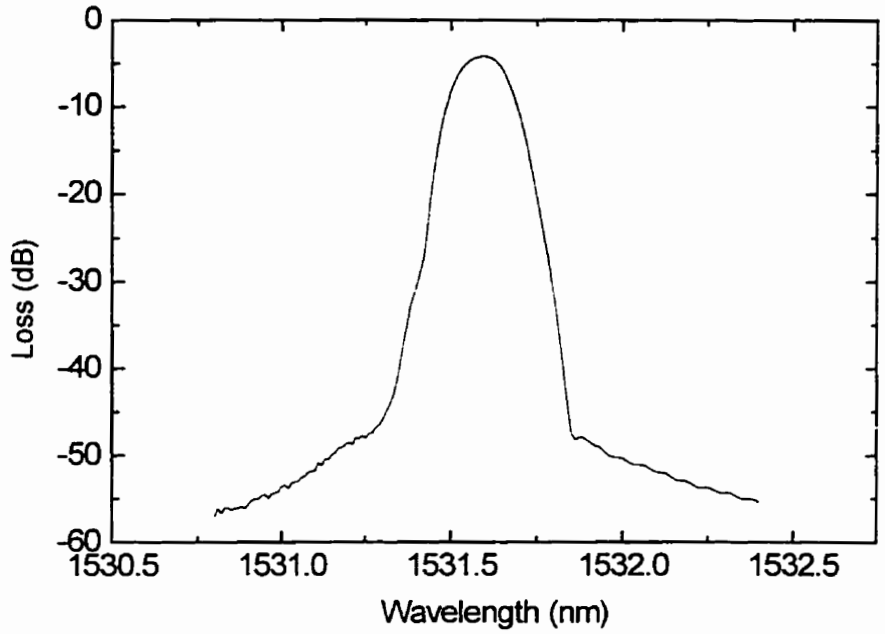

Fig. 3.10d Design D with FWHM of 0.15 nm and diffraction loss of 4.2 dB for channel 192

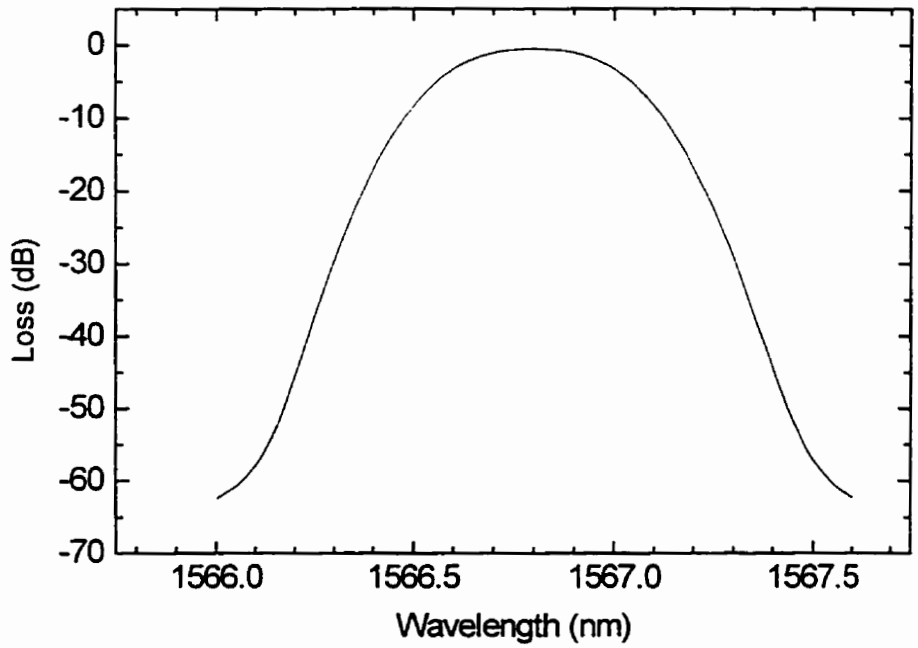

Fig. 3.10e Design E with FWHM of 0.4 nm and diffraction loss of 0.5 dB for channel 1
Fig. 3.10 Spectral response of a channel of the demultiplexer of designs A, B, C, D and E.

across the grating is also Gaussian shape, so the Fourier transform of a Gaussian function gives a Gaussian function, as shown in Fig. 3.10. Fig. 3.11 shows the spectral response when light was uniformly distributed across the grating. It is a $sinc^2$ function. If the input field is in a sinc function, then the output spectral response will be in a square shape, which is ideal for WDM applications.

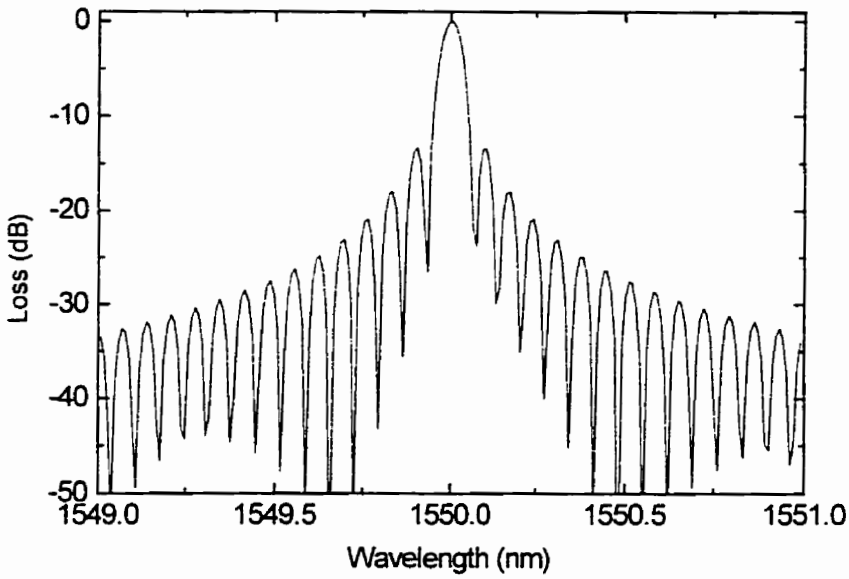

Fig. 3.11 Simulation result for a demultiplexer of design A when the grating is uniformly illuminated

3.2.3 ISOLATION BETWEEN ADJACENT CHANNELS

Fig. 3.12 shows transmission loss as a function of wavelength for two adjacent channels of a demultiplexer of design A. According to simulation, the channel isolation at the center wavelength is higher than 65 dB. But when the wavelength is away from the

center wavelength, the channel isolation will decrease. This is unfavorable in practical WDM applications, since the wavelength of a light souce may drift to some extent.

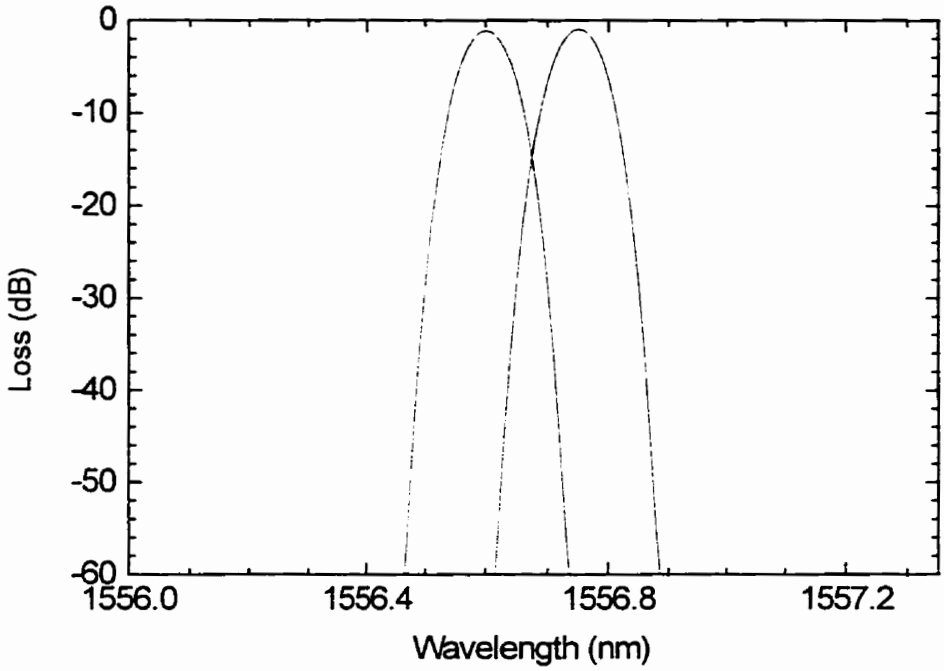

Fig. 3.12 Simulation of cross talk between two adjacent channels for a demultiplexer of design A

3.2.4 SPECTRAL RESPONSE FROM AN OUTPUT CHANNEL WHEN DIFFERENT INPUT CHANNELS WERE USED

Fig. 3.13 shows the spectral responses from channel 20 of a demultiplexer of design C when each of 14 input waveguides is used. By changing the input point from no.1 input waveguide (the input ridge waveguide which is closest to output waveguides) to no.14 input waveguide, the channel center wavelength is increased by 15.6 nm according to

simulations. In WDM fiber optic communication systems, the channel center wavelengths

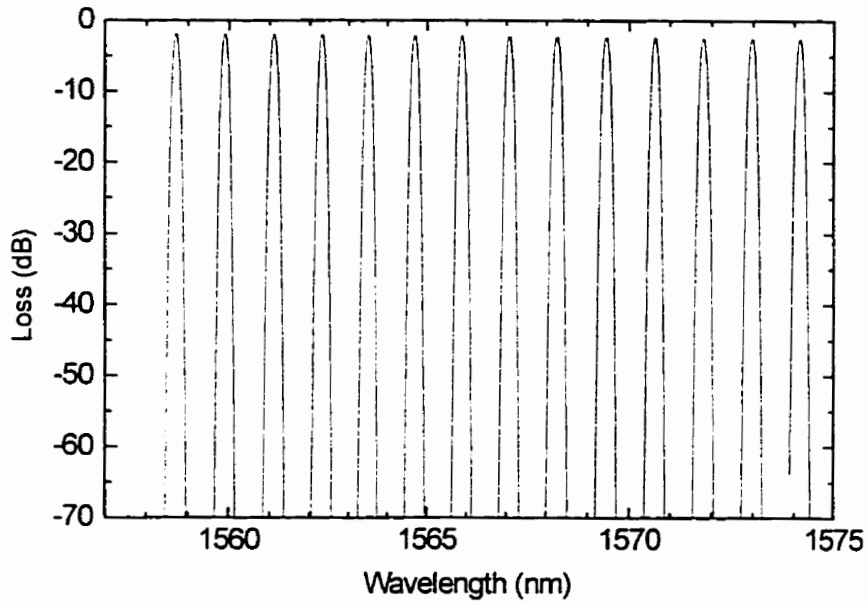

Fig. 3.13 Simulation of the spectral response from channel 20 of a demultiplexer of design C when each of 14 input waveguides are used

are predefined according to ITU standard. But variations in waveguide fabrication will cause the effective index to have an error, which will cause a wavelength error. Input waveguide selection provides a mechanism for wavelength tuning. This issue will be addressed in detail in Chapter five.

3.2.5 DIFFRACTION LOSS AS A FUNCTION OF CHANNEL NUMBER

By keeping an input point fixed and moving an output point from one output channel to another output channel, the spectral response from each output channel as well as

diffraction loss are obtained. Fig. 3.14 is the simulation result for ten adjacent channels of a demultiplexer of design C. The channel spacing is 0.3 nm, which agrees with our

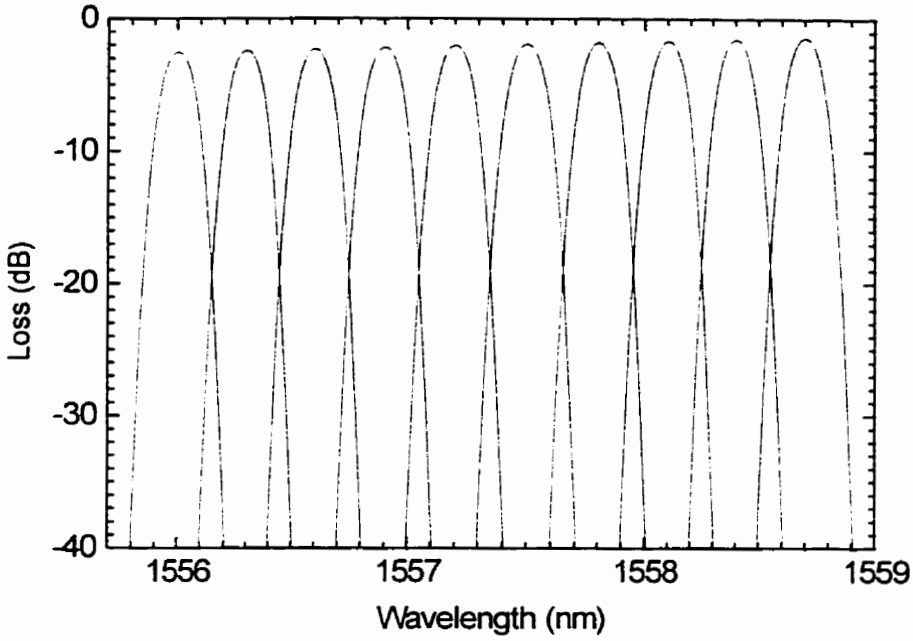

Fig. 3.14 Simulation of the spectral response of ten adjacent channels for a demultiplexer of design C

designed value. Fig. 3.15 shows diffraction losses of this demultiplexer as a function of channel wavelength. Longer wavelength channels are closer to the input point. Since our grating design is optimized to reflect light back to the point of incidence, when the output point is moved away from the input point, the grating will have high diffraction losses.

3.2.6 INPUT FIELDS WITH DIFFERENT MODE SIZE

In Fig. 3.16 input fields with different mode size have been used in simulations to see how the modesize ($2w_0$) affects the resolution and diffraction loss of a concave grating. When $w_0 = 2.2$, the grating has the highest resolution and loss. As mode size increases, both of the resolution and diffraction loss of the grating decreases. The angular divergence of the beam inside the slab waveguide is:

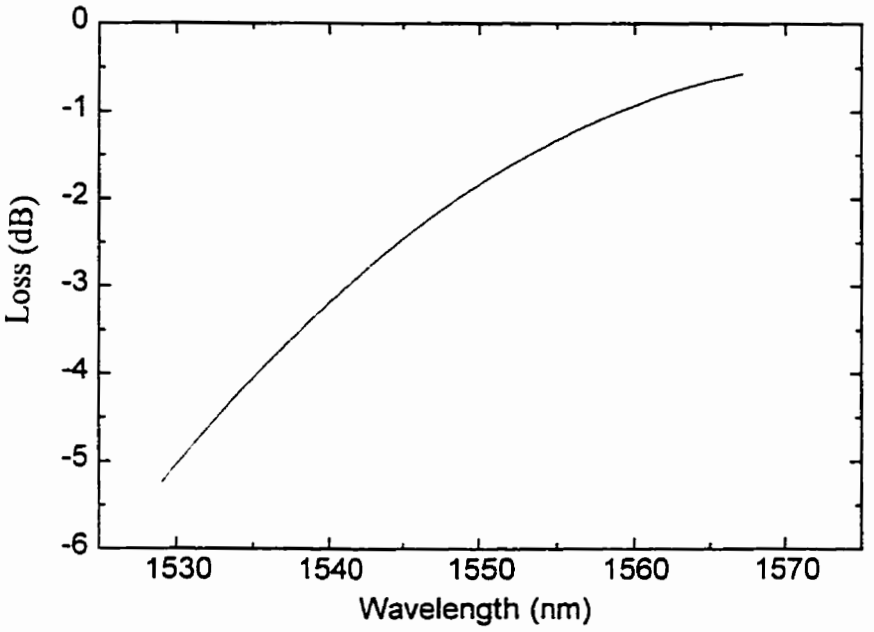

Fig. 3.15 Simulation of the diffraction loss as a function of channel wavelenght for a demultiplexer of design C

$$\theta_0 = \frac{\lambda}{\pi w_0} \tag{3.29}$$

the smaller the w_0, the bigger the θ_0 is. As w_0 decreases, more of the grating is illuminated, increasing resolution, spherical aberration and insertion loss. Nonetheless,

grating aberrations contribute only ≈ 0.5 dB at 1559.3 nm for our demultiplexers where $2w_0 = 6.4$ μm was used.

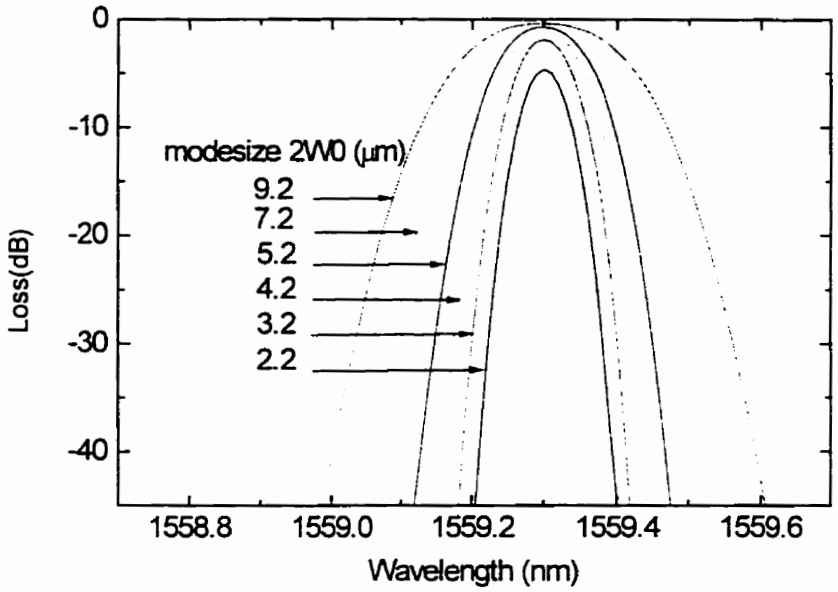

Fig. 3.16 Simulation of the spectral response from a channel of a demultiplexer of design A where input field has different mode size $2w_0$. No waveguide loss was assumed in the simulations

CHAPTER FOUR

FABRICATION OF DEMULTIPLEXERS ON Si SUBSTRATES

Demultiplexers were fabricated at the Alberta Microelectronic Center in the structure of SiO_2/SiON/SiO_2/Si by standard semiconductor technology. In this chapter, the fabrication procedure, such as the choice of substrates, film fabrication, and reactive ion etch (RIE), is discussed. We emphasize our efforts to improve the etch process to get vertically etched sidewalls.

4.1 THE USE OF Si SUBSTRATES FOR DEMULTIPLEXERS

Si, InP, GaAs are typical substrates for the demultiplexer based on concave grating. Components fabricated on InP or GaAs, which are composed of $Ga_xIn_{1-x}As_yP_{1-y}$ or $Al_xGa_{1-x}As$, have the advantage of being suitable for monolithic integration of detectors or optical amplifiers. In order to make use of $Ga_xIn_{1-x}As_yP_{1-y}$ or $Al_xGa_{1-x}As$, the materials have to be deposited epitaxially onto InP or GaAs substrates by Metal Organic Chemical Vapor Deposition (MOCVD), Liquid Phase Epitaxy (LPE), Molecular Beam Epitaxy (MBE), or other methods. These are very complicated and expensive processes. Advantages of glass waveguides on silicon substrates are:

1. The silicon substrate has many useful qualities, such as its good mechanical properties, the perfect quality of the crystal, the large range of commercially available wafers, and the possibility of cleaving which makes it possible to dispense with the polishing of the input and output planes of optical circuits for interconnection purposes.

2. With the outstanding advanced technology associated with Si substrate, one can not only choose between many well-known processes in order to achieve the required components, but also take advantage of all the progress made in the field of microelectronics through research on both silicon itself and the materials usually associated with it, such as silica, silicon nitride and aluminum.

3. With the use of Si substrate, both optical and electrical circuits can be combined on the same chip to improve the reliability, compactness and performance of the final device.

4.2 DEPOSITION OF SiO_2/SiON/SiO_2 LAYER STRUCTURE

To fabricate demultiplexers, a single mode slab waveguide composed of a 2 μm SiON core with refractive index of 1.492, a 0.5 μm SiO_2 upper cladding and 5 μm SiO_2 lower cladding with refractive index of 1.45 was first deposited onto Si substrates by Plasma Enhanced Chemical Vapor Deposition (PECVD). PECVD is a Chemical Vapor Deposition (CVD) process whose deposition rate is enhanced at a low temperature by energy supplied from plasma. PECVD is generally performed at substrate temperatures in the range 200-350°C, compared to typical CVD temperatures of 400-900°C. The major attraction of PECVD is its low deposition temperature. The range of deposition temperatures of PECVD makes it particularly attractive for use on compound semiconductors susceptible to thermal decomposition. For our glass waveguide deposition, low deposition temperature results in low stress build-up inside the glass film due to the difference of thermal expansion coefficients between the glass and the Si substrate, which will result in low stress birefringence. When SiH_4 and N_2O were mixed inside the reactor, the chemical reaction

$$SiH_4 + 2N_2O \rightarrow SiO_2\downarrow + 2H_2\uparrow + 2N_2\uparrow \qquad (4.1)$$

produced SiO_2 thin film, where ↑ stands for gas state and ↓ stands for solid state. In order to control the chemical reaction rate, the dilution gas N_2 and He were introduced inside the reactor. When SiH_4 and NH_3 was mixed, Si_3N_4 thin film was produced by the chemical reaction

$$3SiH_4 + 4NH_3 \rightarrow Si_3N_4\downarrow + 12H_2\uparrow \quad (4.2)$$

By mixing SiH_4, N_2O, and NH_3, both (4.1) and (4.2) occurred at the same time, producing a thin film that is a mixture of SiO_2 and Si_3N_4, called SiON. If x is the mole ratio between SiO_2 and Si_3N_4, the refractive index of SiON was determined by (4.3) (Baak, 1982).

$$n_{sio2} = 1.45,\ n_{Si3N4} = 2.0$$

$$n_{siON} = x\, n_{sio2} + (1-x)\, n_{Si3N4} \quad (4.3)$$

4.3 RIE ETCH PROCESS WITH PHOTORESIST AS MASK

After the layer structure SiO_2/SiON/SiO_2 was grown on Si substrates, an etching process was used to simultaneously etch concave gratings and input and output ridge waveguides into a slab waveguide. Fig. 4.1 is an etching process flow chart with photo resist used as the mask. Each step is explained as follows.

4.3.1 PHOTORESIST COATING

There are two types of photoresist: a negative type in which an exposed area remains after development, and a positive type in which an exposed area is removed after development.

Required characteristics for photoresist are sensitivity, resolution, adhesiveness to the substrate, coating uniformity, and resistance against etching solution. In general, positive photoresist is high in resolution, but poor in sensitivity, adhesiveness, and heat resistance.

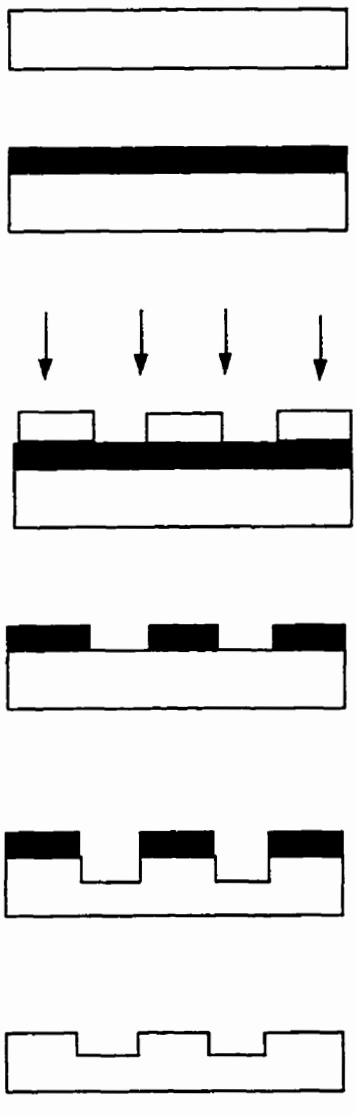

Fig.4.1 The flow chart for etching process

Positive photoresist was chosen for our experiments. By spin coating, a thin layer of photoresist was applied onto the surface of a slab waveguide. If the photoresist is too thick, it will decrease the etch resolution, while too thin a photoresist will be stripped off before the RIE etch process is finished. After thin photoresist film was formed on the surface of a slab waveguide, the sample was subjected to soft baking in an oven at appropriate temperatures to increase film adhesiveness.

4.3.2 UV LIGHT EXPOSURE

A high-pressure mercury lamp that had a peak spectrum at a wavelength of 365 nm was used for ultraviolet (UV) light exposure. There are a few methods for pattern exposure on photoresist. The contact printing method was used for this work. The mask that is shown in Fig. 3.6 was contacted with sample surface. Good contact is essential for successful photolithography. The mask was carefully cleaned to ensure there was no visible dust before each photolithography. Exposure time is a critical parameter for achieving an ideal photoresist pattern.

4.3.3 DEVELOPMENT

After UV exposure, photoresist was developed by spraying with the developer solution. The sensitivity depends on the developer and the temperature. After developing, the

photoresist that remained was postbaked for 1-2 hours at 100 to 200°C to increase resistance against etching. At this point, the photoresist patterning work was completed. The most important parameter here is the developing time.

4.3.4 RIE

The sample patterned with photoresist was put inside a RIE set-up, as shown in Fig. 4.2. O_2 and CHF_3 with certain flow rates were introduced inside the chamber. RF power was fed into the cathode (substrate holder) of the parallel planar electrodes to produce reactive gas plasma at an approximate pressure of less than 10 Pa (0.1 Torr). Once plasma was built inside the chamber, the cathode was then self-biased at negative dc potential. The dc electric field yielded in the vicinity of the sample surface accelerated the positive ions

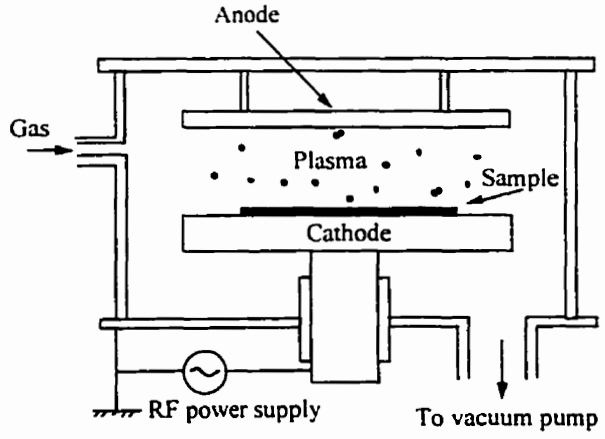

Fig. 4.2 Schematic of the RIE set-up

in the plasma toward the sample and these positive ions physically sputtered glass film away. On the other hand, the ions from O_2 and CHF_3 chemically reacted with glass film

and etched it away. So, the chemical and physical mechanisms were therefore incorporated in the etching. The details of the RIE etching mechanism is not quite clear, and four possible mechanisms were proposed by Winters et al. (1983), Flamm et al. (1981) and Steinbruchel et al. (1985):

1. Chemically enhanced physical sputtering: the role of the ions is to physically remove reaction products which are loosely held on the substrate surface.

2. Ion bombardment: ion bombardment is visualized as creating a damaged surface with sites particularly suitable for reaction.

3. Chemical sputtering: ion bombardment provides the energy required for certain exothermic reactions to occur in the near-surface region of the substrate which lead to products desorbing into the gas phase.

4. Direct reactive ion etching: energetic reactive ions serve as the main reactants in the overall etching reaction, in other words, ions themselves do most of the etching, rather than radicals.

By accurately controlling the total gas pressure, the partial gas pressure for O_2 or CHF_3, and the rf power, perfect anisotropic etching of SiO_2 and SiON could be achieved.

4.3.5 PHOTORESIST STRIPING

After finished RIE, the sample was taken out of the chamber. There are two ways to strip off the photoresist on the sample surface; one way is to use O_2 plasma to burn off the photoresist, which is referred as ashing; another way is to dissolve the photoresist with acetone. The latter method was used throughout our experiment.

4.3.6 THE VERTICALITY OF SIDEWALL

The verticality of sidewalls is a critical feature since tilt will cause reflected light to be at an incorrect angle to couple back into the waveguide. Loss as a function of tilt angle will be addressed in Chapter Five both theoretically and experimentally. However, it is illustrative to see how important the tilt angle is just simply from the point of view of ray optics, as shown in Fig. 4.3. If the tilt angle is big enough, all the light from the slab waveguide will

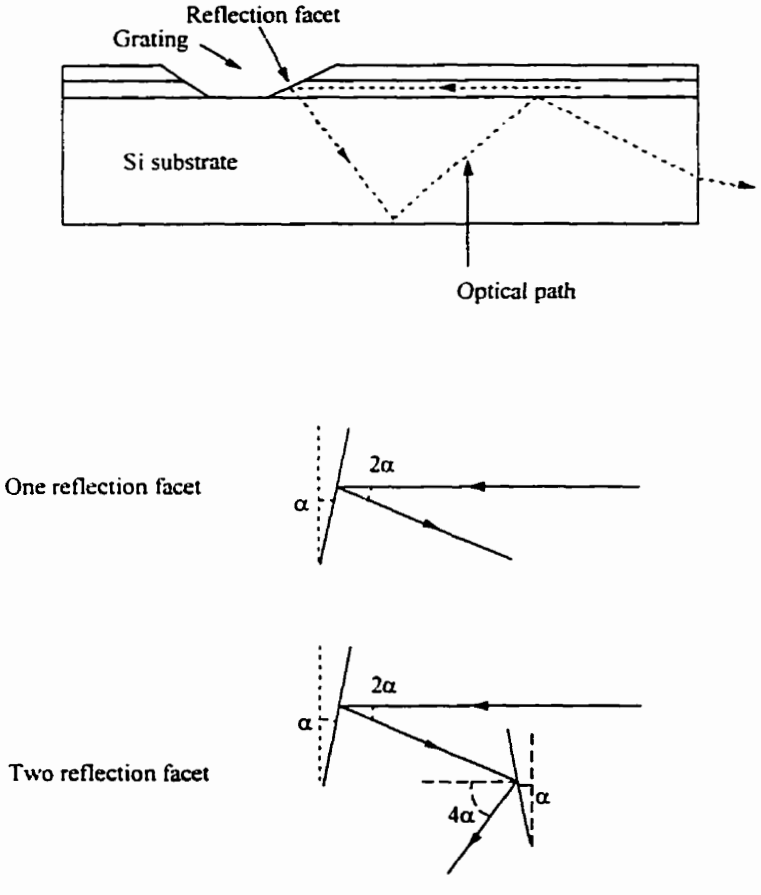

Fig. 4.3 Illustration of how nonvertical sidewalls cause optical loss

be reflected towards the Si substrate. When the wall tilt angle is α, the reflected light will be away from horizontal by 2α for one reflection, and 4α for two reflections. Since two reflection configuration was used in our grating design, it is especially important to have vertically etched sidewalls.

Fig. 4.4 schematically shows four factors that cause tilt of sidewalls:

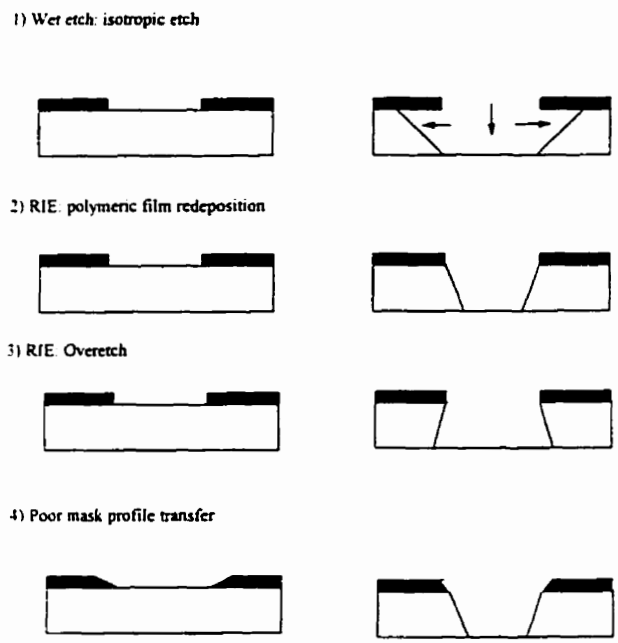

Fig. 4.4 Factors that cause nonvertical sidewalls

1. Isotropic wet etching: for most of wet etching, the etching rate is isotropic. That means the etch rates in both horizontal and vertical direction are the same, which results in 45° slope of sidewalls.

2. Polymeric film redeposition during RIE: whenever the C/F ratio increases beyond a certain critical point (the polymer point), deposition of polymers occurs on the sample surface and sidewalls. The thin polymeric film extends from the top of the

photoresist to the bottom of the etched trough, thus causes nonvertical sidewalls (Coburn, 1979).

3. Overetch during RIE: if the O_2 is in excess of the optimum at a given pressure, it will lead to overetched profile (Steinbruchel et al., 1985).

4. Poor mask profile: if the etch selectivity between the etched material and mask is not very high, the nonvertical sidewalls of the mask will be transferred somehow to the etched sidewalls.

To get vertical sidewalls, one must work in a relatively limited regime in terms of gas composition and pressure in order to obtain maximum selectivity and a minimum of polymer deposition. For the mask that does not have very high selectivity over the etched materials, it is critical to have a mask with vertical sidewalls.

When keeping the partial pressure between CHF_3 and O_2 the same, and varying the total pressure, it was found that after 40 mTorr the total pressure didn't have much effect on the sidewalls, as shown in Fig. 4.5.

Different hard baking time was used, and experiments (see Fig. 4.6) indicated that it had no significant influence on the angle of sidewalls.

Pure CHF_3 was also used to etch SiO_2/SiON under different pressures. For some reason, the lowest working pressure could be set for the system was 32 mTorr. It turned out that the lower the pressure the better the sidewalls were. It was anticipated that if the working pressure could be set below 32 mTorr, better sidewalls would have been achieved with pure CHF_3. Fig.4.7 shows that with high rf power, better sidewalls were achieved, however, when power was over 150 W, the integrity of the photoresist during

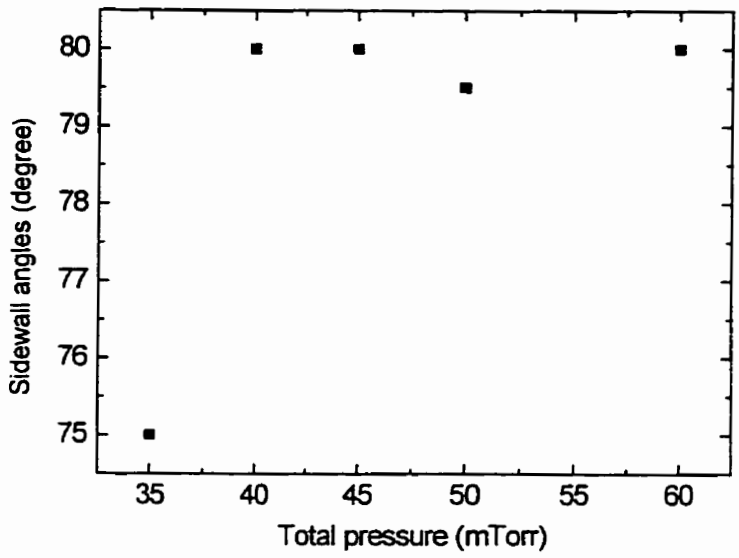

Fig. 4.5 Sidewall angle as a function of total pressure with non-optimized gas flow rates

RIE could not be maintained.

After the above experiments, the best sidewalls we could achieve were 84.5° with optimum etch conditions. Fig. 4.8a is the SEM photography of the sidewalls of a ridge waveguide. Fig. 4.8b is the profile of the photoresist mask used to prepare the ridge waveguide. From these two pictures, we can easily find the reason why we could not get vertically etched sidewalls. At the beginning of RIE, the tip of the photoresist mask functioned as a real mask, and after the tip was worn away, the real mask moved towards the inside. This caused nonvertically etched sidewalls. To get a photoresist with good profile, different photolithography conditions, such as exposure time and developing time, were tested. After improving lithography, a photoresist mask with good profile was achieved (Fig. 4.9a

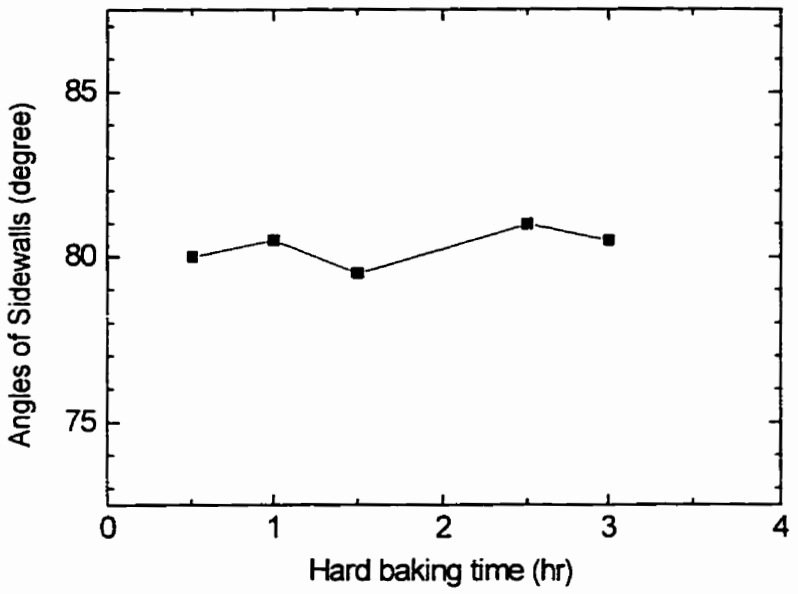

Fig. 4.6 Sidewall angle as a function of hard baking time with O_2 and CHF_3 as etching gas

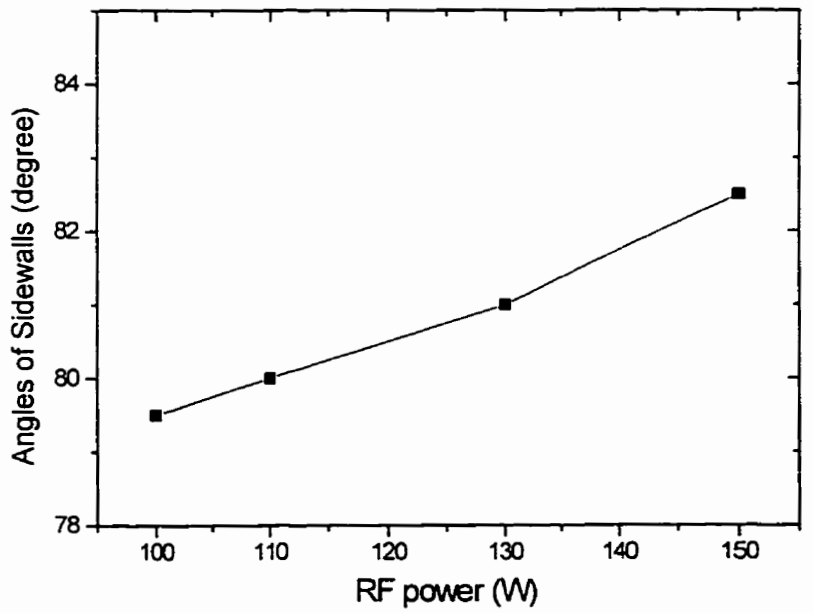

Fig. 4.7 Sidewall angles as a function of RF power with pure CHF_3, 32 mTorr

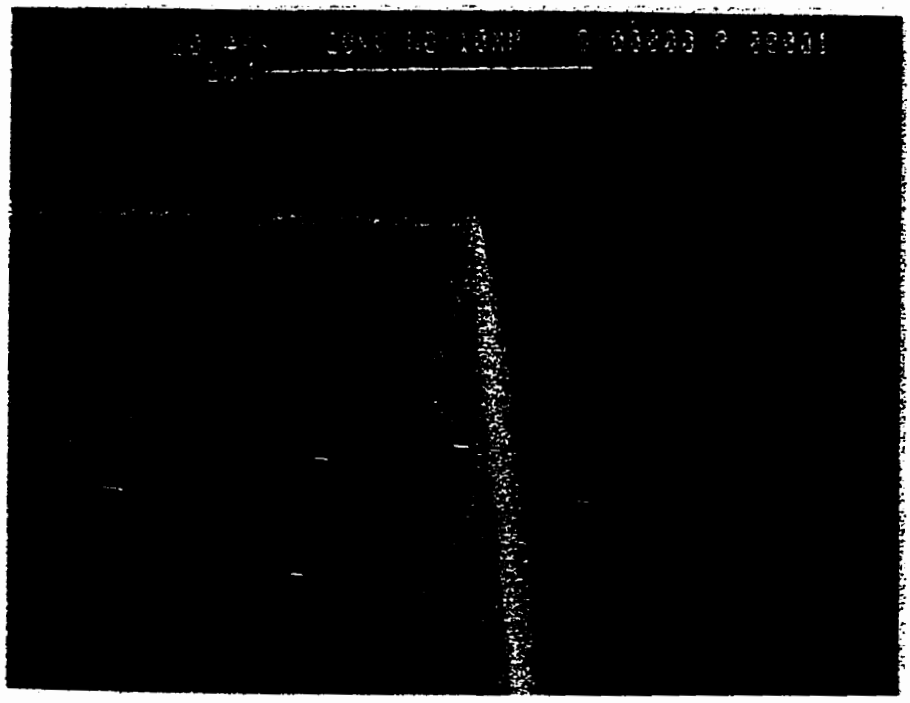

Fig. 4.8a SEM of a waveguide sidewalls produced by RIE with optimized gas flow rates and a photo resist mask

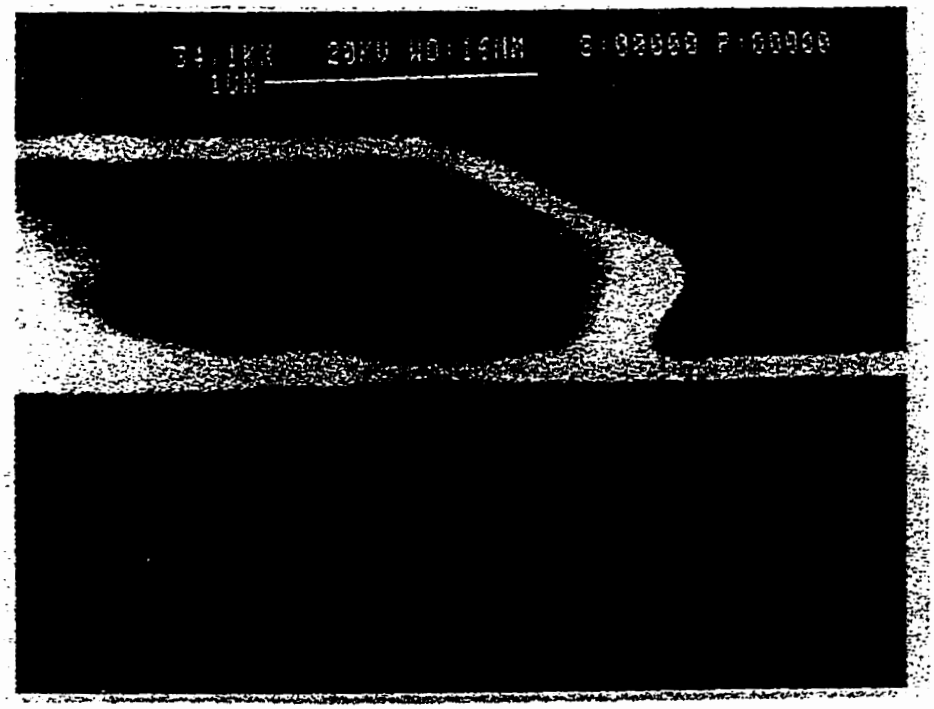

Fig. 4.8b Profile of the mask to prepare the above waveguide

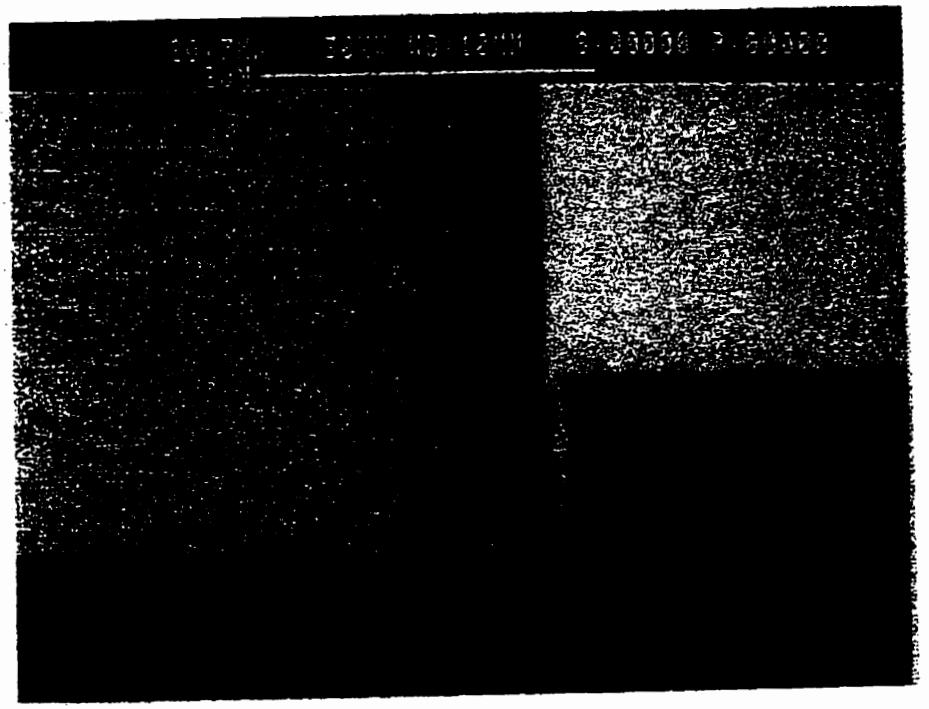

Fig. 4.9a Profile of a photoresist mask after improving photolithography parameters

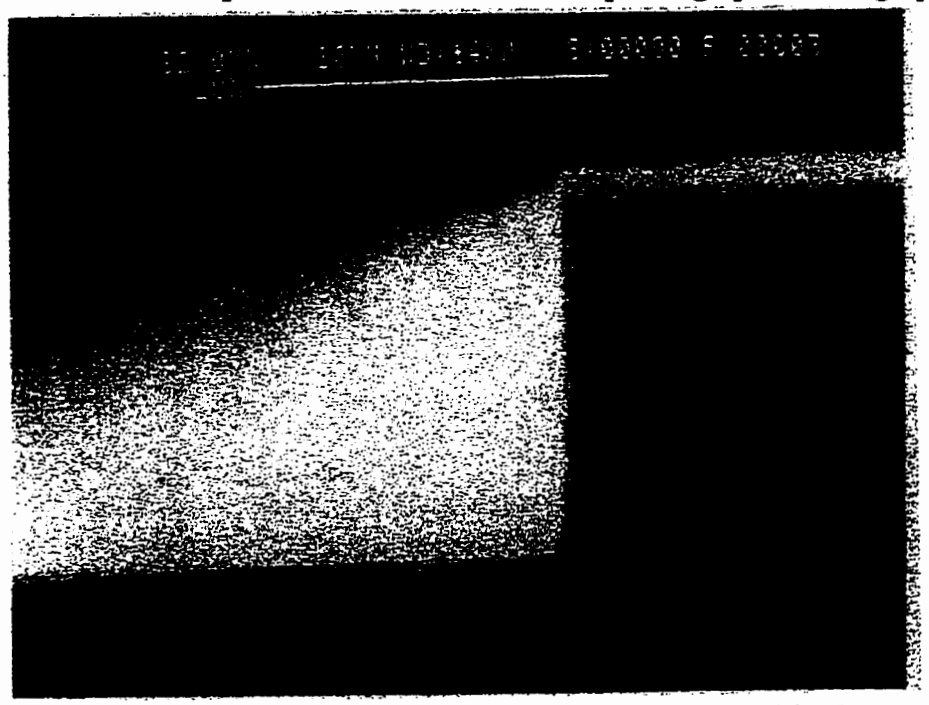

Fig. 4.9b SEM of a waveguide sidewalls produced by RIE with the above photoresist mask

). With this photoresist mask, ridge waveguides with perfect sidewalls were produced, as shown in Fig. 4.9b. Unfortunately, it was very hard to reproduce this result.

To make photoresist hard, UV light was used to bake photoresist before RIE. Different hard baking time and temperatures were tested, and it turned out that there was little improvement on the sidewalls. So, we selected Cr as mask.

4.4 RIE ETCH PROCESS WITH Cr AS MASK

Fig. 4.10 shows the etch process flow chart. For this process, two more steps were used compared to the process with photoresist as mask. After layer structure SiO_2/SiON/SiO_2 was fabricated, a layer of Cr thin film was added to the sample surface by RF sputtering. Following photolithography, the photoresist pattern was transferred to Cr by chemical etch. then the photoresist was removed by acetone.

Fig. 4.11 is the SEM photograph of a waveguide sidewall produced by RIE with Cr mask. The photograph shows that the etching depth is approximately 2 μm but inside the trough glass was not completely removed. There are a lot of materials structured like grass. This may be understood as follows: during RIE, Cr atoms moved around due to sputtering effect, and when they moved into trough, the etch process was stopped for the glass underneath the Cr while the etch process for the rest of glass continued. This resulted in grass structure, as indicated in Fig. 4. 12. To avoid this problem, a layer of photoresist is needed to protect the Cr during RIE.

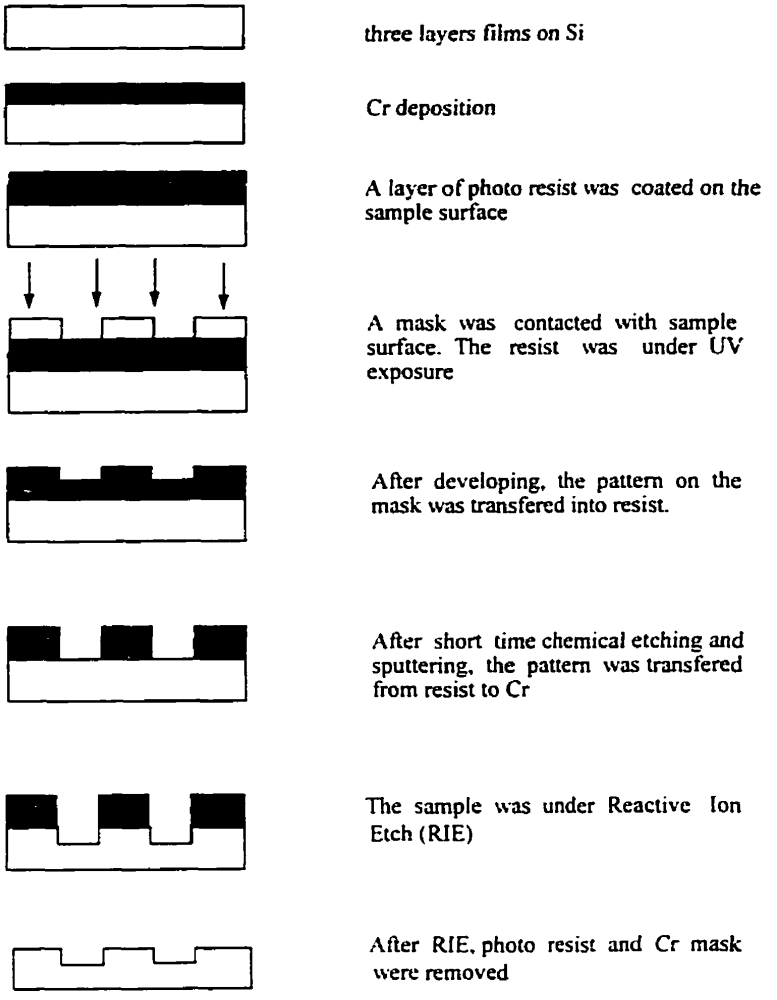

Fig.4.10 The flow chart for the etching process with Cr as mask

4.5 RIE ETCH PROCESS WITH PHOTORESIST AND Cr AS MASK

In this process, after the photo resist pattern was transferred into Cr by chemical etch, the photoresist was not removed. During RIE, the Cr was protected by photoresist, so there was no grass structure inside the etched trough, as we can see from Fig. 4.13a. Even the optimum etch condition was used, the sidewall was only around 82°. Before RIE, the

photoresist and Cr mask were checked by SEM. It was found that during chemical etch, the Cr was overetched, see Fig. 4.13b. So at the beginning of RIE, the tip of photoresist functioned as a real mask. As the tip was worn away, the Cr might function as a real mask. This caused nonvertical sidewalls.

To get vertically etched sidewalls, the Cr must be protected by photoresist, at the same time one must find a way to make sure there is no undercut of the Cr. Fig. 4.14 suggests a solution. After photolithography, two etch steps were used to transfer the

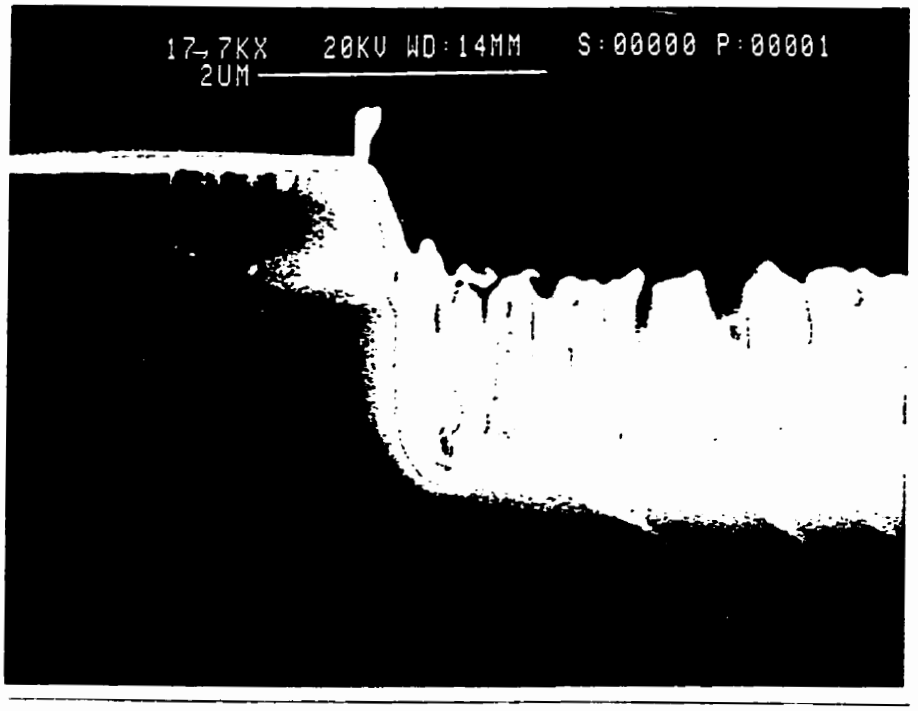

Fig. 4.11 SEM of a waveguide sidewall produced by RIE with Cr as mask

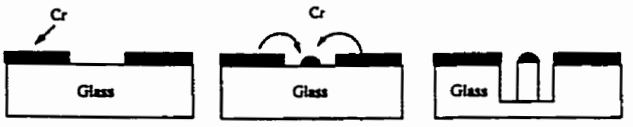

Fig. 4.12 Redeposition of Cr produces grass structure

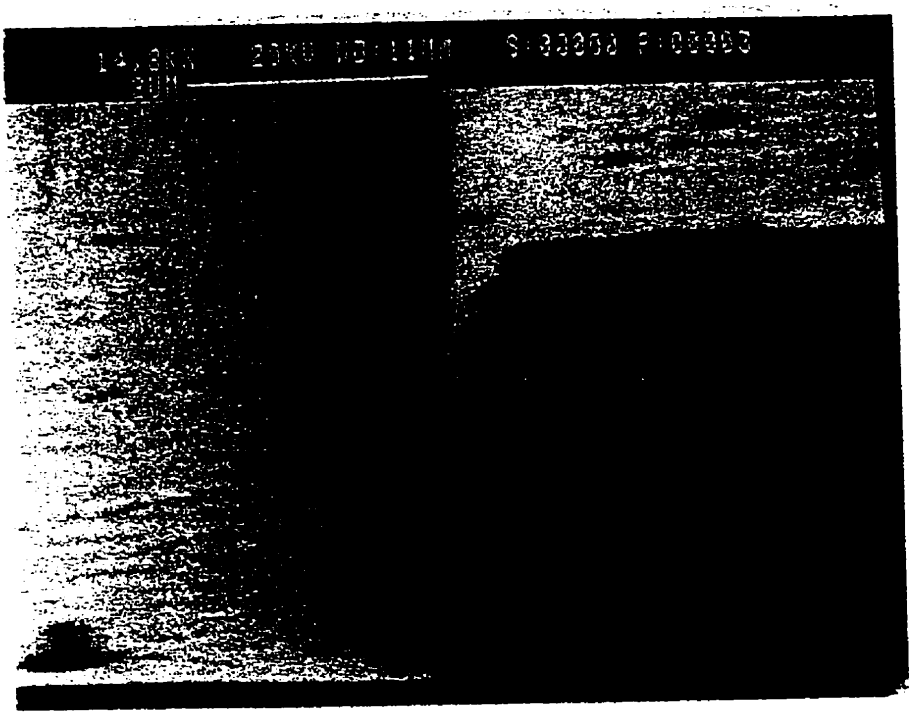

Fig. 4.13a SEM of a waveguide sidewall produced by the RIE with layers of photoresist and chrome as the mask

Fig. 4.13b The profile of the mask used to prepare the above waveguide.

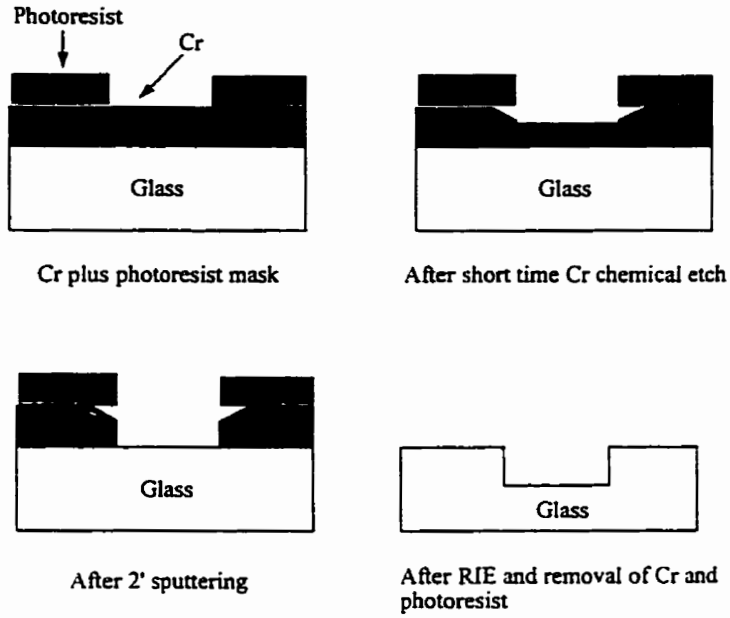

Fig. 4.14 Two etching steps for the Cr mask

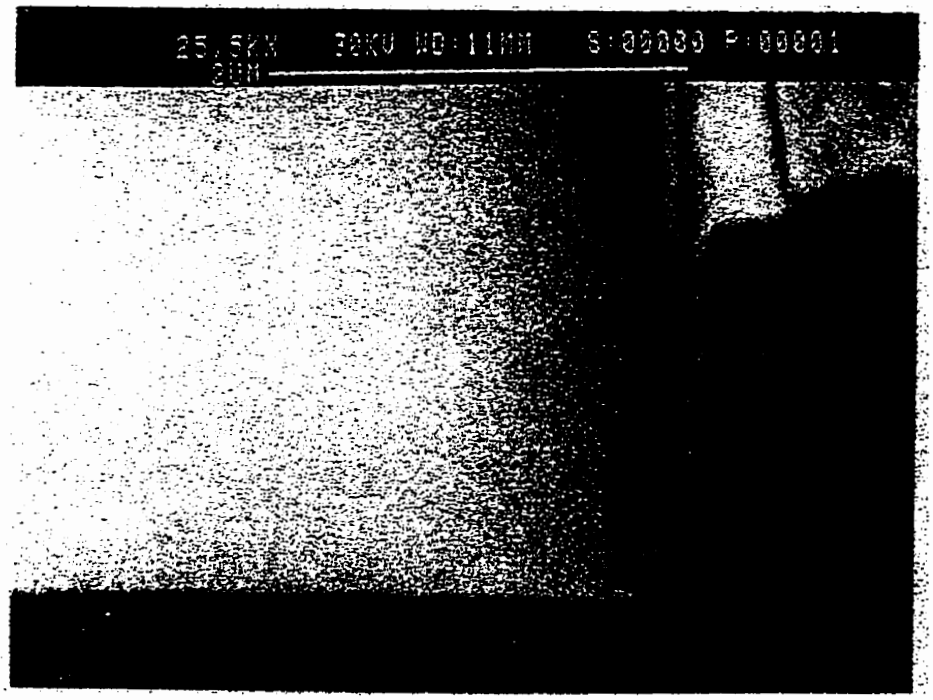

Fig. 4.15 SEM of a waveguide sidewall with Cr/Photoresist mask which was prepared by two etch steps

photo resist pattern to Cr. First, a short time chemical etch was used to etch most of Cr away. Second, the rest of Cr was removed by sputtering. With such a recipe, ridge waveguides with nearly vertical sidewalls were produced, as indicated in Fig. 4.15. In our demultiplexer design, the etch depth should be 3 μm, while the etch depth in Fig. 4.15 was only around 1.8 μm. The same sample was under RIE for another half an hour. Fig. 4.16 is the SEM photograph of this sample. We can see that the grass came again! This is because photoresist was striped off during the latter RIE, and the Cr without the protection of photoresist caused grass structure.

By slightly increasing the thickness of photoresist, adjusting the sputtering parameters and using appropriate RIE time, demultiplexers with 89.4° sidewalls (Fig. 4.17) were produced. The etching depth was around 2.5 μm, as measured by a stylus profilometer (Fig. 4.18).

This recipe for vertical etched sidewalls was proven to be reproducible.

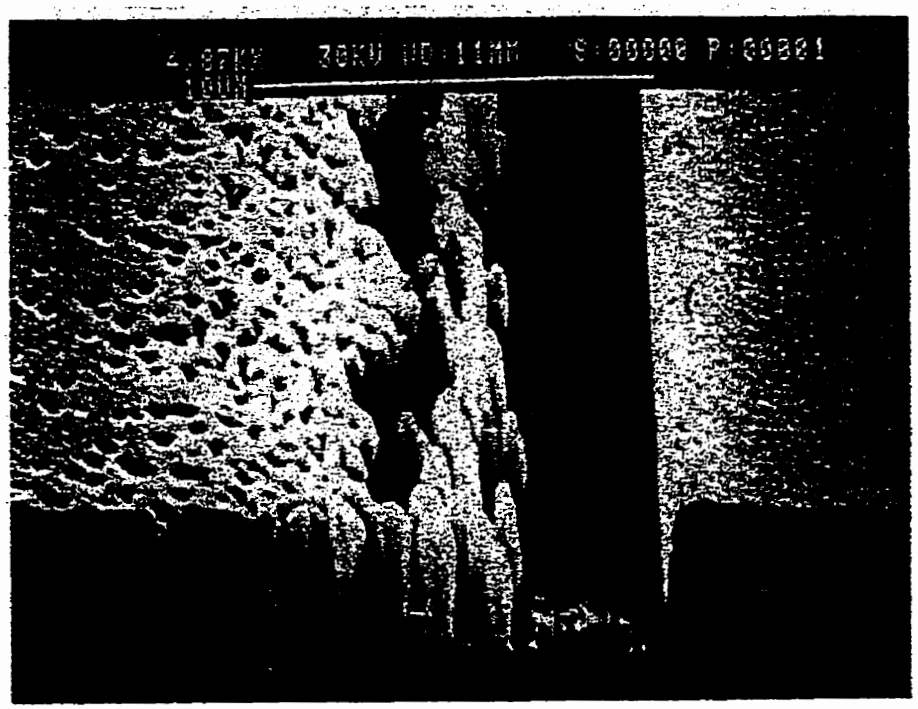

Fig.4.16 SEM of the waveguide in Fig. 4.15 after additional etching by RIE

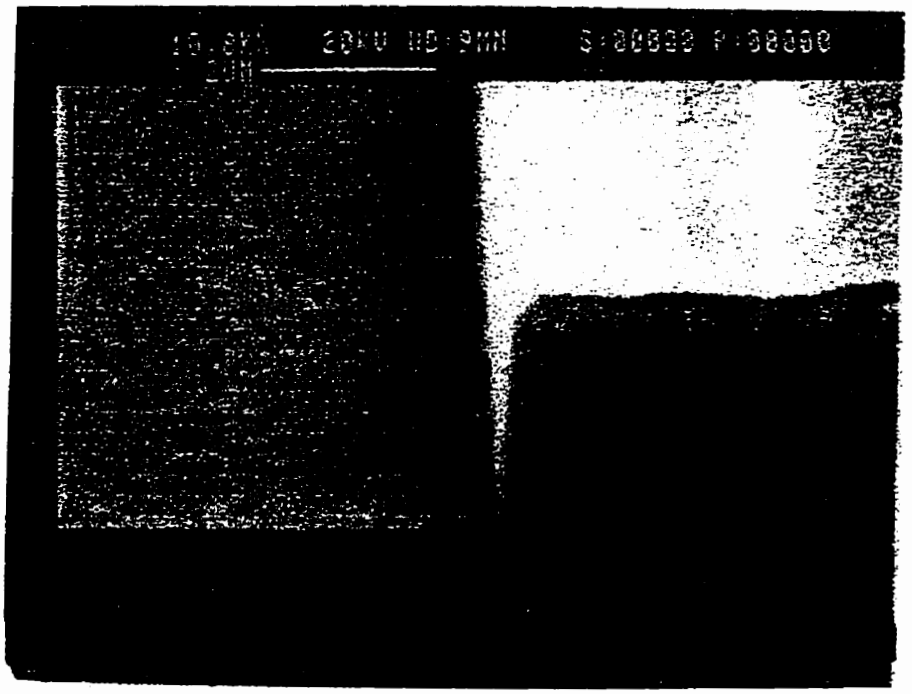

Fig. 4.17 SEM of a waveguide sidewall produced by RIE with a thicker photoresist/Cr mask and improved sputtering parameters

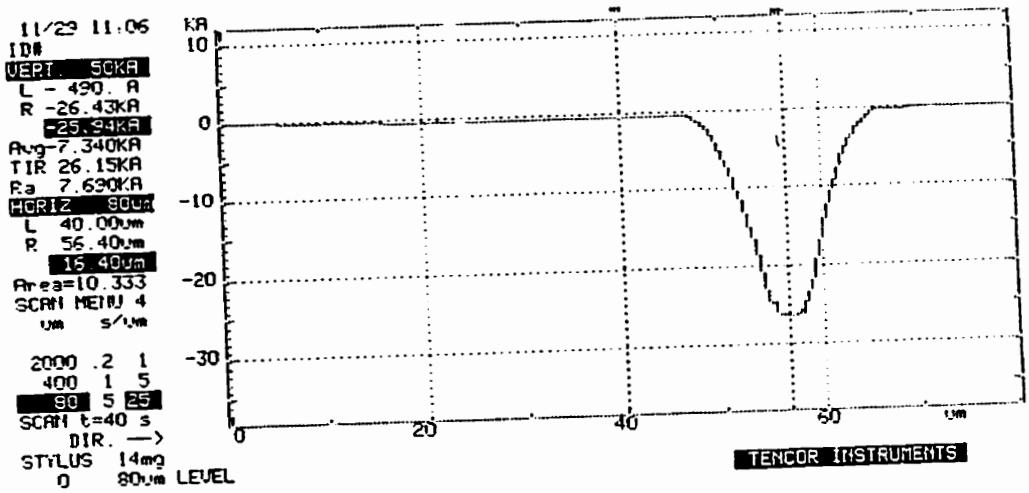

Fig.4.18 The thickness of a waveguide in Fig. 4.17 measured by a stylus profilometer

4.6 RIE ETCH PROCESS WITH α-Si AS MASK

By using the etching process in section 4.5, vertical sidewalls were reproducibly produced, however, Cr mask sometimes caused rough sidewalls resulting in high scattering loss for ridge waveguides and concave gratings. Bazylenko et al. (1996) found that the sidewall roughness appeared to be consistently higher for a photoresist mask than for a α-Si mask. According to our SEM results, the sidewall roughness was even higher for Cr mask than for a photoresist mask. As far as sidewall roughness is concerned, a α-

Si mask is the best choice while a Cr mask is the worst choice. Some preliminary investigations have been done for a α-Si mask.

After the layer structure SiO_2/SiON/SiO_2 was fabricated, another layer of α-Si was in-situ deposited by PECVD where the reactant gas was SiH_4. In doing photolithography, the exposure time had to be optimized again due to the difference in surface reflectivity between α-Si and Cr. After lithography, the mask pattern was transferred to photorersist.

To transfer the mask pattern further from photoresist to α-Si, a α-Si etching step was needed. α-Si is usually etched in halogen-containing plasmas. The etching of silicon in fluorine-containing plasmas is well understood today (Kuo, 1990, Loewenstein, 1988, and Oehrlein et al., 1989). After α-Si was etched in O_2 and SF_6 for two minutes by RIE, the mask pattern was transferred into α-Si, and pure CHF_3 was used to etch SiO_2/SiON inside the same RIE setup.

Two wafers were fabricated by using α-Si mask, and the tilt of sidewalls was around 6°. During the etching of α-Si, O_2 and SF_6 partial pressure are needed to be optimized further to produce an α-Si mask with vertical sidewalls.

CHAPTER FIVE

CHARACTERIZATION OF DEMULTIPLEXERS

After the demultiplexers were fabricated, a wafer saw was used to dice out the devices into 12 chips. In this chapter, the performances of demultiplexers, such as insertion loss, dispersion, polarization dependence, channel spacing, isolation, temperature stability, and noise floor are thoroughly characterized. Some experimental results are compared with simulation results, and it was found that in most cases they agreed well with each other.

5.1 APPARATUS & EXPERIMENTAL PROCEDURES

Fig. 5.1 is the set-up used to characterize demultiplexers. The light source is a New Focus 6200 series External-Cavity Tunable Diode Laser. The laser can be operated manually or remotely using computer control. The laser cavity is schematically shown in Fig. 5.2. A

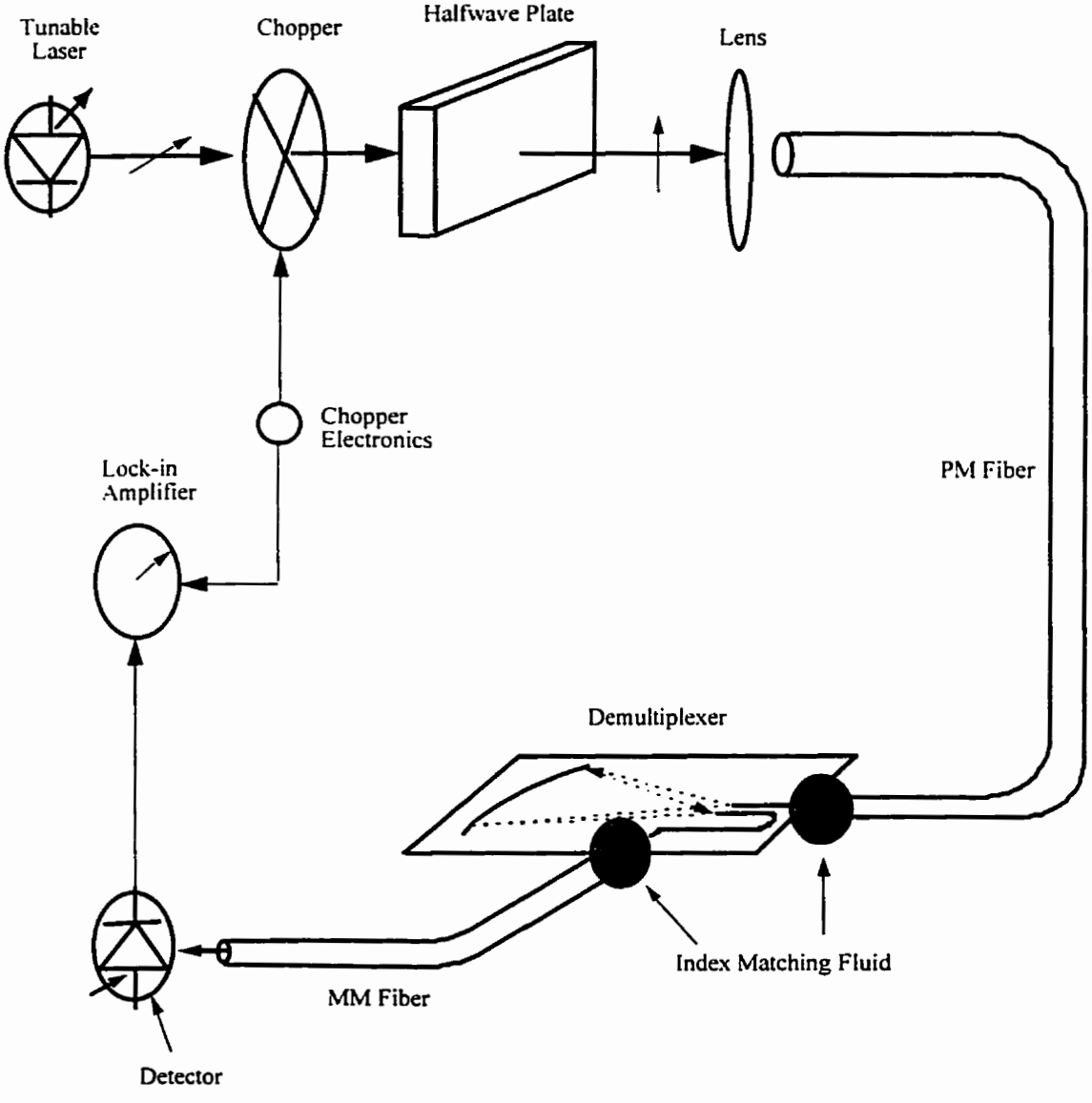

Fig.5.1 The set-up used to characterize demultiplexers

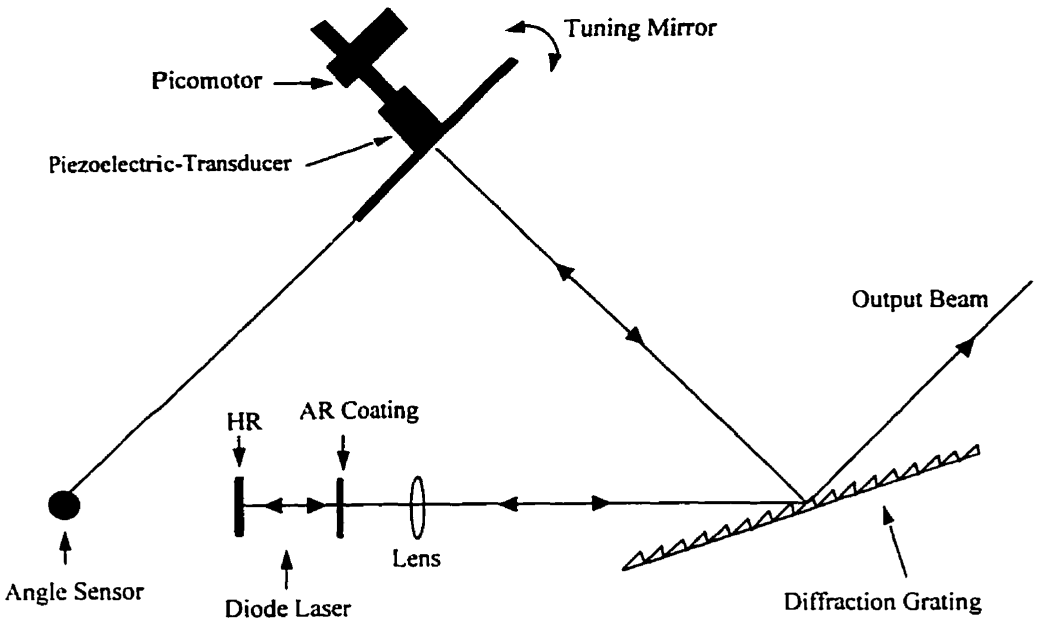

Fig. 5.2 Schematic view of the tunable laser head

high-reflection coating on one end of the diode laser forms one end of the cavity and a high-reflecting tuning mirror forms the other. Starting from the diode the beam in the cavity passes through a collimating lens and then strikes a diffraction grating at near grazing incidence. The beam is diffracted toward a tuning mirror, which reflects the light back on itself for the reverse path. Part of the light from the diode is reflected, not diffracted, by the grating. The portion forms the output beam. Different wavelengths diffract off the grating at different angles. However, only one wavelength leaves the grating in a direction that is exactly perpendicular to the surface of the tuning mirror forming the resonant laser cavity. This is the lasing wavelength, because it is the only one that will survive for many cavity round trips. It follows then, that we can tune the laser by changing the angle of the tuning mirror through either a picomotor or a piezoelectric-transducer. The laser wavelength can be coarsely tuned from 1520 nm to 1575 nm by a

picomotor. Using a piezoelectric-transducer, the laser wavelength can be fine tuned with sub-angstrom precision.

Light is externally modulated by a chopper, so that a lock-in amplifier can be used to record the signal across a photo detector. Light from the semiconductor laser is in TE mode (horizontally polarized). To test the response of a demultiplexer to both TE and TM (vertically polarized) input light, a half waveplate is employed to change TE light to TM light. After light passes through a half waveplate, the electric field along the slow axis will change phase by π while the field along the fast axis will keep its phase unchanged, as shown in Fig. 5.3. So for a linearly polarized light whose polarization direction is in α with respect to the fast axis of a half waveplate, its direction of polarization will be changed by 2α after passing through half waveplate (see Fig. 5.3). For a TE light, if its direction of polarization is in 45° with respect to the fast axis of half waveplate, it will become TM light after passing through the half waveplate. Light from the laser is coupled

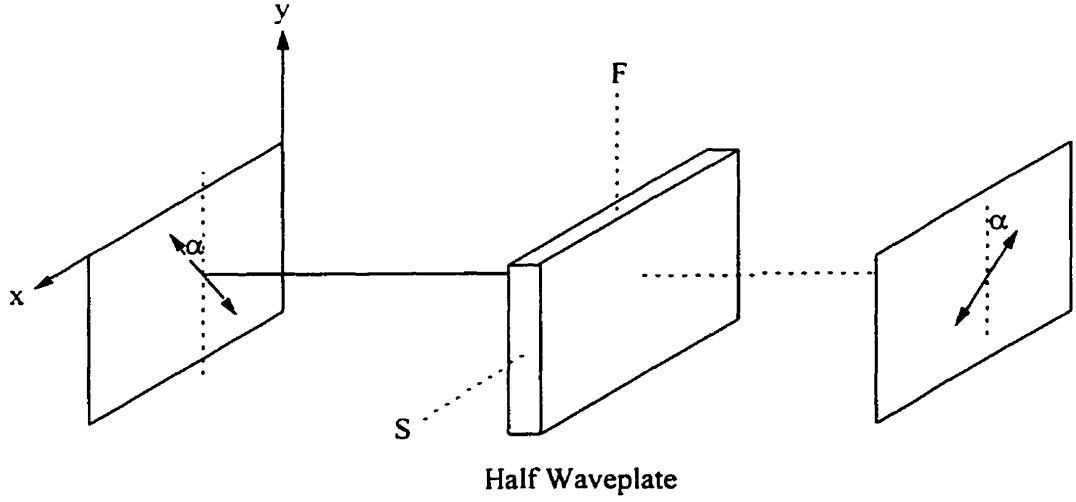

Fig. 5.3 Operation of the half waveplate

into a single mode, polarization maintaining fiber which, in turn, is butt-coupled to an input waveguide. The single mode polarization maintaining (PM) fiber is composed of two sections which are connected by a demountable connector. Through this connector, visible light can be coupled into a device from a visible light laser diode. This makes it much easy to align a fiber with a waveguide in a device during test, since once the red light comes out from the desired waveguide, it means the waveguide and fiber are approximately aligned. After switching light source from visible laser to IR laser, the relative position of the fiber and the device can be further optimized to get a maximum signal.

A multimode (MM) fiber is butt-coupled to an output waveguide. Both input single mode polarization maintaining fiber and pick-up multimode fiber are aligned with waveguides by using three dimension positioners. Ideally, the end-faces of waveguides and fibers should be prepared accurately orthogonal to their axes of propagation. The axes are then aligned. Since devices are cut by a wafer saw, the endface of waveguides are usually very rough and not perpendicular to their axes. Index matching fluid is used between fibers and waveguides to increase coupling efficiency. The fiber could be displaced from their ideal relative positions by (a) a short axial distance Δz, (b) a small transverse distance Δx, or (c) a rotational misalignment $\Delta\theta$. All such errors result in reduced coupling efficiency. With the help of an optical microscope, the error (a) and (b) are easily eliminated. According to Hutcheson (1987), $\Delta\theta = 1°$ will cause 2 dB coupling loss if two waveguides are in the same dimensions. Special care must be taken in making a fiber and a ridge waveguide parallel with each other.

The output light from the multimode fiber is measured with a germanium diode and a lock-in amplifier. The reverse-biased germanium diode with the bias voltage of 1.5 V is in series with a load resistor, see Fig. 5.4. The voltage across the load resistor is measured by a lock-in amplifier. To increase the sensitivity and signal to noise ratio (SNR) of the detector, a large load resistor should be chosen. But too large a resistor will cause nonlinearity of a detector response. 33 kΩ was found to be the maximum resistor that did not cause nonlinearity of the detector response, therefore this resistor was used for all experiments.

A personal computer was used to control both the lock-in amplifier and the semiconductor laser. To characterize each peak in the spectral response, the tunable laser was coarse tuned with 0.1 nm steps over 2 nm range and fine tuned with 0.01 nm steps over 0.28 nm range. During wavelength tuning, the output power of the laser fluctuated about 3 dB, as shown in Fig. 5.5. This fluctuation would have caused extra error in the characterization of demultiplexers. A reference reading, which was proportional to the output power, was used to normalize the output signal. After normalization, we can see from Fig. 5.6 that the fluctuation was greatly reduced.

5.2 WAVEGUIDE LOSS

Our demultiplexers were composed of two types of waveguides, one was slab waveguide, the other was ridge waveguide. For slab waveguide, there are two loss mechanisms: scattering loss and absorption loss. Both surface roughness and refractive index

fluctuations will cause scattering loss. Since conventional Si substrate was used in our experiment, the scattering loss due to surface roughness was negligible. By comparing the tested channel center wavelength with the designed channel center wavelength, the

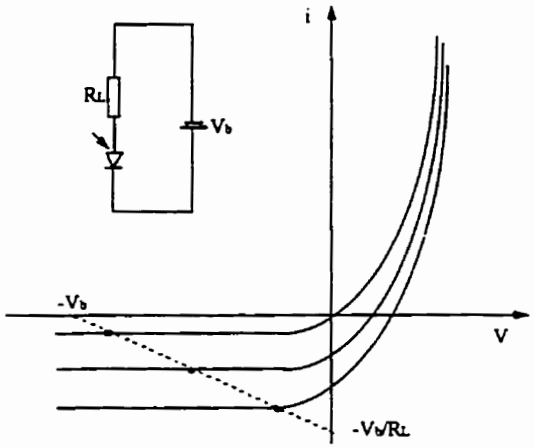

Fig. 5.4 Reverse-biased operation of a Gemanium photodiode with a load resistor. The operating point lies on the dashed line

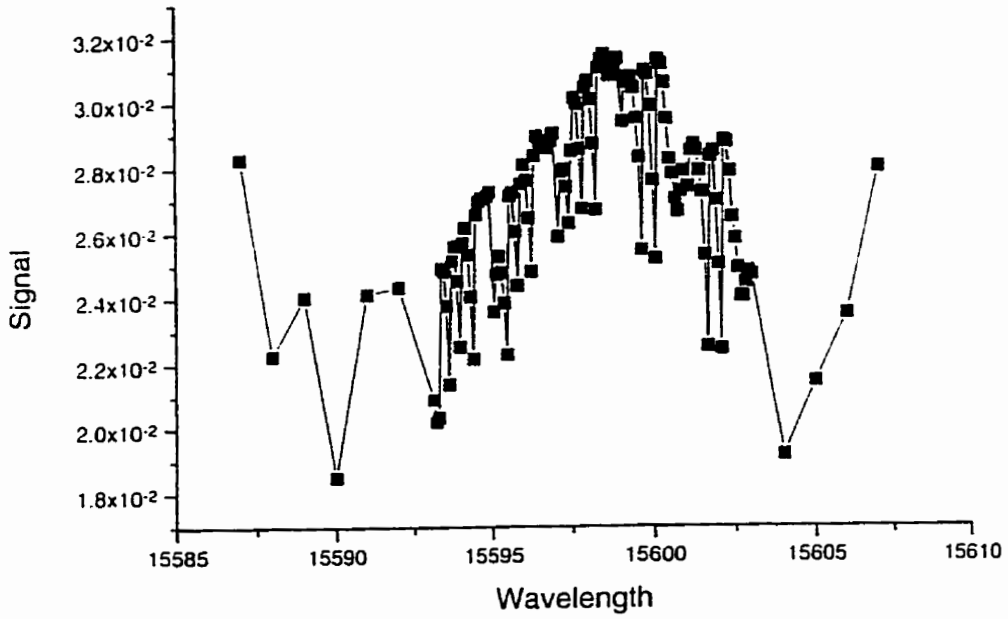

Fig. 5.5 Fiber-to-fiber signal without normalization has a large variation with wavelength

fluctuation of refractive index from chip to chip can be found. Fig. 5.7 shows refractive index fluctuations in a wafer that had seven working chips. The data shows that

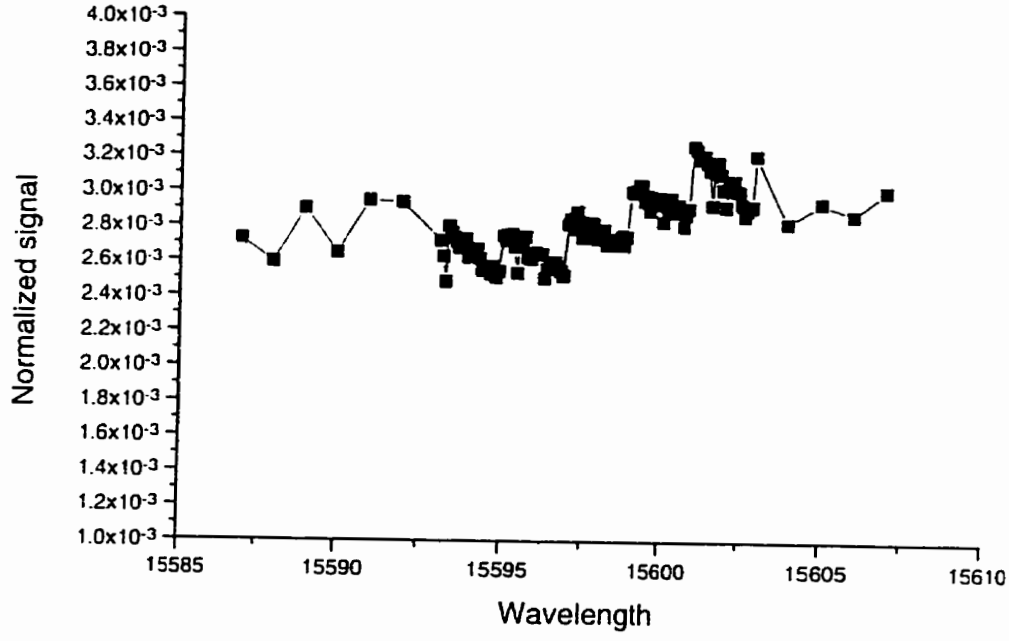

Fig. 5.6 Fiber-to-fiber signal normalized by the reference power from laser source has a relatively small variation with wavelength

the refractive index fluctuations are smaller than 0.4%, so the scattering loss due to this refractive index fluctuations are expected to be very small. Absorption loss due to the Si-H and N-H overtone bands near 1500 nm (Bruno, 1991) was the main contribution to slab waveguide loss. For ridge waveguides, besides all loss mechanisms in the slab waveguide, there were two additional loss mechanisms: scattering loss due to roughness of waveguide side walls and radiation loss due to the changing of propagation direction. Since ridge waveguide sidewalls were covered by air, the refractive index difference between the core and air was 0.492. Such high refractive index difference would cause

very high scattering loss if sidewall roughness were beyond a certain value. On the other hand, the high refractive index difference caused little radiation loss even though curved waveguides only have a radius of 250 μm.

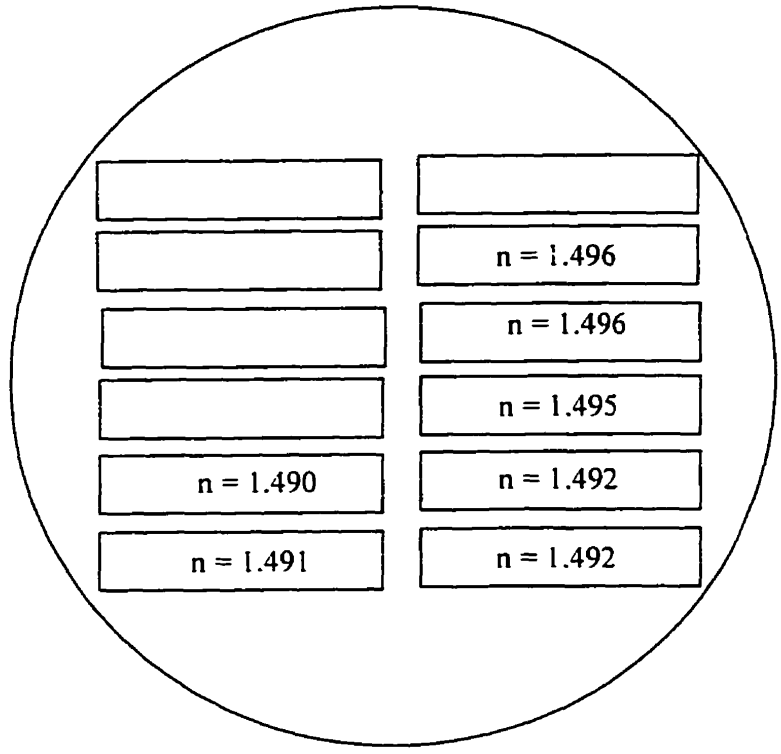

Fig. 5.7 Refractive index distribution across a wafer. This was determined by comparing the tested channel center wavelength with the designed channel center wavelength. The wafer was fabricated by using Photoresist/Cr mask, and the angle of sidewall of gratings was 89.4°.

5.2.1 SLAB WAVEGUIDE LOSS

To measure slab waveguide loss, a single mode fiber with mode field size of 6.5 μm or 10.5 μm was used to launch light into a slab waveguide. The slab waveguide was obtained by cutting a grating and the input waveguides away from a demultiplexer. A multimode fiber with core diameter of 125 μm was used as a pick-up fiber. Index

matching fluid was used to increase coupling between fibers and the slab waveguide. Since the light will diverge freely inside the slab waveguide, even if there is no any waveguide loss, the received signal by multimode fiber will be much smaller than the input signal. The fields inside the single mode fiber and the slab waveguide can be approximately taken as Gaussian beam. The following equations can be used to calculate the slab waveguide loss:

$$P_{in} = \int_{-\infty}^{+\infty} I_0 e^{-2\left(\frac{x}{w_0}\right)^2} dx = I_0 \sqrt{\frac{\pi}{2}} w_0 \tag{5.1}$$

$$I(x,z) = I_0 \frac{w_0}{w(z)} e^{-2\left(\frac{x}{w(z)}\right)^2} \tag{5.2}$$

$$w(z)^2 = w_0^2 + \left(\frac{\lambda}{\pi w_0} z\right)^2 \tag{5.3}$$

$$P_{out} = \int_{\frac{125}{2}\mu m}^{\frac{125}{2}\mu m} I(x,z)dx \approx (125\mu m) I_0 \frac{w_0}{w(z)} \tag{5.4}$$

$$2w_0 = 6.5\ \mu m \text{ (or } 10.5\ \mu m) \tag{5.5}$$

The coordinate system is shown in Fig. 5.8. Supposed that after propagating through a

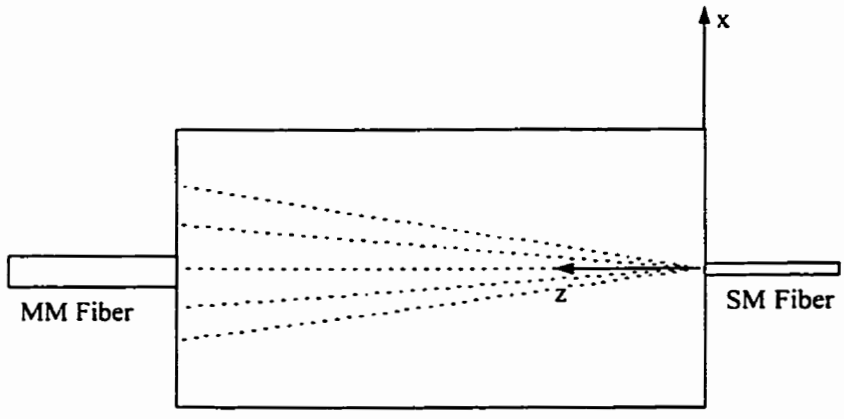

Fig. 5.8 The coordinate system used to measure slab waveguide loss

slab waveguide, the signal received by a multimode fiber is V_{out}. Keeping the laser output power constant and removing a slab waveguide away from between two fibers, two fibers are aligned to get a maximum signal from multimode fiber with V_{in}. Then, the fiber to fiber loss for the slab waveguide is:

$$L = 10\log\frac{\left(\frac{V_{out}}{V_{in}}\right)}{\left(\frac{P_{out}}{P_{in}}\right)} \tag{5.6}$$

To know slab waveguide loss, the coupling loss has to be taken off from the total loss L. Since index matching fluid was used in our experiments, the coupling loss due to reflection at the end of the fiber was negligible. The coupling loss was mainly due to mode field mismatch between the fiber and the slab waveguide. By using the overlap integral (Syms et al.. 1992), the coupling loss due to modefield mismatch is Lc = 10log(η). and

$$= \frac{\left|\int_{-\infty}^{+\infty} E_{in} E_{v} dx\right|^2}{\int_{-\infty}^{+\infty} E_{in}^{\,2} dx \int_{-\infty}^{+\infty} E_{v}^{\,2} dx} \tag{5.7}$$

where E_{in} is the field inside single mode polarization maintaining fiber. In a single mode fiber, the fields are described by Bessel functions (Mickelson, 1993) and the fundamental mode can be approximated as

$$E_{in} = c\exp(-\frac{x^2 + y^2}{w_0^{\,2}}) \tag{5.8}$$

where c is a constant and w_0 is modefield radius which is defined as the radius when the field amplitude is decreased by a factor of 1/e. Two kinds of polarization maintaining

fibers were used, one with w_0 = 3.25 μm (ThorLabs Inc., FS-PM-7811HT), the other with w_0 = 5.25 μm (OZ Optics LTD., PMJ-33-1550-9/125-3-3-1). In Equation (5.7), E_v is the

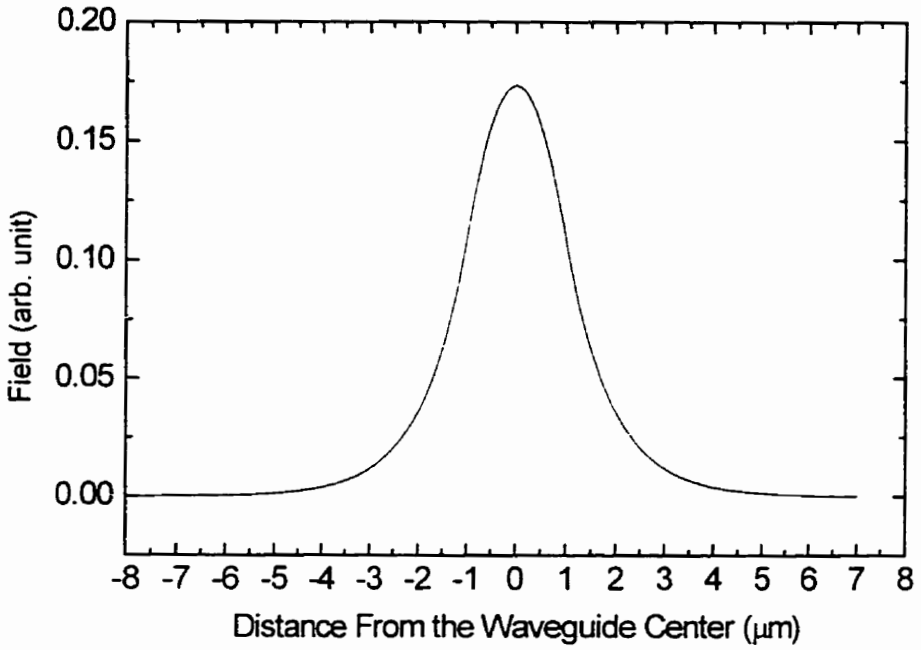

Fig. 5.9 Mode field distribution along the x direction (perpendicular to the slab surface). The slab waveguide had 2 μm core layer with refractive index of 1.492 and infinite thickness of upper and low cladding with refractive index of 1.45.

modefield distribution along x direction (perpendicular to the slab surface). By using the matrix method that is discussed in Chapter Six, E_v is found in Fig. 5.9 assuming infinite top and bottom cladding, and neglecting the effect of the ridge.

Fig. 5.10 shows the coupling losses between our slab waveguide and input fibers with different modefield size ($2*w_0$). The coupling loss is –0.9 dB for the input fiber with $2*w_0$ = 6.5 μm,and -2.4 dB for the input fiber with $2*w_0$ = 10.5 μm.

By using the above method, a typical slab waveguide loss was found to vary between 1.8 dB/cm at 1549 nm and 7.1 dB/cm at 1522 nm, as shown in Fig. 5.11. This absorption wavelength dependence also varied from chip to chip in a wafer. The absorption contributed to high insertion loss and large insertion loss variations from channel to channel for our demultiplexers. According to Bruno (1991) and Jackson(1997)

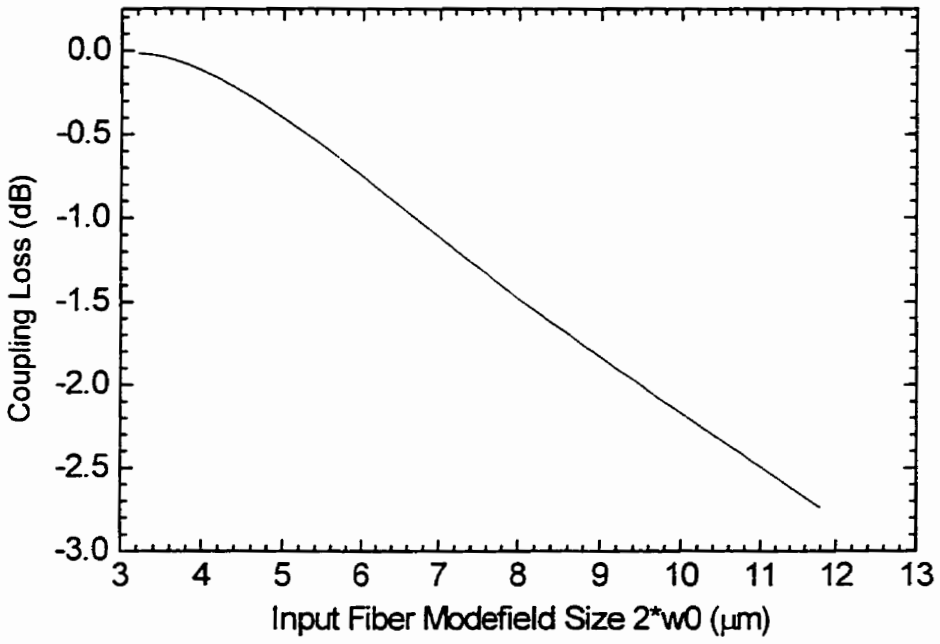

Fig. 5.10 Coupling loss between the slab waveguide in Fig. 5.9 and input single mode fiber with different modefield size

by annealing the wafers, the absorption coefficient and its wavelength dependence can be greatly reduced.

Several annealing conditions were tested. The loss of a straight ridge waveguide was found to be reduced from 2.8 dB/cm to 0.8 dB/cm at 1550 nm after annealing at 1050°C for one hour.

There were two wafers, one wafer was annealed at 1050°C for 1.5 hour before RIE and the other was not annealed. The etching conditions for those two wafers were exactly the same, which resulted in 86.3° sidewalls. Two demultiplexers of design A from

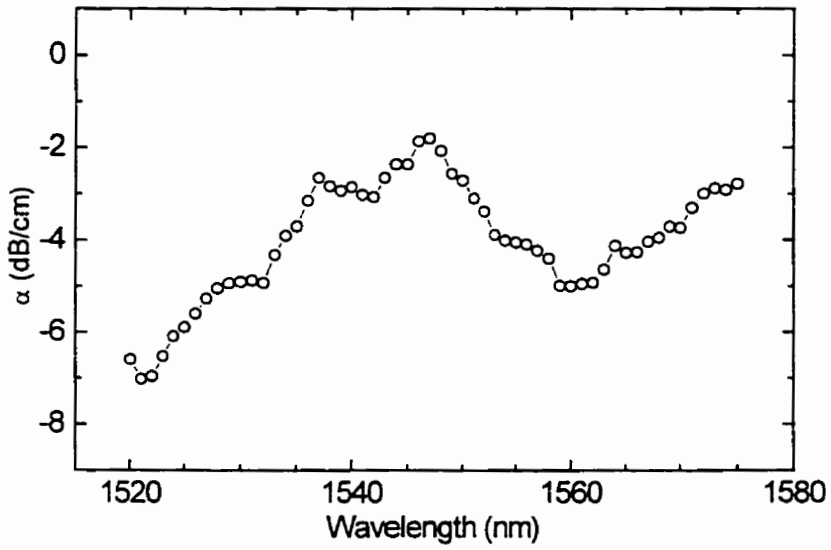

Fig. 5.11 Slab waveguide absorption loss as a function of wavelengths

each of these two wafers were tested. The fiber-to-fiber insertion loss of the annealed demultiplexer was 10 dB less than that of the other demultiplexer, as shown in Fig. 5.12. Besides decreasing absorption loss, annealing also causes an increase of refractive index and decrease of waveguide thickness. The change of refractive index makes it even more difficult to control the absolute channel wavelength. Table 5.1 and Table 5.2 give the annealing effect on the refractive index and the waveguide thickness where samples were annealed at 1050°C. From those two tables, we can see that after annealing the refractive

indices were increased by 0.2% to 1.42%. This is contrary to the result obtained by Arnica (1991) where the refractive indices were reduced by 0.5% after annealing. Fig. 5.13 shows TE and TM spectral response for a dumultiplexer both before and after annealing. It suggests that after annealing, the refractive index be increased.

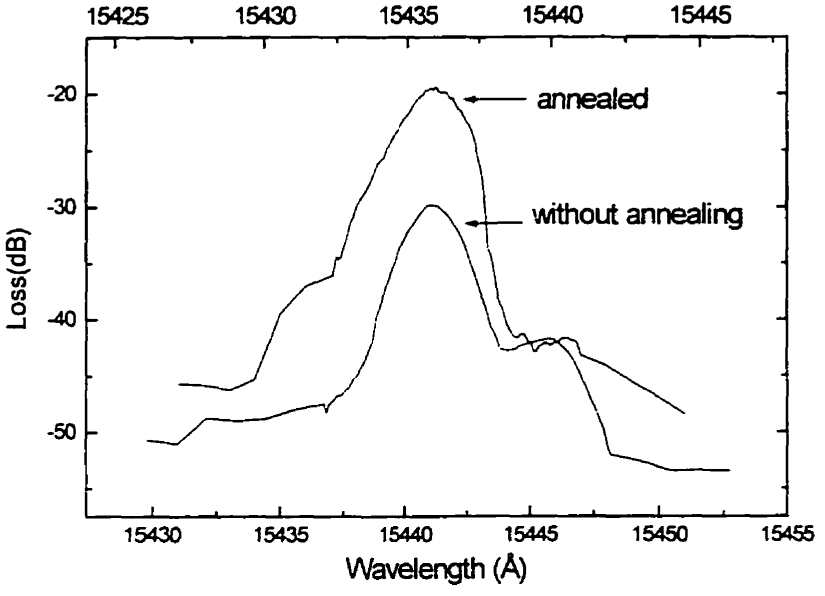

Fig. 5.12 Transmission losses versus wavelength for the two demultiplexers of design B; one was annealed and the other not. Signals were from channel four and light was coupled into devices through no.1 input ridge waveguides for two demultiplexers

Refractive index was measured by a prism coupler method (Lee et al., 1988) with an He-Ne laser source (0.6328 μm). Fig. 5.14 shows a typical rotation spectrum showing the reflection intensity as a function of rotation angle. The sample is two layer film $SiON/SiO_2$ with SiON thickness of 1.4971 μm and SiO_2 thickness of 5.9985 μm. The dips in reflection intensity are due to coupling of energy into slab waveguides. The modes are broadened due to attenuation by leakage both into the Si substrate and into the prism. The refractive index at 1.5550 μm was calculated by following equations (Baak, 1982):

In equations (5.9 - 5.12), the fitting parameter is x_{SiO2} or x_{Si3N4}. According to these equations, the refractive index of 1.501 at 0.6328 μm will be 1.492 at 1.555 μm.

$$n_{SiON} = x_{SiO2} \times n_{SiO2} + x_{Si3N4} \times n_{Si3N4} \tag{5.9}$$

$$x_{SiO2} + x_{Si3N4} = 1 \tag{5.10}$$

$$n_{SiO2}^2 - 1 = \frac{1.09877\lambda^2}{\lambda^2 - 92.4317^2} \tag{5.11}$$

$$n_{Si3N4}^2 - 1 = \frac{1.09877\lambda^2}{\lambda^2 - 139.67^2} \tag{5.12}$$

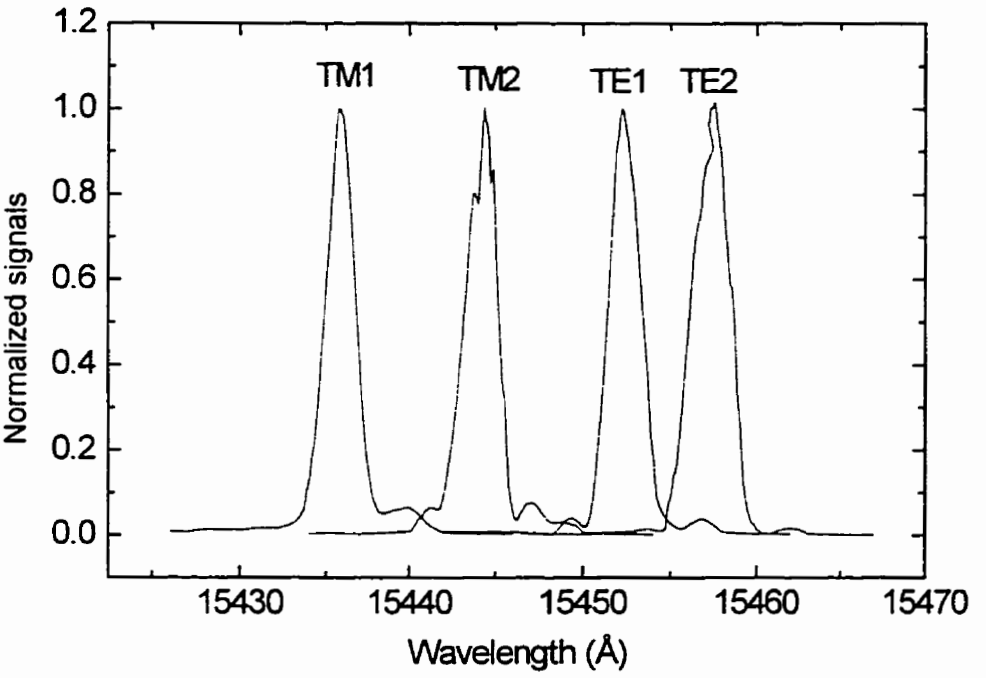

Fig. 5.13 Spectral responses of two demultiplexers of design B from channels with the same number. TE_1, TM_1 are for the sample without annealing, and TE_2, TM_2 are for the annealed sample

Table 5.1 Annealing effects on refractive index n and thickness t

n_0	time (hr.)	$(n - n_0)/n_0$	$(t - t_0)/t_0$
1.5069	1	0.8%	-7.4%
1.5316	1.5	1.42%	-10.5%
1.4666	1.0	0.06%	-0.46%
1.5940	1.6	0.74%	-7.5%
1.5526	1.6	1.2%	-8.7%

Table 5.2 Annealing effects on refractive index n and thickness t

n_0	time (hr.)	$(n-n_0)/n_0$	$(t-t_0)/t_0$
1.4667	1.0	0.4%	-1.3%
1.5838	1.0	0.2%	-0.8%
1.505	1.0	0.7%	-0.7%

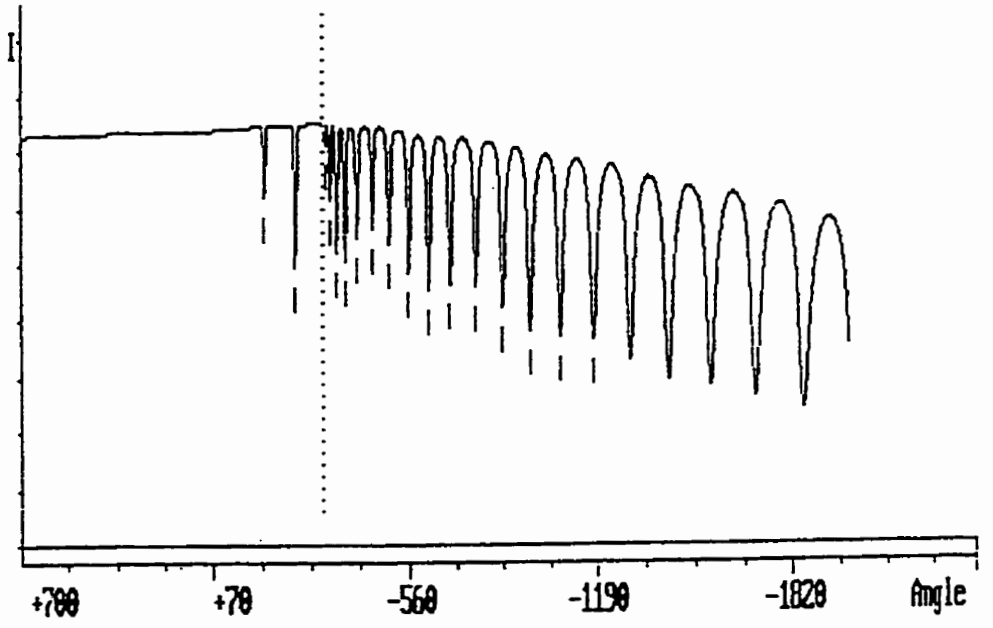

Fig. 5.14 Typical rotation spectrum for $SiON/SiO_2$ film on Si

5.2.2 RIDGE WAVEGUIDE LOSS

By cutting a grating and input waveguides away from a demultiplexer, straight ridge waveguides and curved ridge waveguides were available for loss testing. A simple method for direct measurement of transmission losses, which is called cut-back method, is to compare the transmittances of waveguides having different lengths. The same set-up that was used to characterize a slab waveguide was used here. At the waveguide length of l_1, the received signal was V_1, then the waveguide was cut to the length of l_2, and the received signal was V_2. The propagation losses are given by:

$$\alpha = \left| \frac{10\log(V_1 / V_2)}{l_1 - l_2} \right| \text{ dB/unit length} \qquad (5.13)$$

High quality waveguide edges must be prepared so that each input/output coupling efficiencies may be reproduced for each measurement. For almost all demultiplexers reported in this thesis, their straight ridge waveguides typically exhibited a loss of 2.8 to 3.6 dB/cm at 1550 nm measured by the above cut-back method.

A waveguide transmission loss can also be found by cutting pieces off the waveguide, measuring the loss after each cut, and plotting the total insertion losses as a function of waveguide lengths. The waveguide transmission loss is found to be the gradient of the graph. Fig. 5.15 shows the total insertion loss for several waveguide lengths when single mode polarization maintaing fiber with 9 μm core and 125 μm cladding butt-jointed to the waveguides with 4 μm × 2 μm core, which is our typical output waveguide. The best fit to the data (shown as a solid line) was calculated by linear

regression. The slope of the line indicates that the attenuation of the waveguides is 3.6 ± 0.6 dB/cm. From the intercept we find that the coupling loss is 7.6 ± 0.98 dB.

Experimentally finding the input coupling loss between the single mode polarization maintaing fiber and input ridge waveguides will help us to better understand the total fiber-to-fiber insertion loss of a demultiplexer. Since input waveguides were only 0.6 cm long, we could only cut the waveguide into two pieces. The cut-back method was used here to determine the coupling loss. The experiment procedure is as follows:

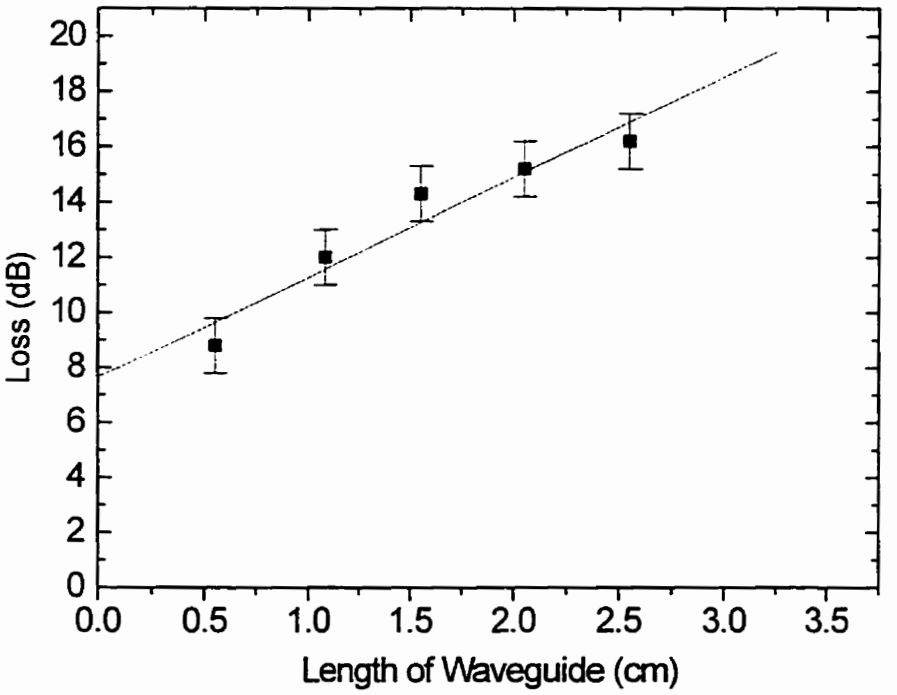

Fig. 5.15 The total insertion losses as a function of waveguide length indicates that waveguide attenuation is 3.6 ± 0.6 dB/cm

Step 1: 14 input waveguides were cleaved away from a demultiplexer. All waveguides had a length of l_1 = 0.56 cm.

Step 2: A single mode polarization maintaining fiber was aligned with a multimode pick-up fiber. The fiber-to-fiber signal recorded by lock-in amplifier was 1100 μV, and this input signal level was kept constant throughout the experiment.

Step 3: The waveguides were inserted between the input and pick-up fiber, and each of 14 waveguides was aligned with the fibers. The output signal from the pick-up fiber was recorded as V_1 in Table 5.3 for each waveguide. Since the distance between the two fibers was very small, the signal going through air and the Si substrate had to be subtracted, especially when the two fibers were only several millimeters apart. We did it in an approximate way. After the waveguides under test were removed from between the two fibers, the two fibers were kept l_1 apart, and the signal going through air from input fiber into the pick-up fiber was recorded as v_1 = 30 μV. The total insertion loss for the waveguides with the length of l_1 was:

$$L_1 = \left| 10\log(\frac{V_1 - v_1}{1100}) \right| \text{ dB} \tag{5.14}$$

which was recorded for each of 14 waveguide in Table 5.3.

Step 4: The waveguides were cleaved into two parts and the part which was close to the input fiber in step 3 was used for further test. The length of those waveguides was l_2 = 0.29 cm.

Step 5: The procedure in step 3 was repeated. The output signal from each waveguide was recorded as V_2 in Table 5.3. The sign going through air into the pick-up fiber was v_2 = 100 μV. The total insertion loss for the waveguides with the length l_2 was:

$$L_2 = \left| 10\log(\frac{V_2 - v_2}{1100}) \right| \text{ dB} \tag{5.15}$$

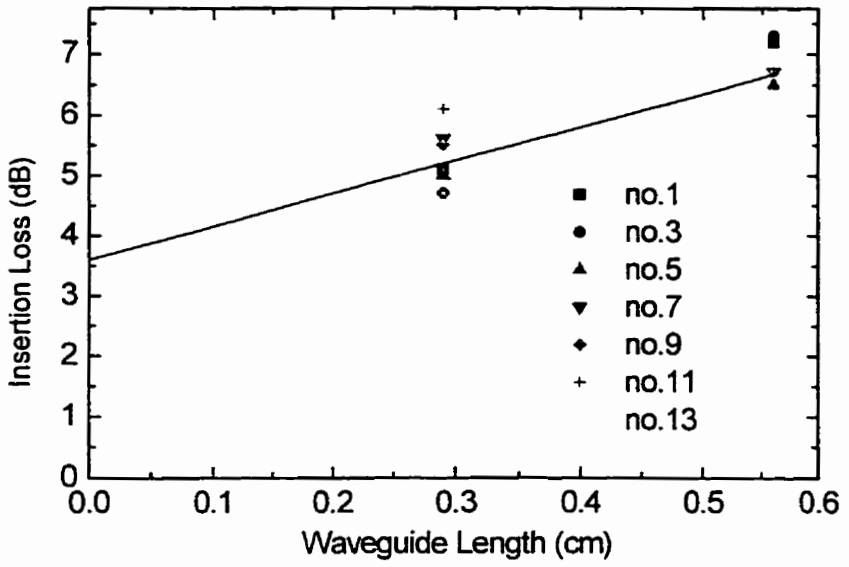

Fig. 5.16 Insertion losses as a function of waveguide lengths for seven input waveguides with a width of 7 μm.

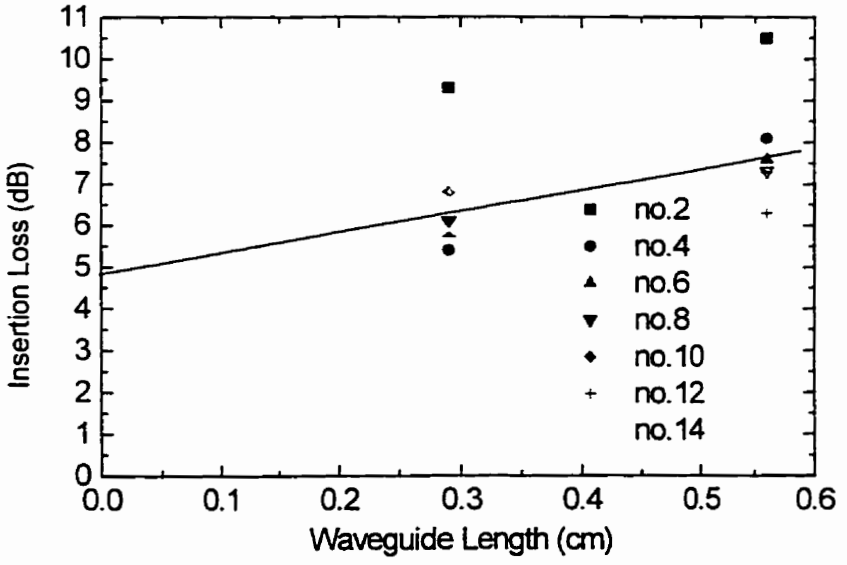

Fig. 5.17 Insertion losses as a function of waveguide lengths for seven input waveguides with a width of 10 μm.

Step 6: The insertion losses as a function of waveguide lengths were plotted in Fig. 5.16 and Fig. 5.17 for 7 μm input waveguide and 10 μm waveguide respectively. By doing the best linear fitting and extrapolating the line to cross vertical axis, the coupling loss was found to be 3.6 dB for the 10 μm waveguide, and 4.8 dB for the 7 μm waveguide. The coupling loss found in experiments included both input and output coupling losses. Since the pick-up fiber was much larger than waveguide, there was no output coupling loss.

So far, the coupling losses between single mode polarization maintaining fiber with modefield size of 10.5 μm and ridge waveguides with width of 4 μm, 7 μm and 10 μm were experimentally determined. All ridge waveguides had a thickness of 2 μm. By using overlap integral

$$\eta_v = \frac{\left| \int_{-\infty}^{+\infty} \int_{-\infty}^{+\infty} E_{in} E_v \, dxdy \right|^2}{\int_{-\infty}^{+\infty} \int_{-\infty}^{+\infty} E_{in}^2 \, dxdy \int_{-\infty}^{+\infty} \int_{-\infty}^{+\infty} E_v^2 \, dxdy} \tag{5.16}$$

where E_{in} is the modefield distribution inside the input fiber, and E_v is the *vth* mode field distribution inside a ridge waveguide, the coupling loss due to modefield mismatch is

$$L_c = 10 \log\left(\sum_{v=1}^{v=m} \eta_v \right) \tag{5.17}$$

where m is the total number of modes inside a ridge waveguide.

To do the integration of (5.16), one has to know the solutions of E_{in} and E_v. The Equation (5.8) can be used here for E_{in}, but the exact solution of E_v for a ridge waveguide with step index distribution is extremely complicated, and has not been obtained yet.

However, Marcatili (1969) has derived an approximation solution by analyzing the structure shown in Fig. 5.18. The key assumption made in Marcatili's analysis is that the

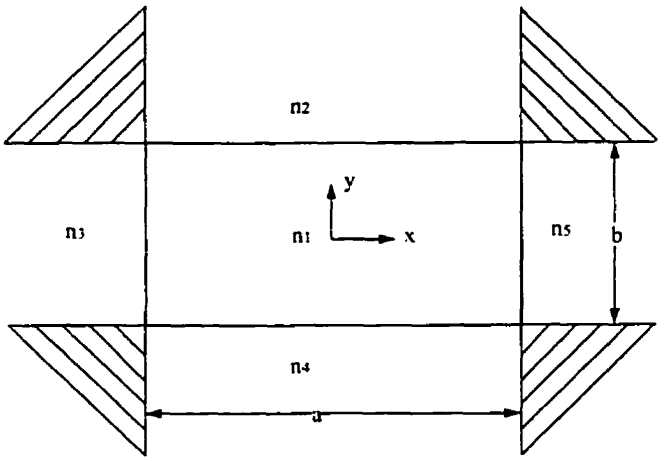

Fig. 5.18 Cross-sectional view of a rectangular dielectric waveguide bounded by regions of smaller index of refraction

modes are well guided, i.e., well above cutoff, so that the field decays exponentially in Regions of 2, 3, 4, and 5, with most of the power being confined to Region 1. The magnitudes of the fields in the shaded corner regions of Fig. 5.18 are small enough to be neglected. Hence, Maxwell's equations can be solved by assuming relatively simple sinusoidal and exponential field distributions, and by matching boundary conditions only along the four sides of Region 1.

For our ridge waveguide with a width of 4 μm, there are six possible modes according to Marcatili's analysis. Since the field inside the input fiber is symmetric, only symmetric modes are excited inside the ridge waveguide. There are three symmetric modes along x axis and only one mode along y axis, as shown in Fig.5.19. The coupling coefficient η for the 1^{st}, 3^{rd}, 5^{th} mode was calculated to be 0.305, 0.028 and 0.013

respectively. Therefore, the coupling loss between the input fiber with modefield size of $2w_0$ = 10.5 μm and the ridge waveguide with a width of 4 μm is -4.6 dB.

By following the same procedure as above, the coupling losses between the input fiber and ridge waveguides with widths of 7 μm and 10 μm were also calculated. Table 5.3 summaries the results both from experiments and simulations. In doing simulations, we assumed the cladding was infinite, and with only 0.5 μm upper cladding and 5 μm bottom cladding, the actual coupling loss will increase by about 1 dB. After taking this into account, the coupling losses obtained from simulations are close to that obtained from experiments.

Table 5.3 Coupling Loss between Fiber and Ridge Waveguides with Different Size

Width	4 μm	7 μm	10 μm
Experiment	7.6 dB	4.8 dB	3.6 dB
Simulation	4.6 dB	3.0 dB	2.5 dB

Every output waveguide was composed of four straight segments and three curved waveguides. Any curvature of a waveguide results in a loss additional to the normal propagation loss. Fig. 5.20 illustrates the effect, which is caused by continuous conversion of the guided light into radiation modes. One way to understand the underlying cause of the radiation is to consider the profile of the transverse field as the guided mode travel round the bend. To keep in step this pattern must rotate around the center of curvature of the guide, like a spoke in a rotating wheel. Consequently, the further from the center, the faster the field must move. However, the outermost evanescent part of the field extends to infinite radius, so at some distance from the core

the field would have to exceed the speed of light in the substrate material to keep up. The portion of the field outside this point must be radiated, reducing the power in the guided mode. Bend loss is therefore very dependent on the confinement offered by the guide. Typically it is found that the guided power falls off as

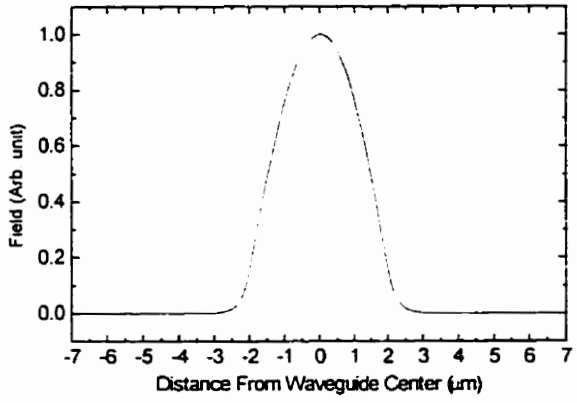

(a) First mode in x direction

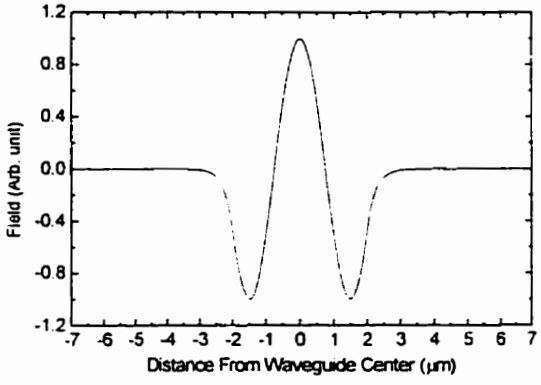

(b) Third mode in x direction

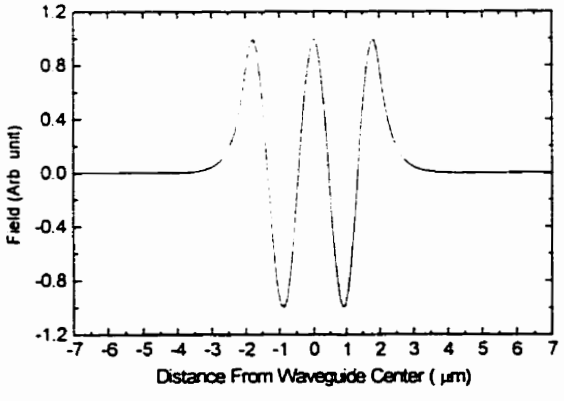

(c) Fifth mode in x direction

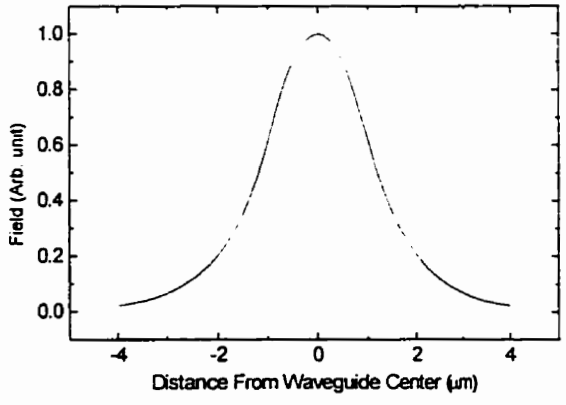

(d) Single mode in y direction

Fig. 5.19 Modefield distribution in the ridge waveguide with a width of 4 μm according to Marcatili's analysis

$$P_z = P_0 \exp(-\alpha z) \qquad (5.18)$$

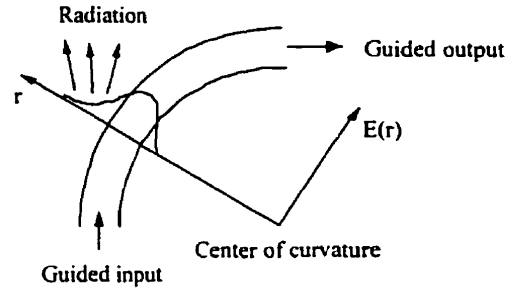

Fig. 5.20 Radiation Loss at a waveguide bend

where P_z is the power after traveling a distance z and P_0 is the input power. The attenuation coefficient α has the semi-empirical form:

$$\alpha = c_1 \exp(-c_2 r) \tag{5.19}$$

Nishihara (1987), Hunsperger (1991), Delage (1992), and Kitoh (1995) have adopted different approaches to calculate c_1 and c_2. By using their formulas, the radiation losses from our curved waveguides were calculated to be negligible, even when the side walls were immersed with index matching fluid which had refractive index of 1.45.

Fig. 5.21 is the schematic of the set-up used to study the effect of index matching fluid on the radiation loss. There was a very small amount of index matching fluid (1.45) between single mode fiber and waveguide at the input point. Since the curved part was far away from the input point, the index matching fluid would not flow there. When there was no index matching fluid between pick-up fiber and the waveguide, a signal

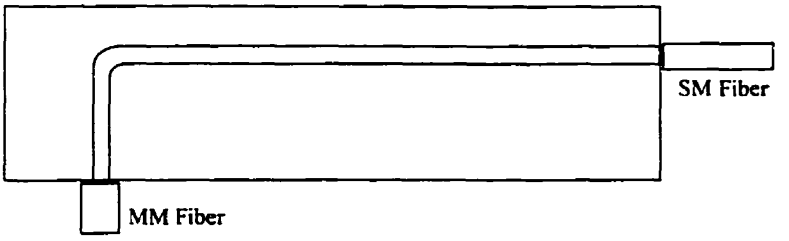

Fig. 5.21 The schematic of the set-up used to study the effect of index matching fluid on radiation loss

was received. Then, a drop of index matching fluid was applied to the tip of pick-up fiber and the fiber was brought to contact the waveguide. At the moment of contact, the signal would dramatically increase (to a level depending on the quality of the end face of output waveguide, usually between 2 dB to 20 dB, we will talk this problem latter), then decrease by 4-6 dB. Index matching fluid improved the coupling between the fiber and the waveguide, which is why the signal increased dramatically at the moment of contacting. Once the fiber contacted with the waveguide, the index matching fluid flowed all the way to the curved segment, and caused 4-6 dB extra radiation loss. The extra radiation loss caused by index matching fluid with refractive index of 1.40 was about 0.6-0.7 dB. Since each output waveguide had three curved segments, the extra radiation loss was 12-18 dB for index matching fluid of n=1.45, and 1.8-2.1 dB for index matching fluid with n = 1.40. The latter was chosen for all our experiments with demultiplexers.

If etch process is not well controlled, ridge waveguides will have rough sidewalls. In one case, ridge waveguides with rough sidewalls had very high scattering loss (around 13 dB/cm). By dipping in HF diluted solution for 40 sec., the roughness of sidewalls was reduced and ridge waveguides only had a loss of 0.4 dB/cm. Unfortunately, this process seemed to have destroyed the grating.

Because of wafer saw, the chip edge was very rough (rms roughness on the order of 2-5 μm). In some cases, the end face of an output waveguide has a large slope and this causes total internal reflection, as shown in Fig. 5.22. This caused very high coupling loss, thus greatly increased the fiber-to-fiber loss. Fluid having refractive index with appropriate value had to be used between a fiber and an output waveguide to remove total internal reflection. Fig. 5.23 shows insertion loss as a function of channel number for a demultiplexer of design A. The top data was collected without using index matching fluid between fiber and output waveguides. By using index matching fluid (n = 1.40), the insertion loss variations from channel to channel were greatly reduced. For some channels, the detected signals were increased by more than 20 dB after using index matching fluid. As we have discussed before, the index matching fluid (n = 1.40) also caused about 2 dB extra loss for the curved waveguides. In practical applications, output channels have to be connected with fibers or detectors using epoxy. The commercially available epoxy with the lowest refractive index is 1.45, and this will cause our demultiplexer 12-18 dB extra loss. One solution is to increase the effective index of our design by 0.5. Another solution is to put a cross bar at the end of output waveguide to prevent epoxy from flowing, as shown in Fig. 5.24.

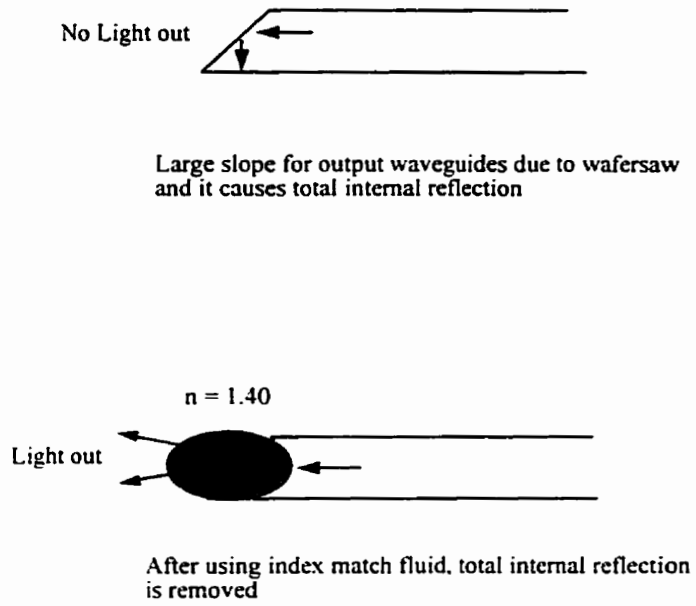

Fig. 5.22 Decreasing the coupling loss due to rough waveguide end faces as a result of using index matching fluid

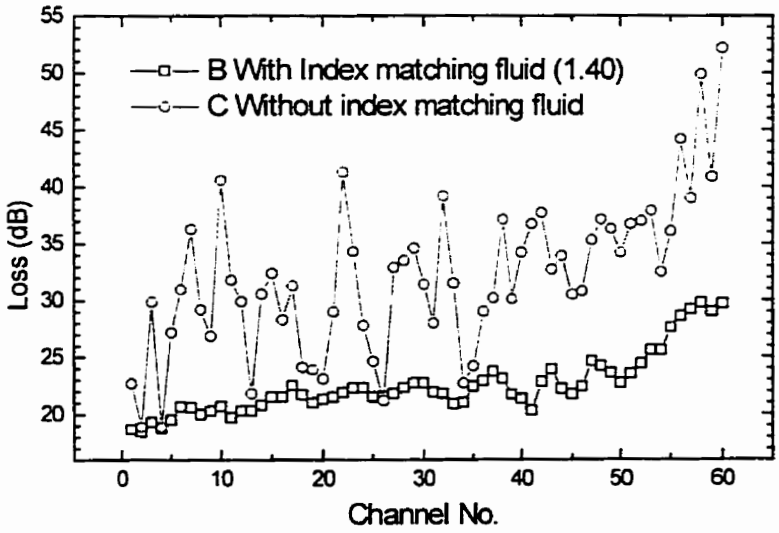

Fig. 5.23 Loss versus channel No. with and without index matching fluid between pick-up fiber and output waveguides.

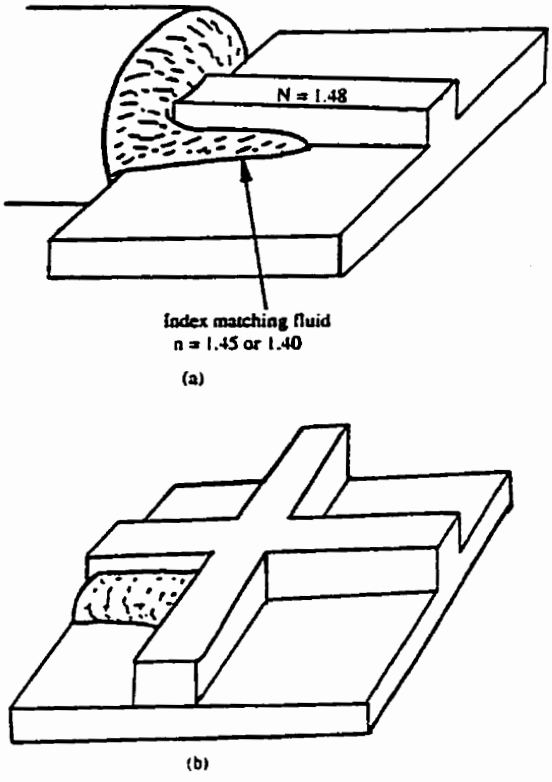

Fig. 5.24 Use of cross bar to stop index matching fluid or epoxy from flowing along the edge of waveguide

5.3 DEMULTIPLEXERS

5.3.1 OVERVIEW

To characterize a demultiplexer, red light from a visible laser diode was first launched into one of 14 input ridge waveguides. Once input single mode polarization maintaining fiber was aligned with the desired input ridge waveguide, the red light would be uniformly spread out inside the slab waveguide (one could see it clearly with his eyes). Then, IR laser with either TE polarization or TM polarization was used instead of visible

laser. After a multimode fiber was aligned with one of output waveguides, one could manually adjust the laser wavelength until a maximum signal was obtained. The signal might be further maximized by optimizing the relative position between the polarization maintaining fiber and the input ridge waveguide. An 80486 based personal computer was used to control both the lock-in amplifier and semiconductor laser. The laser wavelength was scanned over 2 nm range. After the test, the demultiplexer was removed, and the single mode polarization maintaining fiber was aligned with multimode fiber. The recorded signal was supposed to be the input signal for the demultiplexer. By comparing this input signal with the output signal from one of output waveguides, the fiber-to-fiber insertion loss for a demultiplexer at a particular channel was obtained.

In a wafer with 89.4° sidewalls, demultiplexers of several different designs (which are referred as designs A, B, C, D, and E) were thoroughly characterized in this thesis. The wafer was not annealed.

5.3.2 INSERTION LOSS

All of our demultiplexers (with the tilt angle of 0.6°) had at least a fiber-to-fiber insertion loss of 18.6 dB at long wavelength range and even 42 dB at short wavelength range. This prevents them from practical WDM applications. Waveguide loss was the main contribution to the total insertion loss. The waveguide loss has been discussed in section 5.2. Without annealing, the typical loss for slab waveguide was 1.8 dB/cm at 1550 nm, and 2.8 dB/cm for ridge waveguide. The loss value would increase dramatically when

laser wavelength was shorter than 1538 nm, as shown in Fig. 5.11. In the case of large tilt angle (>4°), the loss from the grating will be higher than 10 dB. The coupling loss between pick-up fiber and output waveguides could also be higher than 20 dB if index matching fluid was not used or index matching fluid with high value of refractive index was used, as indicated in Fig. 5.23. The diffraction loss also contributed to the total loss. The diffraction loss was calculated in Chapter three. From Fig. 3.15, we know that diffraction loss for the first channel was about 0.5 dB, and about 5.5 dB for the last channel. The loss difference between TE and TM light is referred as polarization dependent loss (PDL). The PDL of a demultiplexer in practical WDM systems should be as small as possible since the polarization state of light is usually uncertain. In the following sections, the grating loss, PDL, and total loss are discussed.

5.3.2.1 Grating Loss

In Chapter three we have discussed how to fabricate a grating with vertical sidewalls. From Fig. 5.25, we will find how the verticality of sidewalls affects the insertion loss of the device. Both of the devices are the same type (design B) and the signals were measured from output channel 5 where light was coupled into no.1 input waveguide. The two demultiplexers had tilt angle difference of 3.1°, and the insertion loss difference was 10 dB.

According to Marcuse (1986), the formula to calculate the loss in dB due to the tilt of sidewall is:

$$L = 20\log(e)\left(\frac{\beta w}{2}\right)^2 \frac{1}{4}\left(\frac{\sin^2(2\alpha)}{2-\sin^2\alpha}\right) \tag{5.20}$$

$$\beta = \frac{2\pi N}{\lambda} \tag{5.21}$$

N = effective index = 1.484λ = 1.55 μm

w = Gaussian mode width = 1.59 μm

α = phase tilt due to reflection

θ = out of plane tilt of facet normal

$= 2\sqrt{2}\theta$ for two 45° reflection

Fig. 5.26 shows the calculated loss versus tilt angle. The calculated loss is much smaller than experimental results. This may be due to oversimplifying the treatment for the calculated results.

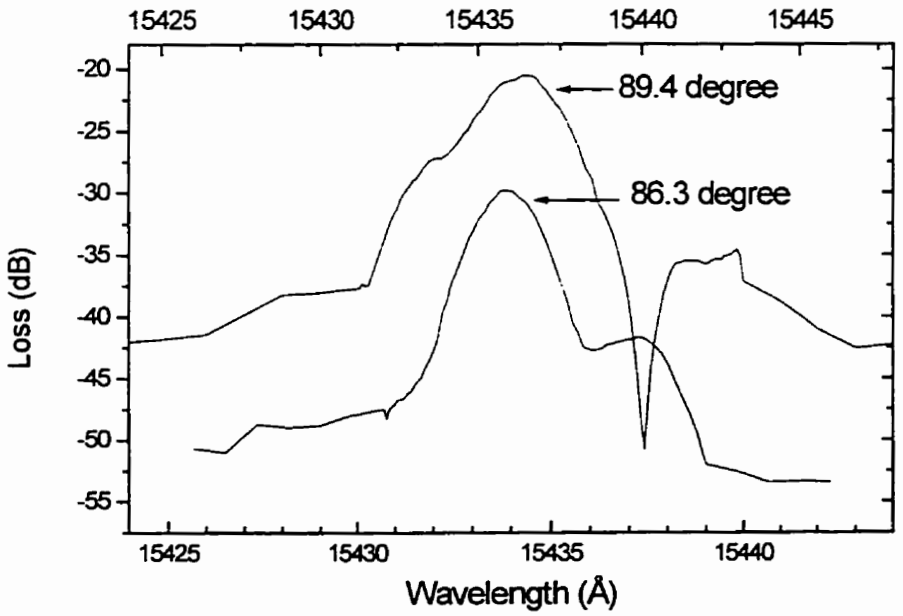

Fig. 5.25 Transmission losses versus wavelengths for channels with the same channel number of two demultiplexers of design B, one with sidewall angle of 89.4° and the other with sidewall angle of 86.3°.

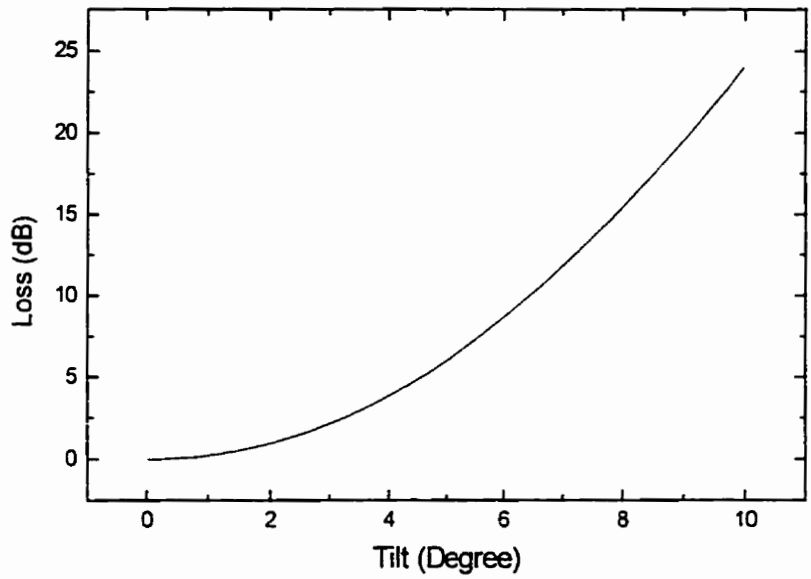

Fig. 5.26 Loss versus the tilt angle of grating predicted by Marcuse's theory

The roughness of grating facets also contributed to grating losses. A grating had vertically etched sidewalls but rough facets, and its loss was found to be 12 dB. Lee et al. (1991) have done modeling of rough-surface effects in an optical turning mirror. The RMS roughness of 60 nm will cause 3 dB loss according their results. If we extrapolate their results, 12 dB loss corresponds to the RMS roughness of about 110 nm. After dipping with diluted HF solution, the sidewalls of the grating became nonvertical. Scattering loss was greatly reduced, but at the same time, the loss due to the tilt of sidewall was dramatically increased. So, HF dipping can decrease waveguide loss, but not the loss from grating.

5.3.2.2 PDL

Here, we define PDL as L_{TM} - L_{TE}, where L_{TM} , L_{TE} are losses for TM and TE light respectively (For this definition, it is assumed that L_{TM} and $L_{TE} > 0$). Fig.5.27 shows PDLs as a function of channel numbers for a demultiplexer of design A. From this figure, it is known that PDL = 0.45 ± 0.08 dB. That means output signal for TE light was 0.45 dB higher than that of TM light on the average.

If we consider the light inside slab waveguide as a plane wave, Fresnel equations (Saleh and Teich, 1991) can be used to calculate reflection coefficients for both TE, and TM light, as shown in Fig. 5.28. From this figure we can see that when the incident angle is smaller than the critical angle, the refection coefficient for TE mode is always greater than TM mode. A more careful treatment would decompose the incident guided mode into plane wave with a distribution of incident angles. If the distribution of incident angle is wider than 7°, then some of the incident plane wave components would not experience total internal reflection, which results in loss and PDL. Fig. 5.29 shows PDL as a function of incident angle when a wave propagates within a medium having an index of refraction equal to 1.5 and is incident on a medium having an index of refraction equal to 1.0.

5.3.2.3 Total Loss

Fig. 5.30 shows 60 main lobes of a demultiplexer of design A. The fiber-to-fiber loss ranges from 18.6 to 29.8 dB. The loss is lowest for the long wavelength channels. The long wavelength channels collect light at points that are closer to the input point and thus have a lower diffraction loss since the blaze is optimized for retroreflection to the input

point. The long wavelength channels also have shorter output waveguides, thus they have lower waveguide propagation loss.

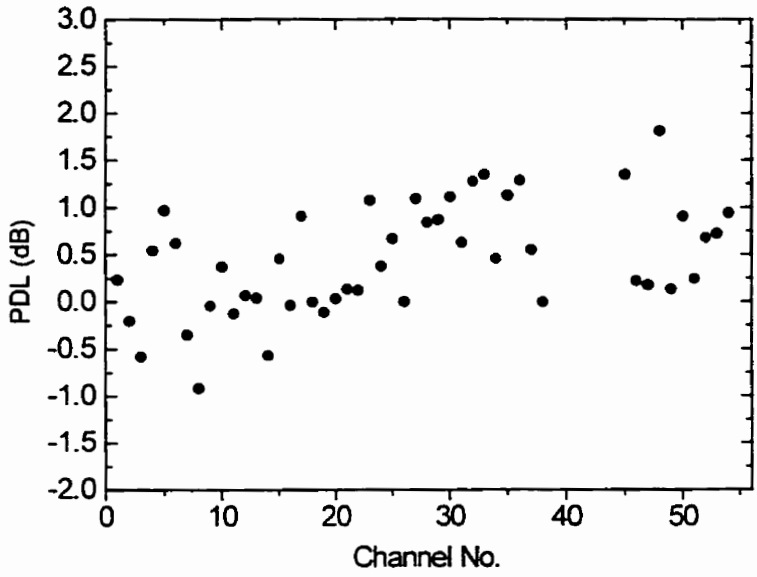

Fig. 5.27 PDLs as a function of channel numbers for a demultiplexer of design A. PDL = L_{TM} - L_{TE}, where L_{TM} , L_{TE} are losses for TM and TE light respectively (assumed to be positive)

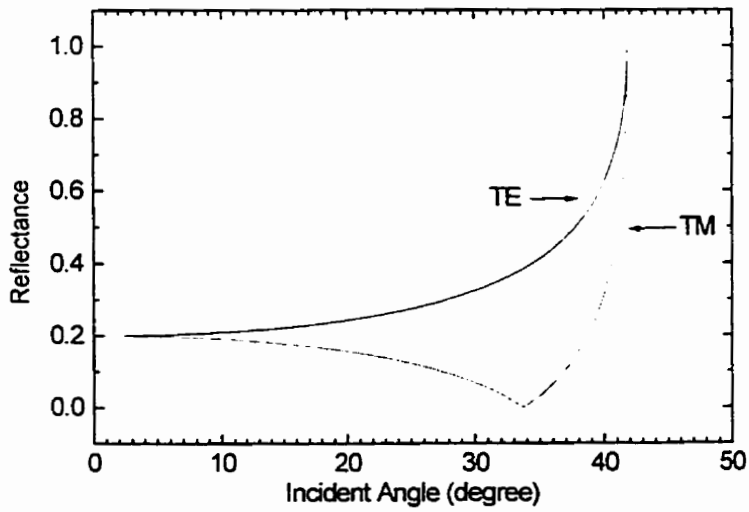

Fig. 5.28 Reflection coefficients as a function of incident angles when a wave is incident from n_1 = 1.5 medium to n_2 = 1.0 medium.

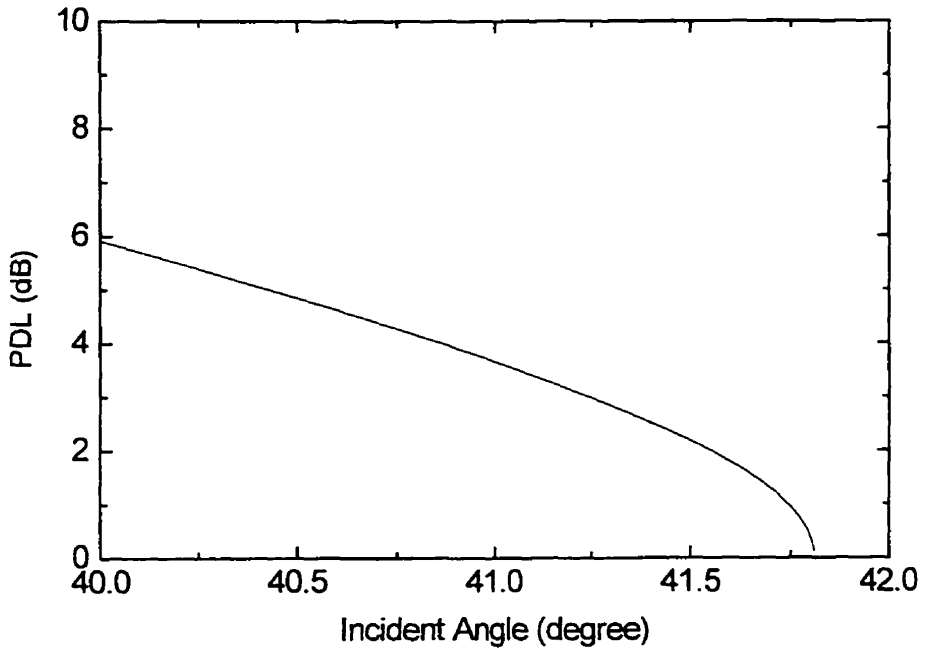

Fig.5.29 PDL as a function of incident angles when a plan wave is incident from n_1 =1.5 medium to n_2 = 1.0 medium. PDL = | L_{TM} | - | L_{TE} |, where L_{TM} , L_{TE} are losses for TM and TE light respectively

Fig. 5.31a shows main lobes of 94 adjacent channels for a demultiplexer of design C where light was launched into the device through the no.1 input waveguide. Due to high waveguide absorption loss at short wavelength range, data could not be obtained for output waveguides 95 to 120. Fig. 5.31b shows data when light entered the no. 11 inputwaveguide. Changing the input waveguide shifted the wavelength for each output channel by 12 nm, and brought all output channels into a wavelength range with sufficiently low absorption for measurements. Measurements were made on 80 channels (including channel 48 to 120) of the 120 channels before the device was accidentally broken. The seven channels not shown in Fig. 5.31b had loss values in the range from 19.9 dB to 22 dB. The output channels that were not tested with input no.11, had been

previously demonstrated to be in working order through the measurements with input no.1 waveguide.

Here, we use the term "channel loss" to mean the fiber-to-fiber loss in a particular channel at a wavelength that maximize the transmission. The channel loss, L, can be described by

$$L = A\,\alpha(\lambda)d_i + L_D + L_C \qquad (5.22)$$

where d_i is the length of propagation through the sample, $\alpha(\lambda)$ is absorption coefficient measured on a piece of a slab waveguide, as shown in Fig. 5.11, and A is a fitting parameter to account for the fact that the absorption was not uniform across a wafer. d_i depends on the output channel number according to $d_i = (68.6 + 0.18i)$ mm. $\alpha(\lambda)$ was found to vary between -1.8 dB/cm at 1549 nm and -7.1 dB/cm at 1522 nm and

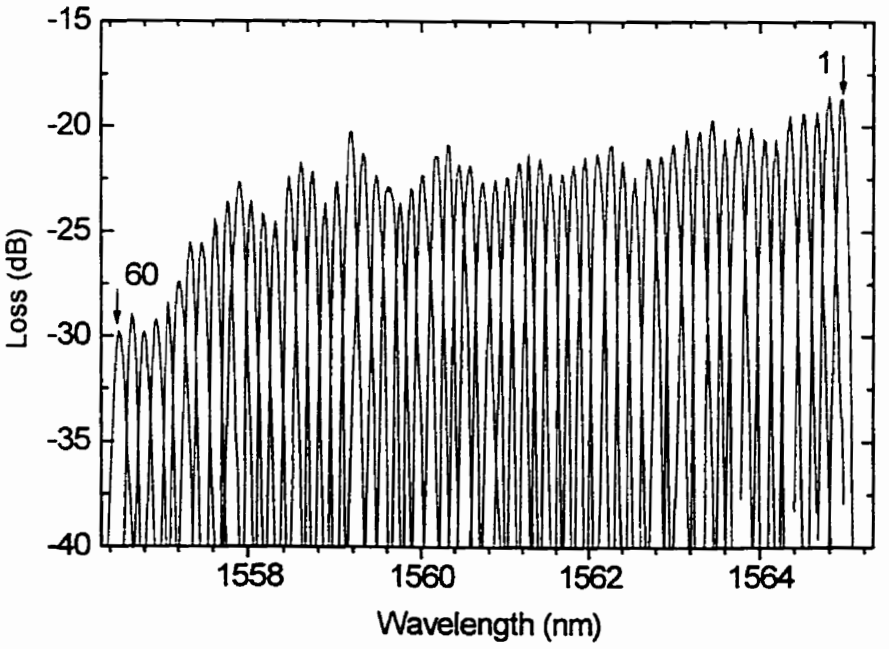

Fig. 5.30 Spectral response for 60 output waveguide of a demultiplexer of design A. Each output waveguide has a peak response of a different wavelength. For clarity, only the central lobe of each response function is shown

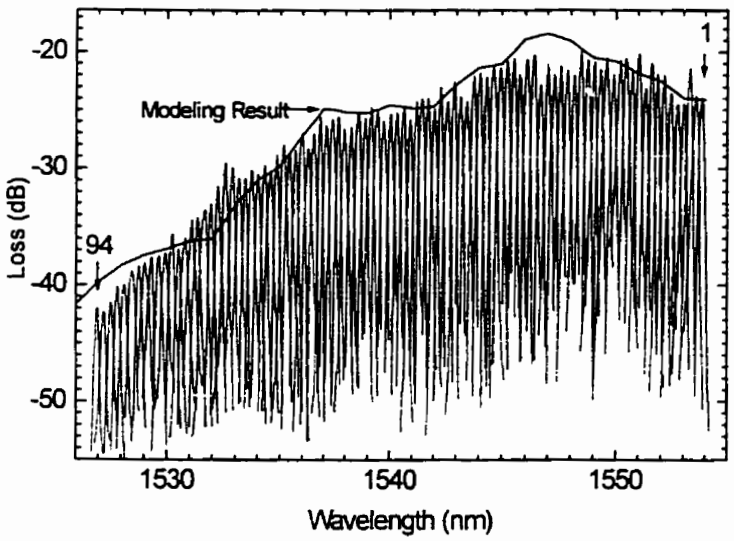

Fig. 5.31a 94 main lobes for a demultiplexer of design C. Light was coupled into the device through input no.1 waveguide; the input light was in TM mode

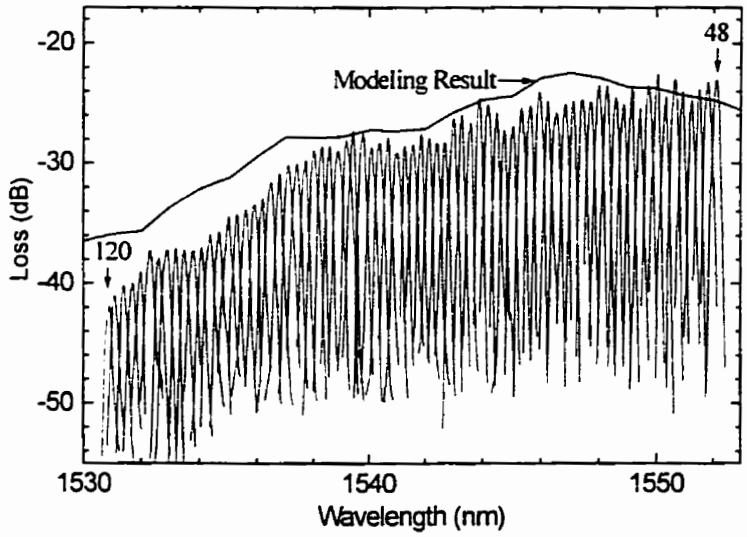

Fig. 5.31b 73 main lobes for a demultiplexer of design C. Light was coupled into the device through input no.11 waveguide; the input light was in TE mode

Fig.5.31 Spectral response for 120 output waveguide of a demultiplexer of design C. Each output waveguide has a peak response of a different wavelength. For clarity, only the central lobe of each response function is shown

as shown in Fig. 3.15. L_C, the input coupling loss, was found to be –3.6 dB from the experiment in section 5.2.2. In Fig. 5.31 the lines over main peaks are the modeling results. The fact that eq. 5.22 fits the data of Fig. 5.31a and b indicates that the loss was primarily due to absorption and the loss at the grating was probably less than 1 dB.

Fig. 5.32a is the close up of ten adjacent channels in Fig. 5.31a, and Fig. 5.32b is the simulation results. The experimental data agreed well with the simulation results. By annealing, the waveguide loss could be reduced to 0.8 dB/cm for all wavelengths. In Fig. 5.33, the top line is the channel loss as a function of channel number predicated by eq. 5.22 where $\alpha(\lambda) = 0.8$ dB/cm was used. The open circles were the experiment data for a demultiplexer of design C, and the solid line which crosses open circles was calculated from eq. 5.22 where $\alpha(\lambda)$ is the same as in Fig. 5.31a and Fig.5.31b.

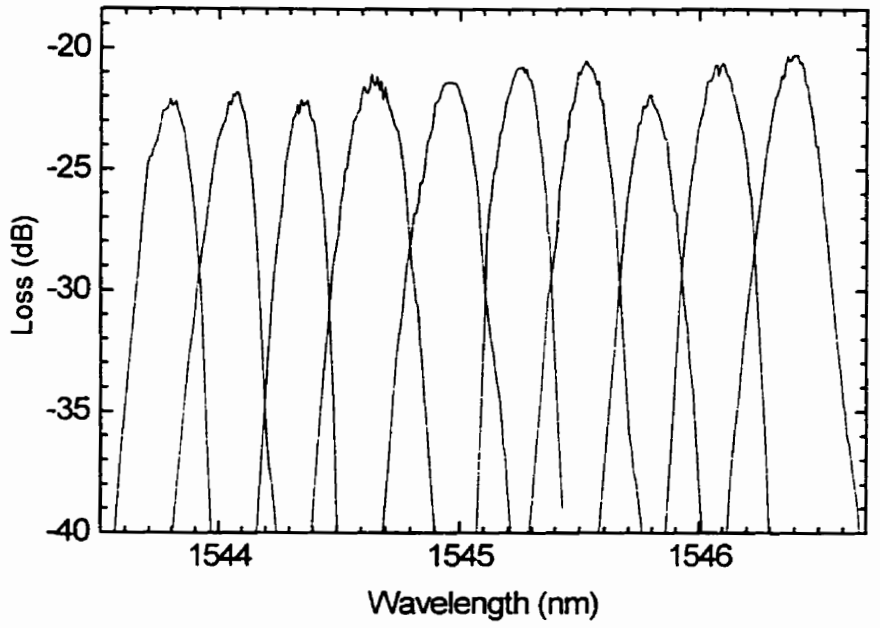

(a) Experiment

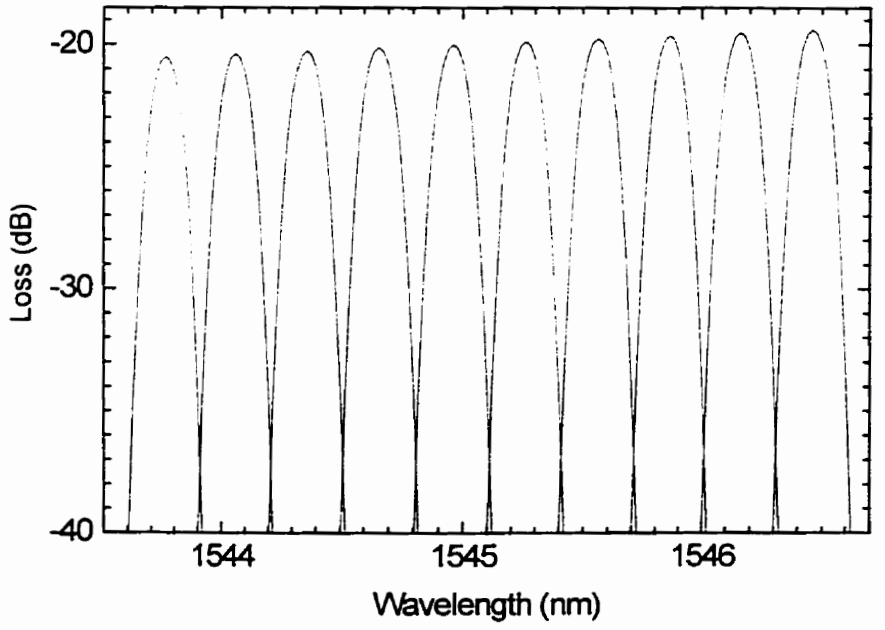

(b) Simulations

Fig. 5.32 Spectral response for 10 output waveguide of a demultiplexer of design C. Each output waveguide has a peak response of a different wavelength. For clarity, only the central lobe of each response function is shown. The experimental data (a) can be compared with the simulated data (b)

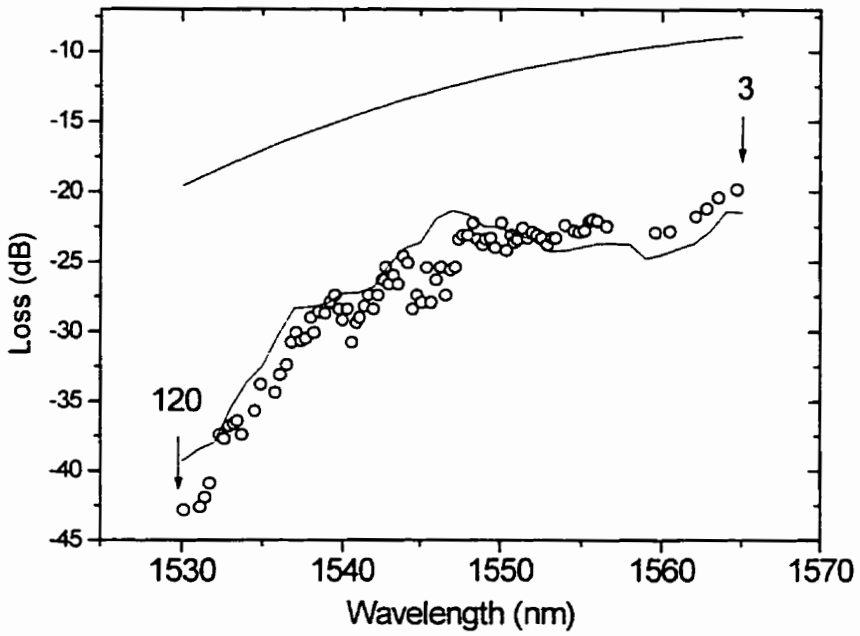

Fig. 5.33 Fiber-to-fiber loss as a function of wavelengths for a demultiplexer of design C; open circles were experimental data and the line across these open circles was the simulation result for the unannealed wafer; the top line was the result predicted by eq. 5.22 when waveguides have a wavelength independent loss of 0.8 dB/cm

5.3.3 DISPERSION

5.3.3.1 Channel Spacing

Fig. 5.34 shows the channel center wavelengths as a function of channel numbers for the demultiplexer of design A, design B and design C. The average channel spacing was 0.144 nm for design A, which was our design value, and 0.288 nm for both design B and design C. The designed channel spacing for demultiplexer B and C was 0.3 nm.

To test the stability of channel center wavelengths, five separate tests for the same channel of a demultiplexer of design A (Table 5.4) and design C (Table 5.5) were carried out in a two month period. The center wavelength for each channel was very stable within our experimental uncertainty, but the loss varied by about 3 dB. Since the alignment for each test could not be exactly the same, and this caused the loss variations from run to run.

Table 5.4 Five separate tests for a demultiplexer of design A

No. of testing	Center Wavelength	FWHM	Loss
test1	1564.66 nm	0.11 nm	19.0 dB
test2	1564.63 nm	0.11 nm	24.0 dB
test3	1564.61 nm	0.09 nm	18.9 dB
test4	1564.68 nm	0.12 nm	23.7 dB
test5	1564.68 nm	0.11 nm	23.9 dB

Table 5.5 Five separate tests for a demultiplexer of design B

No. of testing	Center Wavelength	FWHM	Loss
test1	1544.12 nm	0.25 nm	19.4 dB
test2	1544.12 nm	0.26 nm	20.2 dB
test3	1544.16 nm	0.22 nm	18.7 dB
test4	1544.15 nm	0.28 nm	20.3 dB
test5	1544.13 nm	0.23 nm	22 dB

5.3.3.2 Center Wavelength Tuning

"Channel center wavelength" is the wavelength that maximizes the transmission. By choosing different input waveguides, the channel center wavelength from the same output

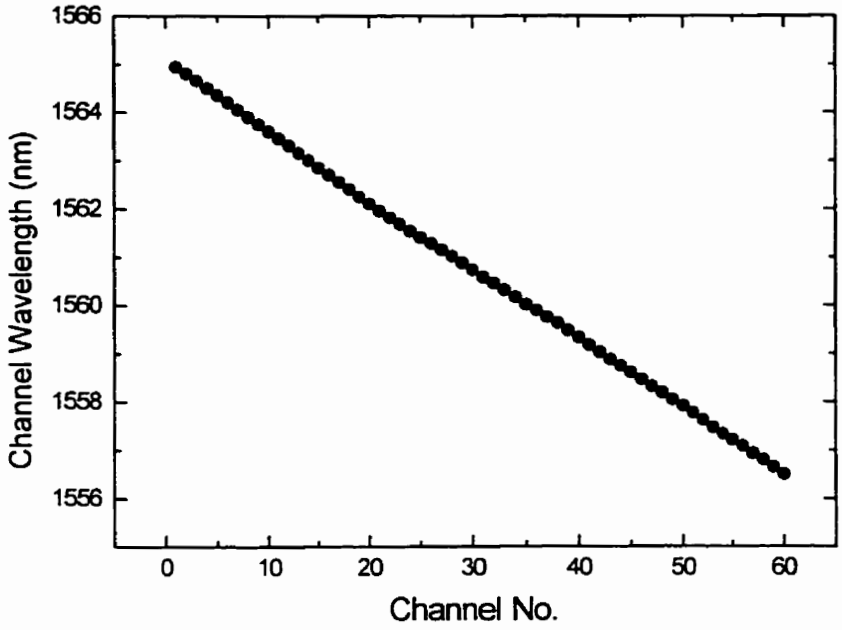

Fig. 5.34a Design A

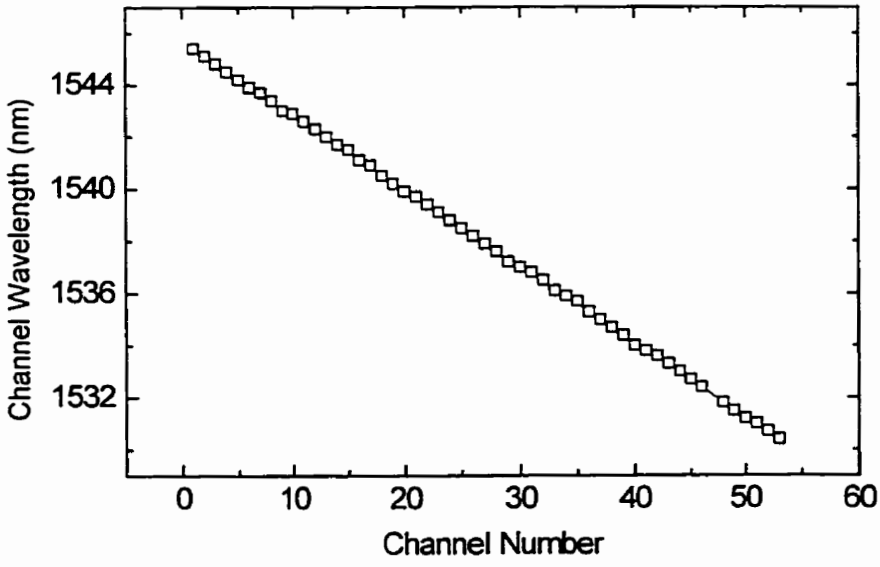

Fig. 5.34b Design B

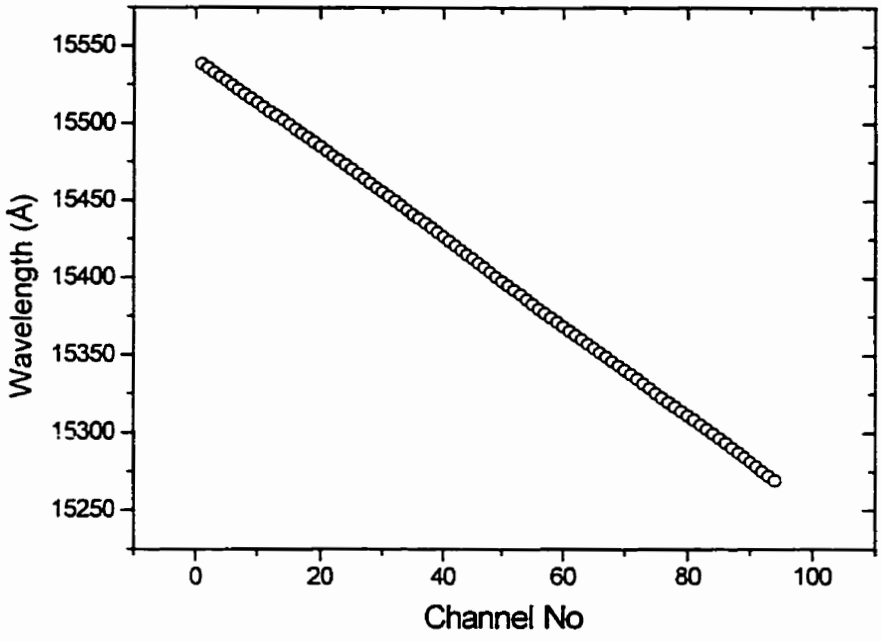

Fig. 5.34c Design C

Fig. 5.34 Channel center wavelength (ie. the peak in the response function)) as a function of channel numbers for design A, (b) design B, and (c) design C. Not every channel is shown for each design. The expected linear dependence was observed

waveguide can be increased or decreased to some extent. Fig. 5.35a gives the transmission loss against wavelength from the output channel 2 of a demultiplexer of design A. Each peak in the figure corresponds to data when light was applied to one of the 14 input waveguides. The channel center wavelength was increased by 0.6 nm when the input waveguide no.2 was used instead of no.1. By moving input fiber from the input no.1 to input no.14 waveguide, the center wavelength could be increased by 8.4 nm. For design B, as shown in Fig. 5.35b, the channel center wavelength could be adjusted by about 1.2 nm when adjacent input waveguides were used. Fig. 5.36 shows the transmission loss against wavelength from the output channel 20 of a demultiplexer of design C when the light was applied to input waveguides no.1 to no.14. The channel

center wavelength was increased by about 1.2 nm when the input waveguide no.2 instead of no.1 was used. By moving input fiber from the input no.1 to input no.14 waveguide, the center wavelength was increased by 15.0 nm according to experimental results in Fig. 5.36a and 15.6 nm according to simulation results in Fig. 5.36b. The difference is due to the fabrication errors in refractive indices of core layer and cladding layers. The transmission losses from experimental results in Fig. 5.36a agree reasonably well with that from simulation results in Fig. 5.36b. But for the same device when the output channel 99 was used, as shown in Fig. 5.37, the transmission loss when no.1 input waveguide was used deviated from the simulation result by 15 dB! When we did simulation, the waveguide losses were assumed to be wavelength independent, but from Fig. 5.11 we can see that the waveguide losses are heavily wavelength dependent, especially when wavelength is shorter than 1539 nm. The absorption wavelength dependence contributes to the loss difference when 14 input waveguide were used in Fig. 5.37a.

The selection of input waveguides provides a wavelength tuning mechanism, and will be very useful in the commercial production of demultiplexers. According to International Telecommunication Union (ITU), the useable wavelengths are predefined. When one designs a WDM demultiplexer, he should set the channel center wavelength by ITU standard. But waveguide fabrication variation will cause the effective index, n, to have an error, δn, which will cause a wavelength error, $\delta\lambda$, in the wavelength of light that is centered at a stigmatic output point. The errors are related by $\delta\lambda/\lambda_0 = -\delta n/ n_0$, where λ_0 is the free space stigmatic wavelength and n_0 is the designed value for the effective index.

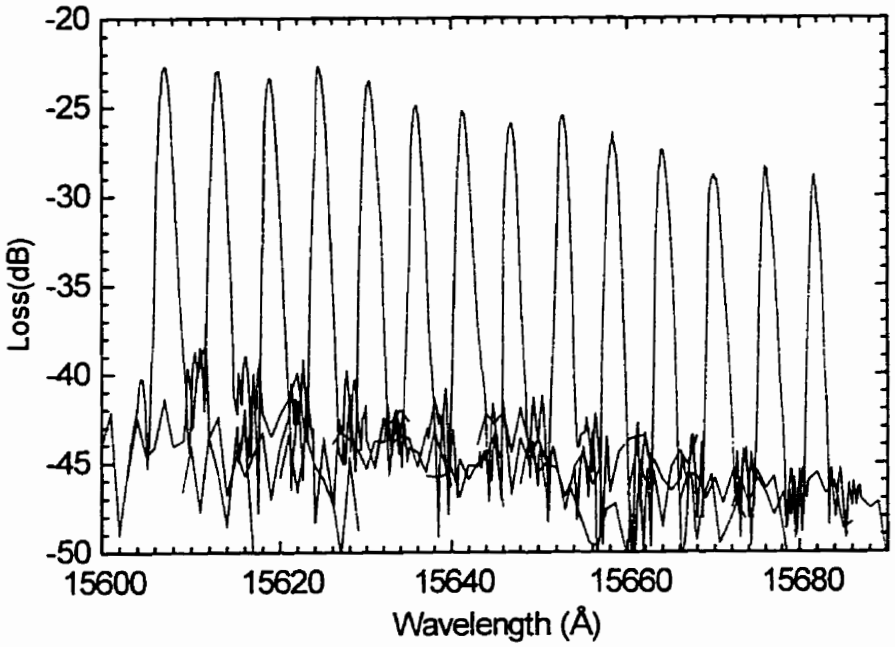

Fig. 5.35a Design A, from channel 2

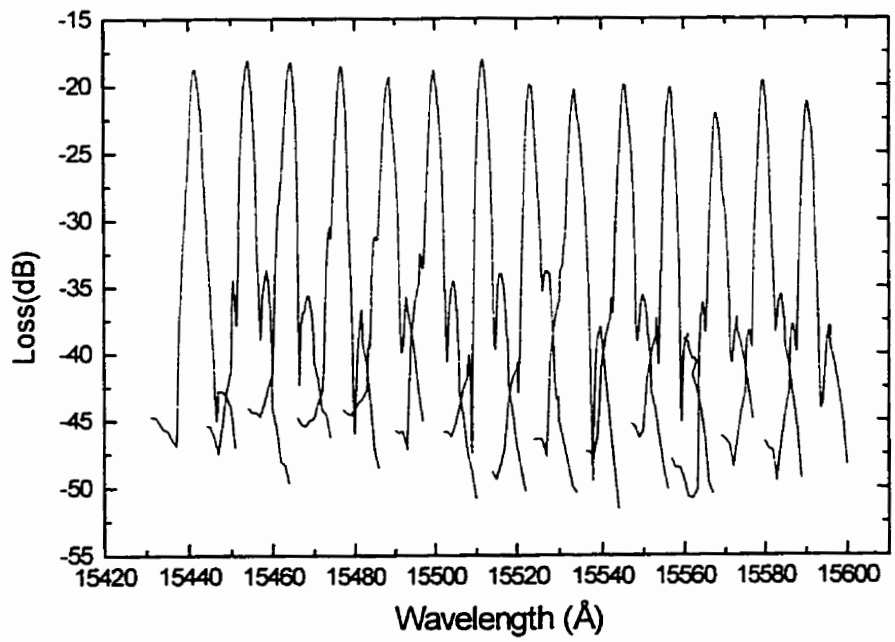

Fig. 5.35b Design B, from channel 3

Fig. 5.35 14 transmissivity spectra for demultiplexer design A and B. Each spectrum corresponds to a different input waveguide. Output waveguide number 20 was used for each spectrum.

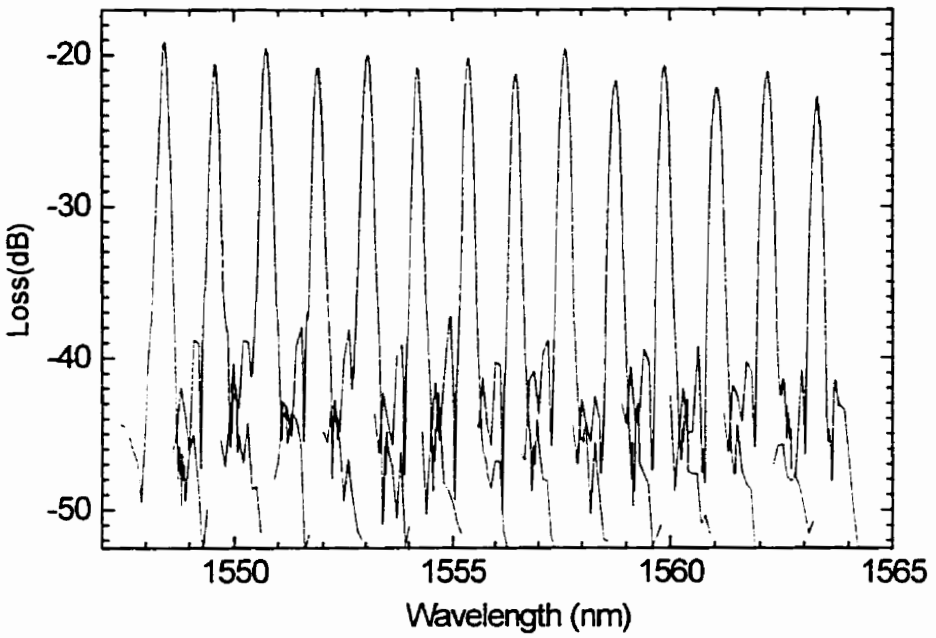

5.36a Experiments

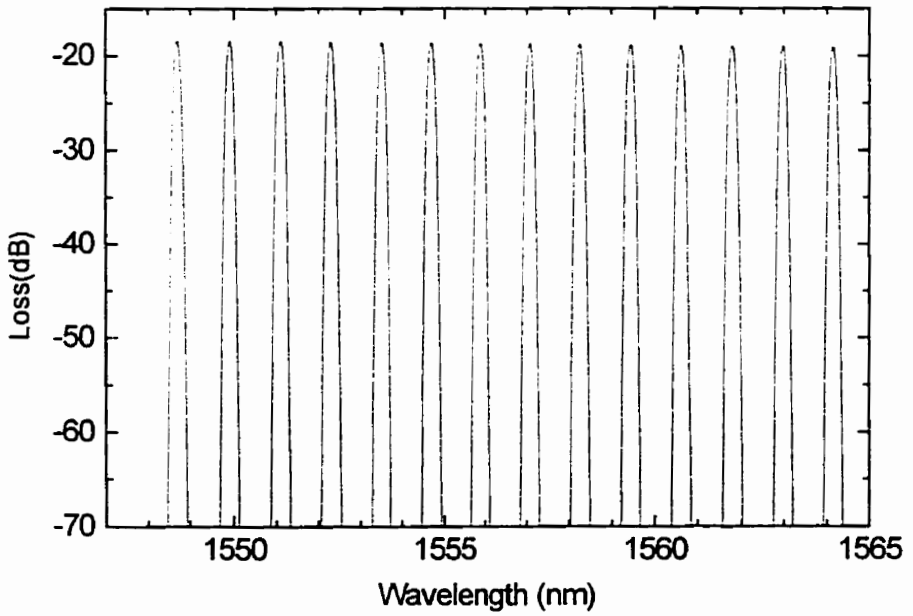

5.36b Simulations

Fig. 5.36 14 transmissivity spectra for demultiplexer design C. Each spectrum corresponds to a different input waveguide. Output waveguide number 20 was used for each spectrum. The simulated results (5.36b) agree reasonably well with the experimental results (5.36a)

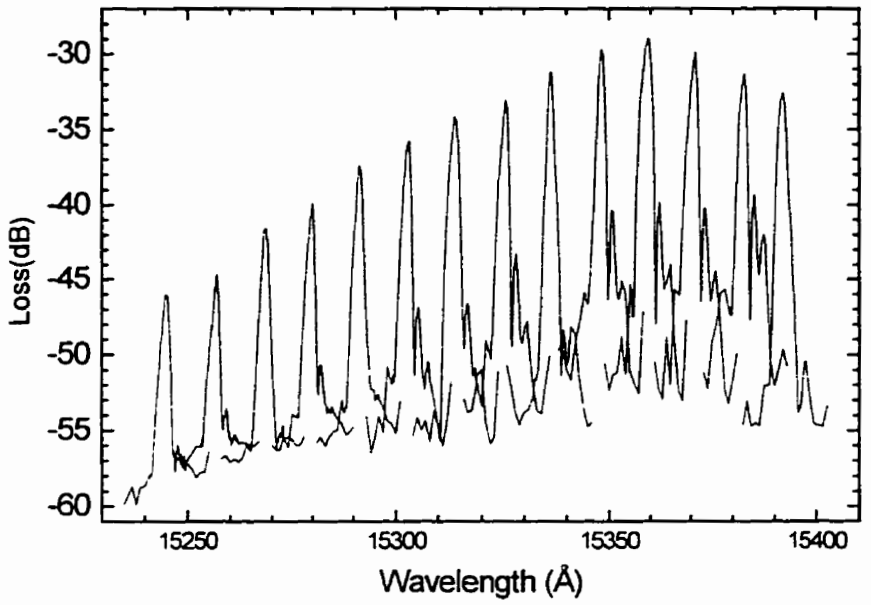

Fig. 5.37a Experiments

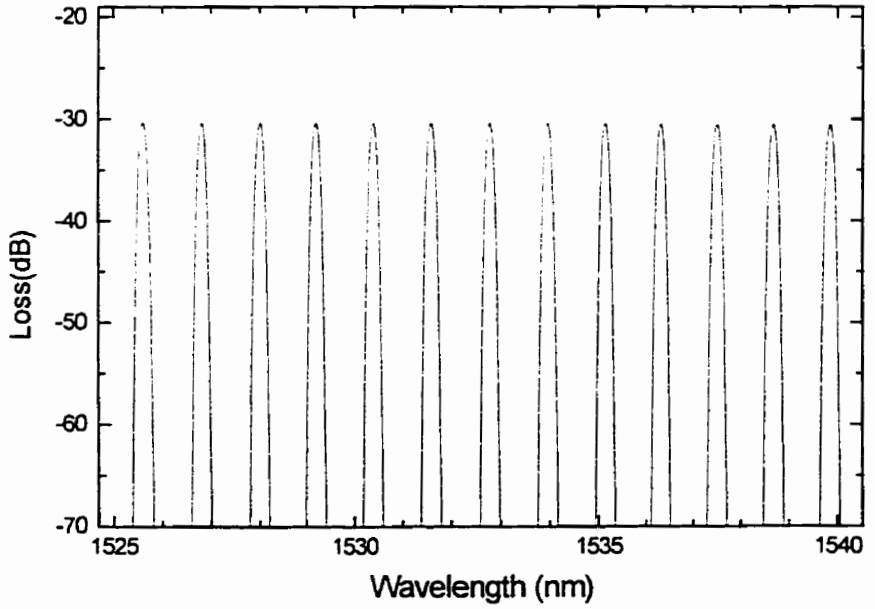

Fig. 5.37b Simulations

Fig. 5.37 14 transmissivity spectra for demultiplexer design C. Each spectrum corresponds to a different input waveguide. Output waveguide number 99 was used for each spectrum. The simulated results (5.37b) do not agree with the experimental results (5.37a)

If the device is to demultiplex optical signals in the 1550 nm range with a channel wavelength separation, $\Delta\lambda$ = 0.8 nm (by ITU standard), and the error in channel wavelength is required to be less than 10% of the channel spacing, then the allowed errors is $\delta n / n_0 \leq \Delta\lambda/10\lambda_0 = 0.0048$. Variations in the film thickness and refractive index cause errors that are at least an order of magnitude larger than this.

In the present design, input waveguide selection provides coarse tuning, i.e. it will get center wavelength within ± 0.6 nm for design A. This is not good enough for a WDM receiver. However, in future designs, we could get center wavelength within ± 0.015 nm. For the design A, the output waveguide separation is 10 μm and input waveguide separation is 40 μm. For the future design A, the output waveguide separation is still 10 μm, the number of output waveguides will be 64 + 4×13 = 116. The separation between the first input waveguide and the second input waveguide is 41 μm; the separation between the second and the third is 42 μm; the separation between the third and the fourth is 43 μm, and so on. The separation between the fourteenth and thirteenth input waveguide is 53 μm. All other design parameters are the same as the old design A. Supposing first 64 channels are initially chosen for a WDM demultiplexer or a spectrometer, and light is coupled into the device through no.1 input waveguide. If light is coupled into the device through no.2 input waveguide, the center wavelength for all first 64 channels will be increased by 0.6 nm + 0.015 nm. Now, we could use no. 5 to no. 68 channels as our all 64 channels. Compared with the case of no.1 input waveguide, the center wavelength is increased by 0.015 nm for all 64 channels. If light is coupled into the

device through no.14 input waveguide, and channel 53 to channel 116 as our 64 channels; the center wavelength for all 64 channels will be increased by 0.195 nm.

5.3.3.3 Polarization Dependent Dispersion (PDD)

In practical optic fiber communications systems, light in a fiber can be in any polarization state. Ideally, parameters such as channel center wavelengths and losses should be polarization independent. Due to waveguide birefringence and stress birefringence, the effective indices N_{TE} for the TE mode and N_{TM} for the TM mode are different from each other for slab and ridge waveguides. The value of the birefringence is defined as $B = N_{TE} - N_{TM}$. This causes the channel center wavelength difference when light is changed from TE mode to TM mode. In our experiments, TE light was coupled into one of the input waveguides, and was taken out from one of the output waveguides. A spectral response was obtained for the TE mode by wavelength scanning, as shown in Fig. 5.38. Keeping both input and pick-up fibers fixed and changing TE light to TM light by turning half waveplate by 45°, the spectral response for TM mode was obtained, see Fig. 5.38. The channel center wavelength difference for TE and TM is 1.06 nm. The following equations can be used to calculate birefringence from Fig. 5.38:

$$\Delta L = m\frac{\lambda_0}{N} \tag{5.23}$$

$$\Delta L = m\frac{\lambda_{TE}}{N_{TE}} \tag{5.24}$$

$$\Delta L = m\frac{\lambda_{TM}}{N_{TM}} \tag{5.25}$$

$$\lambda_{TE} = \frac{N_{TE}\Delta L}{m} \tag{5.26}$$

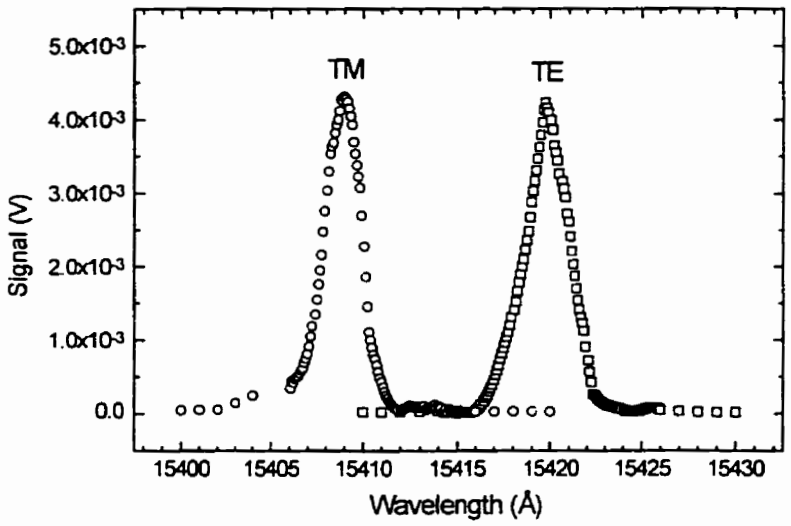

Fig. 5.38 The birefringence for a demultiplexer of design B causes the TE light response to occur at a wavelength that is 1.06 nm larger than the TM light response

$$\lambda_{TM} = \frac{N_{TM}\Delta L}{m} \tag{5.27}$$

$$\lambda_{TE} - \lambda_{TM} = \Delta\lambda = \frac{\Delta L}{m}(N_{TE} - N_{TM}) = \frac{\Delta LB}{m} \tag{5.28}$$

$$B = \frac{N\Delta\lambda}{\lambda_0} \tag{5.29}$$

where ΔL is the path difference between any two adjacent facets. m is the diffraction order of the grating. λ_0 , N, λ_{TE} ,N_{TE} ,λ_{TM} ,N_{TM} , and B correspond to stigmatic wavelength (1.548 μm), the designed effective index of slab waveguides (1.484), the channel center wavelength for TE mode, the effective index seen by TE light, the channel center wavelength for TM mode, the effective index seen by TM light and birefringence. By

using 5.29, the birefringence B is calculated to be 1.01×10^{-3}. This is composed of stress birefringence and waveguide birefringence:

$$B = B_{stress} + B_{waveguide} \tag{5.30}$$

Stress birefringence originates from the compressive stress, which results from the difference between the thermal expansion coefficients of the silica cladding and the substrate. It can be expressed as follows (Suzuki, 1994):

$$B_{stress} = N_{TE} - N_{TM} = KE(\alpha_{cladding} - \alpha_{sub})\Delta T \tag{5.31}$$

where K and E are the photoelastic coefficient and Young modulus of silica glass, α_{sub} (= 3.5×10^{-7} $°C^{-1}$ for Si substrate) and $\alpha_{cladding}$ (= $6.0\times10^{-7}°C^{-1}$,) are the thermal expansion coefficients of the substrate and cladding glass and ΔT is the difference between the glass consolidation temperature and room temperature (Suzuki, 1994). Typical value for B_{stress} is -2×10^{-4}.

Waveguide birefringence originates from the refractive index difference between the core layer and the cladding layer. The higher the difference, the higher $B_{waveguide}$ will be. To get a negligible $B_{waveguide}$, the small refractive index difference between core and cladding is usually used ($<5\times10^{-3}$). Smaller refractive index difference means thicker core layer. The maximum etch depth for our RIE process is 3 μm, which gives us the maximum core layer of 2 μm. To design a single mode slab waveguide with such thickness, the smallest refractive index difference between the core and the cladding is 4.2×10^{-2}, which leads to $B_{waveguide} = 1.21\times10^{-3}$. By improving the RIE etch process, we can design a slab waveguide with thicker core layer (about 3 μm), such that its waveguide birefringence cancels the stress birefringence.

Fig. 5.39a shows birefringence as a function of channel number for demultiplexer A. Across the chip, the birefringence is a constant with the experimental errors. But for demultiplexer B, see Fig. 5.39b, the birefringence was higher for the long wavelength channels, and became much smaller for short wavelength channels. The least squares fit on graph software Origin has been carried for the experimental data in Fig. 5.39b. It gives -0.64492 for "R", the "linear-correlation coefficient" and 0.0001 for "P", the probability that R is zero. The nonuniformity of birefringence from channel to channel makes it more difficult to find a way to completely control birefringence across the chip.

To increase coupling between waveguides and fiber, a core layer with the same thickness as the fiber (7-10 μm) has to be chosen. In this case, the stress birefringence is the main contribution to the total birefringence. Many approaches have been used to successfully control birefringence, such as α-Si films (Takahashi et al., 1993), the use of a TE/TM converter with λ/2 waveplate (Okamoto, 1996), the use of a pure silica substrate

(Suzuki, 1994), interposing a high refractive index material between the core and cladding (Aarnio, 1991), and the use of different array orders for TE and TM (Spiekman, 1996) of a phased-array demultiplexer. Our work on interposing a high refractive index material between the core and cladding is addressed in Chapter Six

5.3.3.4 Noise Floor

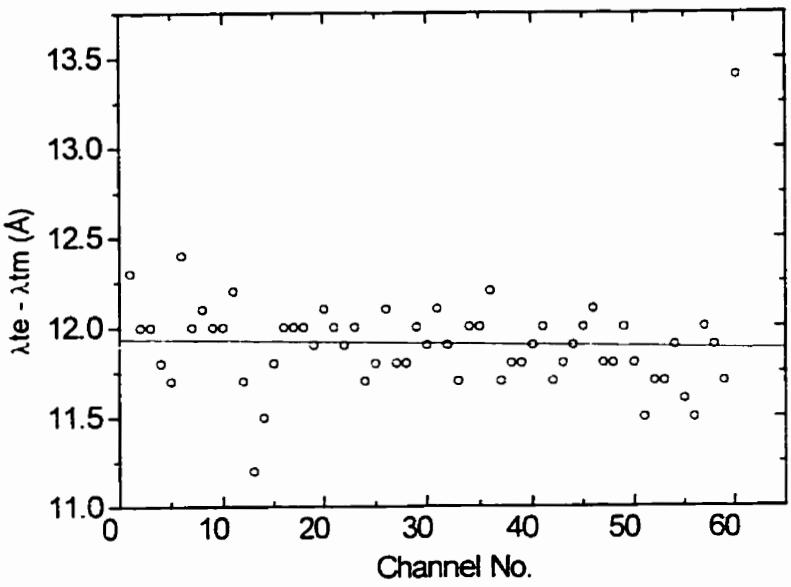

Fig. 5.39a Design A

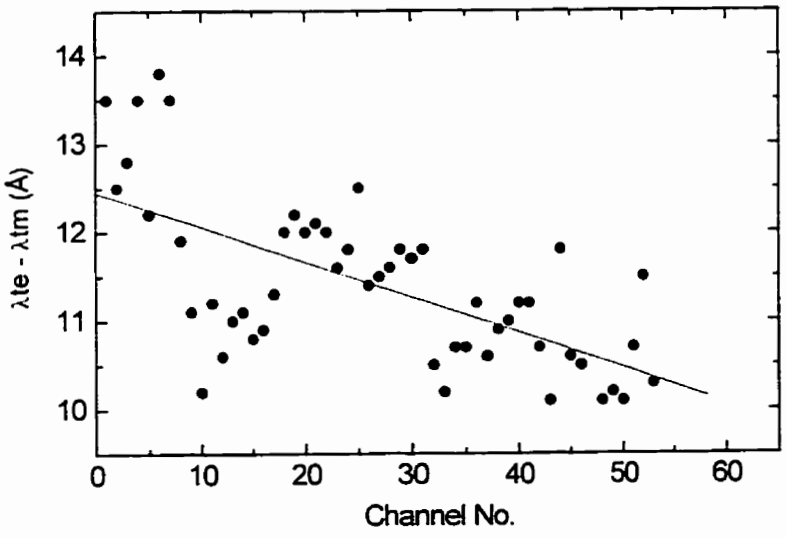

Fig. 5.39b Design B

Fig. 5.39 Birefringence as a function of channel no. for demultiplexers of design A and design

When a long range wavelength scanning was performed, as shown in Fig. 5.40, the noise floor can be measured. The noise floor for demultiplexer C was 30 dB below the main peaks. For demultiplexer A, the noise floor was 30 dB below the main peak outside the grating bandwidth, but only 20 dB below the main peak inside the bandwidth, see Fig. 5.40b. Since demultiplexer A has small Free Spectral Range, there were three passbands when the signal wavelength was scanned from 1520 nm to 1570 nm. The one at short wavelength side had high loss because of waveguide absorption.

5.3.3.5 Light From Input Waveguides

When visible laser light was coupled into one of input waveguides, red light was observed coming out from almost all output waveguides, as well as some other input waveguides. It is easy to understand that light comes out from output waveguides, but why from other input waveguides? An experiment was conducted for IR light to see how many signals came out from other input waveguides. The light was launched into input waveguide no. 1 of demultiplexer A, then a multimode fiber was aligned with input waveguide no.7. Fig. 5.41 shows the spectral response. Four peaks with the wavelength separation of 0.6 nm were recorded, and each peak had a loss of about 30 dB. The center wavelength for the first peak was 1548.6 nm. According to experimental data in Fig. 5.30, when light was coupled into the first input waveguide, the center wavelength for the first output channel is 1564.9 nm. The distance between the first output channel and the seventh input channel is 340 μm, and the dispersion is 0.0144 nm/μm. So when light is launched into the first input waveguide, the center wavelength for the light out

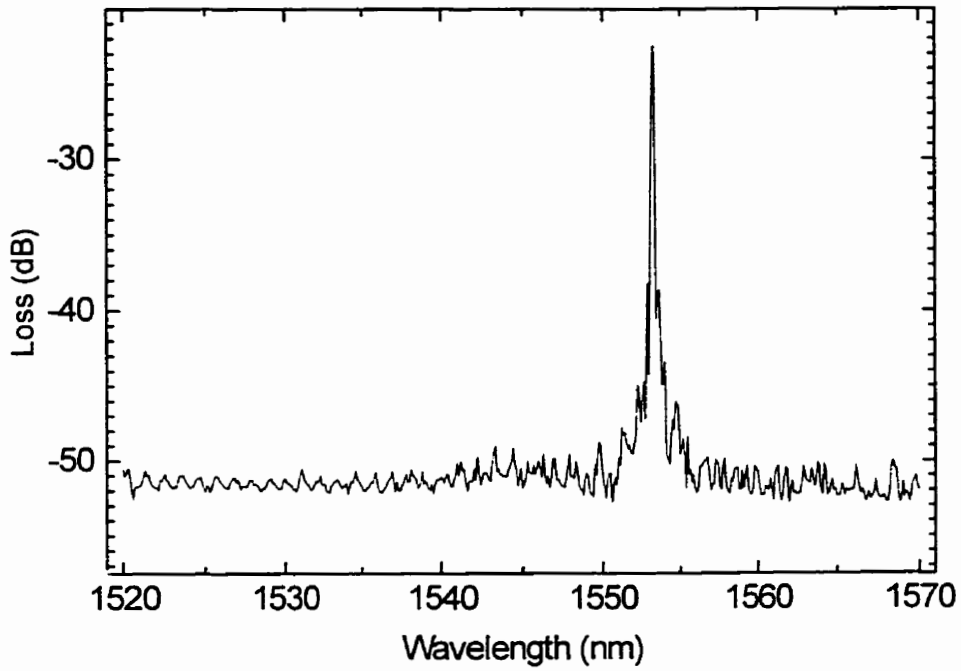

Fig.5.40a Design C

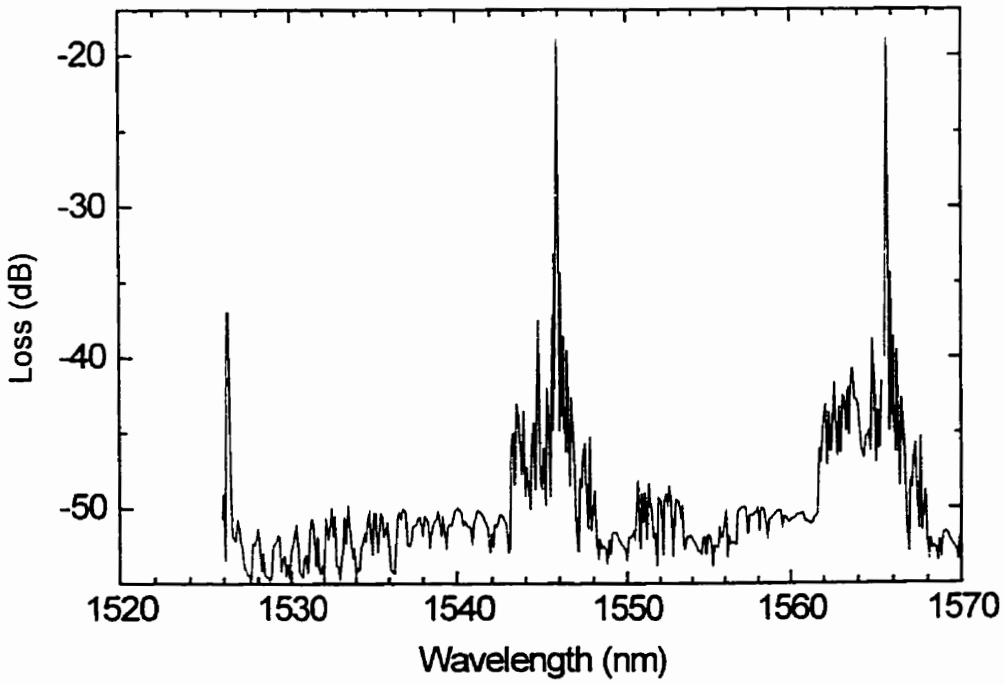

Fig. 5.40b Design A

Fig. 5.40 Noise floor for demultiplexers of design C and design A

from the seventh input waveguide should be 1564.9 + 340×0.0144 = 1569.8 (nm). This corresponds to 75th diffraction order. The center wavelength corresponding to 76th diffraction order is 1569.8×75/76 = 1549.1 (nm). This is very close the second peak in Fig. 5.41. So, peaks in Fig. 5.41 are corresponding to a different diffraction order (76th). When a long range wavelength scanning was performed, as shown in Fig. 5.40, the noise floor can be measured. The noise floor for demultiplexer C was 30 dB below the main peaks. For demultiplexer A, the noise floor was 30 dB below the main peak outside the demultiplexer A, the spectral range is 1555.4 nm to 1565 nm. Fortunately, the light coming out from other input waveguides is outside of our spectral range.

5.3.4 CHANNEL PASSBAND

Typical spectral response for one demultiplexer channel is shown in Fig. 5.42a for design A, (64 channels and 0.144 nm channel spacing), in Fig. 5.42b for design B (64 channels and 0.3 nm channel spacing), in Fig. 5.42c for design C (128 channels and 0.3 nm channel spacing), in Fig. 5.42d for design D (256 channels and 0.2 nm channel spacing) and in Fig. 5.42e for design E (64 channels and 0.6 nm channel spacing). In design A, the FWHM was typically 0.09 nm, which is the highest resolution ever achieved by integrated concave gratings. Fig. 5.43 shows individual channel's FWHM as a function of channel numbers for a demultiplexer of design A, and the average FWHM for all 60 channels is 0.09 nm. For this particular demultiplexer, the last four channels were

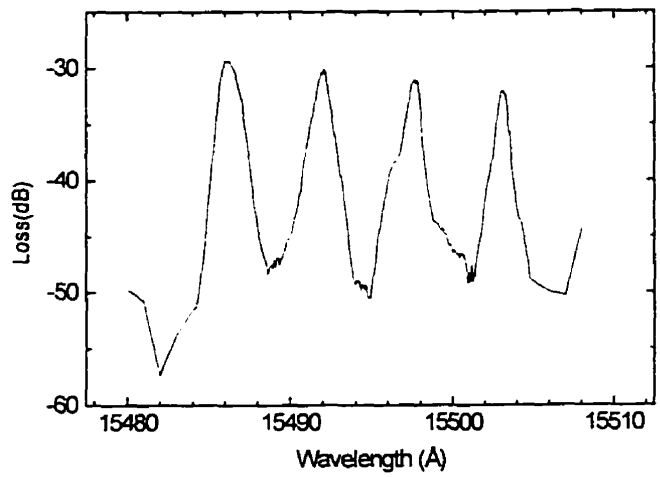

Fig. 5.41 Transmissivity spectra for demultiplexer design A. Light was coupled into the device through no.1 input waveguide, and taken out from no.7 input waveguide

severely damaged, so we reported results from all remaining 60 channels in this thesis. The FWHM for demultiplexer B and demultiplexer C were typically 0.24 nm and 0.18 nm respectively. Although both of the design B and design C had the same channel spacing, the FWHM of design C was much smaller than that of design B. This is because the facet size for design C was only 9.1 μm while the facet size for design B was 18.2 μm. The typical FWHM for design D was 0.8 nm. This design had very high side lobes, as indicated in Fig. 5.42d, and high fiber-to-fiber loss. Fig. 5.42e shows the typical spectral response for design E. The FWHM for this design was 0.37 nm. Table 5.6 summaries the FWHM for each design.

Table 5.6 FWHM for the demultiplexer of designs A, B, C, D, and E

Demultiplexer type	A	B	C	D	E
FWHM (nm)	0.09	0.24	0.18	0.08	0.37

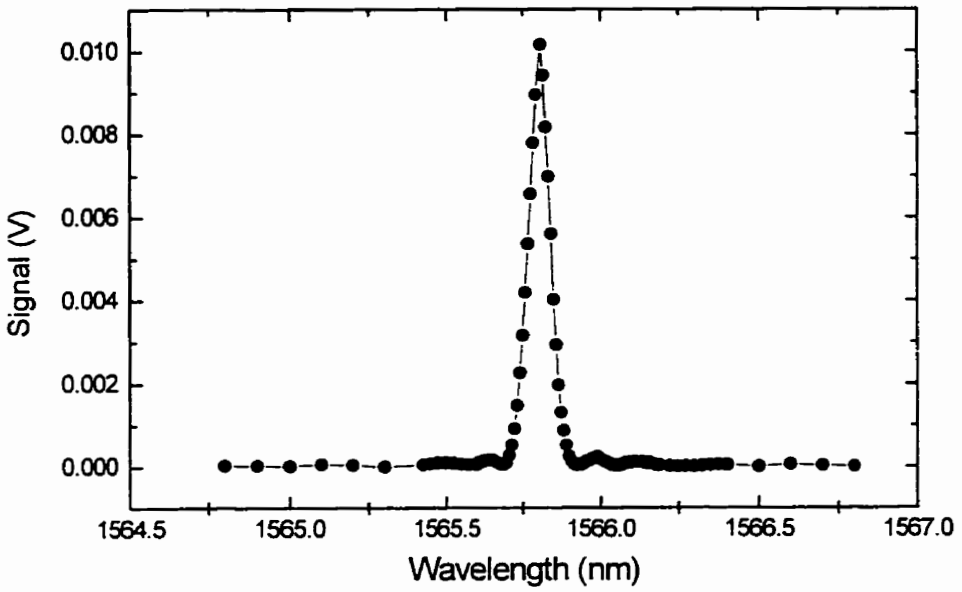

Fig. 5.42a Design A

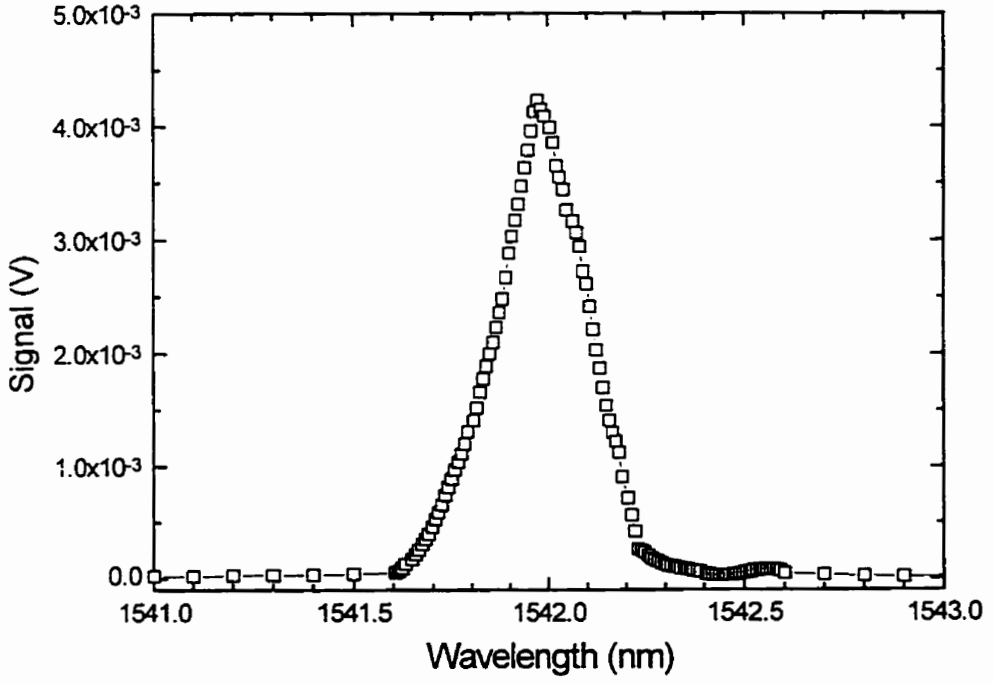

Fig. 5.42b Design B

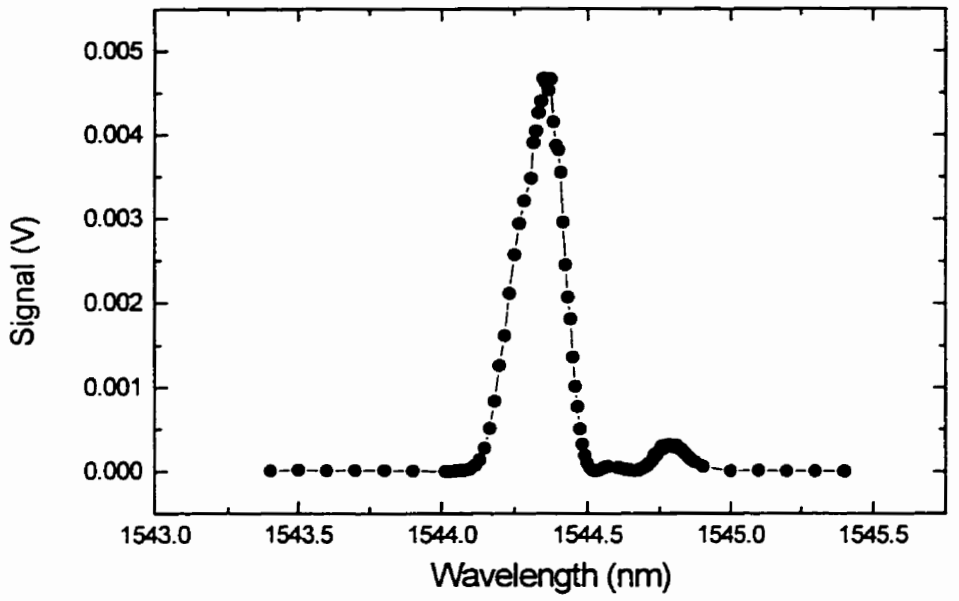

Fig. 5.42c Design C

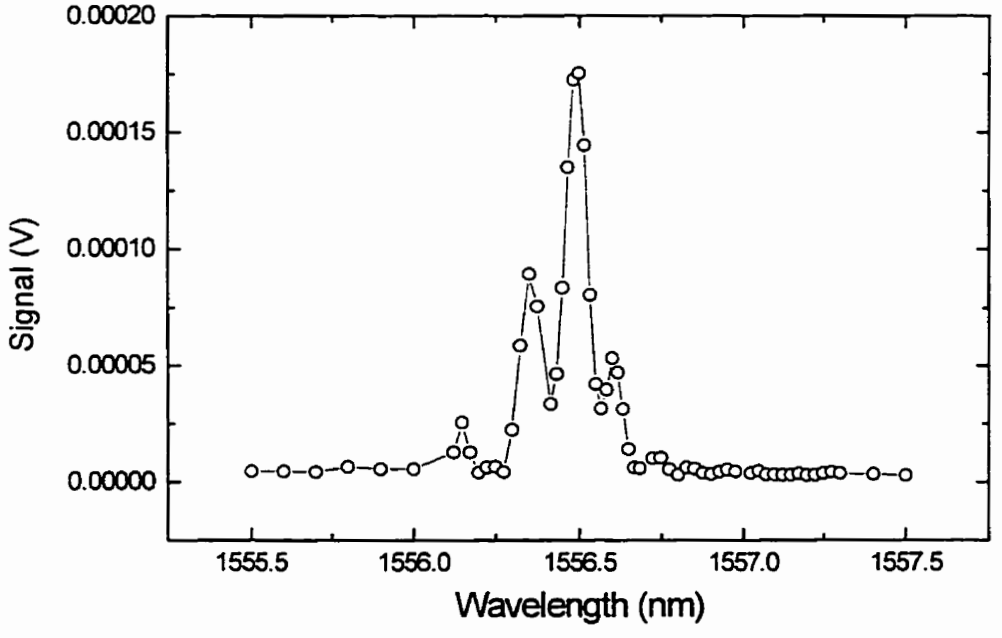

Fig. 5.42d Design D

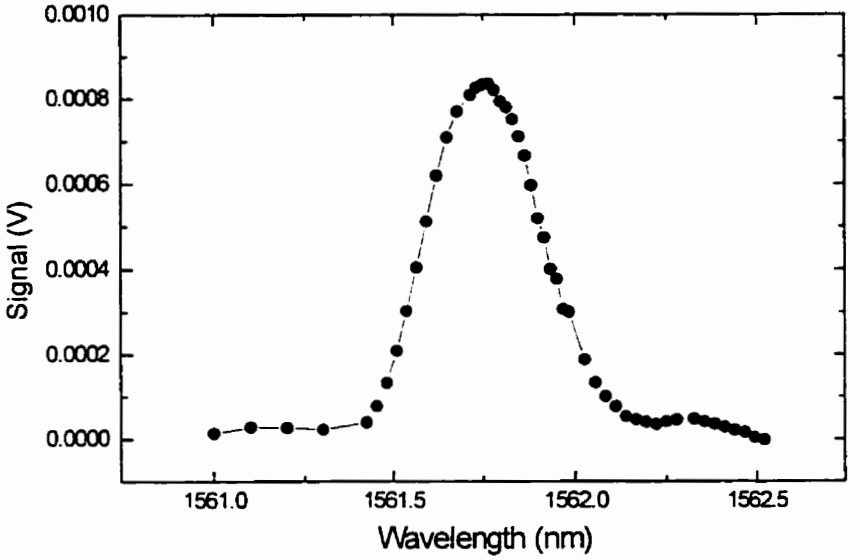

Fig 5.42e Design E

Fig. 5.42 Typical spectral response from one of demultiplexers channels for (a) design A, (b) design B, (c) design C, (d) design D, (e) design E

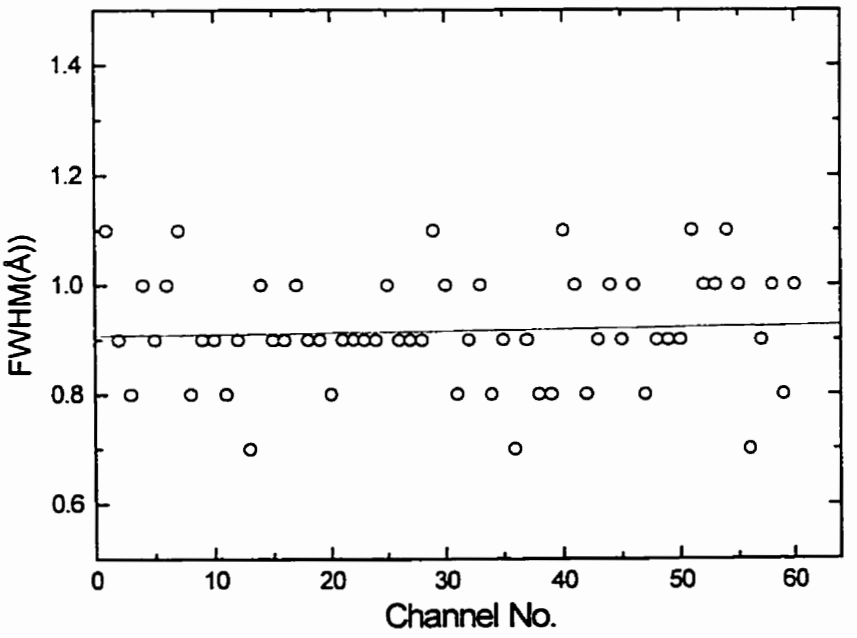

Fig. 5.43 The individual channel's FWHM as a function of channel number for a demultiplexer of Design A

To increase coupling between the device and fiber, index matching fluid was applied between the input waveguide and the single mode fiber, if too much index matching fluid was used, index matching fluid would flow all the way along the sample surface, and this would decrease the channel resolution and increase the channel wavelength, as shown in Fig. 5.44. Since the upper cladding layer was only 0.5 μm thick, index of the slab waveguide was increased when there was a layer of index matching fluid (1.40) over upper cladding layer, thus the center wavelength of the demultiplexer was increased. When sidewalls of an input ridge waveguide were surrounded by index matching fluid, the mode size of the field inside the input waveguide increased. As indicated by our simulations in Fig. 3.16, the FWHM of the output spectral response increased when the mode size of the input field increased.

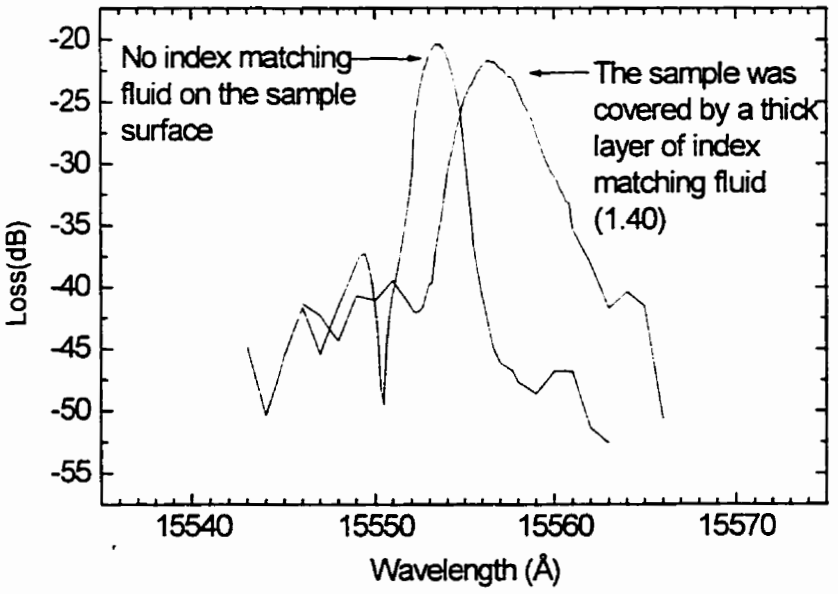

Fig. 5.44 The effect of index matching fluid on the FWHM of a channel of design C

Fig. 5.45 shows the field distributions of the first mode in one of input ridge waveguides (7 μm wide). After the waveguide was covered by index matching fluid (n = 1.40), the field modesize was only increased by about 0.4μm. According to the simulations in Fig. 3.16, the FWHM of the grating will be increased by about a factor of 1.2. But the FWHM of demultiplexer C was found to be increased by a factor of two (see Fig. 5.44) after the device was covered by a thick layer of index matching fluid (n = 1.40). Also, there is no any noticeable difference in FWHM between 7 μm input ridge waveguides and 10 μm input ridge waveguides for all tested demultiplexers. The disagreement between simulation and experiment may come from the fact that there is more than one mode in an input ridge waveguide (both 7 μm and 10 μm), and fields inside ridge waveguides cannot be simply modeled as Gaussian beam.

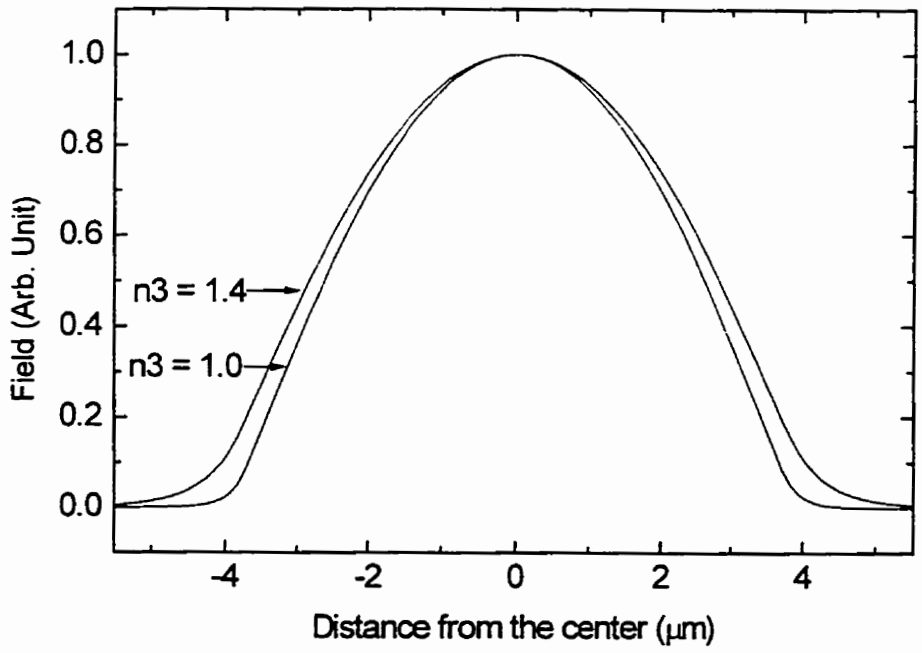

Fig. 5.45 The first mode field distribution for one input waveguide (7 μm wide) along x direction with air (n_3 = 1.0) and index matching fluid (n_3 = 1.4) surrounded the sidewalls of the waveguide

All the spectral responses consisted of a central lobe and several side lobes. Different designs had different levels of side lobes. The side lobes decreased the isolation between channels, and we will talk about this issue shortly. The main lobes were in Gaussian shape. For practical WDM systems, flat and wide band characteristics are required in order to suppress loss variation due to wavelength drift of the light source. To achieve such characteristics, a rectangular optical field has to be generated at a connection point between slab and input or output waveguides. For the demultiplexer based on phased-array waveguides, many kinds of methods as we mentioned in Chapter Two have been proposed. For the demultiplexer based on concave grating, this could be done with the use of some of the methods used for phased-array demultiplexers.

5.3.5 ISOLATION

Isolation is a critical parameter in fiber optic communication systems where the minimum requirement is usually 22 dB. Fig. 5.46 is the ten adjacent channels of a demultiplexer of design C where the channel isolation at a center wavelength is around 18 dB. Fig. 5.47 shows the two adjacent channels for demultiplexer A and the isolation at a center wavelength is only 15 dB. According to simulation result in Fig. 3.12, the channel isolation at the center wavelength was higher than 65 dB. For both of the demultiplexers, low isolation is due to high side lobes. To increase isolation, side lobes have to be suppressed. Fig. 5.48a-e shows typical transmission loss versus wavelength for one channel of demultiplexer of design A (Fig. 5.48a), design B (Fig. 5.48b), design C (Fig. 5.48c), design D (Fig. 5.48d) and design E (Fig.5.48e). The five demultiplexers shown in

Fig. 5.48 came from the same wafer, which means they should have the same sidewalls (89.4°) and same waveguide loss. For an unknown reason, losses for design A, design B, design C and Design E were around 20 dB for the channel with short waveguides, and above 38 dB for Design D. It seems that from this figure, the higher the channel resolution, the higher the levels of side lobes are. For design E which had the lowest channel resolution (FWHM = 0.37 nm), the side lobes were very low. Design D, which had the highest channel resolution (FWHM = 0.08 nm), had very high side lobes. The side lobes for design B were much smaller than those of design C although they had the same channel spacing. There are two possible sources, which cause side lobes as indicated in Fig. 5.49. One possible source is: light from the grating hits boundaries between two adjacent output waveguides, and the scattering light enters the output waveguide under test. The other possible source is: light from adjacent output waveguides enters the testing output waveguide by coupling. The latter was verified by a separate experiment. When there was no index matching fluid between pick-up fiber and output waveguide, the first side lobes were 18 dB below the main lobe, see Fig. 5.50a. But after index matching fluid was applied between pick-up fiber and output waveguide, the side lobes were only 9 dB below the main lobes as we can see from Fig. 5.50b. This can be explained as follows: the index matching fluid flowed along output waveguides and filled the gap between output waveguides, thus greatly increased the coupling between output waveguides. By slightly increasing the separation between output waveguides, side lobes might be greatly suppressed.

5.3.6 TEMPERATURE DEPENDENCE

Temperature stability is another concern for fiber optic communications systems. To test the temperature dependence of a demultiplexer, the device was put onto the surface of a resistive heater. First, the spectral response from a channel of a demultiplexer at room temperature was recorded (Fig. 5.51), then the sample was heated to 23°C above the room temperature. The spectral response for the same channel as before was recorded (Fig. 5.51). When the temperature of the sample was increased by 23°C, the channel center wavelength was decreased by 0.52 nm as shown in Fig. 5.51. So, the temperature dependence of the dispersion was 0.023 nm/°C. A temperature controller is needed for practical application. An interesting thing that worth noting is that after heating, the fiber to fiber insertion loss was decreased by 3 to 6 dB. There might have some water on the surface of facets, which caused extra losses. After heating, water was evaporated, and the insertion loss of demultiplexers was decreased.

5.4 CONCLUSIONS

In a wafer with 89.4° sidewalls, demultiplexers with design A, design B, design C, design D and design E were thoroughly characterized in this chapter. Demultiplexer of design A had a channel spacing of 0.144 nm which is about one order of magnitude smaller than that of any integrated concave grating that have been previously reported. Demultiplexer of design C had 120 working channels. This kind of demultiplexer may This kind of

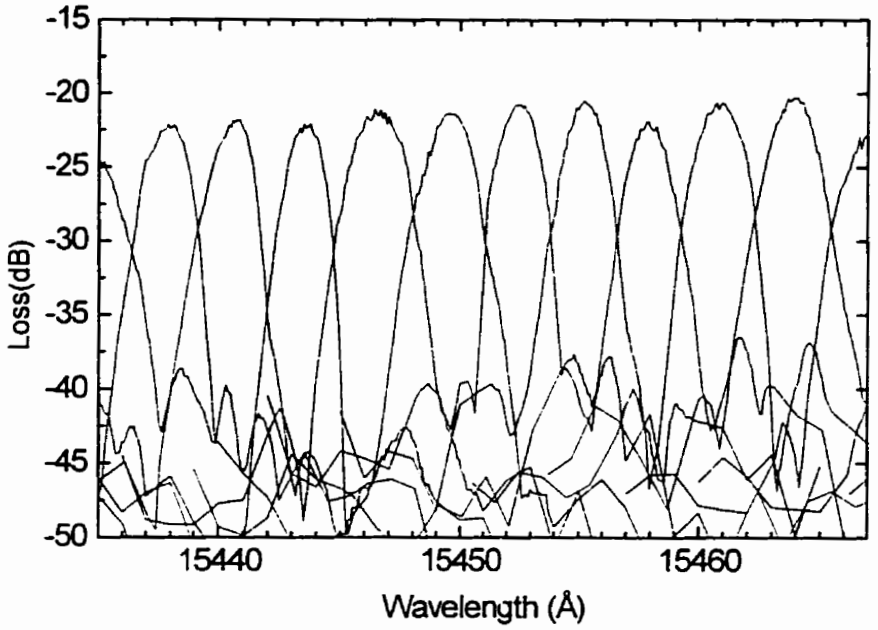

Fig. 5.46 Cross talk is illustrated by the overlapping of the spectral response of ten adjacent channels for a demultiplexer of design C

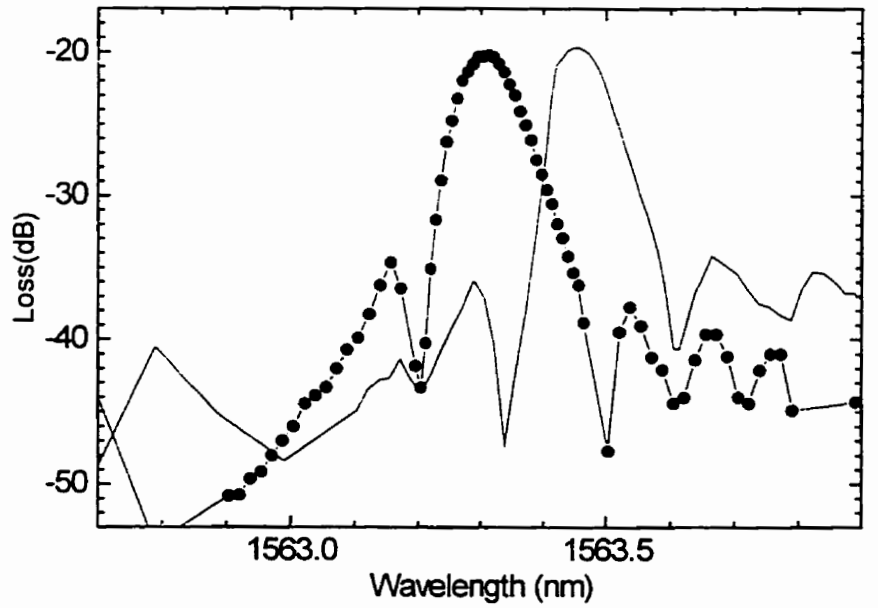

Fig. 5.47 Cross talk is illustrated by the overlapping of the spectral response of two adjacent channels for a demultiplexer of design A

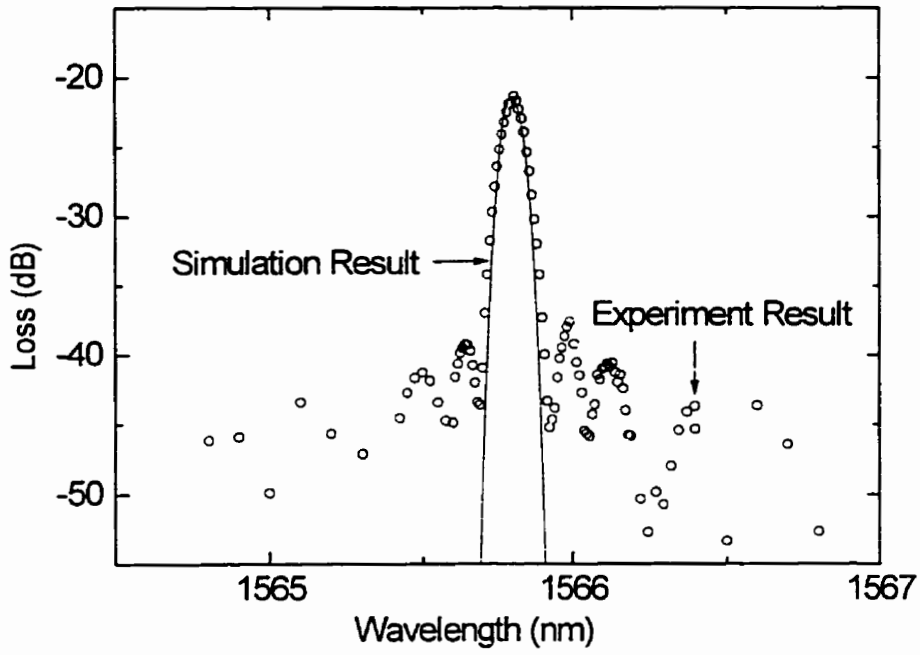

Fig 5.48a Design A

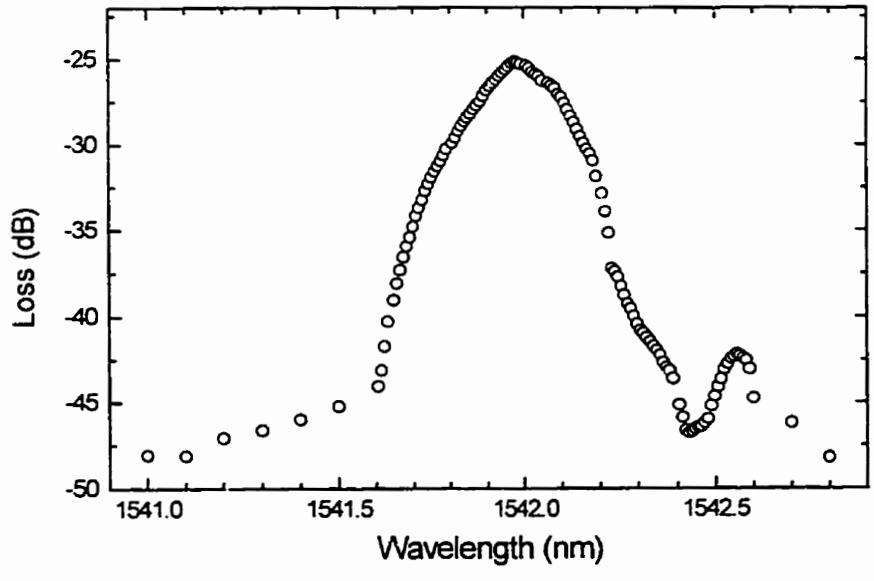

Fig. 5.48b Design B

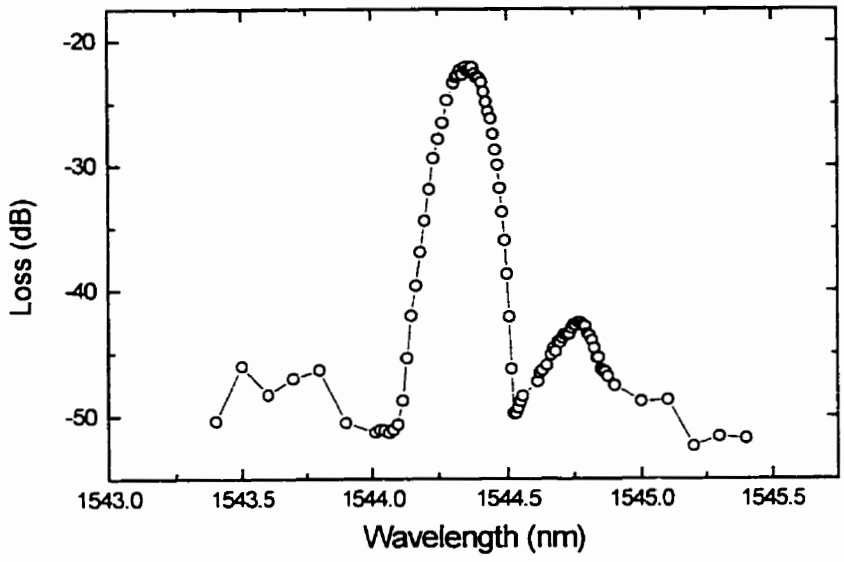

Fig 5.48c Design C

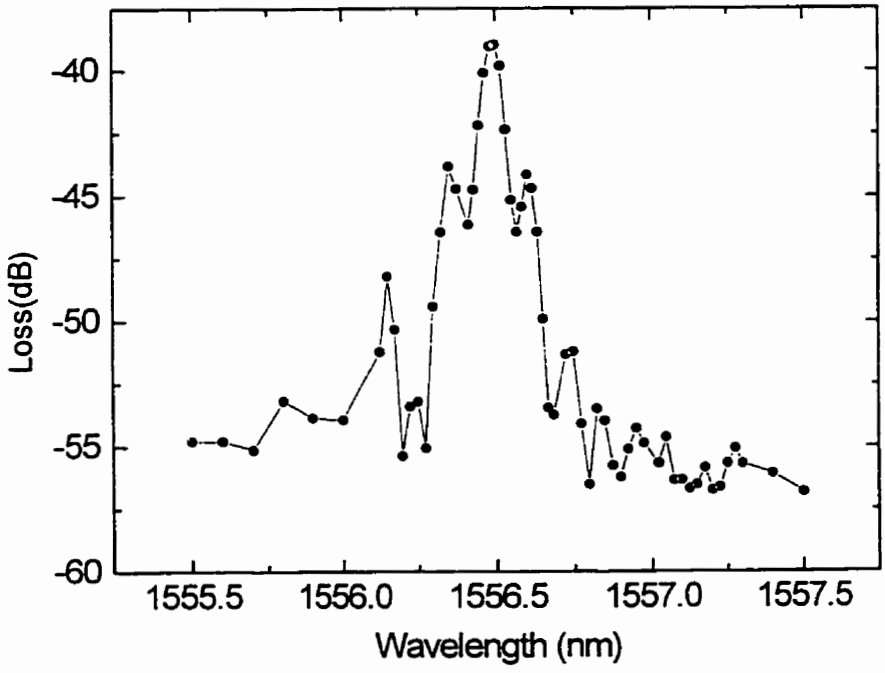

Fig. 5.48d Design D

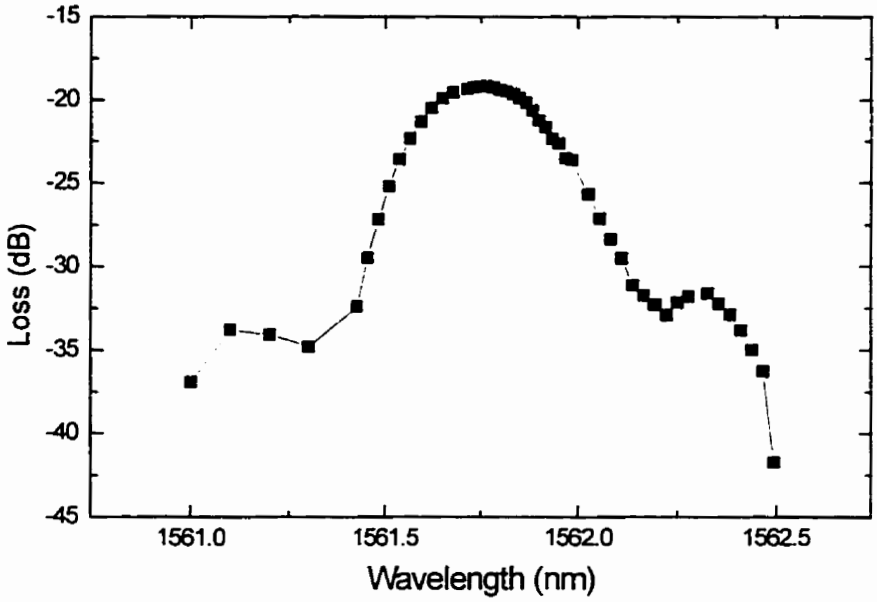

Fig. 5.48e Design E

Fig. 5.48 Detail of the spectral response shows side lobes in addition to the central lobe. Data is shown here for one channel of demultiplexer of (a) design A, (b) design B, (c) design C, (d) design D and (e) design E

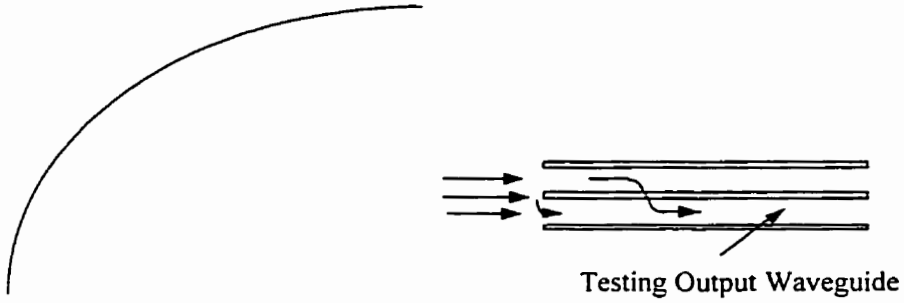

Fig. 5.49 As shown, coupling between channels may produce side lobe in the spectral response

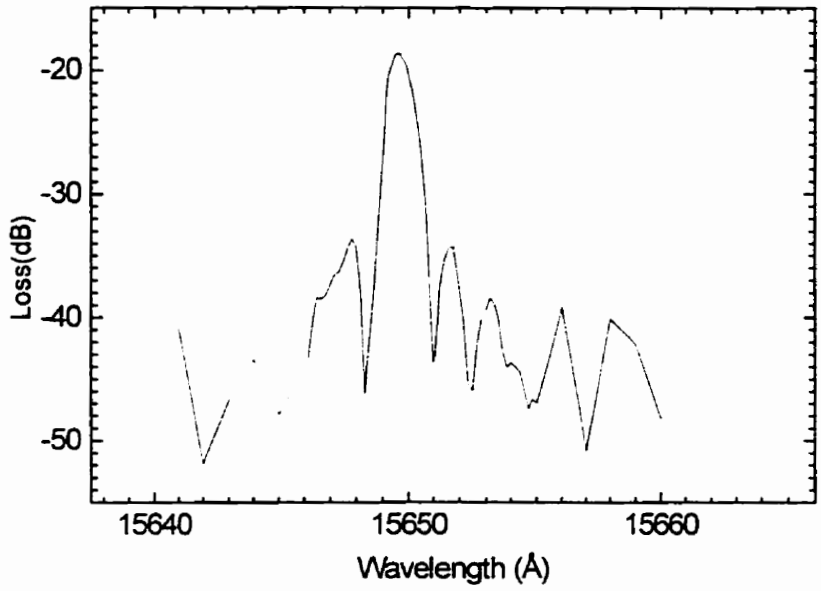

(a)

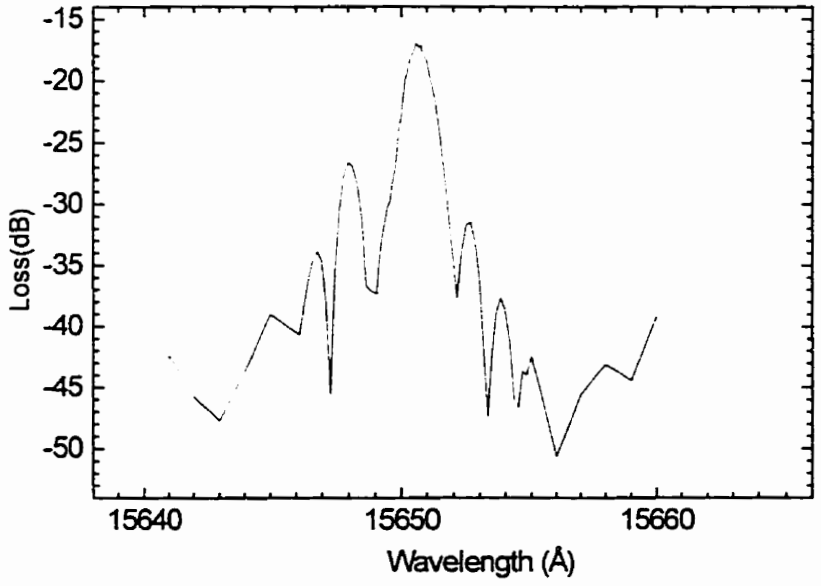

(b)

Fig. 5.50 The levels of side lobes (a) without (b) with index matching fluid (1.40)

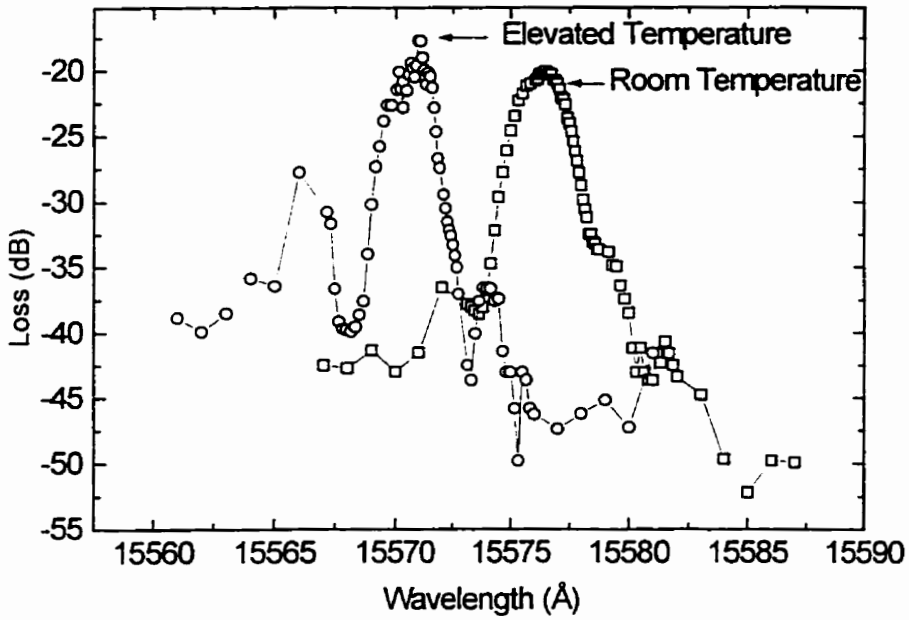

Fig. 5.51 Temperature dependence of central wavelength for a demultiplexer of design C. The sample was heated to 23° higher than room temperature

demultiplexer may find wide application in future fiber optic communications. Demultiplexer of design E had 0.6 nm channel spacing and small side lobes. In this wafer, demultiplexers of design A, B, C, E all had a loss of about 20 dB, but demultiplexer of design D has a loss of 38 dB and very high channel spacing side lobes. Waveguide absorption loss was the main contribution to the high insertion loss of demultiplexer and it will be greatly reduced by annealing.

Demultiplexers studied in this chapter may find applications in integrated spectrometer and WDM fiber optic communication systems. For integrated spectrometer application, the noise floor, side lobes and PDL of the present demultiplexer needs to be further improved. For WDM applications, the insertion loss, PDD, and the shape of channel passband needs to be further improved; the channel spacing are needed to be

designed according to ITU standard. In chapter six, a layer structure is investigated to reduce PDD while other issues remain for the future work.

CHAPTER SIX

BIREFRINGENCE CONTROL WITH LAYER STRUCTURES

As we mentioned in chapter five, many approaches have been used to successfully control birefringence, and among them, interposing a high refractive index layer between cladding and core invented by Aarnio et al. (1991) may be one of easiest ways. However, there is no report about how to calculate the thickness of high refractive index layer. In this chapter, the theory to calculate the thickness of high refractive layer is illustrated. The calculated results by using this theory are compared with published results. Based on preliminary experimental data, layer structures used to cancel birefringence was designed and fabricated.

6.1 THEORY TO CALCULATE THE THICKNESS OF HIGH REFRACTIVE INDEX LAYER

Fig. 6.1 is a slab waveguide and its coordinate system, which we will use throughout this

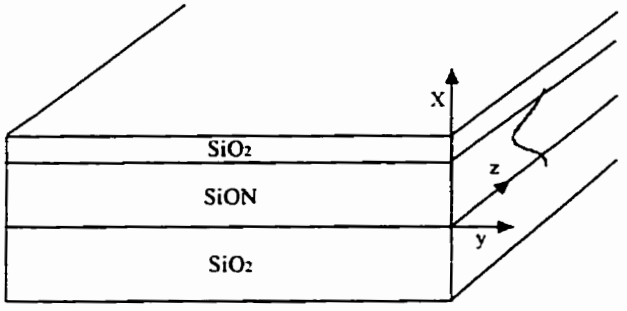

Fig. 6.1 Typical geometry used in this chapter. The refractive index varies along the x axis, y is a perpendicular axis, and z is the direction of propagation of light

chapter. For a monochromatic wave, we can write Maxwell's equation in the form

$$\nabla \times \mathbf{E}(\mathbf{r}) = i\omega\mu_0 \mathbf{H}(\mathbf{r}) \qquad \text{(a)}$$

$$\nabla \times \mathbf{H}(\mathbf{r}) = -i\omega\varepsilon \mathbf{E}(\mathbf{r}) \qquad \text{(b)}$$

$$\nabla \cdot (\varepsilon \mathbf{E}(\mathbf{r})) = 0 \qquad \text{(c)}$$

$$\nabla \cdot \mathbf{H}(\mathbf{r}) = 0 \qquad \text{(d)} \qquad (6.1)$$

In anticipation of assuming a definite propagation direction (z) that will break off vector symmetries, we write out the two curl equation (6.1a) and (6.1b) explicitly, to obtain

$$\begin{aligned}
\frac{\partial E_z}{\partial y} - \frac{\partial E_y}{\partial z} &= i\omega\mu_0 H_x \\
\frac{\partial E_x}{\partial z} - \frac{\partial E_z}{\partial x} &= i\omega\mu_0 H_y \\
\frac{\partial E_y}{\partial x} - \frac{\partial E_x}{\partial y} &= i\omega\mu_0 H_z \\
\frac{\partial H_z}{\partial y} - \frac{\partial H_y}{\partial z} &= -i\omega\varepsilon E_x \\
\frac{\partial H_x}{\partial z} - \frac{\partial H_z}{\partial x} &= -i\omega\varepsilon E_y \\
\frac{\partial H_y}{\partial x} - \frac{\partial H_x}{\partial y} &= -i\omega\varepsilon E_z
\end{aligned} \tag{6.2}$$

It is obvious that in the absence of other symmetries, (6.2) is a hopelessly coupled system. For example, H_x will drive E_z and E_y, while E_z drives both H_x and H_y, and E_y drives both H_x and H_z, where H_z in turn drives E_x. All the field components are therefore coupled. Clearly more simplification is necessary before one can make any general statements about the system of (6.2). Since we are looking for modal solutions of (6.2) with z directed propagation, an additional simplification is indeed available. For an electromagnetic disturbance to be a mode, it must retain its shape when being propagated forward. That is to say that the transverse dependence of the field cannot change, and the only effect of a translation along the propagation is to multiply the function by a phase factor. As the medium under consideration must not change along the propagation direction if there are to be modes, then it makes no difference where we start our translation. It is therefore clear that the phase function must be linear in the translation distance, and therefore one could write

$$\mathbf{E}(\mathbf{r}) = \mathbf{E}(x,y,z) = \mathbf{E}(x,y)e^{i\beta z}$$

$$\mathbf{H}(\mathbf{r}) = \mathbf{H}(x,y,z) = \mathbf{H}(x,y)e^{i\beta z} \tag{6.3}$$

giving

$$\mathbf{E}(\mathbf{r},t) = \mathbf{E}(x,y,z) = \mathrm{Re}[\mathbf{E}(x,y)e^{i\beta z}\, e^{-i\omega t}]$$

$$\mathbf{H}(\mathbf{r},t) = \mathbf{H}(x,y,z) = \mathrm{Re}[\mathbf{H}(x,y)e^{i\beta z}\, e^{-i\omega t}] \tag{6.4}$$

If the functions $\mathbf{E}(x,y)$ and $\mathbf{H}(x,y)$ can be chosen to be real (as we shall soon see they can in a lossless, slablike medium), then equation (6.4) indicates that the mode shapes E(x,y) and H(x,y) propagate forward like plane waves with flat fronts, and therefore, from the tracing of the ray paths, one can say that all the energy is propagated directly down the z axis.

Using (6.3) and (6.2), one immediately finds the system of equations (Marcuse 1982)

$$\begin{aligned}
&\frac{\partial E_z}{\partial y} - i\beta E_y = i\omega\mu_0 H_x \\
&i\beta E_x - \frac{\partial E_z}{\partial x} = i\omega\mu_0 H_y \\
&\frac{\partial E_y}{\partial x} - \frac{\partial E_x}{\partial y} = i\omega\mu_0 H_z \\
&\frac{\partial H_z}{\partial y} - i\beta H_y = -i\omega\varepsilon E_x \\
&i\beta H_x - \frac{\partial H_z}{\partial x} = -i\omega\varepsilon E_y \\
&\frac{\partial H_y}{\partial x} - \frac{\partial H_x}{\partial y} = -i\omega\varepsilon E_z
\end{aligned} \tag{6.5}$$

In slab waveguide, we can assume that there was no y variation in the problem. So, the modes of this structure must be of infinite extent in the y dimension. For such a case, we can assume that the y derivative must always be zero. Using this assumption in equation (6.5), one immediately finds that the system of (6.5) decomposes into two systems of three equations each, which can be written in the form (Mickelson 1992, Chapter 2)

$$\begin{aligned} \frac{\partial H_z}{\partial x} &= i\beta H_x + i\omega\varepsilon E_y \\ i\omega\mu_0 H_x &= -i\beta E_y \\ \frac{\partial E_y}{\partial x} &= i\omega\mu_0 H_z \end{aligned} \tag{6.6}$$

and

$$\begin{aligned} \frac{\partial E_z}{\partial x} &= i\beta E_x - i\omega\mu_0 H_y \\ -i\omega\varepsilon E_x &= -i\beta H_y \\ \frac{\partial H_y}{\partial x} &= -i\omega\varepsilon E_z \end{aligned} \tag{6.7}$$

The structures of these two field systems are sketched in Fig. 6.2. There it was noticed that the plane structure discussed gave rise to two natural polarization states, one with always transverse E-field (TE) and one with an always transverse H-field (TM).

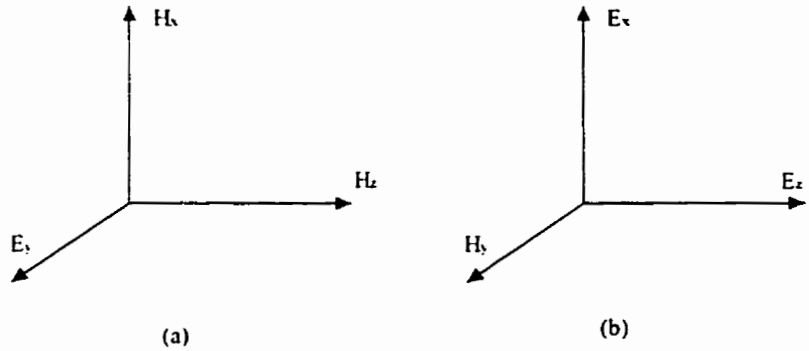

Fig. 6.2 Field configuration for (a) TE (b) TM mode

When one considers an abrupt interface, one knows that the tangential fields will be continuous across the interface. Using this boundary condition, we can further simplify equation (6.6) and (6.7) as

$$\frac{\partial^2 E_y}{\partial^2 x} + (k^2 - \beta^2) E_y = 0 \tag{6.8}$$

subject to boundary conditions

$$E_y, \frac{\partial E_y}{\partial x} \text{ are continuous}$$

$$\frac{\partial^2 H_y}{\partial^2 x} + (k^2 - \beta^2) H_y = 0 \tag{6.9}$$

with

$$H_y, \frac{1}{\varepsilon}\frac{\partial H_y}{\partial x} \text{ continuous}$$

where $k = \lambda/2\pi$, and λ is the wavelength in the medium.

We will use equation (6.8) to find the propagation constant β for TE mode in a slab waveguide where a layer of high refractive index is interposed between cladding and core. After the β is found, the effective index for TE mode is calculated by

$$N_{TE} = \frac{\beta}{k_0} \tag{6.10}$$

Fig. 6.3 shows three configurations that may be used to interpose a high refractive index layer into a slab waveguide. We will illustrate how to find waveguide birefringence for the first case. Waveguide birefringence for the rest configurations can be found by following the same procedure. In all cases we assumed that the top and bottom cladding thickness was infinite.

Fig. 6.4 shows layer structure and the coordinate system we will use to do calculation.

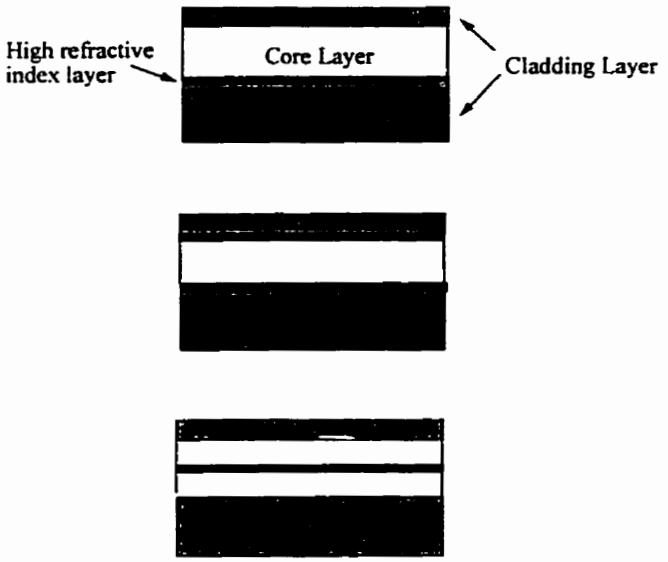

Fig. 6.3 Layer structures to cancel birefringence

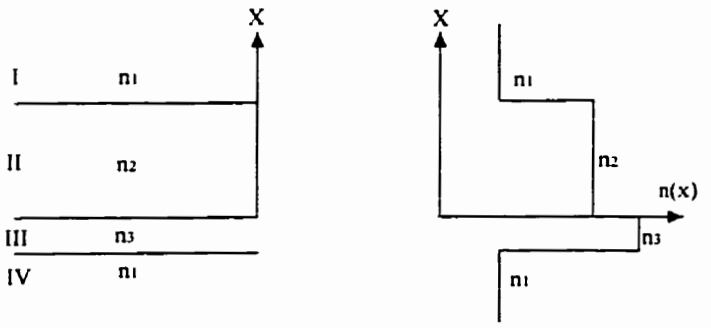

Fig. 6.4 The coordinate system used to do calculations

The TE modes of the slab waveguide must satisfy Equation (6.8) in each region and at the two boundary interfaces, must satisfy both conditions of (6.8). Now for a mode to be guided, it must have a finite percentage of its energy propagating within region II and III of the structure of Fig. 6.4. Now as the solutions to the equations

$$\frac{\partial^2 \phi}{\partial^2 x} + \zeta \phi = 0 \tag{6.11}$$

are of the form

$$\phi(x) = A\cos\sqrt{\zeta}x + B\sin\sqrt{\zeta}x \quad , \zeta>0 \text{ (a)}$$

$$\phi(x) = Ae^{\sqrt{|\zeta|}x} + Be^{-\sqrt{|\zeta|}x} \quad , \zeta<0 \text{ (b)} \tag{6.12}$$

One can determine the solution to (6.8) throughout space by just applying the boundary conditions and the condition for a mode to be guided, as was stated above. The argument is as follows: As the mode fields we wish to find must be in some manner normalized in order to carry finite power in region 2 and 3, they must be of finite transverse extent in x. In order to satisfy this requirement, we see that the solutions in regions I and IV must be of the form:

$$\phi_i(x) = A_i e^{\kappa_i x} + B_i e^{-\kappa_i x} \tag{6.13}$$

where i = 1,4, A_i and B_i are constant to be determined from the finiteness and continuity conditions of (6.8), and

$$\kappa_i = \sqrt{\beta^2 - k_i^2} \quad \text{(a)}$$

$$k_i^2 = k_0 n_i^2 = \frac{2\pi}{\lambda} n_i^2 \quad \text{(b)} \tag{6.14}$$

Clearly, the condition of finiteness in region I and III will also require that $A_1 = B_4 = 0$. The continuity conditions are also going to require that the solution in region II and III be of the form

$$\phi_i(x) = A_i \cos\gamma_i x + B_i \sin\gamma_i x \tag{6.15}$$

where i = 2,3, and γ_i defined by

$$\gamma_i = \sqrt{k_i^2 - \beta^2} \tag{6.16}$$

The conditions of (6.8) will yield six equations. These equations are expressible in the form

$$A_1 e^{\kappa_1 x_{12}} + B_1 e^{-\kappa_1 x_{12}} = A_2 \cos\gamma_2 x_{12} + B_2 \sin\gamma_2 x_{12}$$

$$\kappa_1 A_1 e^{\kappa_1 x_{12}} - \kappa_1 B_1 e^{-\kappa_1 x_{12}} = -\gamma_2 A_2 \sin\gamma_2 x_{12} + \gamma_2 B_2 \cos\gamma_2 x_{12}$$

$$A_2 = A_3$$

$$\gamma_2 B_2 = \gamma_3 B_3$$

$$A_3 \cos\gamma_3 x_{34} + B_3 \sin\gamma_3 x_{34} = A_4 e^{\kappa_4 x_{34}} + B_4 e^{-\kappa_4 x_{34}}$$

$$-A_3\gamma_3 \sin\gamma_3 x_{34} + B_3\gamma_3 \cos\gamma_3 x_{34} = \kappa_4 A_4 e^{\kappa_4 x_{34}} - \kappa_4 B_4 e^{-\kappa_4 x_{34}} \tag{6.17}$$

where x_{12} is the coordinate of the interface between regions I and II, and in Fig. 6.4 we can see that $x_{12} = t$ is the thickness of the slab waveguide. $x_{23} = 0$, and x_{34} is the coordinate of the interface between regions III and IV, $-x_{34} = d$ is the thickness of high refractive index layer. Clearly, A_1 and B_4 could have been set to zero in (6.17) but have been left in for the moment, for a reason we shall soon see.

One can attempt to manipulate Equations (6.17) directly to obtain the dispersion relation (equation for determining β) and the one-parameter string which will define $B_1, A_2, B_2, A_3, B_3, A_4$. The two sets of boundary conditions of equation (6.17) can be written as matrix equations. Defining the follow matrices

$$\mathbf{R}_1 = \begin{pmatrix} e^{\kappa_1 t} & e^{-\kappa_1 t} \\ \frac{\kappa_1}{k_0} e^{\kappa_1 t} & -\frac{\kappa_1}{k_0} e^{-\kappa_1 t} \end{pmatrix} \qquad \mathbf{L}_2 = \begin{pmatrix} \cos\gamma_2 t & \sin\gamma_2 t \\ -\frac{\gamma_2}{k_0}\sin\gamma_2 t & \frac{\gamma_2}{k_0}\cos\gamma_2 t \end{pmatrix}$$

$$\mathbf{R}_2 = \begin{pmatrix} 1 & 0 \\ 0 & \gamma_2 \end{pmatrix} \qquad \mathbf{L}_3 = \begin{pmatrix} 1 & 0 \\ 0 & \gamma_3 \end{pmatrix}$$

$$\mathbf{R}_3 = \begin{pmatrix} \cos\gamma_3 d & -\sin\gamma_3 d \\ \dfrac{\gamma_3}{k_0}\sin\gamma_3 d & \dfrac{\gamma_3}{k_0}\cos\gamma_3 d \end{pmatrix} \qquad \mathbf{L}_4 = \begin{pmatrix} e^{-\kappa_4 d} & e^{\kappa_4 d} \\ \dfrac{\kappa_4}{k_0}e^{-\kappa_4 d} & -\dfrac{\kappa_4}{k_0}e^{\kappa_4 d} \end{pmatrix} \tag{6.18}$$

where $\mathbf{R}_i(\mathbf{L}_i)$ denotes the matrix for the right(left)-hand side of the *i*th medium, and the vectors

$$\mathbf{V}_i = \begin{pmatrix} A_i \\ B_i \end{pmatrix} \tag{6.19}$$

According to Mickelson (1993), one can express Equations (6.17) in the form

$$\begin{aligned} \mathbf{R}_1\mathbf{V}_1 &= \mathbf{L}_2\mathbf{V}_2 \\ \mathbf{R}_2\mathbf{V}_2 &= \mathbf{L}_3\mathbf{V}_3 \\ \mathbf{R}_3\mathbf{V}_3 &= \mathbf{L}_4\mathbf{V}_4 \end{aligned} \tag{6.20}$$

From Equations (6.20), one can write that

$$\begin{aligned} \mathbf{V}_1 &= \mathbf{R}_1^{-1}\mathbf{L}_2\mathbf{V}_2 \\ \mathbf{V}_2 &= \mathbf{R}_2^{-1}\mathbf{L}_3\mathbf{V}_3 \\ \mathbf{V}_3 &= \mathbf{R}_3^{-1}\mathbf{L}_4\mathbf{V}_4 \end{aligned} \tag{6.21}$$

to obtain

$$\mathbf{V}_1 = \mathbf{R}_1^{-1}\mathbf{L}_2\mathbf{R}_2^{-1}\mathbf{L}_3\mathbf{R}_3^{-1}\mathbf{L}_4\mathbf{V}_4 = \mathbf{T}\mathbf{V}_4 \tag{6.22}$$

Where Equation (6.22) should serve as a definition equation for the transmission matrix **T**. Writing out (6.22) in explicit detail, one finds that

$$\begin{pmatrix} A_1 \\ B_1 \end{pmatrix} = \begin{pmatrix} T_{11} & T_{12} \\ T_{21} & T_{22} \end{pmatrix} \begin{pmatrix} A_4 \\ B_4 \end{pmatrix} \tag{6.23}$$

From the finiteness condition that $A_1 = B_4 = 0$, it becomes immediately obvious that the dispersion relation (between β and k_0) becomes

$$T_{11} = 0 \tag{6.24}$$

and that, following solution of (6.24) for β, the required β value back substituted into (6.18) and then A_2, B_2, A_3, B_3, and A_4 expressed in terms of B_1 through the use of (6.21). The effective index as well as modefield distribution for TE mode is thus found.

Using Equation (6.9) and its boundary conditions, and following the above procedure again one will find the effective index and modefield distribution for TM mode. The difference between N_{TE} and N_{TM} is the waveguide birefringence after the high refractive index layer is introduced.

6.2 THE CONSISTENCY OF OUR CALCULATED RESULTS WITH PUBLISHED RESULTS

The first layer structure shown in Fig. 6.3 was first studied. With waveguide thickness t = 5 μm, core layer refractive index n_2 = 1.457, cladding layer refractive index n_1 = 1.45, and high refractive index layer n_3 = 1.97, waveguide birefringence as a function of thickness of high refractive index layer was calculated as in Fig. 6.5. The parameters used here are the exactly the same as those used by Aarnio (1991). The simulation result is consistent with the results calculated by Aarnio. From our calculations, we see that after interposing a 20 nm Si_3N_4 (n = 1.97) layer between core and cladding, the waveguide birefringence will be increased by about 1×10^{-3} which is enough to cancel stress birefringence. Fig. 6.6 shows fundamental mode field distributions in the slab waveguide.

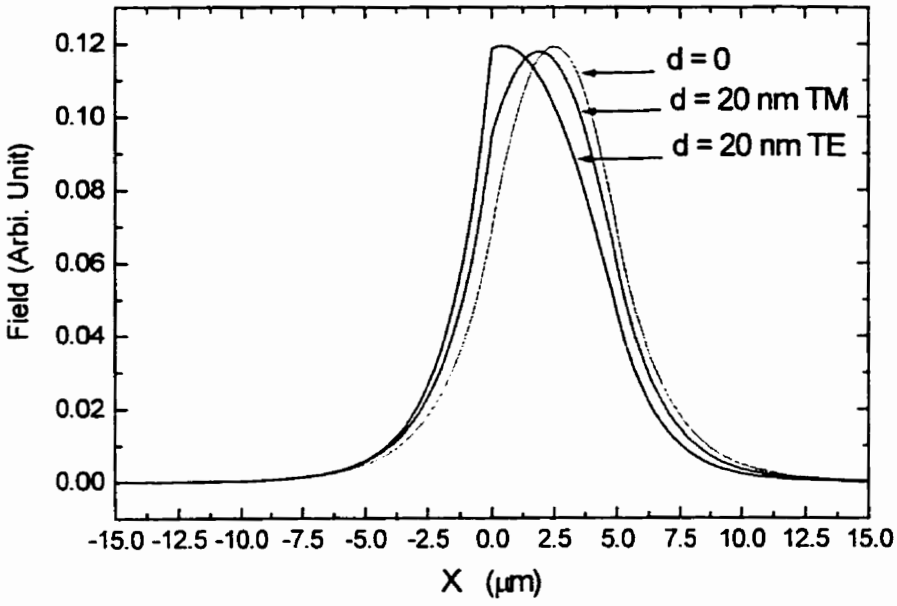

Fig. 6.6 Fundamental modefield distributions inside a slab waveguide with 20 nm Si_3N_4 layer between core and lower cladding; The Field coordinate is for the electric field for TE mode in y axis direction, and the magnetic field for TM mode in y axis. When d = 0, the field distributions for both TE and TM modes are the same.

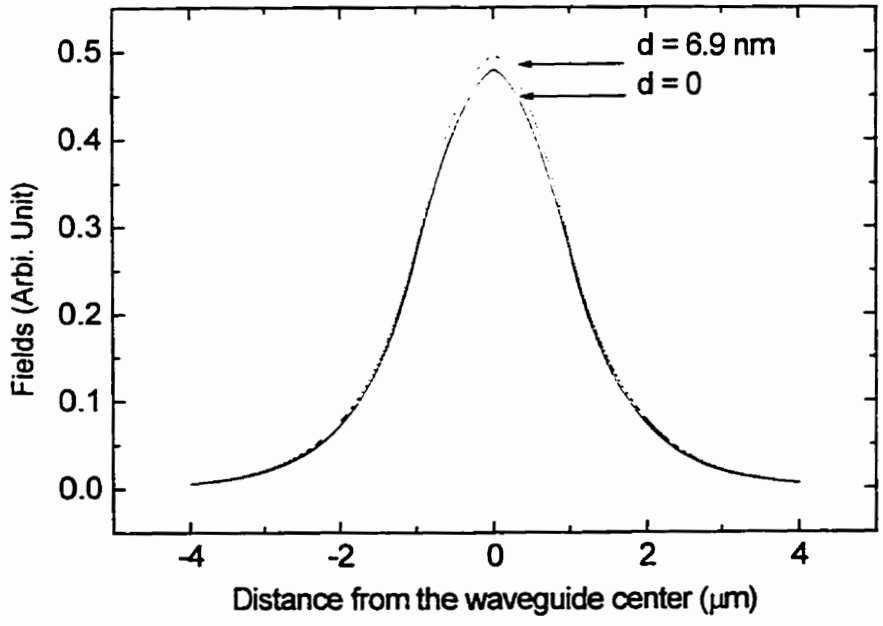

Fig. 6.7 Fundamental modefield distributions in a slab waveguide with high refractive index layer $n_3 = 1.97$ at the center of the core

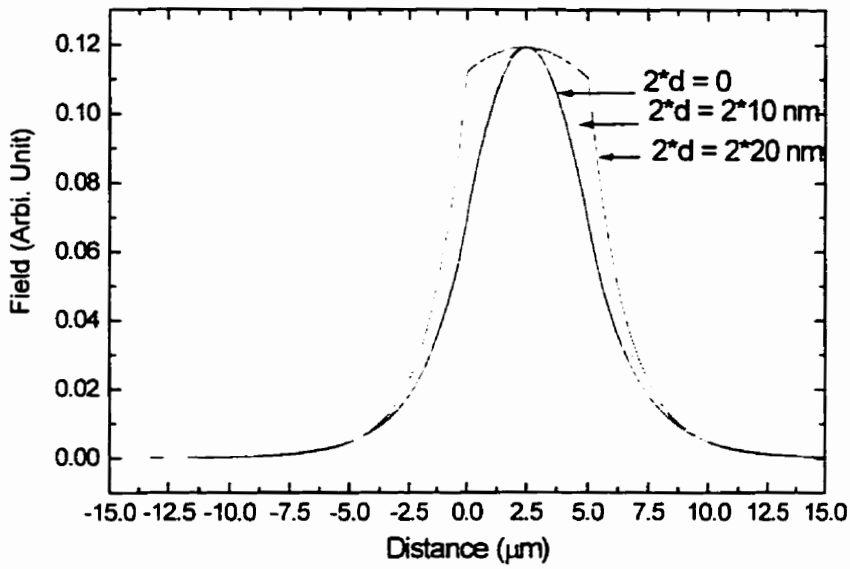

Fig. 6.8 Fundamental modefield distribution in a slab waveguide with two high refractive index layers on both sides of core. The Field coordinate is for the electric field for TE mode in y axis direction, and the magnetic field for TM mode in y axis. When d = 0, the field distributions for both TE and TM modes are the same.

6.3 BIREFRINGENCE CONTROL FOR OUR DEMULTIPLEXERS

Fig. 6.9 indicates that our total birefringence is $B_{total} = 1.06\times10^{-3}$, thus our objective should be to decrease the waveguide birefringence B_{wg} by 1.06×10^{-3}. Unfortunately, a sign error was made and our chosen objective was to increase B_{wg} by 1.06×10^{-3} to 1.8×10^{-3}. According to the calculation method described in section 6.1, this second objective could be met by introducing a thin, high index core layer with an index and thickness chosen from any point on the curve shown in Fig. 6.10.

Fig. 6.11 shows birefringence for the fabricated layer structure. The fact that the total birefringence increased rather than decreased was due to the sign error described in

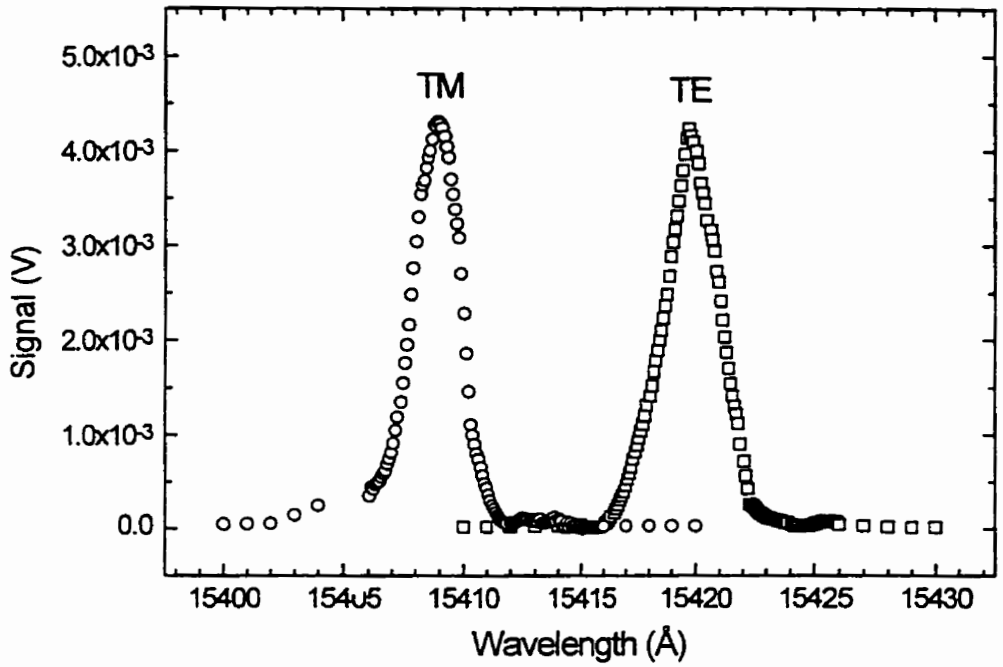

Fig. 6.9 Birefringence for a demultiplexer of design B separates the spectral response functions for the TE & TM modes

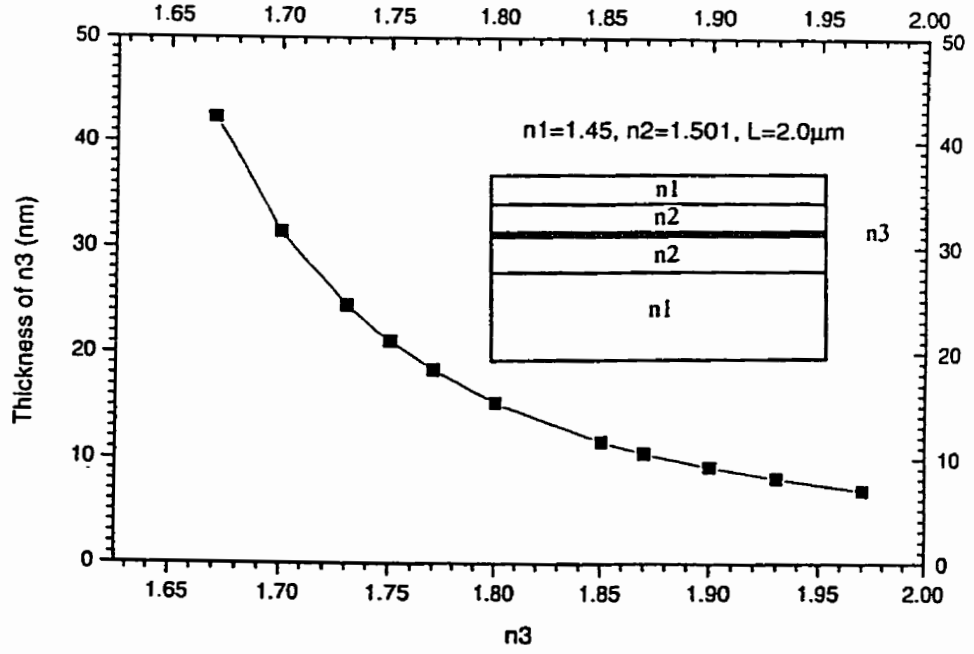

Fig. 6.10 The thickness of high refractive index layer as a function of its refractive index when waveguide birefringence is 1.8×10^{-3}, which gives zero total birefringence

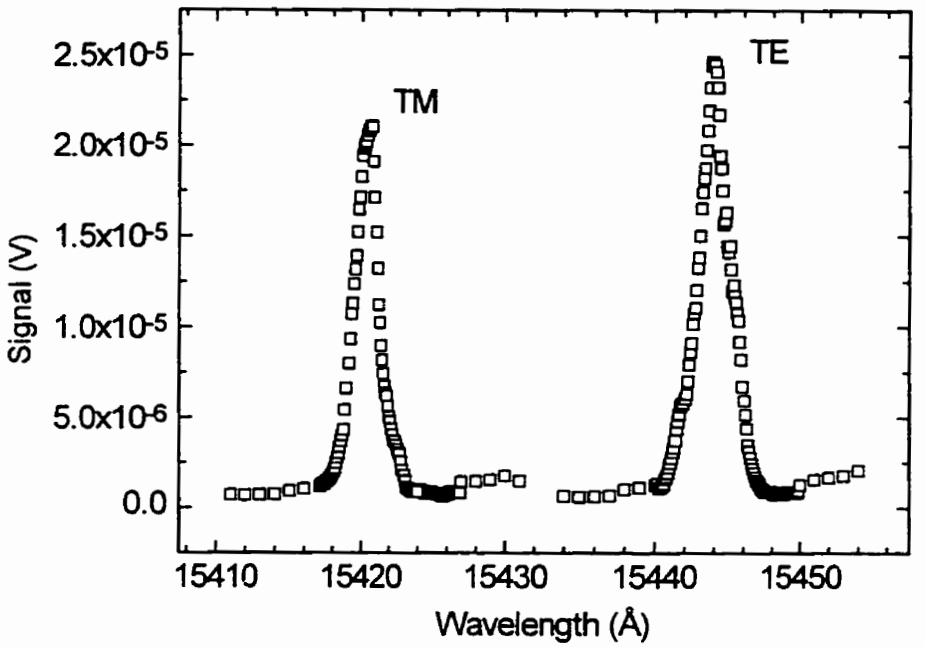

Fig. 6.11 Birefringence of a demultiplexer with 12 nm high refractive index layer at the center of slab waveguide separates the spectral response for the TE & TM modes

the proceeding paragraph. However, the fact that one peak moved relatively to the other by approximately amount we expected shows our design method was effective.

The fact that the total birefringence changed by 1.24 nm, rather than the designed change of 1.1 nm may be attributed to:

1. In doing simulations, we neglected the effect of air and substrate, supposing the upper cladding and lower cladding go to infinity. In fact, upper cladding is only 0.5 μm thick, air will have some influence on the effective index of slab waveguide. The lower cladding is 5 μm, and Si substrate may still have some effects on the effective

index of slab waveguide. If those two layers have to be considered, four extra matrices must be added into (6.22).

2. Both errors in thickness of high refractive index layer and thickness of slab waveguide caused errors in birefringence control.
3. Errors in refractive indices for high refractive index layer, core layer and cladding will also cause errors in birefringence control.

6.4 CONCLUSIONS

Preliminary results on birefringence control by interposing a high refractive index layer at the center of the core are reported in this chapter. With 12 nm SiON of refractive index 1.85 at the center of the core layer, TM peak moved relative to TE peak by an amount that is approximately equal to the designed amount. Smith and McGreer (1997) have calculated layer structures assuming a finite top cladding thickness and found a solution for total birefringence B = 0 that may be practical. Their work is in progress. Our work was useful in that it prepared some of the groundwork and demonstrated to AMC and TRLabs that we could manipulate the birefringence by changing the layer structure.

CHAPTER SEVEN

DESIGN OF CONCAVE GRATINGS WITH SINGLE PASSBAND

For demultiplexers we have discussed so far, their gratings have only one diffraction order. This kind of grating has many passbands, with one passband every Free Spectral Range (FSR). For WDM demultiplexer applications, the operation wavelengths are predefined. By choosing suitable diffraction order, all operation wavelengths can be put into one passband of a grating. But for multifrequency laser applications, gratings with multiple passbands will cause lasing instability. By designing a grating with only one passband, the above problem will be solved. In this chapter, concave gratings with several

chirping profiles are studied. Demultiplexers based on chirped concave gratings are designed.

7.1 BACKGROUND

Cost effective WDM transmission systems and networks rely on the availability of tunable sources that are spectrally stable with aligned channel frequencies (Kaminow, 1993). One can, of course, select discrete devices at the right wavelengths. This approach, however, is quite cost intensive. Also, these sources would have to be separately packaged and tuned with respect to each other; shifts in the spectral characteristics due to aging is another problem (Woodward, 1993).

Recently, a new approach to the wavelength control problem emerged. Multifrequency lasers, that are based on the integration of optical multiplexers with amplifiers are capable of producing a set of frequencies that are spaced very precisely. Soole et al. (1992a, 1992b) demonstrated for the first time such a source employing amplifier sections and a reflective concave grating. A wide tuning range and multifrequency emission (Poguntke, 1993), were demonstrated with this laser. However, concave gratings employed in their multifrequency lasers had multiple passbands. In which passband and in how many passbands laser oscillation occurred for each channel was determined only by the amplifiers. This makes it difficult to control the absolute lasing wavelength, and multiple passband lasing results in instability in the laser output (Doerr, 1995).

7.3 LINEARLY CHIRPED CONCAVE GRATING

Fig. 7.1 is five passbands of a concave grating with diffraction order of 75. This grating was employed in the demultiplexer of design A in Chapter Three to Chapter Five. For a fixed channel, there is one passband every 20.7 nm.

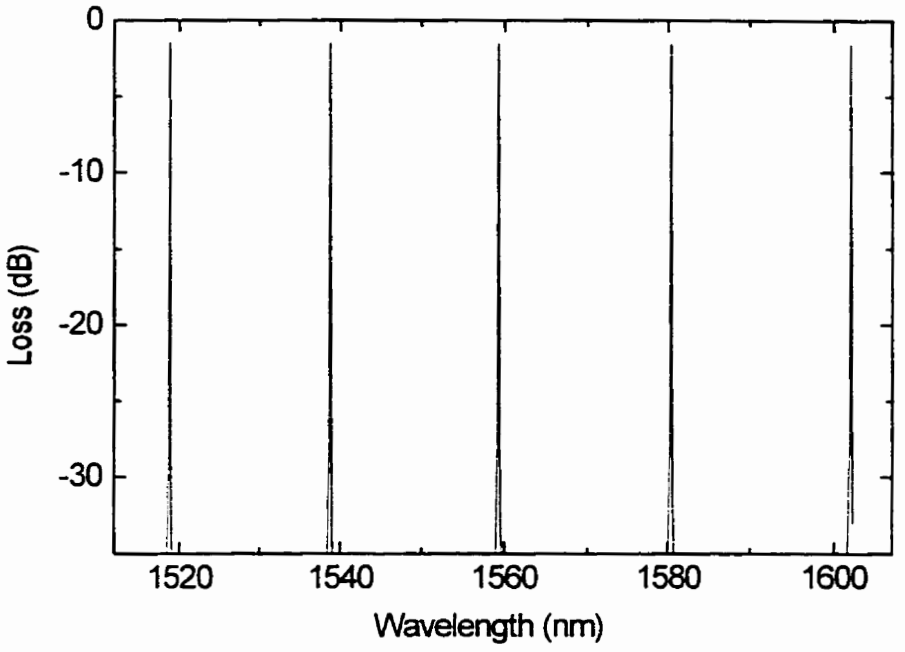

Fig. 7.1 Five passbands of a nonchirped concave grating with diffraction order of 75

Instead of one diffraction order, one can use two diffraction orders across a grating. Fig. 7.2 shows five passbands of a grating whose diffraction order is 78 for the upper half and 72 for the lower half. The extinction ratio between dominant passband and other passbands is about 3 dB. For passbands other than dominant passband, they are composed of two peaks, with one corresponding to diffraction order of 78, and the other

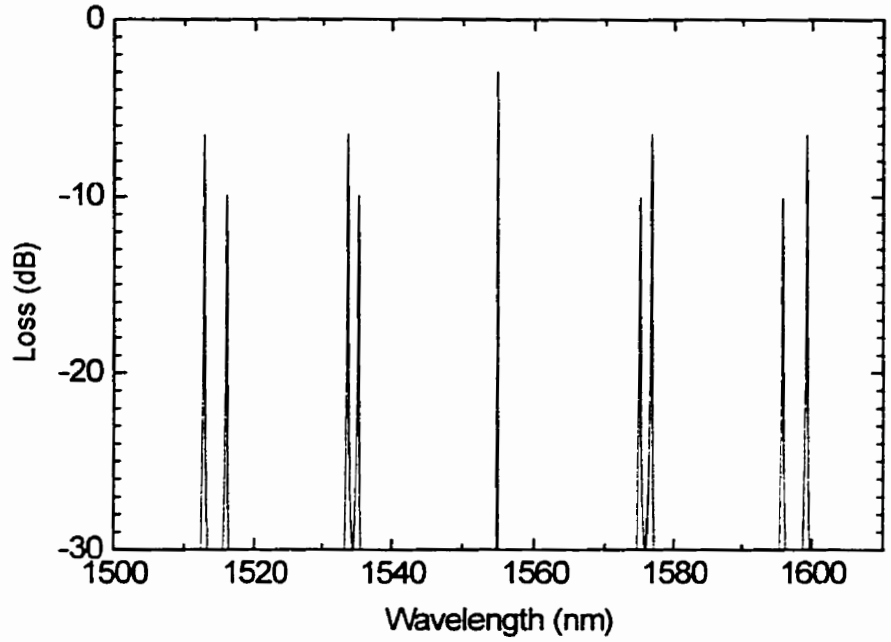

Fig. 7.2 Five passbands of a concave grating whose diffraction order is 78 for the upper half grating and 72 for the lower half grating

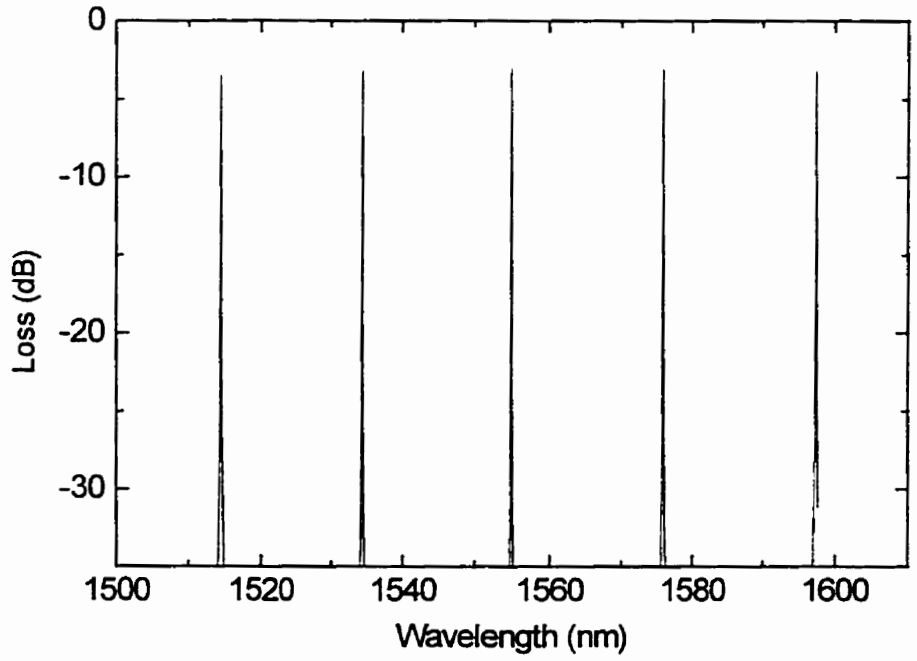

Fig. 7.3 five passbands of a concave grating whose diffraction orders are alternatively 72 and 78 between any adjacent facets across the grating

corresponding to diffraction order of 72. We call this as two-grating design. Fig. 7.3 shows five passbands of a concave grating which was designed in this way: the diffraction order between every adjacent facets was alternatively 72 and 78 across the grating. The grating behaves totally differently from two-grating design. The extinction ratio between dominant passband and other passbands is very small, and the whole grating works like a grating with diffraction order of (72+78)/2 = 75.

Fig. 7.4 shows five passbands of a two-grating design whose diffraction orders are 65 and 85. The extinction ratio between dominant passband and other passbands is about 3 dB again. Diffraction orders of 65 and 85 have been used to design the same kind of grating as in Fig. 7.3. The extinction ratio between the dominant passband and other passbands is very small, see Fig. 7.5, and the grating behaves again like a grating with diffraction order of (65+85)/2 = 75.

We have designed a grating whose diffraction orders between adjacent facets vary according to (75, 74, 72, 76, 77, 79, 73, 78, 71) repeated patterns for the upper half, and (72, 76, 75, 74, 71, 73, 78, 79, 77) repeated patterns for the lower half. Fig. 7.6 shows five passbands of a channel of this grating. The extinction ratio between the dominant passband and other passbands is very small. Fig. 7.7 shows diffraction orders as a function of facet numbers. Instead of changing diffraction order abruptly from facet to facet, we changed diffraction order gradually across a grating, as shown in Fig. 7.9. The extinction ratio between the dominant passband and other passbands is 6 dB as shown in Fig. 7.8. From the results shown in Fig.7.6 and Fig. 7.8 we can see that in order to have a high extinction ratio between the dominant passband and other passbands, the diffraction orders have to vary gradually across a grating.

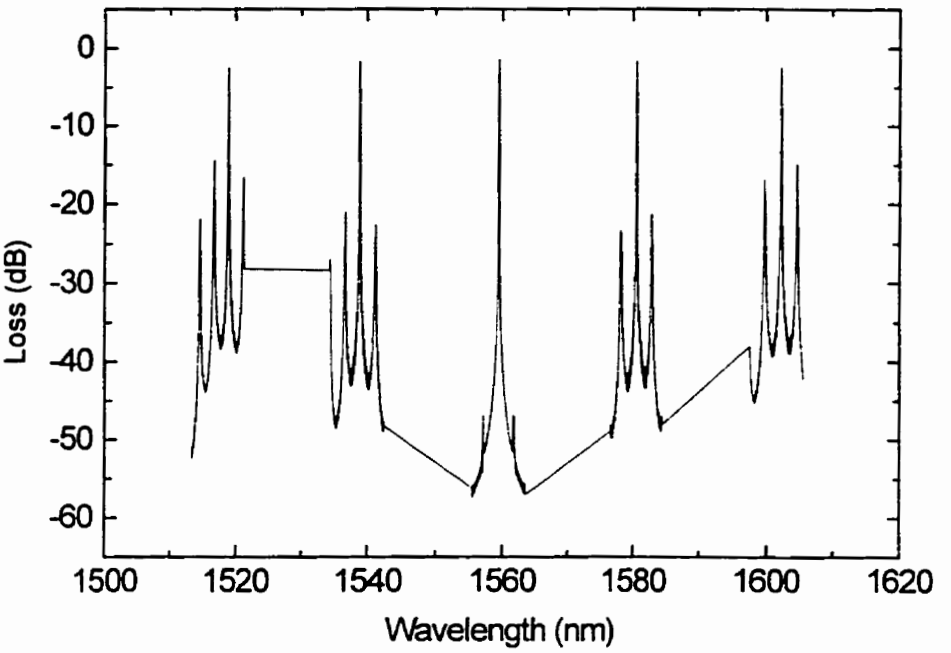

Fig. 7.6 Five passbands of a concave grating whose diffraction orders vary randomly across the grating.

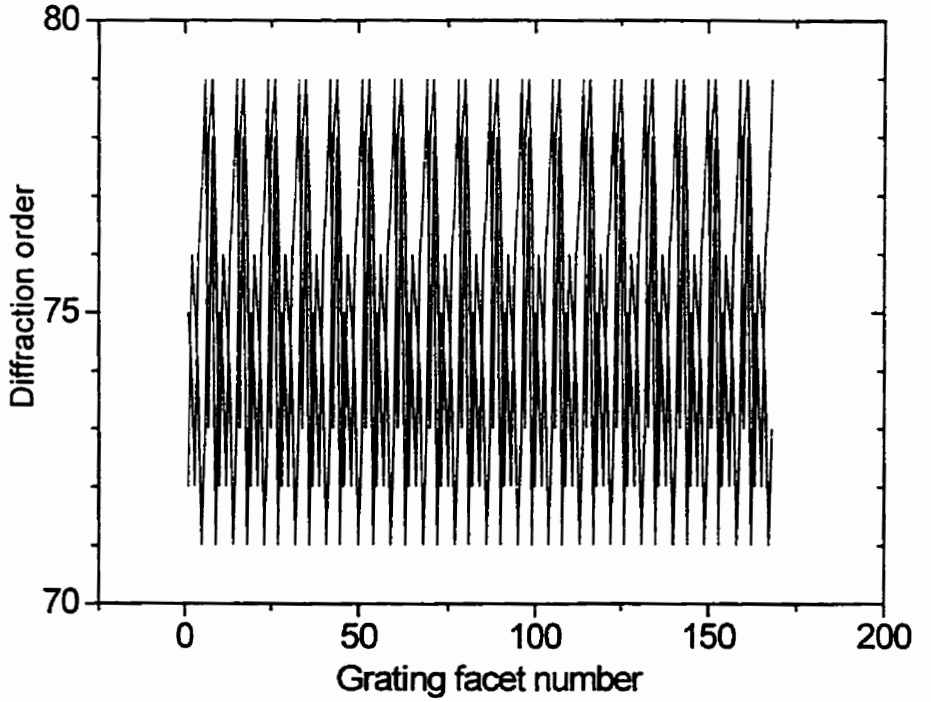

Fig. 7.7 Diffraction order as a function of facet number for the grating in Fig. 7.6

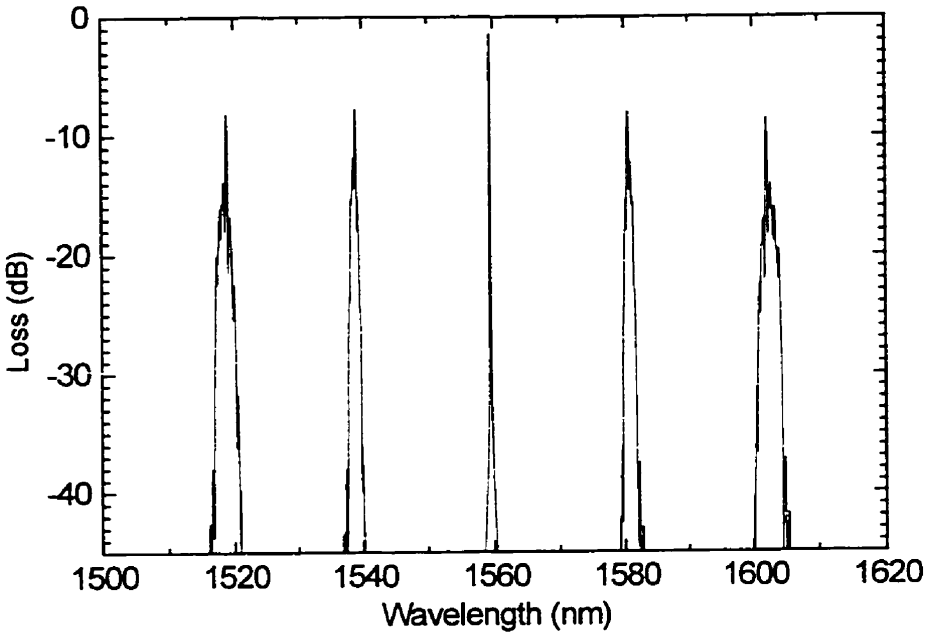

Fig. 7.8 Five passbands of a concave grating whose diffraction orders vary gradually across the grating

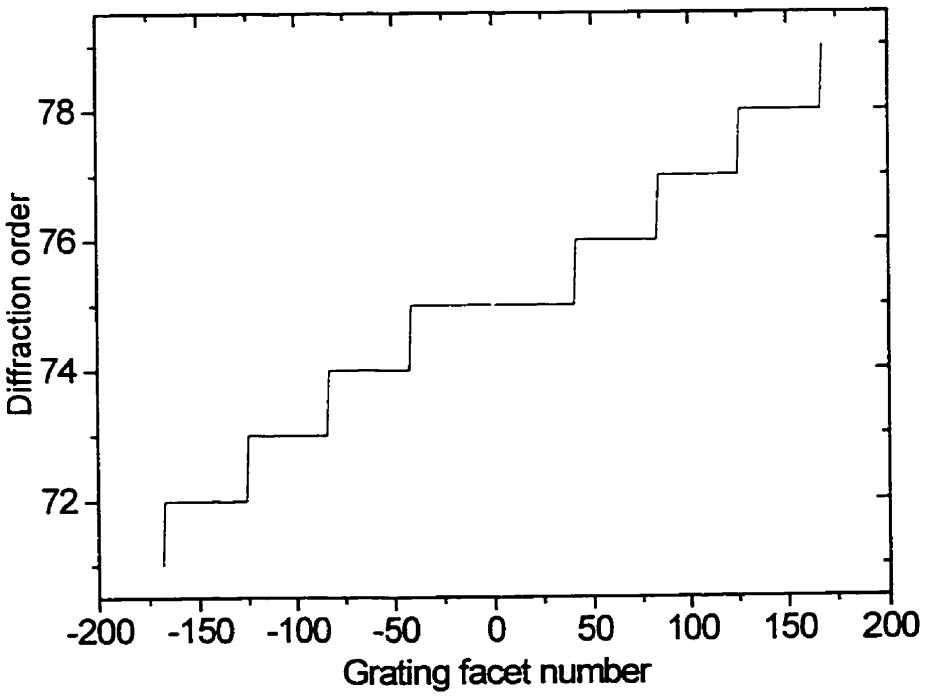

Fig. 7.9 Diffraction order as a function of facet number for the grating in Fig. 7.8

For a linearly chirped concave grating, diffraction orders are determined by the following equations:

$$m_j = C_1 + round\left[\frac{j-1}{C_2}\right] \text{ for the upper half of the grating,}$$

$$m_j = C_1 - round\left[\frac{j-1}{C_2}\right] \text{ for the lower half of the grating,}$$

where C_1 is the averaged diffraction order, and C_2 determines how fast diffraction orders change across the grating.

Fig. 7.10 shows diffraction order as a function of facet number for a linearly chirped concave grating. For this grating, C_2 = 4, i.e. four consecutive facets have the same diffraction order, and the averaged diffraction order is C_1 = 75. Fig. 7.11 shows diffraction order as a function of facet position and from this we see that for a linearly chirped concave grating, diffraction order varies parabolically with facet position (x direction). This is verified mathematically as follows:

$$\frac{dx}{di} = m_i\lambda \tag{7.10}$$

$$m_i = m_0 + \frac{i}{4} \tag{7.11}$$

$$x = \int m_i\lambda di = \int (m_0 + \frac{i}{4})\lambda di = \lambda m_0 i + \frac{\lambda i^2}{8} + c \tag{7.12}$$

$$x = 4m_0(m_0 - m_i)\lambda + 2\lambda(m_0 - m_i)^2 + c \tag{7.13}$$

Where x, m_0, m_i, i, λ, c are facet x axis coordinate, diffraction order at the pole, diffraction order at *i*th facet, facet number, wavelength and integral constant respectively.

The extinction ratio between the dominant passband and other passbands for this grating is 20.1 dB, as shown in Fig. 7.12. Fig. 7.13 is the close up of the dominant passband. The FWHM of this peak is 0.09nm. Fig. 7.14 shows diffraction loss as a function of channel center wavelength for a demultiplexer based on the linearly chirped concave grating. As a result of chirping, the diffraction loss is increased by about 0.5 to 1.0 dB compared to the grating designed in chapter three.

Fig. 7.15 shows five passbands of a linearly chirped concave grating whose diffraction orders vary every eight facets ($C_2 = 8$). The averaged diffraction order is $C_1 = 75$. The extinction ratio between the dominant passband and other passbands is only 17.0 dB.

Fig. 7.16 shows five passbands of a linearly chirped concave grating whose diffraction orders vary every two facets ($C_2 = 2$). The averaged diffraction order is 75. The extinction ratio is 21.2 dB between the dominant passband and the two first passbands and 19.4 dB between the dominant passband and the two second passbands. By comparing Fig. 7.12 with Fig. 7.15 and Fig. 7.16, we know that for a linearly chirped concave grating with averaged diffraction order of $C_1 = 75$, $C_2 = 4$ gives the best extinction ratio between the dominant passband and other passbands.

Fig. 7.17, Fig. 7.18 and Fig. 7.19 show five passbands of linearly chirped concave gratings where $C_2 = 4$ and averaged diffraction order C_1 is 100, 150 or 200. The higher the averaged diffraction orders the lower the extinction ratio between the dominant passband and other passbands is.

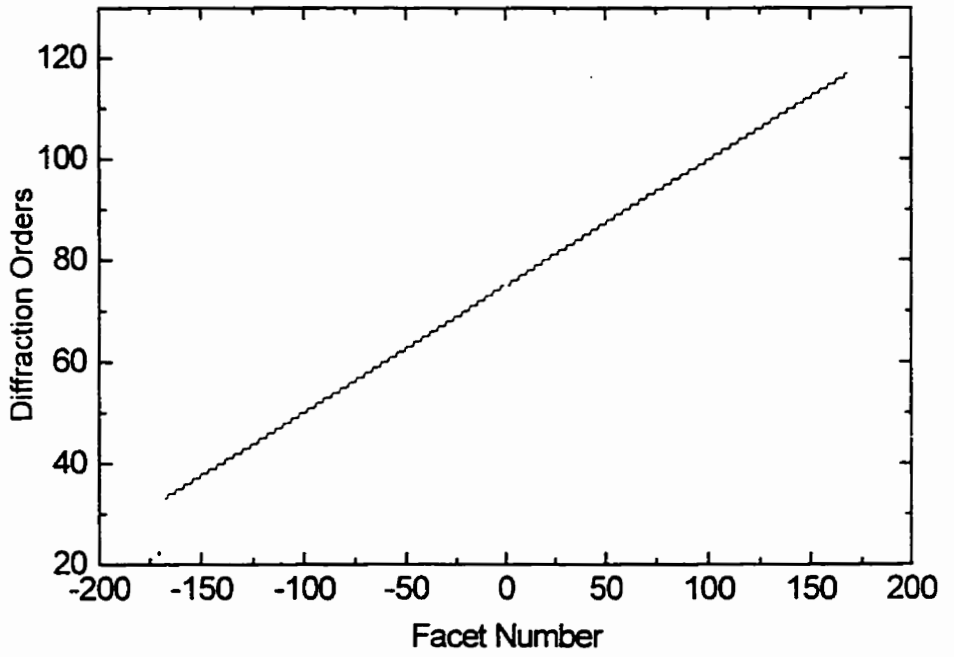

Fig. 7.10 Diffraction orders as a function of facet number for the linear chirped concave grating with $C_1 = 75$, $C_2 = 4$.

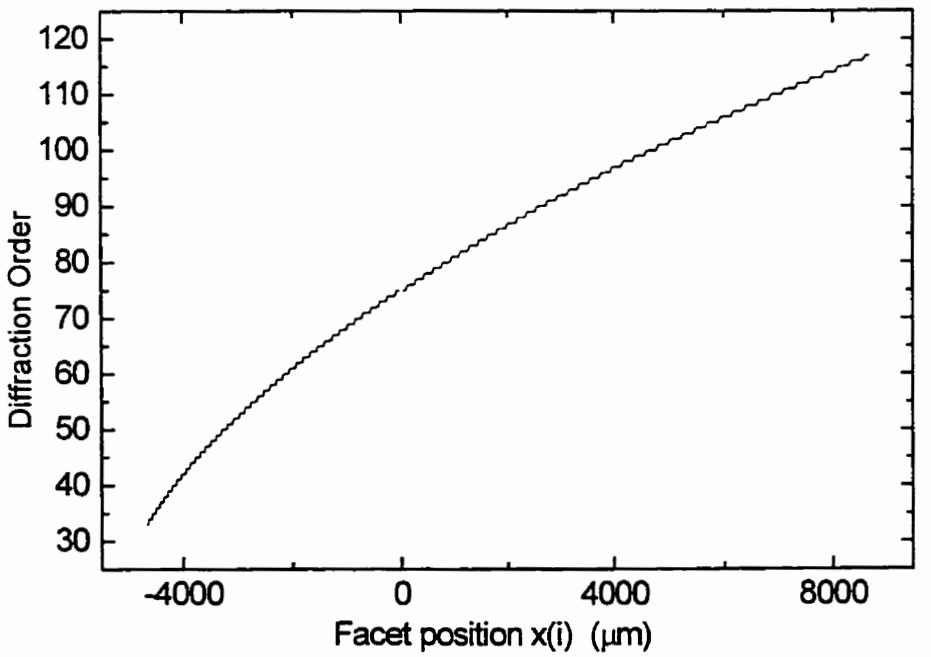

Fig. 7.11 Diffraction order as a function of facet position for the linearly chirped concave grating in Fig. 7.10

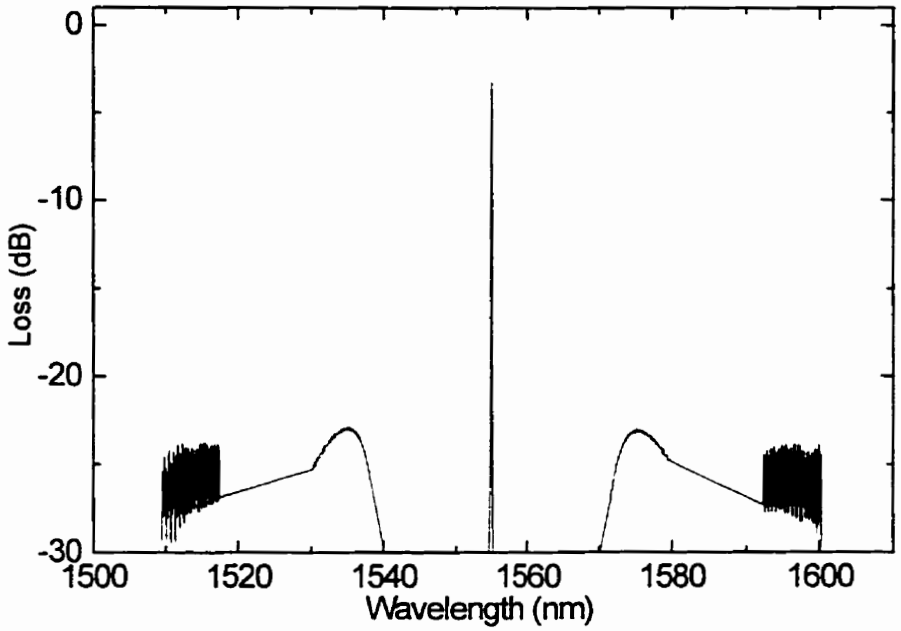

Fig. 7.12 Five passbands of a linearly chirped concave grating with diffraction order shown in Fig. 7.10 and 7.11.

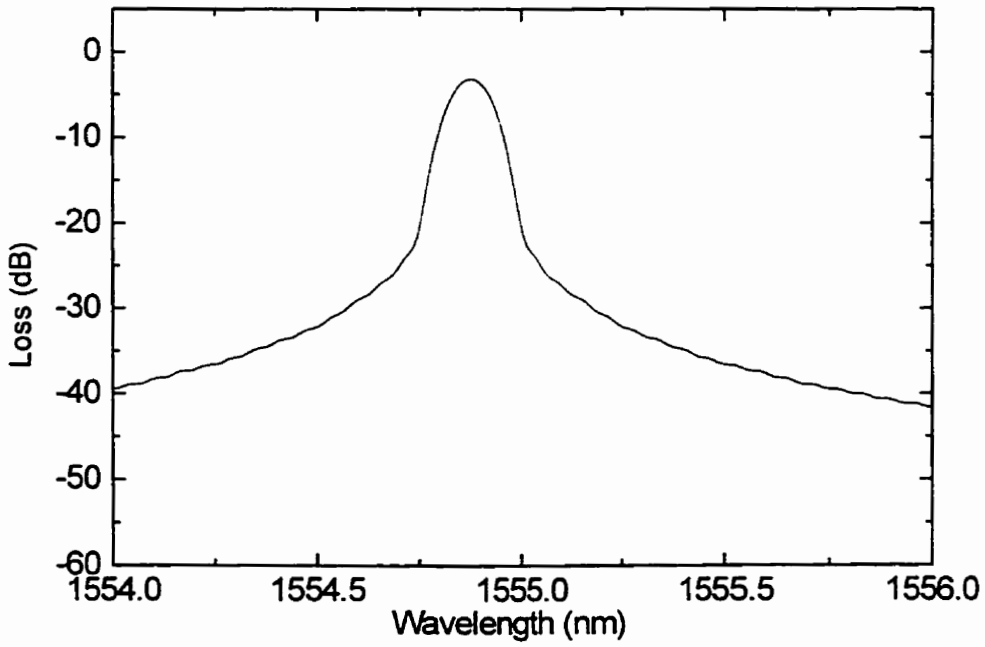

Fig. 7.13 The close-up of the dominant passband in Fig. 7.12.

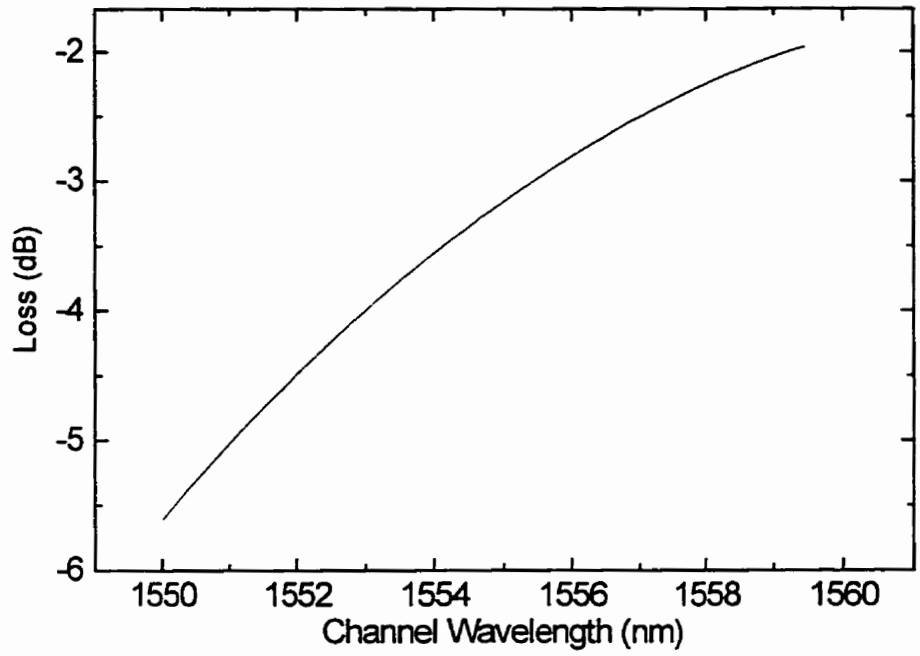

Fig. 7.14 Diffraction loss as a function of channel wavelength for a demultiplexer based on the chirped concave grating in Fig. 7.12

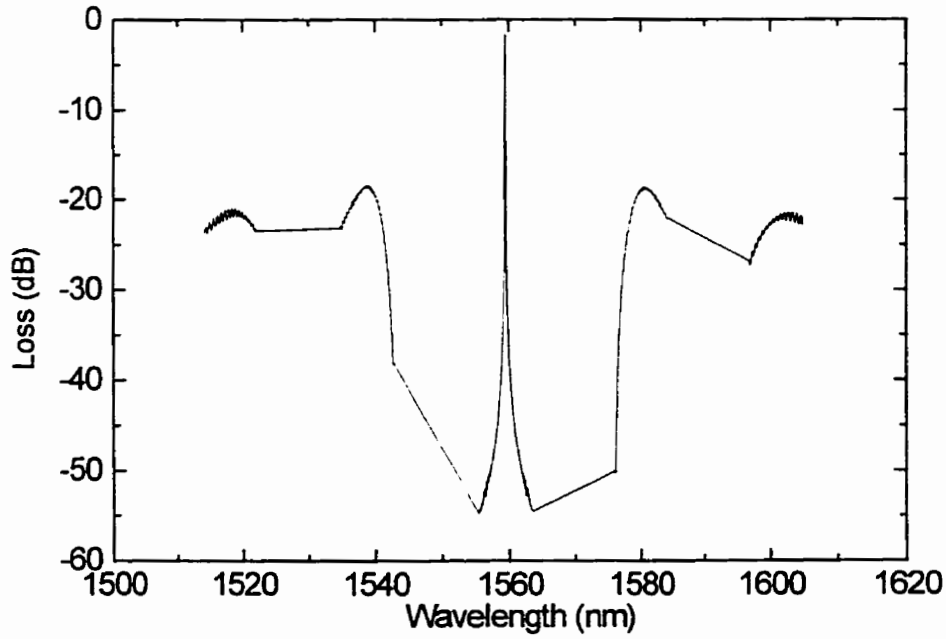

Fig. 7.15 Five passbands of a linearly chirped concave grating with $C_1 = 75$ and $C_2 = 8$

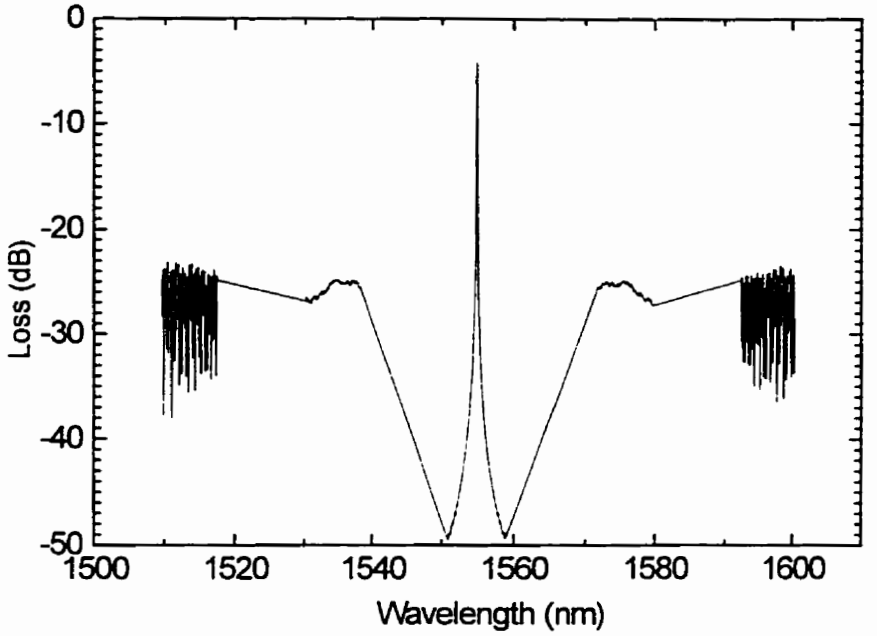

Fig. 7.16 Five passbands of a linearly chirped concave grating with $C_1 = 75$ and $C_2 = 2$. The extinction ratio between the dominant passband and other passbands is 19.4 dB.

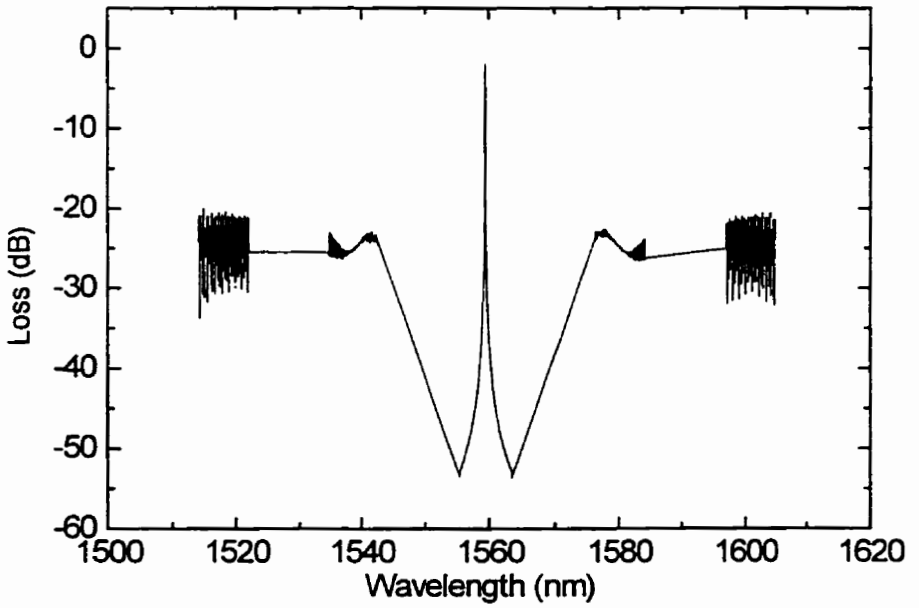

Fig. 7.17 Five passbands of a linearly chirped concave grating with $C_1 = 100$, $C_2 = 4$. The extinction ratio between the dominant passband and other passband is 19.8 dB.

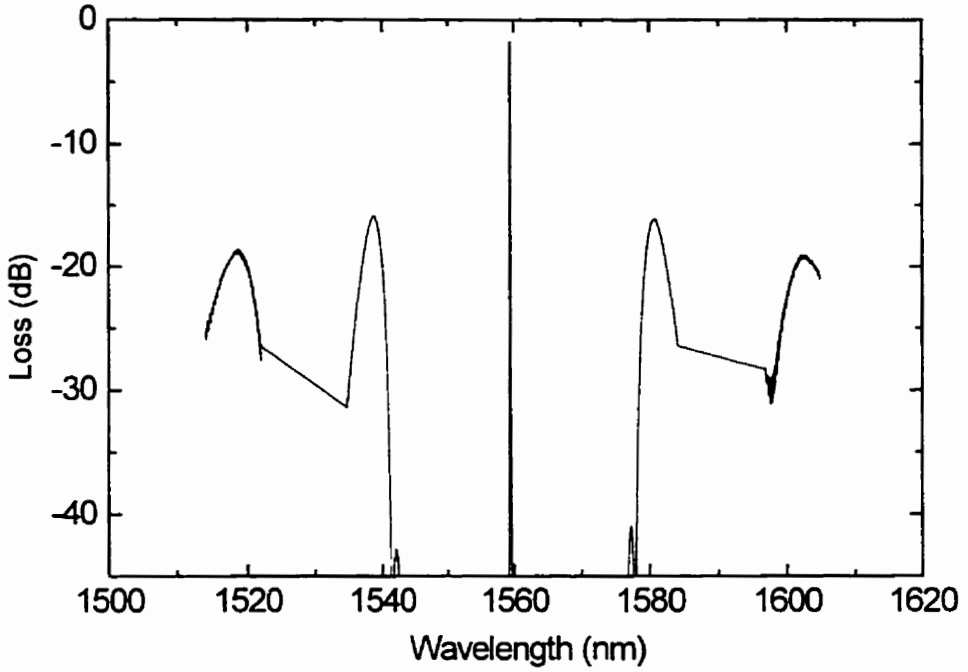

Fig. 7.18 Five passbands of a linearly chirped concave grating with $C_1 = 150$, $C_2 = 4$. The extinction ratio between the dominant passband and other passband is 14.4 dB.

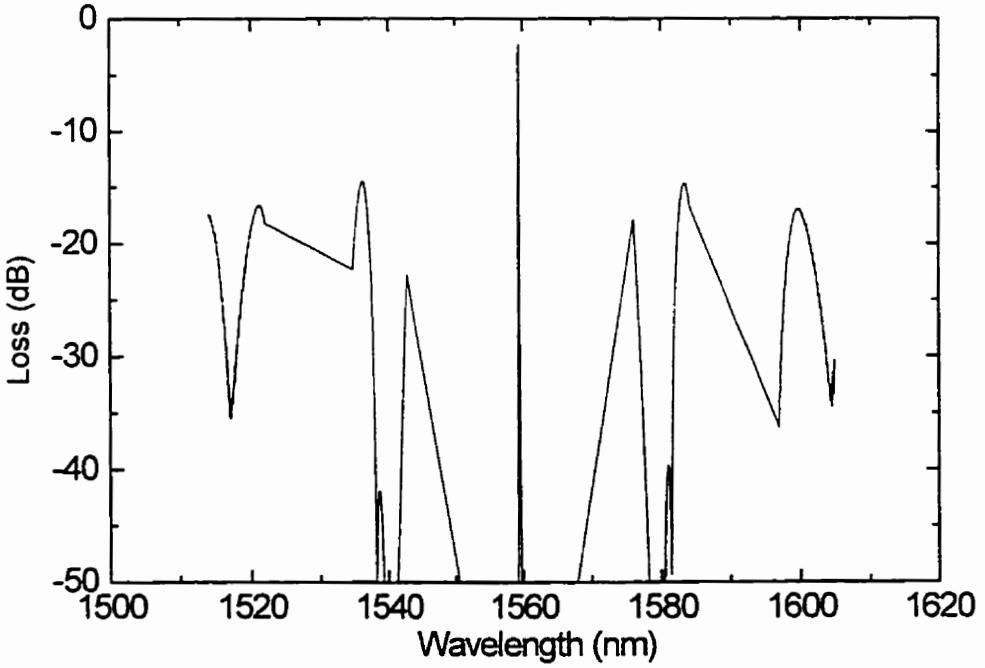

Fig. 7.19 Five passbands of a linearly chirped concave grating with $C_1 = 200$, $C_2 = 4$. The extinction ratio between the dominant passband and other passband is 12.5 dB.

7.4 EXPONENTIALLY CHIRPED CONCAVE GRATINGS

The following equations are used to generate exponentially chirped concave gratings:

$$m_j = C_1 + round\left[\exp^{C_2(C_n+j)}\right] \text{ for the upper half grating}$$

$$m_{-j} = C_1 + round\left[\exp^{C_2(C_n-j)}\right] \text{ for the lower half grating}$$

where C_1, C_2 and C_n are diffraction order at the grating pole, chirping depth, and maximum facet number respectively.

Fig. 7.20 shows diffraction orders as a function of facet number for an exponentially chirped concave grating where $C_1 = 2$, $C_2 = 1/68$, $C_n = 12000/75$.

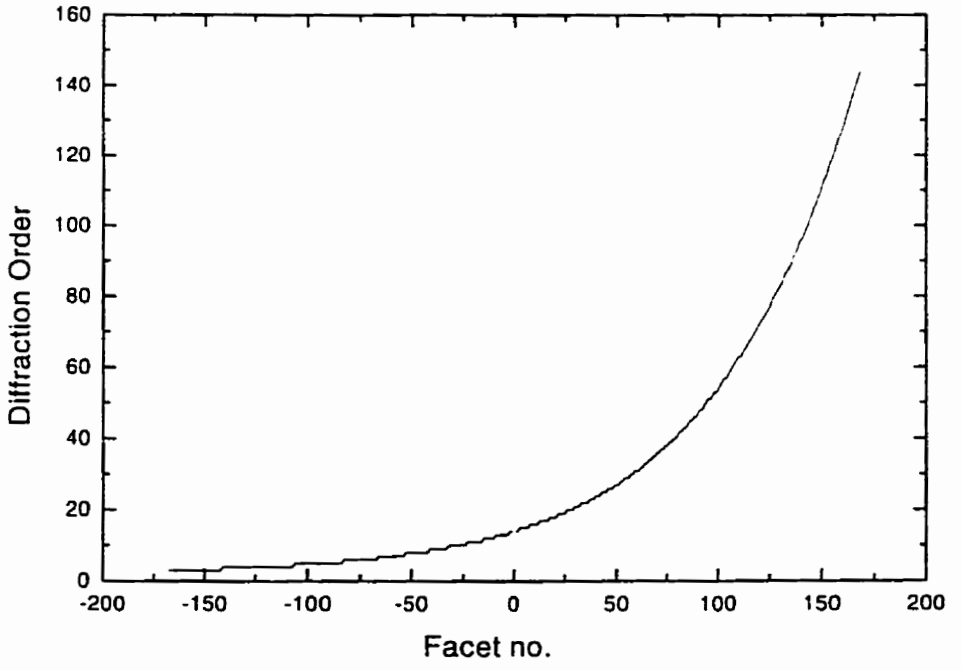

Fig. 7.20 Diffraction order as a function of facet number for a exponentially chirped concave grating with $C_1 = 2$, $C_2 = 1/68$, $C_n = 12000/75$

the diffraction order is linearly proportional to the facet position (x direction), as shown in Fig.7.21. Fig. 7.22 shows five passbands of this exponentially chirped concave grating. The extinction ratio is 20.4 dB between the dominant passband and the two first passbands, and 19.2 dB between the dominant passband and the two second passbands.

7.5 PARABOLICALLY CHIRPED CONCAVE GRATINGS

To produce parabolically chirped concave gratings, diffraction order between any adjacent facets is determined by the following equations:

$$m_j = round\left[C_1(C_n + j)^2\right] + C_2 \text{ for the upper half grating}$$

$$m_j = round\left[C_1(C_n - j)^2\right] + C_2 \text{ for the lower half grating}$$

where C_1, C_2 and C_n are chirping depth, diffraction order at the grating pole, and the maximum facet number respectively.

Fig. 7.23 shows diffraction order as a function of facet number for a parabolically chirped concave grating where $C_1 = 1/500$, $C_2 = 10$, $C_n = 12000/75$. The extinction ratio between the dominant passband and other passbands is 18.2 dB, as shown in Fig. 7.24. After decreasing the chirping depth to $C_1 = 1/1000$ and keeping other parameters the same as before, the extinction ratio between the dominant passband and other passbands is 20.9 dB, as shown in Fig. 7.25.

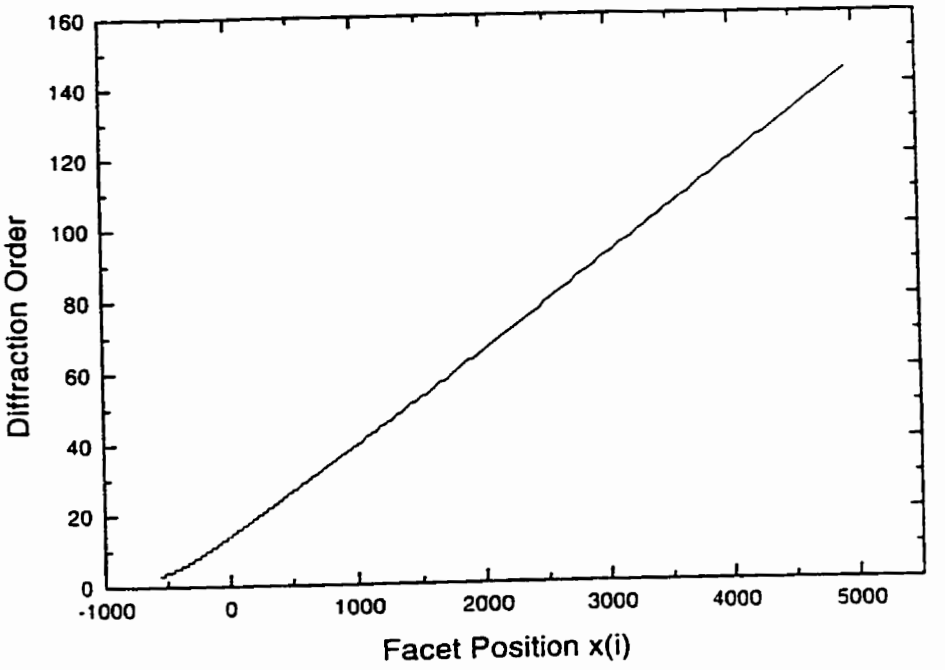

Fig. 7.21 Diffraction order as a function of facet position (x direction) for the exponentially chirped concave grating in Fig. 7.20

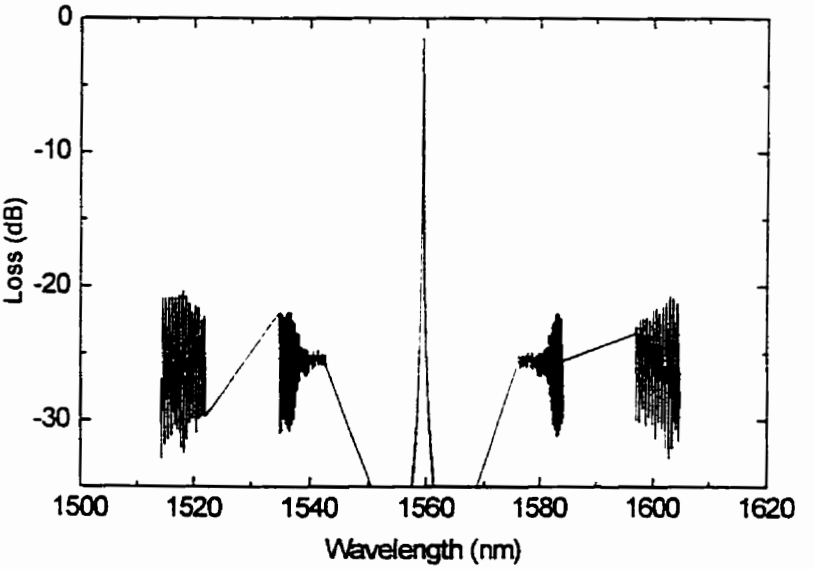

Fig. 7.22 Five passbands of the exponentially chirped concave grating in Fig. 7.20. The extinction ratio between the dominant passband and other passbands is 19.2 dB

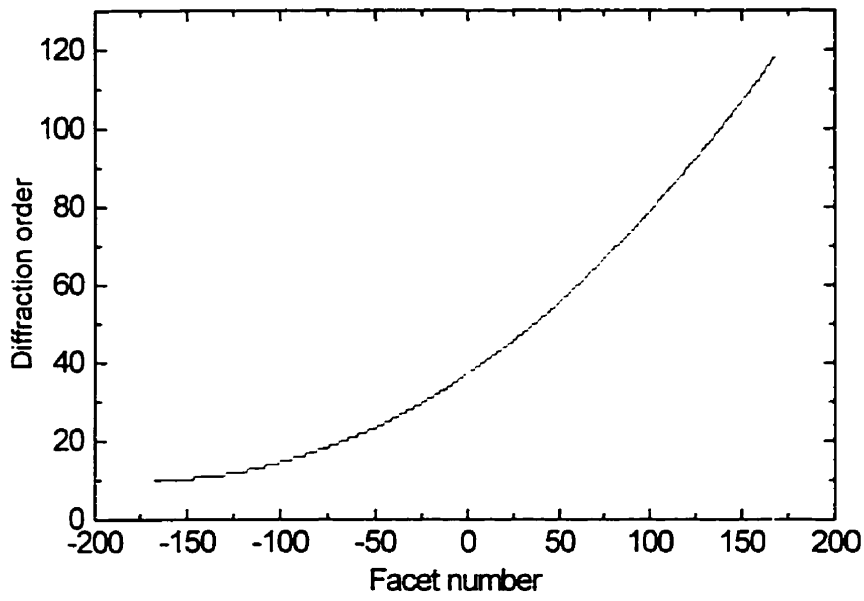

Fig. 7.23 Diffraction order as a function of facet number for a parabolically chirped concave grating with $C_1 = 1/500$, $C_2 = 10$, $C_n = 12000/75$.

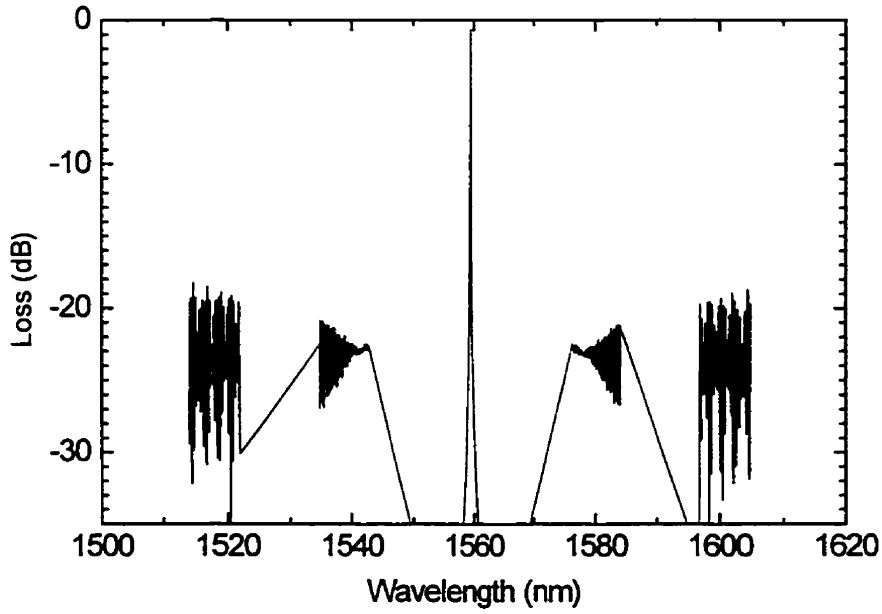

Fig. 7.24 Five passbands of a parabolically chirped concave grating with $C_1 = 1/500$, $C_2 = 10$, $C_n = 12000/75$. The extinction ratio between the dominant passband and other passbands is 18.2 dB.

Table 7.1 Parameters for chirped concave gratings

Chirping	C_1	C_2	C_n	Extinction Ratio
Linear	75	4	N/a	20 .1 dB
Linear	100	4	N/a	19.8 dB
Parabolic	1/500	10	12000/75	18.2 dB
Parabolic	1/1000	10	12000/75	20.9 dB
Exponential	2	1/68	12000/75	19.2 dB

Based on the above five chirped concave gratings, five demultiplexers were designed. Those demultiplexers had common parameters: $a_1 = 22.5$ mm, $b_1 = 0$ mm, $a_2 = 22.5$ mm, $b_2 = -0.765$ mm, $n = 1.484$, $\lambda_0 = 1555$ nm, $\theta = 90°$, $(d\lambda/du_2)_0 = 0.015$ nm/μm.

Fig. 7.26 shows the mask generated by L-Edit, and based on this, a Cr hard photolithographic mask can be produced by electron-beam writing system.

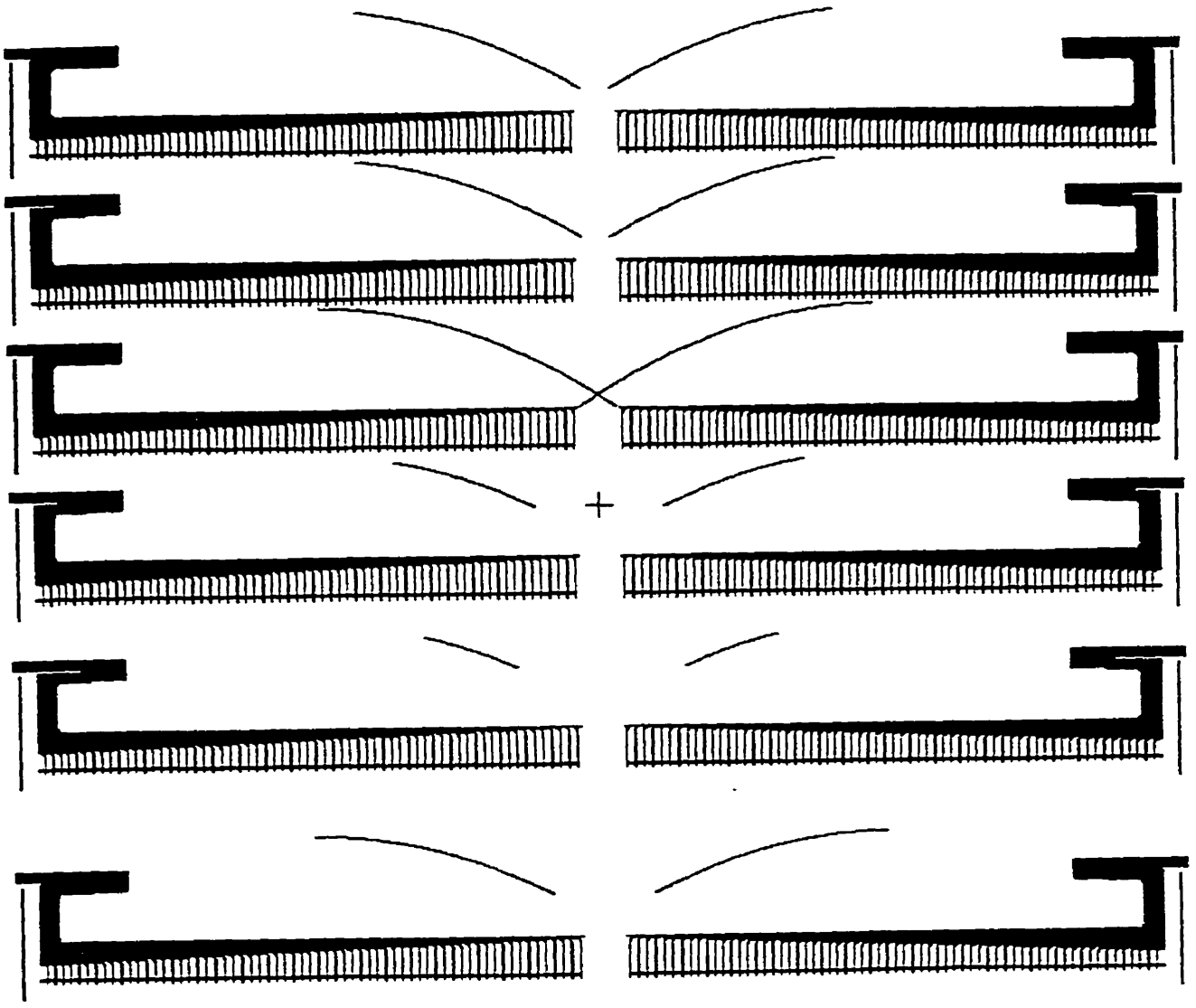

Fig. 7.26 The mask generated by L-Edit with five demultiplexers on each side corresponding to five different design in Table 7.1

CHAPTER EIGHT

CONCLUSIONS

8.1 CONTRIBUTIONS OF THIS WORK

(1) With the use of photoresist and Cr as mask, the author has developed a novel RIE etch process which can produce demultiplexer with nearly vertical sidewalls (89.4°). The demultiplexer with 89.4° sidewalls has a fiber-to-fiber loss of around 20 dB. For concave gratings with two reflection facets, it is critical to have vertically etched

sidewalls. Demultiplexer with 84° sidewalls usually has a fiber-to-fiber loss higher than 50 dB.

(2) In a wafer with 89.4° sidewalls, demultiplexers of several different designs (which we refer to as designs A, B, C, D, and E) have been thoroughly characterized in this thesis. A demultiplexer of design A had a channel spacing of 0.144 nm which was about one order of magnitude smaller than that of any integrated concave grating demultiplexer that had been previously reported. Demultiplexer of design C had 120 working channels. This kind of demultiplexer may find wide applications in future fiber optic communications. A demultiplexer of design E had 0.6 nm channel spacing and small side lobes. In this wafer, demultiplexers of designs A, B, C, E all had a loss of about 20 dB, but the demultiplexer of design D had a loss of 38 dB and very high side lobes.

(3) Based on Fraunhofer diffraction theory in two dimensions, simulations have been carried out on demultiplexers. From simulations it is known that waveguide absorption is the main contribution to the fiber-to-fiber loss and loss variations from channel to channel. By choosing suitable parameters, annealing can greatly reduce absorption loss and the wavelength dependence of absorption loss. By annealing a demultiplexer at 1050° for 1 hour, the fiber-to-fiber loss was reduced by about 10 dB.

(4) Preliminary results on birefringence control by interposing a high refractive index layer at the center of core layer is reported in this thesis. With 12 nm SiON of refractive index 1.85 at the center of core layer, TM peak moved relative to TE peak by an amount that was approximately equal to the designed amount. Further work will be

required to shift the peak in the opposite direction in order to cancel the stress birefringence.

(5) Concave gratings with several chirping profiles are studied. The extinction ratio between dominant passband and other passbands can be higher than 20.9 dB for linearly or parabolically chirped grating. Five demultiplexers with linear, parabolic, and exponential chirping were designed.

8.2 RECOMMENDATIONS FOR FUTURE WORK

(1) Although with the use of photoresist and Cr as mask, vertical sidewalls can be reproducibly fabricated, Cr mask sometimes causes rough sidewalls which give rise to a very high scattering loss. Using amorphous silicon as a mask results in small roughness of sidewalls according to Bazylenko (1996), therefore should be used in the future.

(2) In this work, sidewalls of ridge waveguides are surrounded by air, and high refractive index difference between air and core causes high scattering loss when the sidewalls are rough. In latter work, another layer of cladding may be added to the sample surface after RIE.

(3) For practical WDM systems, flat and wide band characteristics are required in order to suppress loss variation due to wavelength drift of the light source. Demultiplexers in this thesis do not have these characteristics. This could be done in the future with the use of some of the methods mentioned in Chapter Five.

(4) Multiwavelenghth lasers may be fabricated in InGaAsP by integrating chirped concave grating with semiconductor amplifiers.

REFERENCES

1. Aarnio J., Heimala P., Giudice M. Del, and Bruno F., 1991, Electron. Lett., **27**, 2317-2318.
2. Agrawal G. P., 1992, Fiber-Optic Communication system, John Wiley & Sons, Inc., 347.
3. Alexander S. B., 1997, Lightwave, June, 27-32.
4. Alterman L., 1996, Laser Focus World, June, 35-36.
5. Baak T., 1982, Applied Optics, **21**, 6.
6. Ballart R., Ching Y. C. , 1989, IEEE Commun. Mag. , **27**, 8-5.
7. Bazylenko M. V., and Gross M., 1996, J. Vac. Sci. Technol. A, **14**, 2994-3003.
8. Bergano N. S., Davidson C. R., 1996, J. Lightwave Technol., **14**, 1299-1308
9. Beutler H. G., 1945, J. Opt. Soc. Am, **35**, 311-350.
10. Bilodeau F., Johnson D. C., Theriault S., Malo B., Alberta J., and Hill K. O., 1995, IEEE Photon. Technol. Lett., **7**, 388-390
11. Bruno F., Guidice M. del, Recca R., and Testa T., 1991, Appl. Opt., **30**, 4560-4564.
12. Capron B. A., Beranek M. W., Huggins R. W., and Koshinz D. G., 1993, J. Lightwave Technol., **11**, 2009-2014
13. Chaffee D., 1997, Photon. Spect., August, 110
14. Clemens P. C., Marz R., Reichelt A., and Schneider H. W., 1992, IEEE Photon. Technol. Lett., **4**, pp. 886-887.

15. Clemens P.C., Heise G., Marz R., Michel H., Reichelt A., and Schneider H. W., 1994, IEEE Photon. Techno. Lett., **6**, 1109-1111.

16. Coburn J. W. and Kay E., 1979, IBM J. Res. Dev., **23**, 33.

17. Cremer C. C., Heise G., Muller-Nawrath R., Stoll L., Veuhoff E., Baumeister H., 1990, ECOC'90, 110

18. Cremer C., Ebbinghaus G., Heise G., Muller-Nawrath R., Schienle M., and Stoll L., 1991, Appl. Phys. Lett., **59**, 627-629.

19. Cremer C., Emeis N., Schier M., Heise G., Ebbinghaus G., and Stoll L., 1992, IEEE Photon. Technol. Lett., **4**, 108-111.

20. Delage A., McGreer K. A., and Rainville E., 1992, Can. J. Phys., **70**, 1092

21. Delange O.E., 1970, Proc. IEEE, **58**, 1683.

22. Van Dam C., Amerfsoort M.R., Kate G.M. ten, Ham F.P.G.M. van, Smit M.K., Besse P.A., Bachmann M. and Melchior H., 1995, Procs. 7th Eur. Conf. Conf. on Int. Optics (ECIO'95), April 3-6, Delft, The Netherlands, 275-278.

23. Doerr C. R., Zirngible M., and Joyner C. H., 1995, IEEE Photon. Technol. Lett., **7**, 962-964.

24. Doerr C. R., Shirasaki M., and Joyner C. H., 1997, IEEE Photon. Technol. Lett., **9**, 625-627.

25. Doerr C. R., Zirngible M., and Joyner C. H., 1996, IEEE Photon. Technol. Lett., **8**, 500-502.

26. Doerr C. R., Joyner C.H., Zirngible M., and Stulz L. W., 1996, IEEE Photon. Technol. Lett., **8**, 1606-1608.

27. Dragone C., 1991, IEEE Phot. Tech. Lett., **3**, 812-815.

28. Edwards H. G., 1996, Sept., Laser Focus World, 129-134

29. Emura K., 1996, OECC '96 Tech. Digest, 328.

30. Fallahi M., McGreer K. A., Delage A., Templeton I. M., Chatenoud F., and Barber R., 1993, IEEE Photon. Technol. Lett., **5**, 794-797.

31. Flamm D. L. and Donnelly V. M., 1987, Plasma Chem. Plasma Process., **1**, 317.

32. Fujii Y., Aoyama K., and Minowa J., 1980, IEEE J. Quantum Electron., **QE-16**, 165-169.

33. Gonthier F., Lacroix S., Daxhelet X., Black R. J., and Bures J., 1989, Phys. Lett., **54**, 1290-1293.

34. Green P. E., 1996, IEEE J. Selected Areas in Comm., **14**, 764

35. Harada T. and Kita T., 1980, Appl. Opt., **19**, 3987-3993

36. Hill K. O., Fujii Y., Johnson D. C. and Kawasaki B. S., 1978, Appl. Phys. Lett., **32**, 647-649.

37. Hnatiuk H. J., McGreer K. A., and Broughton J. N., 1996, Proceedings of International Conference on Applications of Photonic Technology

38. Hunsperger R. G., 1991 Integrated Optics: Theory and Technology, published by Springer-Verlag Berlin Heidelberg, 83

39. Juma S., 1996, Laser focus world, Nov., s5-s9.

40. Juma S. K., 1997, Laser Focus World, October, 125-130.

41. Kaminow I.P., 1993, IEEE network Magazine, **3**, 2172-2173.

42. Kitoh T., Takato N., Yasu M. and Kawachi M., 1995, J. Lightwave Technol., **13**, 555-562

43. Kikuchi K. and Lorattanasane C., 1994, IEEE Photon. Technol. Lett., **6**, 104-106.

44. Kuo Y., 1990, J. Vac. Sci. Technol. A, **8**, 1702-1705

45. Koch T.L., 1995, Proc. 21st Eur. Conf. on Opt. Comm., **4**, Mo.B.T.2.

46. Lacroix S., Gonthier F., and Bures J., 1986, Opt. Lett., **11**, 671-673

47. Lee S. M., Chew W. C., Moghaddam M., Nasir M. A., Chung S., Herrick R. W., and Balestra C. L., 1991, J. Light. Technol., **9**, 1471-1479

48. Lee H. J., Henry C. H., Orlowsky K. J., Kazarizov R. F., and Kometani T. Y., 1988, App. Opt., **27**, 4104-4109

49. Lewotsky K., 1997, Laser Focus World, Sept., 22-24

50. Leonberger F., Suchoski P., 1997, Lasers&Optronics, September, 13-15

51. Lerner E. J., 1997, Laser Focus World, July, 119-125.

52. Lerner E. J., 1997, Laser Focus World, August, 85-96.

53. Lierstuen L. O. and Sudbo A., 1995, IEEE Phot. Tech. Lett., 7, 1034-1036.

54. Liu K., Tong F., and Bond S.W, 1993, Proc., SPIE Conf. on multigigabit, **2024**, 278-285.

55. Lizuka K., 1985, Engineering Optics, Springer-Verlag, Heidelberg, 38

56. Liu M. M., 1996, Principles and Applications of Optical Communications, IRWIN, 415.

57. Loewenstein L. M., 1988, J. Vac. Sci. Technol. A, **6**, 1984-1988.

58. Marcatilli E. A. J., 1969, Bell Syst. Tech. J. **48**, 2071

59. Marcuse, D. 1982, Optical Electronics, Secon Edition. Van Nostrand Reinhold, New York.

60. Marz R., Cremer C., 1992, J. light. Tech., **10**, 2017-2022

61. Maschmeyer R. O., and Lerminiaux C., 1996, Conference Proceedings, LEOS'96, 32-33 .

62. McGreer K.A., 1995a, IEEE Photonics Technol. Lett., **7** , 324-326.

63. McGreer K.A., 1995b, IEEE Photonic Technol. Lett., **7,** 397-399.

64. McGreer K.A., 1996a, Appl. Opt., **35**, 5904-5910.

65. McGreer K.A., 1996b , IEEE Photon. Technol. Lett., **8**, 551-553.

66. McGreer K.A., Broughton J. N., Hnatiuk H. J., Sun Z. J., and Cameron R., 1996c, Proc. SPIE Conf. Emerging Components and Technologies for all Optical Photonic Systems II., **2918**, 92-99.

67. Mickelson, A. R., 1992. Physical Optics. Van Nostrand Reinhold, New York.

68. Mickelson A. R., 1993, Guided Wave Optics, Van Nostrand Reinhold, NewYork.

69. Nishihara H., Haruna M., and Suhara T., Optical Integrated Circuits, Published by P.R. Donelley & Sons Company, 43

70. Noda H., Namioka T., and Seya M., 1974, J. Opt. Soc. Am., **64**, 1037-1042

71. Nosu K., Ishio H., and Hashimoto K., 1979, Electron. lett., **15**, 414-415.

72. Okamoto K. and Yamada H., 1995, Optics Lett., **20**, 43.

73. Okamoto K. and Sugita A., 1996, Electron. Lett., **32**, 1661.

74. Oda K., Tokato N., Kominato T., and Toba H., 1989, IEEE Photon. Technol. Lett. **1**, 137-141.

75. Oehrlein G. S., Lindstom J. L., 1989, J. Vac Sci. Technol. A, 7, 1035-1042

76. Papoulis A., 1968, Systems and Transformations with Applications in Optics. Toronto: McGraw-Hill, 316.

77. Poguntke K. R. and Soole J. B. D., 1993, J. Light. Tech., **11**, 2191-2200

78. Poguntke K.R., et al., 1993, Appl Phys. Lett., pp. 2024-2026.

79. Potenza M., 1996, IEEE Communications Magazine, August, 96.

80. Rowland H.A., 1883, Phil. Mag., **16**, 197-210.

81. Scobey M. A., Lekki W. J., and Geyer T. W., 1997, March, Laser Focus World, pp. 111-116.

82. Smit M.K., 1988, Electron. Lett. **24**, 385-386.

83. Smith M. and McGreer K. A., "A guide to design of non-birefringence glass waveguide ", in preparation.

84. Soole J.B.D., Poguntke K., Scherer A., LeBlanc H.P., Chang-Hasnain C., Hayes J. R., Caneau C., Bhat R., and Koza M.A., 1992, Appl. Phys. Lett., **61**, 2750-2752.

85. Soole J.B.D., Amersfoort M.R., LeBlanc H.P., Andreadakis N.C., Rajhel A., Caneau C., Bhat R., Koza M.A., Youtsey C. and Adesida I., 1996, IEEE Photo. Technol. Lett., **8**, 1340.

86. Soole J.B.D., Poguntke K., Scherer A., LeBlanc H. P., Chang-Hasnain C., Hayes J. R., Caneau C., Bhat R., and Koza M. A., 1992, Electron. Lett., **28**, 1805-1806.

87. Spiekman L.H., Amersfoort M.R., Vreede A.H. de, Ham F.P.G.M. van, Kuntze A., Pedersen J.W., Demeester P., and Smit M. K., 1996, J. Light. Tech., **14**, 991-995.

88. Steinbruchel Ch., Lehmann H. W., and Frick K., 1985, J. Electrochem. Soc. : Solid stste Sci. Technol., **132**, 180-184.

89. Stewart W. J., Love J. D., 1985, IOOC/ECOC'85, 559-562.

90. Sun Z.J., McGreer K.A., and Broughton J.N., 1997a, Electron. lett., **33**, 1140-1142.

91. Sun Z. J., McGreer K. A., and Broughton J. N., 1997b, Digest of the LEOS Summer Topical Meetings, ThD2, 52-53

92. Sun Z. J., McGreer K. A., and Broughton J. N., 1998, IEEE Photon. Technol. Lett. **10**, 90-92.

93. Suzuki S., 1997, Digest of the LEOS Summer Topical Meeting, FD1, 80-81

94. Suzuki S., Inoue Y., and Ohmori Y., 1994, Electron. Lett., **30**, 642-643

95. Syms R., Cozens J., 1992, Optical Guided Waves and Devices, McGraw-Hill (UK) Limited.

96. Taga H., 1996, J. Lightwave Technol., **14**, 1287-1298

97. Takahashi H., Hibino Y., Ohmori Y., and Kawachi M., 1993, IEEE Photon. Technol. Lett., **5**, 707-709

98. Takahashi H., Suzuki S., Kato K., Nishi I., 1990, Electron. Lett., **26**, 87-88.

99. Takato N., et al, 1990, IEEE J. Selec. Area. Comm., **8**, 1120-27.

100. Toba H., Oda K., Nakato N., and Nosu K., 1987, Electron Lett. **19**, 583-584.

101. Toba H., Oda k., Nakanishi K., Shibata N., Nosu K., Takato N., and Fukuda M., 1990, J. Lightwave Technol. **8**, 1396 (1990).

102. Tong F., Li C. S., Stevens A. E., and Kwark Y. H., 1994, IEEE Photonics Technol. Lett., **6**, 971-973

103. Trouchet D., Beguen A., Prel C., Lerminiaux C., Boex H. and Maschmeyer R. O., 1997, OFC'97, ThM7.

104. Vassallo C., 1990, IEE Proc. J., **137**, 193-202

105. Vellekoop A.R. and Smit M.K., 1989, Electron. Lett. **25**, 946-947.

106. Verbeek B. H., Henry C. H., Olsson N. A., Orlowsky K. J., Kazarinov R. F. and Johnson B. H., 1988, J. Lightwave Technol, **6**, 1011-1013

107. Warzanskyj W., et al., 1988, Appl. Phys. Lett., **53**, 13-15

108.Winzer, Mahlein H., and Reichlet A., 1981, Appl. Opt., **20**, 3128-3135.

109.Winters H. F., Coburn J. W., and Chuang T. J., 1983, J. Vac. Sci. Technol. B, 1, 469

110.Woodward S.L., Parayanthal P., and Koren U., 1993, IEEE Photon. Technol. Lett., **5**, 750-752.

111.Zirngible M., Joyner C. H., Stulz L.W., Koren U., and Chien M.D., 1994a, IEEE Photon. Technol. Lett., **6**, 513-515

112.Zirngible M. and Joyner C. H., 1994b, postdeadline paper PD16, OFC '94, San Jose, CA.

IMAGE EVALUATION
TEST TARGET (QA-3)

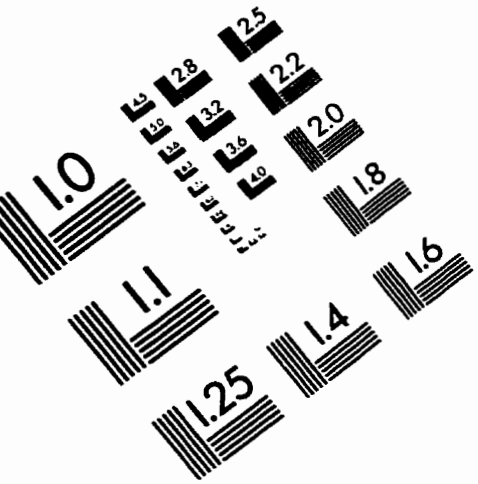

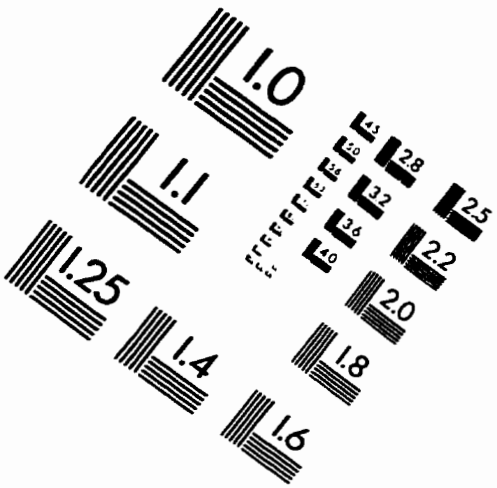

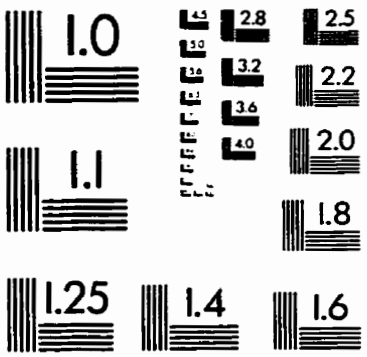

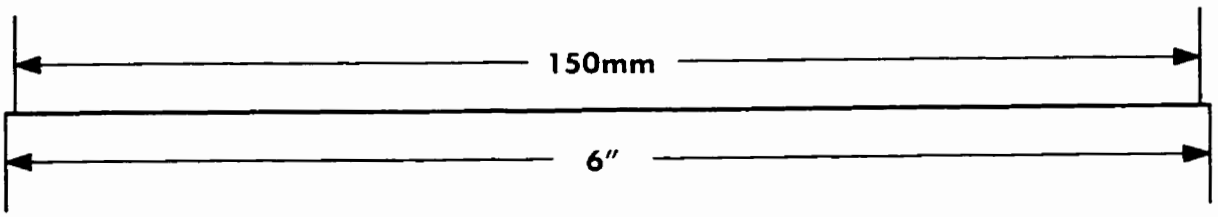

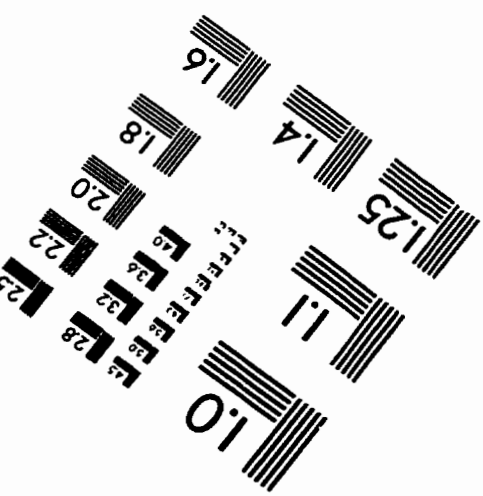

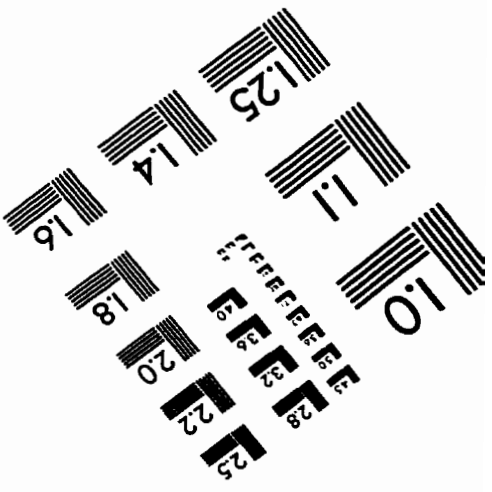

APPLIED IMAGE, Inc
1653 East Main Street
Rochester, NY 14609 USA
Phone: 716/482-0300
Fax: 716/288-5989